Low Temperature Cracking
of
Asphalt Concrete
Pavements

MINNESOTA
DEPARTMENT OF TRANSPORTATION

LRRB
LOCAL
ROAD RESEARCH
BOARD

Research

Technical Report Documentation Page

1. Report No. MN/RC – 2004-23	2.	3. Recipients Accession No.	
4. Title and Subtitle LOW TEMPERATURE CRACKING OF ASPHALT CONCRETE PAVEMENTS		5. Report Date March 2004	
		6.	
7. Author(s) Mihai O. Marasteanu, Xue Li, Timothy R. Clyne, Vaughan R. Voller, David H. Timm, David E. Newcomb		8. Performing Organization Report No.	
9. Performing Organization Name and Address University of Minnesota Department of Civil Engineering 500 Pillsbury Drive S.E. Minneapolis, MN 55455-0116		10. Project/Task/Work Unit No.	
		11. Contract (C) or Grant (G) No. (c) 74708 (wo) 112	
12. Sponsoring Organization Name and Address Minnesota Department of Transportation Office of Research Services 395 John Ireland Boulevard Mail Stop 330 St. Paul, Minnesota 55155		13. Type of Report and Period Covered Final Report 1999-2004	
		14. Sponsoring Agency Code	
15. Supplementary Notes http://www.lrrb.org/PDF/200423.pdf			

16. Abstract (Limit: 200 words)

This report investigates the low temperature behavior of asphalt pavements based on experimental results obtained for three mixtures used in the construction of cells 33, 34, and 35 at Mn/ROAD facility as well as field information acquired over the years at Mn/ROAD.

As a result of this research a new test method was developed to determine the low temperature fracture properties of asphalt mixtures based on tests performed on semi circular specimens tested in bending. This method can be used to select materials with better fracture resistance and therefore better performance in the field.

Two models were developed to predict the low temperature cracking performance of asphalt pavements. The first model predicts the crack spacing in asphalt pavements exposed to low temperatures based on continuum mechanics and the frictional restraint provided by the aggregate base. The second model predicts the accumulation of damage and the propagation of the crack through the asphalt layer as temperature drops based on cohesive zone model.

17. Document Analysis/Descriptors		18. Availability Statement	
Thermal Cracking Asphalt Mixture Crack Spacing Fracture Toughness	Fracture Energy Cohesive Crack Semi Circular Bend Test	No restrictions. Document available from: National Technical Information Services, Springfield, Virginia 22161	
19. Security Class (this report) Unclassified	20. Security Class (this page) Unclassified	21. No. of Pages 228	22. Price

LOW TEMPERATURE CRACKING
OF ASPHALT CONCRETE PAVEMENTS

FINAL REPORT

Mihai O. Marasteanu
Xue Li
Timothy R. Clyne
Vaughan R. Voller
David H. Timm
David E. Newcomb

Department of Civil Engineering
University of Minnesota

March 2004

ACKNOWLEDGEMENTS

Table of Contents

List of Tables

List of Figures

EXECUTIVE SUMMARY

Low temperature cracking is the major distresses in asphalt pavements in the northern U.S. and Canada. The current specifications address this issue based on creep and strength tests performed at low temperatures on both asphalt binders and asphalt mixtures. As part of the newly released Design Guide, a thermal cracking (TC) model was developed that predicts the performance of a given pavement in terms of crack spacing and service life. In the past years an increasing number of researchers have realized the limitations of the current system and started to investigate the use of fracture mechanics based tests and analyses to address the low temperature cracking issue. Anecdotal evidence also indicated the need to consider the effect of the entire pavement system, in particular of the granular base materials, in the analysis.

In this research the role of the aggregate base and the development of fracture mechanics based experimental procedures and analyses are investigated and guidelines to improve the material selection process and the prediction of field performance with respect to low temperature cracking are proposed.

In Part 1 a frictional restraint crack spacing model is developed and tested. In chapter 1.1 a literature search is performed on the existing thermal cracking models. None of the existing models account for traffic effects, and only the Fictitious Crack Model takes interface friction into consideration. Given the limitations of existing models it is recommended that a new thermal cracking model be developed. The model should consider the entire pavement cross section as an integrated engineering system, consider the interface friction between layers, take into account traffic effects on crack development, and simulate heat transfer throughout the pavement structure.

In chapter 1.2 a mechanistic pavement model that predicts thermal crack spacing is developed. The model is based upon a two-dimensional continuum, solved by the finite difference method employed in commercial available software FLAC, and considers the frictional properties of the supporting granular material in the analysis. It was found that the frictional properties of the supporting layer have a significant effect on the stress relief near the free edge of a pavement surface layer. The stress relief region was used to explain the regularity of crack spacing in that cracks will not form in regions below a threshold stress level. Further, through simulation, it was found that the addition of thermal gradients and traffic loads to the

model would effectively shorten the crack spacing and increase the amount of cracking. These observations are consistent with thermal cracking field performance.

In chapter 1.3 a model comparison study was performed to assess whether the thermal cracking model would predict crack spacing consistent with field observations. Data pertaining to four full-scale pavement test sections at Mn/ROAD were gathered and entered into the thermal cracking model. Based on the results of the comparison procedure it may be stated that the thermal cracking model does pass the test of reasonableness.

In chapter 1.4 the model was reexamined and a parametric study was performed to develop a better understanding of how the model behaves and identify the key input variables.

In Part 2, a test procedure was developed to measure fracture mechanics asphalt mixture properties at low temperatures. In chapter 2.1 a literature search was performed. Based on the results of the literature search, two configurations emerged as potential candidates for the low-temperature fracture testing of asphalt mixtures: the modified IDT test and the semi-circular bend test. The SCB test was selected for further use in the experimental work based on a number of advantages over the modified IDT test and a test protocol previously developed at the University of Minnesota was selected for controlling the loading of the SCB specimens.

Chapter 2.2 describes in detail the three asphalt mixtures from Mn/ROAD cells 33, 34, and 35 and the testing protocol details.

In chapter 2.3 the frictional restraint model developed in part 1 is revisited based on new information about the properties of the aggregate base materials. The cohesion (C) and friction angle (Φ) of the base layers obtained from triaxial tests were used to compute the crack spacing in the crack spacing model developed in subtask 1. Significant differences were fund between the predicted and the field crack spacing which indicated the need for accurate material properties for base layers in frozen state.

Part 3 consists of the data analysis of the experimental work and the development of a crack propagation model based on cohesive zone model approach. Chapter 3.1 presents the test results and the procedure used to calculate stiffness, fracture toughness, and fracture energy. Statistical analysis was used to determine the significance of the effects of the type of binder, the density, and the environmental temperature. Both the fracture toughness and the fracture energy changed as the test temperature changed, which clearly indicates that the fracture properties of

asphalt mixture, like the other mechanical properties of asphalt mixture, are temperature-dependent and asphalt mixtures should only be compared at the same specified temperature.

In chapter 3.2 the Thermal Cracking (TC) model, incorporated in the recently released American Association of State Highway and Transportation Officials (AASHTO) Design Guide and the cohesive zone model (CZM) approach were reviewed and the advantages and disadvantages of the two models were discussed.

In chapter 3.3 the crack spacing prediction from the TC model and from the frictional restraint model developed in Part 1 were tested again field data collected from Mn/ROAD. It was found that the frictional restraint model predicted reasonable crack spacing values, which in one case were not significantly different than the field values, while the TC model did not predict any cracking.

Chapter 3.4 describes the development of a cohesive zone model to analyze the thermal cracking mechanism in asphalt pavements exposed to low temperatures. Numerical simulations were performed for the three mixtures to simulate the thermal crack development in an asphalt pavement. Due to the high complexity of the calculations, the model parameters were kept independent of time and temperature, which is an oversimplification of asphalt pavement behavior at low temperatures. The predicted crack evolutions indicate that, based on the material parameters used, the three mixtures do not behave very differently. The analysis also indicates that after the crack initiates it takes very little additional temperature decrease, approximately 0.5°C, to propagate the crack completely. The model developed can be used to effectively simulate the fracture mechanism in asphalt pavements at low temperatures. However, the effectiveness of this model is strongly dependent on material properties that are representative of the material behavior for typical field temperature and loading conditions, which were not available in this project.

Part 4 contains a summary of the findings in this project and recommendations for changing the current specifications to better address low temperature cracking. The recommendations detail the need for a more complex analysis that better simulates field pavement conditions and for obtaining asphalt mixture and aggregate base properties at temperature and loading rates conditions representative of field conditions. These issues will be addressed in the near future as part of a national pooled fund study led by Mn/DOT and University of Minnesota.

PART 1. MODELING

Chapter 1.1. Review of Models

INTRODUCTION

Background

Thermal cracking of asphalt pavements is a common phenomenon in cold regions and has been a recognized problem for some time in Canadian provinces (1, 2, 3, 4, 5, 6) and the northern United States (7, 8, 9, 10, 11). This type of distress is manifested as a series of transverse cracks that extend across the pavement surface in response to cold ambient temperatures (Figure 1.1.1). Yoder and Witczak (12) noted that thermal crack intervals of 6 m to 9 m are typical but may range from less than 1 m up to 30 m. Kirkner and Shen (13) also reported that crack spacing is often regular over the length of a pavement but stated that there was no satisfactory explanation as to why this would occur.
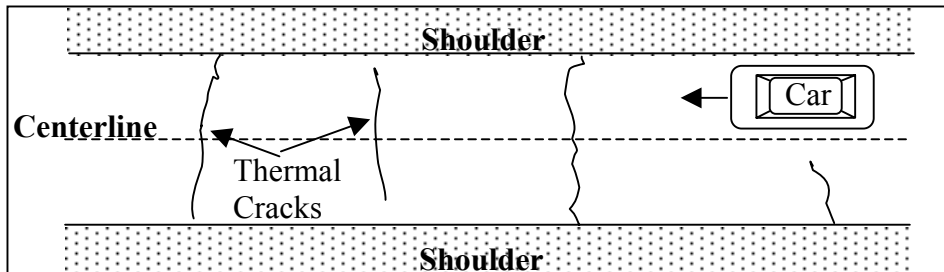
Figure 1.1.1 Thermal Cracking (Plan View)

The primary concern regarding this distress is the ingress of water to the pavement structure through the thermal cracks (14). From a durability standpoint, the presence of water increases the rate of stripping which leads to early deterioration of the asphalt concrete. Additionally, water infiltration promotes pumping of unbound fines in the underlying material leading, in some cases, to a depression at the thermal crack (14). Finally, Fromm and Phang have postulated that an ice lens could form beneath a thermal crack, which would cause an upward lipping or tenting of the crack edges. Additionally, there is mounting evidence that transverse cracks can act as stress focal points from which longitudinal cracks may form.

Much research has been devoted to the problem of thermal cracking. Specifically, a number of thermal cracking models have been developed to predict the onset or amount of cracking that is to be expected for a given set of conditions. This report examines a variety of these models.

Objectives

The primary objective of this report is to identify and characterize existing thermal cracking models for asphalt pavements. Specifically, the models will be examined in light of the fundamental principles on which they are based. An additional objective is to evaluate the models in terms of crack spacing prediction capability, ease of use, required inputs, ability to accommodate interface friction and ability to evaluate traffic effects.

Scope

The model evaluations in this report are based upon the available literature.

REVIEW OF MODELS

Existing thermal cracking models may be categorized as either empirically or mechanistically based. Empirical models, developed through regression analyses of field data, are useful in identifying parameters that affect thermal cracking. However, they are limited to the data set on which they were based and they do not fully explain the cracking phenomenon at a fundamental level. Conversely, mechanistic-based models rely more strongly on mechanics of materials in describing the cracking process at a more fundamental level. However, most existing mechanistic-based cracking models focus on the asphalt concrete layer rather than considering the entire pavement structure as an integrated system. It should also be noted that none of the existing models evaluated in this report account for traffic effects. A discussion of each group of models follows.

Empirically-Based Thermal Cracking Models

In general, empirical models are relatively easy to use once they have been developed and the necessary inputs to the model have been determined. Some model inputs are easily obtained (e.g., pavement thickness), while others require more complicated testing (e.g.,

recovered asphalt penetration). Therefore, the ease of use of a particular model, for a particular agency, depends primarily upon the agency's ability to determine the model inputs.

It is important to keep in mind that the predictive capability of empirical models, as reported by the R^2 value, is strictly limited to the data set on which the model was based. Often, empirical models are extrapolated for use outside of the original inference space and are no longer completely valid.

Fromm and Phang's Empirical Model

Fromm and Phang (14) developed a number of regression equations to predict the cracking index based upon a testing program carried out on 33 pavement sections in Ontario. The cracking index, used by the Ontario Department of Transportation, measures cracking severity on a project wide basis expressed as the amount of transverse cracking per 150 m of two-lane pavement (14):

$$I = N_m + N_f + 0.5*N_h \hspace{5cm} (1)$$

where: I = cracking index

N_m = number of multiple cracking occurrences in 150 m of pavement

N_f = number of full cracking occurrences in 150 m of pavement

N_h = number of half cracking occurrences in 150 m of pavement
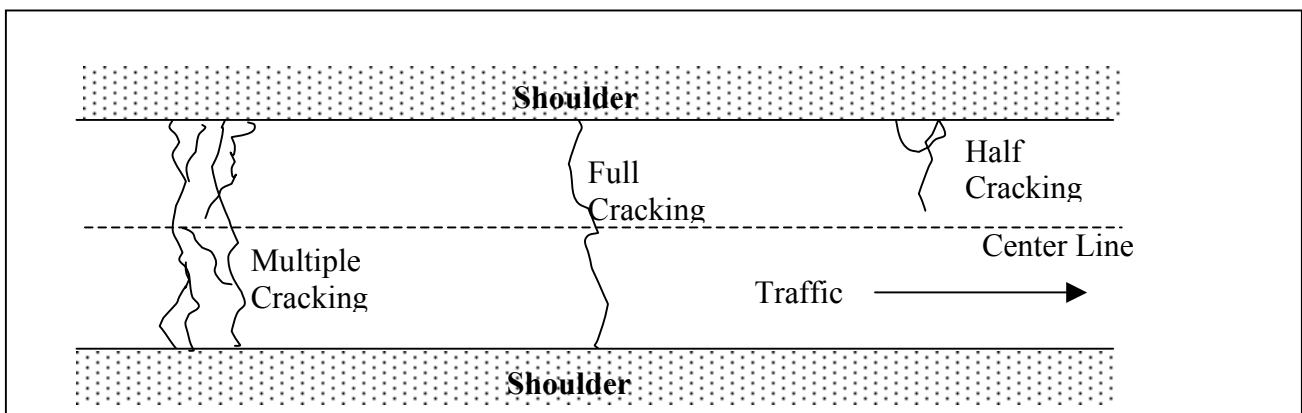
Figure 1.1.2. Cracking Index Crack Definitions (after Fromm and Phang, 1972)

Initially, approximately 40 variables were considered in the statistical analysis. Through step-wise linear regression, Fromm and Phang reduced the parameters down to the eleven listed in Table 1. Three equations were developed, using the parameters, to better characterize the

northern and southern regions of Ontario in addition to a general model describing all of the data. The equations' cracking index predictive capability (R^2) ranged from 0.6 to 0.7 among the three models developed.

Table 1.1.1. Linear Regression Parameters (Fromm and Phang, 1972)

Variable - Description
X_1 - Viscosity Ratio = $\dfrac{Visc@15.6^o C(megapoise)}{Visc@135^o C(centistokes)}$
X_2 - freezing index (degree days)
X_3 - critical temperature, ^oF
X_4 - air voids, % by volume
X_5 - stripping rating
X_6 - recovered asphalt penetration at 25^oC, dmm
X_7 - asphaltenes, % by weight
X_8 - granular base, % Passing 0.075mm sieve
X_9 - asphalt aggregate, % Passing 0.075 mm sieve
X_{10} - granular base, clay content
X_{11} - subbase, % Passing 4.75 mm sieve

Model Input Parameters

Many of the parameters listed in Table 1 are self-explanatory and are commonly used in pavement engineering (e.g., air voids, % passing 0.075mm sieve). However, several parameters are more specific to the problem of thermal cracking and deserve further explanation. These parameters are the freezing index, critical temperature, and stripping rating.

Freezing Index

The freezing index (F.I.) is a measure of the length and severity of winter. It is expressed as the cumulative number of degree-days that are below freezing. Using average historical climatological data, the freezing index may be calculated by (15):

$$\text{F.I.} = \sum_{i=1}^{n} \left(0^{o}C - Tav_i\right) \qquad (2)$$

where: Tav_i = average air temperature on the ith day; n = number of winter days

Critical Temperature

Fromm and Phang (14) devised the critical temperature to measure the flow properties of the asphalt concrete. The critical temperature is the temperature at which the viscous flow under creep loading in one hour equals the temperature shrinkage in one hour. At temperatures higher than the critical temperature, it is believed that the viscous flow of the material is high enough to relieve the stresses developed due to shrinkage. Conversely, at temperatures below the critical temperature, the thermal stresses develop faster than the viscous flow may relax them and cracks are more likely to develop.

To determine the critical temperature, Fromm and Phang (14) made use of two testing methods. First, they conducted tests to determine the thermal coefficient of contraction (α). Next, one hour creep tests were conducted on the material to measure the viscous flow properties at different temperatures. The results of the creep tests were then plotted as shown in Figure 1.1.3 to determine the viscous flow versus temperature relationship. The critical temperature was determined by assuming a temperature decrease in one hour (ΔT), multiplying by α and determining the corresponding temperature on the creep curve. A key assumption of this model is that the assumed ΔT was 10°F per hour. This value was based on climatological data in Ontario and may not be widely applicable.

Stripping Rating

Fromm and Phang (14) used the stripping rating as an indicator of bond strength between the asphalt and aggregate and ultimately tensile strength of the composite material where high stripping ratings corresponding to low tensile strengths. A composite scoring system was used to visually measure the stripping rating (S) of extracted asphalt concrete according to:

5

$$S = P + C + F \tag{3}$$

where: S = stripping rating between 1 and 10

P = index of stripping penetration (Table 2)

C = index of coarse aggregate stripped (Table 3)

F = index fine aggregate stripped (Table 4)
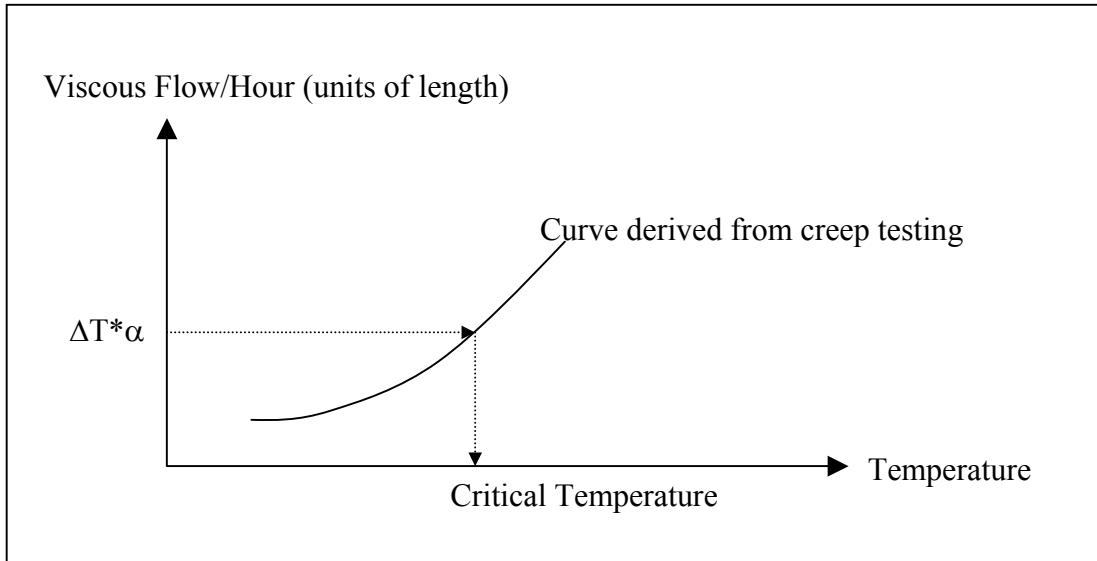
Figure 1.1.3. Critical Temperature Determination (after Fromm and Phang, 1972).

Table 1.1.2. Values of P (Fromm and Phang, 1972)

P	Stripping Penetration, measured from bottom of sample to extent of stripping
1	0 mm
2	< 13 mm
3	13 mm to 25 mm
4	25 mm to 75 mm
5	> 75 mm

Table 1.1.3. Values of C (Fromm and Phang, 1972)

C	Stripped Coarse Aggregate
0	< 10%
1	10% to 30%
2	31% to 60%
3	> 60%

Table 1.1.4. Values of F (Fromm and Phang, 1972)

F	Stripped Coarse Aggregate
0	< 10%
1	10% to 30%
2	> 30%

General Model

The general model predicts cracking index (I) for all the pavement sections. Note that this equation does not use the base or subbase properties shown in Table 1 (Fromm and Phang, 1972):

$$I = 52.22x_1 + 0.0007093x_2 + 0.4529x_3 - 1.348x_4 \qquad (4)$$
$$+ 0.4687x_5 - 0.07903x_6 - 0.4887x_7 - 0.1258x_8 - 0.1961x_9$$

$R^2 = 0.6357$

Northern Model

The northern model represents test sections where penetration graded asphalts of equal to or greater than 110 dmm were used (Fromm and Phang, 1972):

$$I = 30.30x_1 + 0.00602x_2 + 0.5253x_3 - 1.280x_4 \qquad (5)$$
$$+ 0.5190x_5 - 0.02563x_6 - 0.0844x_7 - 1.496x_8 + 0.225x_9$$
$$+ 3.1043x_{10} + 0.097x_{11}$$

$R^2 = 0.6222$

Southern Model

The southern model represents test sections where penetration-graded asphalts of less than 110 dmm were used. Note that this equation, like the general model, does not consider the base and subbase properties (14):

$I = \quad 64.74x_1 + 0.008279x_2 + 0.3935x_3 - 1.491x_4 \hspace{4cm} (6)$

$\hspace{1.5cm} + 0.3246x_5 - 0.0001481x_6 - 0.6069x_7 - 0.8071x_8 - 0.6567x_9$

$R^2 = 0.7038$

In general, it was found that the coefficients associated with each independent variable were consistent with expectations in regard to thermal cracking. A notable exception, however, concerns the pavement voids. The coefficient for air voids determined by Fromm and Phang was less than zero. In other words, more air voids corresponded to less pavement cracking, when the reverse was expected. Fromm and Phang (1972) explained that Ontario pavements were typically constructed with lower air voids than recommended by the Asphalt Institute. They then cited several investigations showing that within certain void limits, the stiffness of a mix may decrease with an increase in voids (Van Draat and Sommer, 1966; Bazin and Saunier, 1967). Therefore, air voids were a proxy for stiffness and a mix having higher voids with lower stiffness should in fact decrease the amount of thermal cracking.

The discussion above highlights an important point regarding empirical models. Namely, they are empirical and are therefore limited to the conditions from which the data were drawn. An engineer using such a model must be cognizant of the limitations or inaccurate predictions may result.

Airport Pavement Model

Haas, et al (16) conducted an empirical study similar to that of Fromm and Phang (14). In the study, data were gathered from 26 airport pavements throughout Canada. After performing a series of laboratory tests on extracted asphalt concrete cores, evaluating the condition of the existing pavement and conducting a series of statistical analyses, the following empirical model was proposed (16):

$$TRANCRAK = 218 + 1.28 \cdot ACTHICK +$$
$$2.52 \cdot MINTEMP + 30 \cdot PVN - 60 \cdot COEFFX \qquad (7)$$

$R^2 = 0.70$

where: TRANCRAK = transverse crack spacing (m)

ACTHICK = thickness of asphalt concrete (cm)

MINTEMP = minimum temperature recorded on site (°C)

PVN = Pen-Vis Number (McLeod, 1976)

COEFFX = coefficient of thermal contraction (mm/1000mm/C)

As shown in equation (7), the original viscosity of the binder has not been taken into account.   It was stated that the original binder viscosity data were not obtainable and therefore were not incorporated in the regression analyses. Therefore, their assumption was that the "correct" initial penetration grade was selected for each site (16). In other words, it was assumed that the binder viscosity was selected so as to preclude thermal cracking and any thermal effects that were observed resulted from the variables in equation (*7*).

Mechanistic-Based Thermal Cracking Models

In contrast to empirically based models, mechanistic cracking models are computationally much more complex. Mechanistic models, based upon principles of mechanics, usually require the solution of a system of linear or non-linear equations. Despite the increased complexity, when compared to empirical models, they tend to explain the thermal cracking phenomenon at a more fundamental level.

Most mechanistic thermal cracking models, including those examined below, focus almost exclusively on the asphalt concrete surface in the modeling process. The last model, known as the fictitious crack model, does include interface friction, but does so as a special boundary condition imposed on the asphalt concrete.

Hills and Brien - Fracture Temperature Prediction

Hills and Brien (17) developed a means of predicting the temperature at which a bituminous mixture will fracture. Their method was later extended for use as a mix evaluation tool (18). It is important to realize that this method does not predict amount or frequency of cracking, only the temperature at which cracks may form.

The governing principle of their approach is illustrated in Figure 1.1.4. As the temperature decreases, right to left, thermal stresses develop due to the assumption that the material is fully restrained. The tensile strength curve in the figure is representative of laboratory test results. When these two curves intersect, the stress has exceeded the strength and it is assumed that a thermal crack develops.

A key component of the model is the determination of thermally induced stress. Hills and Brien (17) considered an elastic isotropic material whereby the state of stress in any one of the principle directions may be expressed by the inverse of Hooke's Law:

$$\sigma_i = \frac{1}{1+\upsilon} \cdot E \cdot \varepsilon_i + \frac{\upsilon}{1+\upsilon} \cdot 3 \cdot p \qquad i = x, y, z \tag{8}$$

where:

$$p = \frac{\sigma_x + \sigma_y + \sigma_z}{3} \qquad\qquad \upsilon = \text{Poisson's ratio}$$

E = stiffness
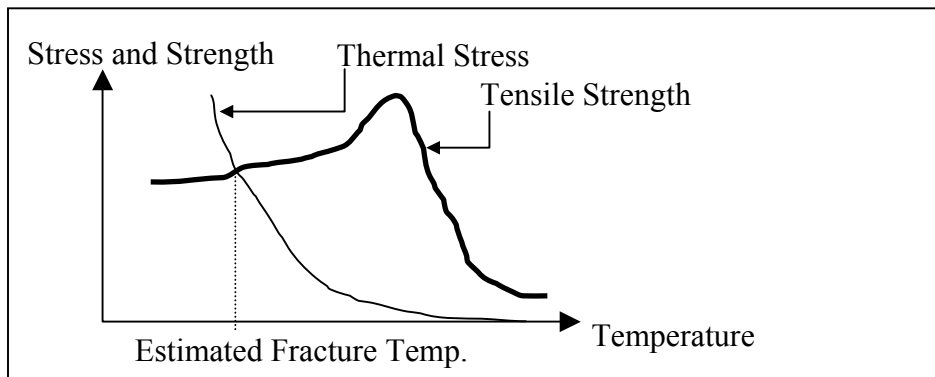
ε_i = strain

σ = stress

Figure 1.1.4. Method of Estimating Fracture Temperature (after Hills and Brien, 1966)

Hills and Brien (17) imposed certain stress and strain conditions to approximate the behavior of asphalt concrete as either an infinite beam or an infinite slab. Table 1.1.5 summarizes these conditions and the resulting expressions for stress.

Table 1.1.5 Two Stress Formulations (after Hills and Brien, 1966).

Case	Stress and Strain Conditions	p =	σ_x =
Infinite Beam	$\sigma_y = \sigma_z = 0$	$\dfrac{\sigma_x}{3}$	$E\varepsilon_x$
Infinite Slab	$\sigma_z = 0$ $\varepsilon_x = \varepsilon_y$	$\dfrac{2 \cdot \sigma_x}{3}$	$\dfrac{1}{1-v} \cdot E\varepsilon_x = \sigma_y$

According to the theory of elasticity, the total strain (ε_t) in a material may be expressed as the summation of the mechanical (ε_m) and thermal strains (ε_{th}) or:

$$\varepsilon_t = \varepsilon_m + \varepsilon_{th} \tag{9}$$

where: $\varepsilon_m = \varepsilon_x$ as in Table 5

   ε_{th} = thermally induced strain = $\alpha\Delta T$

   α = linear coefficient of thermal contraction/expansion

   ΔT = change in temperature

However, due to the assumed infinite nature of the problem, the total strain at any point in the material must equal zero, and (9) becomes:

$$0 = \varepsilon_m + \varepsilon_{th} \tag{10}$$

Substituting the appropriate terms into (10) and solving for σ_x in either the infinite slab or beam cases yields:

$$\sigma_x = -E\alpha\Delta T \qquad\qquad \text{Infinite Beam} \tag{11}$$

$$\sigma_x = -\frac{E}{1-v}\alpha\Delta T \qquad\qquad \text{Infinite Slab} \tag{12}$$

Finally, Hills and Brien (17) recognized that the stiffness (S) of asphalt concrete is a function of both temperature (T) and time of loading (t). They therefore substituted stiffness (S(T,t)) for elastic modulus (E) in equations (11) and (12):

$$\text{Infinite Beam: } \sigma_x = \int_{T_i}^{T_f} S(T,t)\alpha dT \tag{13}$$

Infinite Slab: $\sigma_x = \int_{T_i}^{T_f} \frac{S(T,t)}{1-v} \alpha dT$ (*14*)

In order to validate the prediction model, Hills and Brien (17) conducted a number of laboratory experiments on asphalt concrete beams to compare predicted and measured fracture temperatures. The specimens were fully restrained beams of asphalt concrete cooled at approximately 10°C/hour. Though their predictions were not exact, they did yield a decent fracture temperature approximation. Further, Hills and Brien (17) asserted that their model predicted the benefit in using a soft binder in terms of reduced fracture temperature.

The Hills and Brien (17) approach is fundamentally sound, assuming that a pseudo-elastic representation of asphalt concrete is valid. Also, the method is relatively simple and the inputs to the model may be obtained by well-established laboratory testing methods. However, it is limited to predicting fracture temperature and not the amount of cracking and thus has limited applicability.

Christison, Murray and Anderson - Thermal Stress Prediction

As further validation of the Hills and Brien approach (17), Christison, Murray and Anderson (19) employed the model to predict fracture temperatures of field test pavements in Canada. The objective of their study was to examine a number of different stress analyses and compare fracture temperature predictions to that measured in the field. Central to this effort was the construction of two test pavements. The first pavement was constructed in central Alberta in 1966 (20). The second pavement was constructed in Manitoba in 1967 and is commonly known as the St. Anne Test Road (21).

Measured and predicted fracture temperatures and times were compared. Though a number of analyses were used, it was found that a pseudo-elastic beam (equation *13*) analysis yielded reasonable results without the added complexities of modeling the asphalt concrete as a viscoelastic material.

Computer Program COLD

Finn, et al (22, 23) implemented the Hills and Brien (17) approach in the computer program COLD. The three main uses of the program, as viewed by Finn et al, were to aid in the

binder selection process, identify the potential for low temperature cracking of particular mixes in particular locations and to help develop pre-paving specifications (23).

COLD Framework

The framework of the COLD program is pictured in Figure 1.1.5. In the program, Fourier's second law of heat transfer, with special surface boundary conditions, is solved by finite differences to determine the thermal gradient within the pavement. The thermal gradient is then used to calculate the thermal stresses, assuming either a pseudo-elastic slab or beam, by solving equation (*13*) or (*14*) numerically. The governing diffusion equation is:

$$\rho C \frac{\partial T}{\partial t} = k \frac{\partial^2 T}{\partial x^2} \qquad (15)$$

where:

k = thermal conductivity (W/m*K) $\qquad$ t = time (s)

T = temperature (K) $\qquad$ C = specific heat (J/kg*K)

ρ = density (kg/m^3)

The heat flux boundary condition at the pavement surface include terms for convection, radiation and solar absorption:

$$q = h(T_a - T_p) - k \frac{\partial T}{\partial x} + \alpha H_s + \varepsilon\sigma\left(T_a^{\ 4} - T_p^{\ 4}\right) \qquad (16)$$

where:

q = heat flux (W/m^2) $\qquad$ T_a = ambient temperature (K)

h = convective heat transfer coeff. (W/m^{2}K) $\qquad$ T_p = pavement surface temperature (K)

H_s = net solar flux at the surface (W/m^2) $\qquad$ ε = pavement emittance (unitless)

σ = Stefan-Boltzmann constant (W/m^{2}K^4) $\qquad$ α = absorbency of asphalt (unitless)

The other primary component of COLD is the development of a tensile strength versus temperature relationship as illustrated in Figure 1.1.5. This can be derived, as done by Hills and Brien (17), through laboratory testing (e.g., indirect tension testing at cold temperatures). COLD has the added ability to account for the variability of strength with temperature. Therefore, it is possible to incorporate reliability into the analysis by using

13

different percentile strength values as shown in Figure 1.1.6. A higher level of reliability would be achieved by using a lower percentile strength versus temperature curve.

The last component of COLD superimposes strength and stress versus time, as shown in the bottom of Figure 1.1.5. Cracks are assumed to form at the time when the strength is exceeded.

Like the two previous models, COLD does not strictly predict the amount of cracking expected in a pavement. However, a field validation study conducted in Utah established an empirical link between the probability of cracking and amount of expected cracking (23). Whether or not this relationship is widely applicable is not known.
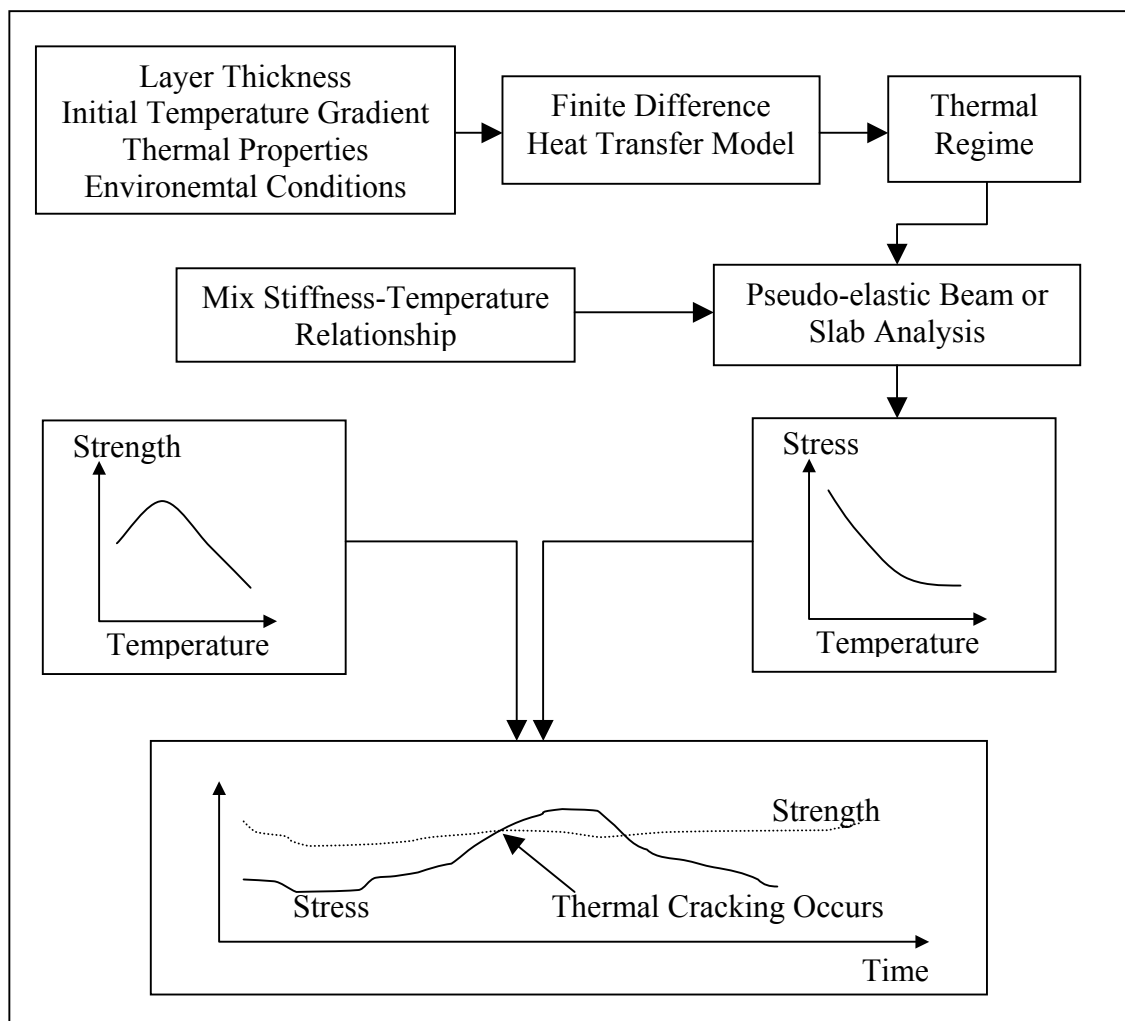
Figure 1.1.5 COLD Framework (after Finn, et al, 1986).
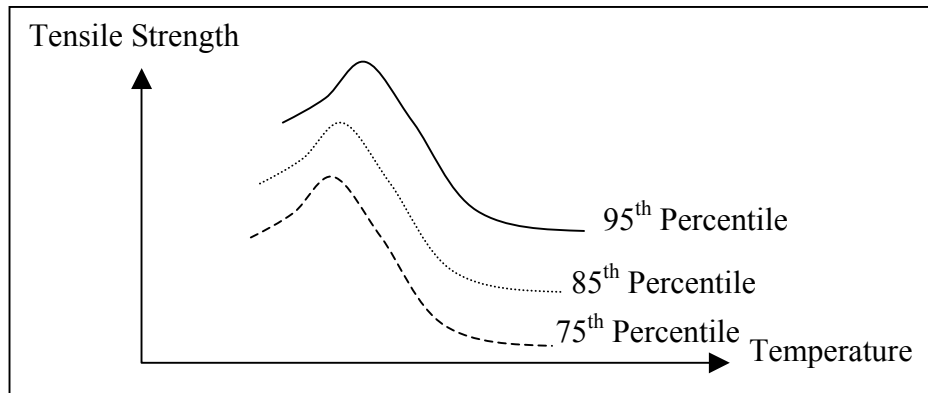
Figure 1.1.6 Tensile Strength Variability with Temperature.

Strategic Highway Research Program (SHRP) A-005 Thermal Cracking Model

Recently, engineers working for SHRP have developed a thermal cracking model to predict the amount of thermal cracking with time (24). The SHRP model uses a viscoelastic representation of the equations developed by Hills and Brien (17) in order to model thermal stresses in the asphalt concrete. This discussion will include the key aspects of the SHRP A-005 model.

Physical Model

Hiltunen and Roque describe the thermal cracking phenomenon in this way (Figure 1.1.7), "…The stresses develop due to contraction of the asphaltic concrete material during cooling. The stresses are not uniform with depth because of a thermal gradient. It is assumed that within the surface layer there are potential crack sites spaced at a distance S. At each of these crack sites, the induced thermal stresses can potentially cause a crack to propagate through the surface layer at which time it is assumed that a transverse crack will be visible on the pavement surface. It is assumed that each of these cracks can propagate at different rates due to spatial variation of the relevant material properties within the surface layer."
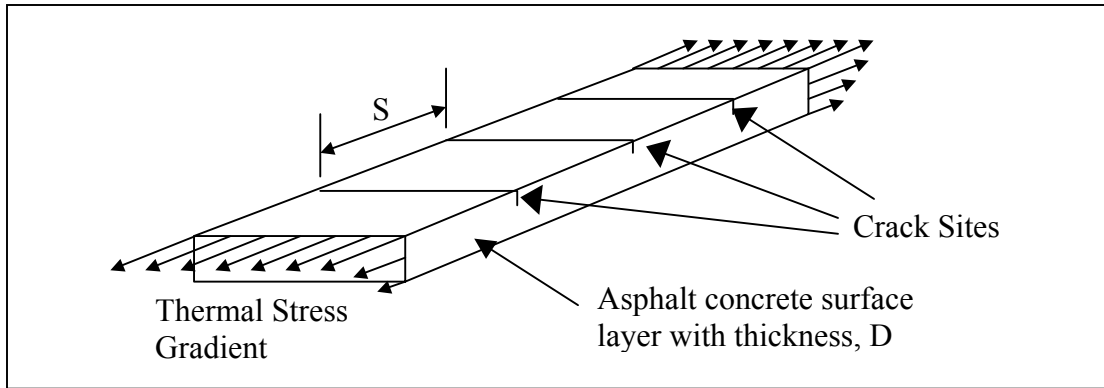
Figure 1.1.7 SHRP A-005 Physical Model (after Hiltunen and Roque, 1995).

The model proposed by Hiltunen and Roque (29) consisted of three primary components. First, a pavement response model to calculate the stress due to cooling. Next, a mechanics-based model to determine the progression of a vertical crack at one crack site having average material properties. The final component is a probabilistic model that determines the global amount of thermal cracking visible on the pavement surface. Figure 1.1.8 illustrates the SHRP A-005 process to determine the amount of thermal cracking. A discussion of each of these components follows.

Pavement Response Model

An important part of the SHRP model, and most thermal cracking models, is the determination of thermal stress for a given change in temperature. The so-called "pavement response model" determines the thermal stress with time. The model employed by Hiltunen and Roque (24) has the following features:

1.   The model is based on a one-dimensional constitutive equation, essentially modeling a uniaxial rod fixed at both ends.

2.   A two-dimensional stress distribution is made by approximation. The approximation procedure determines the thermal stress developed within each uniaxial rod at a particular depth. In this way stress versus depth may be approximated. Figure 1.1.9 illustrates this concept.

3.   The model uses predicted pavement temperatures as input.

4.   The model takes into account the viscoelastic material properties of the asphaltic concrete through a generalized Maxwell model (Figure 1.1.10).

5.   The model makes use of the master relaxation modulus curve, assuming that the material is thermorheologically simple, obtained from indirect tension testing at low temperatures (ITLT).
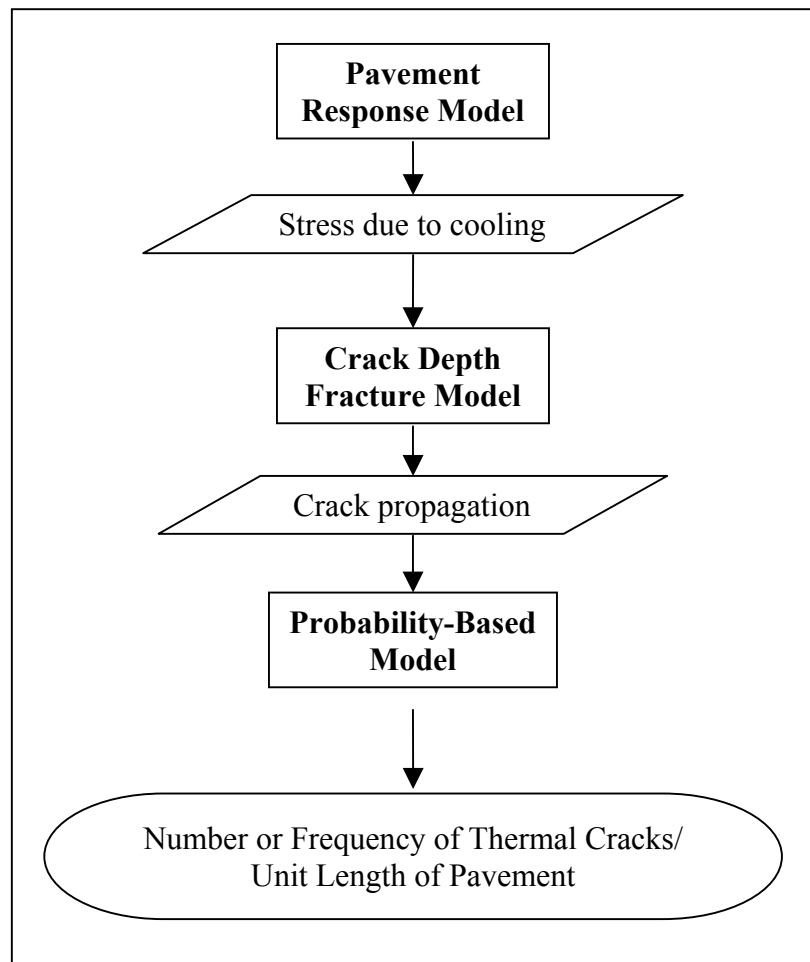
Figure 1.1.8. SHRP A-005 Thermal Cracking Model.
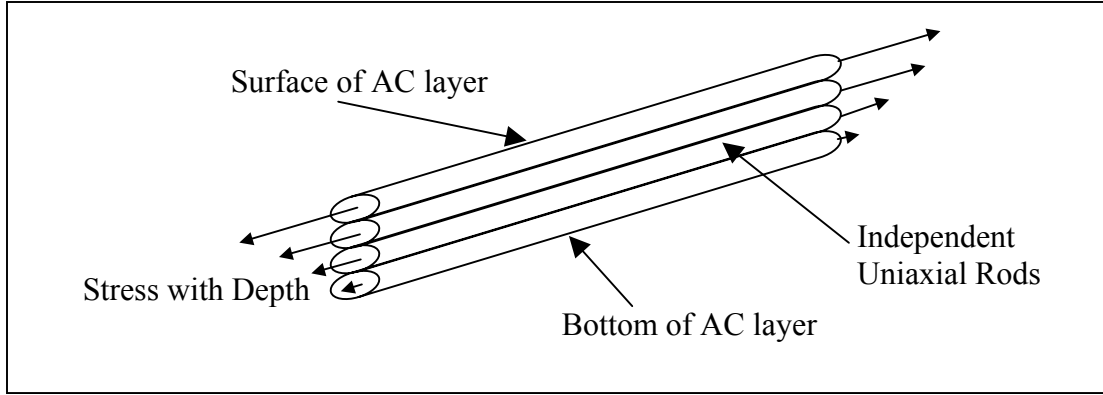
Figure 1.1.9 One-Dimensional Thermal Stress Model.

Hiltunen and Roque (24) model thermal stress according to:

$$\sigma(\xi) = \int_0^\xi E(\xi - \xi') \frac{d\varepsilon}{d\xi'} d\xi' \qquad (17)$$

where: $\sigma(\xi)$ = stress at the reduced time , ξ

$E(\xi-\xi')$ = relaxation modulus at the reduced time, $\xi-\xi'$

ε = strain at the reduced time, ξ

Note that equation (*17*) is essentially the same as that proposed by Hills and Brien (17) in equations (*13*) and (*14*) except that it models a viscoelastic rather than pseudo-elastic material.

Equation (*17*) is expressed in terms of reduced time, ξ. The concept of reduced time is borne out of the process of time-temperature superposition employed in analysis of ITLT data. By definition:

$$\xi = \frac{t}{a_T} \qquad (18)$$

where: t = real time

a_T = temperature shift factor

A full discussion of time-temperature superposition is beyond the scope of this report but may be found in Hiltunen and Roque (25).
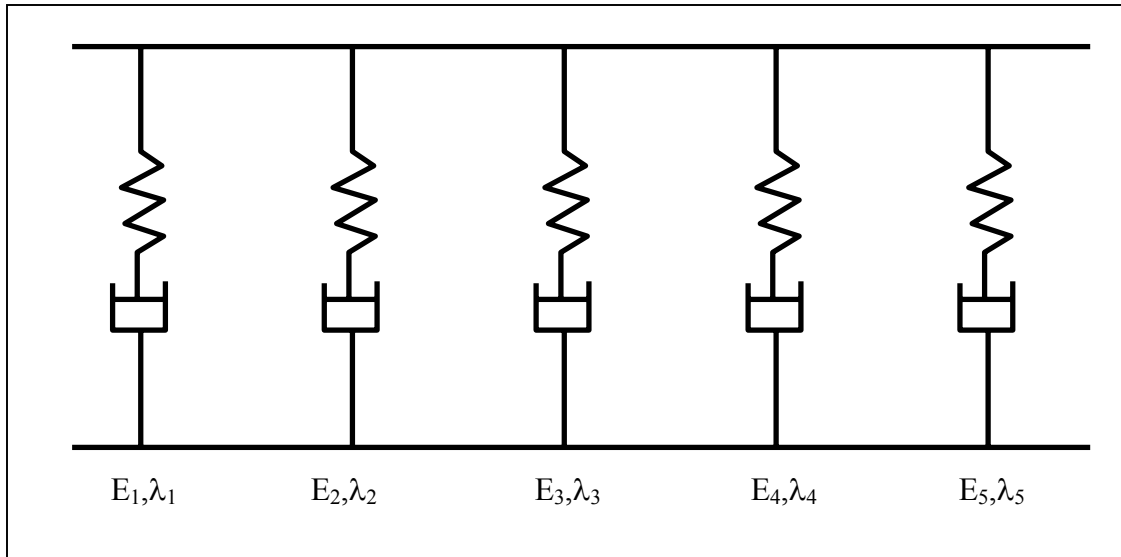
Figure 1.1.10 Generalized Maxwell Model for Relaxation
(after Hiltunen and Roque, 1995).

The thermally induced strain, ε, at reduced time, ξ, may be expressed as:

$$\varepsilon = \alpha\left(T(\xi') - T_0\right) \qquad (19)$$

where: α = linear coefficient of thermal contraction

$T(\xi')$ = pavement temperature at the reduced time, ξ'

T_o = pavement temperature when $\sigma = 0$

ξ' = variable of integration

Equation (*17*) can be written in real time, t, rather than reduced time, ξ, through a change of variables (24):

$$\sigma(t) = \int_0^t E\left(\xi(t) - \xi'(t)\right)\frac{d\varepsilon}{dt'}dt' \qquad (18)$$

By using the above pavement response model, Hiltunen and Roque devised a means of determining the stress gradient within a viscoelastic asphalt concrete surface layer due to a change in temperature. However, in order to predict the rate of crack growth, the pavement response model was coupled with a crack depth fracture model.

Crack Depth Fracture Model

The crack depth fracture model used by Hiltunen and Roque (24) is based upon linear elastic fracture mechanics (LEFM). The fracture model is pictured in Figure 1.1.11. Using the stresses determined by the pavement response model in addition to the pavement structural parameters and material properties, it is possible to predict the stress at the tip of a local vertical crack.
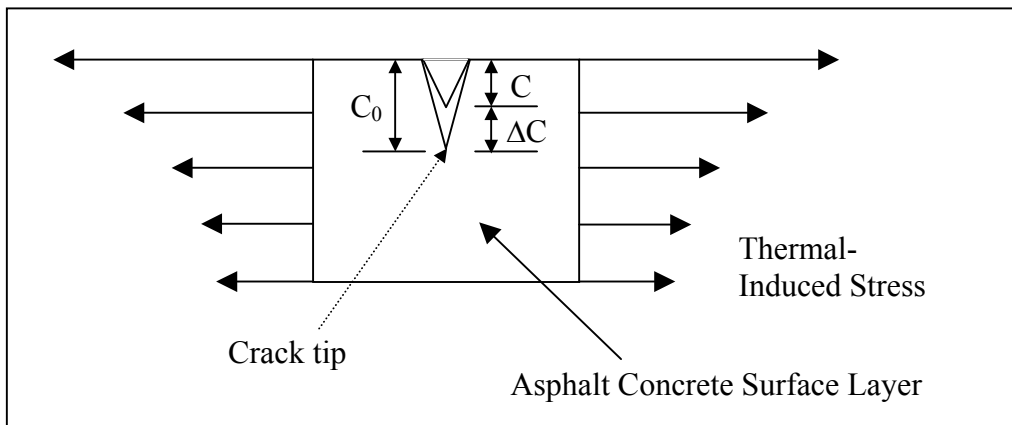
Figure 1.1.11. Crack Depth Fracture Model (after Hiltunen and Roque, 1995).

Hiltunen and Roque (24) employ the Paris Law for crack propagation to determine the change in depth of a local crack subjected to a cooling cycle. The law, based on LEFM, may be expressed as (26):

$$\Delta C = A(\Delta K)^n \qquad\qquad (21)$$

where: ΔC = change in crack depth due to a cooling cycle

ΔK = change in stress intensity factor due to a cooling cycle

A,n = empirically determined fracture parameters

The change in stress intensity, ΔK, involves an additional model. Essentially, the stress intensity model predicts the stress at the tip of the local crack using the far-field stress condition as determined by the pavement response model. The finite element program, CRACKTIP, has been employed by Hiltunen and Roque (24) to model the single vertical crack. CRACKTIP was developed at the Texas Transportation Institute (27).

Schapery (28, 29) has shown that A and n in equation (*21*) are theoretically related to the fundamental viscoelastic properties of the asphaltic concrete. These properties are:

1.   The slope, m, of the linear portion of the logD(t) - log(t) from the master curve obtained from creep tests.

2.   The undamaged tensile strength of the material.

3.   The fracture energy density of the material determined experimentally by monitoring the energy release through crack propagation.

Hiltunen and Roque (25) took these properties into consideration when developing a modified version of an equation, originally developed by Molenaar (30), to determine A and n. Hiltunen and Roque's equation is (25):

$$\log A = 4.389 - 2.52 \cdot \log(K \cdot \sigma_m \cdot n) \tag{22}$$

where: K = field calibrated coefficient = 10,000

σ_m = undamaged mixture strength

The "n" term is experimentally determined and depends upon the slope of the creep compliance curve, m. Lytton, et al (31) developed the equation used by Hiltunen and Roque (25):

$$n = 0.8 \cdot \left(1 + \frac{1}{m}\right) \tag{23}$$

There are several underlying assumptions in Hiltunen and Roque's (24) crack propagation model that deserve mention. As shown in Figure 1.1.9, the pavement layer is discretized into sublayers. For a given cooling cycle, it is assumed that one of two events can occur:

1.   The crack can propagate some finite distance less than the distance between the crack tip and the bottom of the sublayer where the tip is located.

2.   If the crack is predicted to propagate below the sublayer interface, or if the induced stress is greater than the strength of the mix, then the crack is assumed to propagate to the bottom of the sublayer that it is located in.

These assumptions imply that a pavement may not crack in one cooling cycle. Say that the pavement has been discretized into four sublayers, then it would take at least four cooling cycles to propagate a crack through the entire pavement surface layer.

Probability-Based Model

The last component in the SHRP A-005 scheme is the "Crack Amount" model based upon probability and makes use of crack depths as calculated by the crack depth fracture model. There are three main assumptions associated with this model (24):

1. Within a given pavement section, there is a maximum number of thermal cracks that can occur and these cracks are uniformly distributed throughout the section.

2. A crack is not counted as a thermal crack until the crack has propagated through the depth of the entire asphalt concrete layer.

3. The spatial distribution of crack depths is normally distributed, $C \sim N(\mu, \sigma^2)$. C is equal to the crack depth, μ is the crack depth as computed from the fracture model and the variance (σ^2) is unknown.

The cracking amount model was described as a function of the probability that the crack depth is greater than or equal to the thickness of the surface layer. Figure 1.1.12 illustrates the concept specified by these equations (24):

$$AC = \beta_1 \cdot P[\log C > \log D] \qquad (24)$$

or

$$AC = \beta_1 \cdot N\left[\frac{\log \dfrac{C}{D}}{\sigma}\right] \qquad (25)$$

where: AC = observed amount of thermal cracking

β_1 = regression coefficient from field calibration ≈ 381.4

P() = probability that [log C > log D]

N()] = standard normal distribution evaluated at $\left[\dfrac{\log \dfrac{C}{D}}{\sigma}\right]$

σ = standard deviation of log of depth of cracks in pavement ≈ 0.654

C = crack depth as determined from fracture model

D = thickness of surface layer
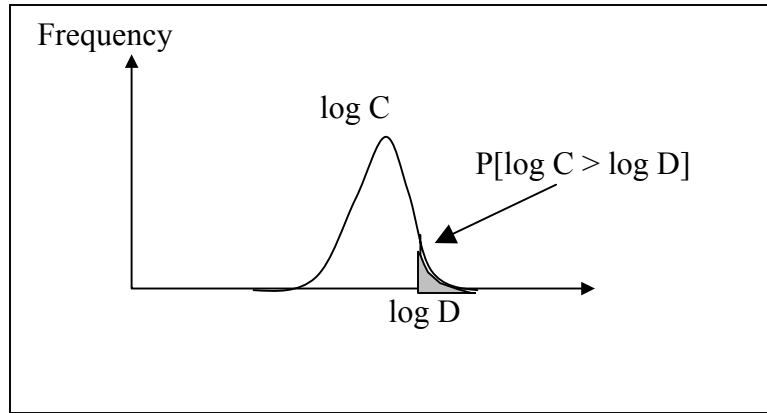
Figure 1.1.12. SHRP A-005 Crack Amount Model.

<u>Model Calibration</u>

The researchers working on the SHRP A-005 model were conscious of the fact that their model was not purely a mechanistic model, but also involved some empiricism. Specifically, the K parameter in equation (*22*), and β_1 and σ in equation (*24*) needed to be determined. This was accomplished by comparing predictions with observations of thermal cracking at 23 different pavement sections. Table 1.1.6 lists each parameter, its corresponding value and the overall R^2 value obtained through the calibration process (24). As seen in the table, their model yields a reasonable prediction when considering the 23 pavement sections evaluated.

Table 1.1.6 Calibrated SHRP A-005 Model Parameters
(Hiltunen and Roque, 1994).

Parameter	Value
K	10,000
β1	381.4
σ	0.654
R^2	0.84

While the predictive capability as shown in Table 1.1. 6 is quite good, like all empirical models, it is strictly limited to the data set on which it was based. The SHRP

23

approach does implement some sophisticated models in predicting thermal cracking. Representing the asphalt concrete as a viscoelastic material is certainly more realistic than elastic or pseudo-elastic as previous models had done (e.g., 17). Additionally, using linear-elastic fracture mechanics and a finite element program to determine stress intensity and crack growth represent significant technological advances in addressing the thermal cracking problem. One could argue, however, that these advances are somewhat extraneous given the empirical component of the model. In words, what are the benefits of using complex mechanical models if they will only be empirically related to field observations at the end of the analysis?

There are a number of other limitations regarding the SHRP A-005 model. First, their framework requires extensive laboratory testing to determine the time-temperature superposition curve and the creep compliance curves of particular mixtures as inputs to the model. Second, the SHRP A-005 model utilizes finite element analysis in what is actually a one-dimensional representation of the problem (Figure 1.1.9). In this sense, finite element analysis could be considered overkill. Third, by assuming a minimum crack spacing (S), the model pre-selects the potential crack locations and the data are therefore inherently skewed toward this assumption. Fourth, the assumption that a crack cannot propagate more than one sub-layer in a single cooling cycle could sometimes pre-define the crack growth rate even though the Paris law is part of the model. Finally, strictly speaking, the probability-based model can only predict half as many cracks that will occur on a given pavement. By definition, the mean crack depth (C) can never be greater than the pavement thickness (D) and therefore, the analysis will end when log C equals log D (Figure 1.1.12). At this point, half the cracks are fully open and the other half are not. Hiltunen and Roque suggest doubling the number of cracks obtained from the analysis to overcome this deficiency.

Fictitious Crack Model

Kirkner and Shen (13) have recently developed a thermal cracking model that uses a different crack propagation model than the SHRP A-005 model. They state that analytical thermal cracking models based upon linear elastic fracture mechanics is of "dubious" value because LEFM does not account for the following observations with respect to thermal cracking (32):

1.   Most thermal cracks start from an uncracked pavement surface and grow through a large portion of the depth of the structure. Therefore, the width of a crack should be used as the primary geometric parameter. As shown in Figure 1.1.11, LEFM uses the crack depth.

2.   Cracking is preceded by micro-cracking.

3.   There is no well defined crack tip, per se, in the cracking of asphalt concrete.

4.   The size of the fracture process zone is usually 50 to 100 mm (or larger) which is usually significant with respect to the pavement thickness. Recall that the LEFM model does not take this into account.

Due to the deficiencies specified above, Kirkner and Shen (13) developed the so-called Fictitious Crack Model (FCM) to predict thermal cracking of asphalt pavements. Their model was first proposed by Hillerborg (33) and represents the meso-scale damage of the asphalt concrete. Central to the model is the concept of the fictitious crack, which is an imaginary line, governed by a softening type stress crack-opening displacement constitutive relationship as shown in Figure 1.1.13 (13). Kirkner and Shen stated that this type of model has been around since the mid 1970's but been gaining greater use more recently (34, 35, 36, 37).
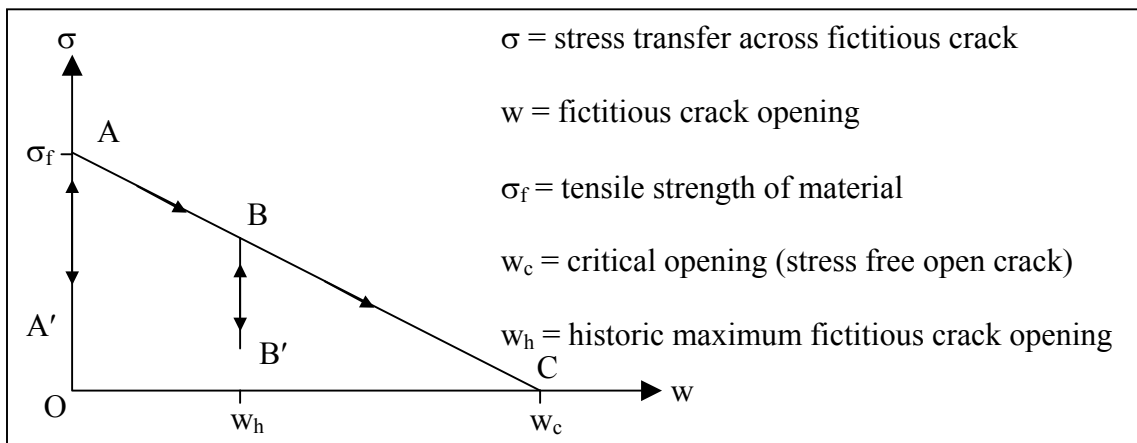
Figure 1.1.13. Constitutive Fictitious Crack Relationship
(after Kirkner and Shen, 1999).

<u>Physical Model</u>

Kirkner and Shen's model is represented schematically in Figure 1.1.14. The key assumptions regarding their model include (13):

1. The damage within a certain distance of a fictitious crack, associated with the thermal effects, is localized into a fictitious crack.

2. λ is the minimum fictitious crack spacing on the order of the aggregate size (10~50 mm).

3. The material outside of the fictitious crack is assumed to be completely undamaged and behaves viscoelastically.

4. The locations and properties of the fictitious cracks are random variables.

5. For a given temperature decrease, ΔT, some fictitious cracks may dominate others. This domination, combined with constraining frictional forces on the interface, will lead to a distribution of major cracks with intervening distances on the macro-scale.

6. The surface thickness is such that there is a uniform temperature profile (i.e, the model is one-dimensional).

7. Interface friction between the asphalt concrete and underlying layer is governed by Coulomb's friction law.

8. As in the SHRP A-005 model, the asphalt concrete is modeled as a viscoelastic thermorheologically simple material (i.e., time-temperature superposition may be used).
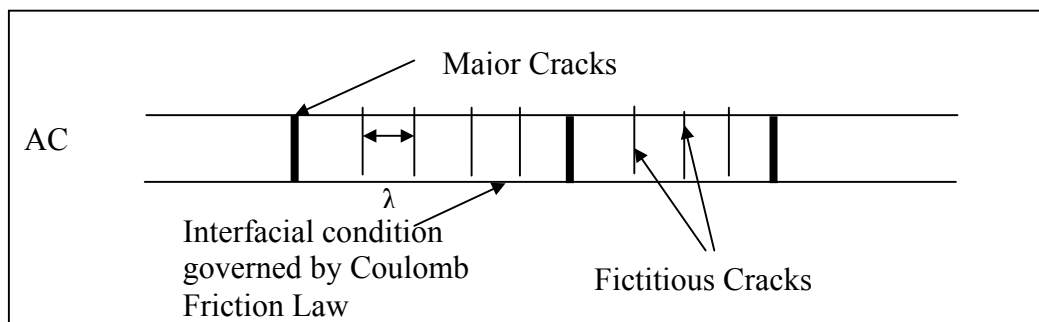
Figure 1.1.14 Fictitious Crack Model (after Kirkner and Shen, 1999).

The fictitious crack is a model that represents the energy dissipation from thermally induced micro-cracking within the characteristic length, λ. Kirkner and Shen (13) present an approximate constitutive relationship for the fictitious crack (Figure 1.1.13). In this model, the two faces of the fictitious crack are completely bound along $\overline{OA}$. Eventually, the tensile

stress may exceed the tensile strength of the material at which time the stress carried across the interface, within λ, will decrease along $\overline{AB}$. At B, the balance point, one of two events may occur. If the fictitious crack continues to open, the stress transfer will continue to decline along $\overline{BC}$ until the critical opening, w_c, has been reached. At this point, the fictitious crack is now a fully open crack and no stress transfer may occur. Alternatively at point B, the conditions that facilitated the crack opening may temporarily cease and the crack will then unload along $\overline{BB'}$ (plastic flow).

Figure 1.1.13 may also be viewed from an energy standpoint. The area under ΔOABB′ represents the energy dissipated in opening the crack to point B. The energy needed to create a completely open crack from undamaged material is represented by ΔOAC (13). This is analogous to the surface energy concept used in linear fracture mechanics. Kirkner and Shen (13) represent the model shown in Figure 1.1.13 by:

$$\sigma = \sigma_f - \frac{\sigma_f}{w_c} w \quad \text{when } w < w_c \text{ and } \frac{\partial w}{\partial t} > 0 \text{ (loading)}$$

$$(26)$$

$$\sigma = 0 \qquad\qquad \text{when } w \geq w_c \text{ (open crack)}$$

where: w_h = maximum historic crack opening displacement

σ_f and w_c = assumed parameters representing the material within λ, set for each fictitious crack based upon the heterogeneity of the material

Numerical Scheme

Kirkner and Shen (13) developed a semi-analytical solution to the one-dimensional physical problem posed above. Figure 1.1.15 illustrates important components of their scheme. The pavement structure is comprised of boundary points, macro-structures, substructures and fixed points. These are defined as (13):

1. **Boundary Point**: A point that separates a region where the structure has moved from a region where no movement has occurred. The stress at a boundary point is simply the thermal stress while the displacements and strains are zero.

2. **Macro-structure**: A region bounded by exactly two boundary points.

3. **Substructures**: A zone between two neighboring fixed points.

4. **Fixed Points**: A point where the displacement equals zero, but the strain does not equal zero.

Figure 1.1.15(a) illustrates the boundary points and a fictitious crack opening within a single macro-structure. Points on either side of the fictitious crack move away from the crack, due to thermal effects, and are resisted by frictional effects. Figure 1.1.15(b) shows how a continuous pavement system may be subdivided into a series of macro-structures that act independently of one another. Kirkner and Shen (13) explain that their numerical solution solves for each macro-structure individually. Finally, Figure 1.1.15(c) represents one sub-structure bounded by fixed points. This substructure contains one major fictitious crack and points on either side of it move away from the crack.

In Kirkner and Shen's scheme, a system of non-linear algebraic equations are obtained by imposing stress continuity at all the fixed points within a single macro-structure. The equations are then solved by the Newton-Raphson method.

Model Behavior with Respect to Friction

By performing numerical simulations, Kirkner and Shen (13) demonstrated the importance of interface friction with respect to thermal crack development. These findings serve as motivation for further investigation into the role of interface friction:

1. Large frictional constraint delays the formation of open cracks. This delay may be represented by the required temperature decrease for cracking to occur, ΔT_c. This is consistent with observations made of thermal cracking in flexible pavements (38).

2. As frictional constraint between the asphalt and base layers is increased, the crack spacing and width of cracks both decrease.

3. When there is high frictional constraint between layers, a greater drop in temperature is required for a fictitious crack to develop into an open crack.

boundary point
σ = σ_th
h
x
boundary point
σ = σ_th
Opening of fictitious crack
Frictional resistance

a) Opening of fictitious crack in one macro-structure

Macro-structure
Macro-structure
Sub-structures
1   2   …   N

b) Pavement divided into a series of macro-structures and sub-structures

Fictitious cracks
k_1 k_2
k_p
k_m
x_k^l
(fixed point)
x_{k1} x_{k2}
x_{kp}
(major fictitious crack)
x_{km}
x_k^r
(fixed point)

c) Sub-structure, k

**Figure 1.1.15 Structure Discretization for Numerical Solution
(after Kirkner and Shen, 1999).**

Perhaps the greatest contribution of the FCM specifically toward this research project is
the incorporation of interface friction in the thermal cracking model. However, in other
aspects their treatment of the problem is overly simplistic by not accounting for the thermal
gradient in the asphalt concrete layer and ignoring the underlying layers' effects on heat
transfer.

SUMMARY

This report was meant to examine and characterize existing models to predict thermal cracking of asphalt pavements. This investigation is important since thermal cracking is a pervasive problem in northern climates and a review of existing models sets the stage for further research and development of new thermal cracking models.

The models investigated were characterized as either empirical or mechanistic-based. While empirical models are easy to use, the inputs may be difficult to determine and they are strictly limited to the data set on which they were based. However, they do indicate which parameters or groups of parameters have the greatest influence on the thermal cracking phenomenon. Though binder properties were most important in the empirical models investigated in this report, the Fromm and Phang (14) equation indicated the need to account for the materials underlying the asphalt concrete.

The mechanistic models studied in this report attempted to predict either fracture temperature or amount of cracking. Sound mechanistic principles were developed by Hills and Brien (17) and later applied by others to predict when cracking would occur, but did not address crack frequency or properties other than that of the asphalt concrete.

The SHRP A-005 model represented a large technological advance in terms of predicting the thermal cracking phenomenon, however its reliance on empirical calibration may not warrant some of the other complex components within the model. The fictitious crack model (FCM), though somewhat simplistic, does account for interface friction and its effect on crack spacing.

Overall, the existing thermal cracking models, investigated in this report, focus almost exclusively on the asphalt concrete surface. None of the existing models account for traffic effects and only the FCM takes interface friction into consideration. Given the limitations of existing models it is recommended that a new thermal cracking model be developed. The model should consider the entire pavement cross section as an integrated engineering system, consider the interface friction between layers, take into account traffic effects on crack development, and simulate heat transfer throughout the pavement structure.

PART 1. MODELING
Chapter 1.2. Model Development

INTRODUCTION

While much research has been directed toward the thermal cracking problem, the question of crack spacing regularity has not been answered in a mechanistic fashion. The models investigated in chapter 1.1 (Review of Models) either did not address crack spacing or defined the locations of possible cracks a priori. The objective of this research was to develop a phenomenological thermal cracking model from which a characteristic crack spacing could be derived. A secondary objective was to model how traffic loads affect crack spacing.

In previous thermal cracking models, it was typically assumed that the asphalt concrete surface was fully restrained as pictured schematically in Figure 1.2.1. Under this assumption, it was possible to determine the state of stress by modeling the material as elastic, visco-elastic or pseudo-elastic. For example, as described by Hills and Brien (17), a one-dimensional elastic beam will develop thermal stress according to:

$$\sigma_x = E\alpha\Delta T \tag{1}$$
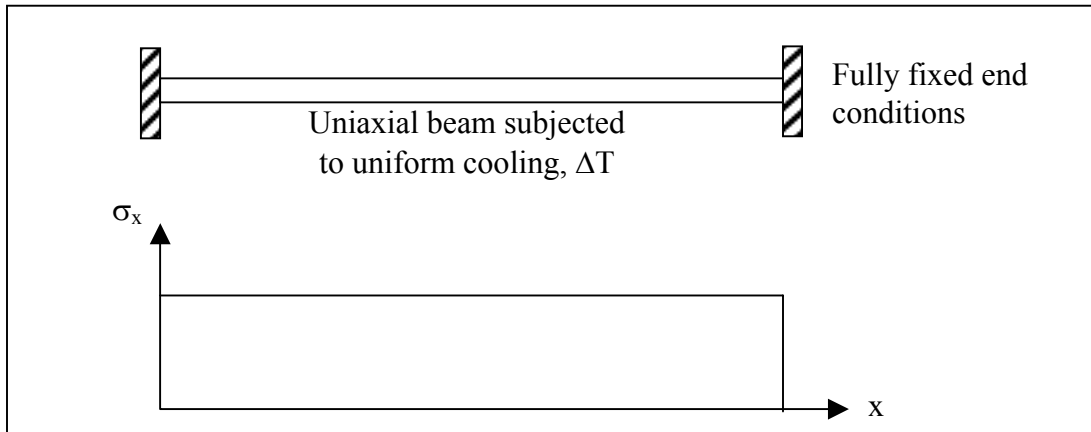
Figure 1.2.1 Fully Restrained Beam Model.

Despite the model chosen, under fully fixed end conditions the stress is constant along the length of the member as shown in Figure 1.2.1. Therefore, the regular crack spacing phenomenon is not explained mechanistically.

The fully restrained condition pictured in Figure 1.2.1 arises from the assumption that the asphalt concrete surface is fully bonded to the underlying material and has infinite length. In reality, however, there must be a so-called "free edge". The free edge can be as well defined as a construction joint or an existing crack or flaw in the pavement. In any case, the free edge is a significant boundary condition that has the potential to alter the stress state along the length of the pavement. Also, the asphalt concrete layer typically rests on an unbound granular material having frictional properties. In geomechanics these types of media are often modeled as Mohr-Coulomb materials. To understand the different boundary conditions, and how these affect thermal stress development, a one-dimensional frictional restraint model was first developed and is explained below. Subsequent sections describe a two-dimensional model where the effects of a uniform temperature change, thermal gradient and finally effects of traffic loads are examined.

ONE-DIMENSIONAL FRICTIONAL RESTRAINT MODEL

Consider an elastic uniaxial beam with support conditions as pictured in Figure 1.2.2. Rather than a fixed-fixed condition as shown in Figure 1.2.1, the beam is restrained by frictional sliders that develop restraining force when the beam deforms. It is assumed that any deformation will fully enact the sliding force, f_s, per unit length in the x-direction. Note that this representation corresponds to a supporting layer with relatively high shear stiffness. In reality, there may be some elastic deformation that occurs before the maximum sliding force is enacted.

It is also assumed that at some location in the beam there will be sufficient frictional resistance to counteract the thermal deformation in the beam. This location will be referred to as the "critical point" for the duration of the analysis. Locations in the beam between the fixed end and critical point act as if fully restrained and do not move while locations between the critical point and free end displace by some amount as will be explained below. Under these conditions, the principle of superposition may be used to solve the problem when a uniform temperature change is applied to the entire beam.

Thermal Displacements

According to the principle of superposition, the frictional slider supports are removed and the temperature change is applied. The thermal displacement may be expressed as:

$$\delta_{th} = x\alpha\Delta T \qquad\qquad (2)$$

where: δ_{th} = displacements due to temperature change (m)

x = distance from fixed end (m)

α = coefficient of thermal contraction (/$^{\circ}$C)

ΔT = temperature change ($^{\circ}$C)
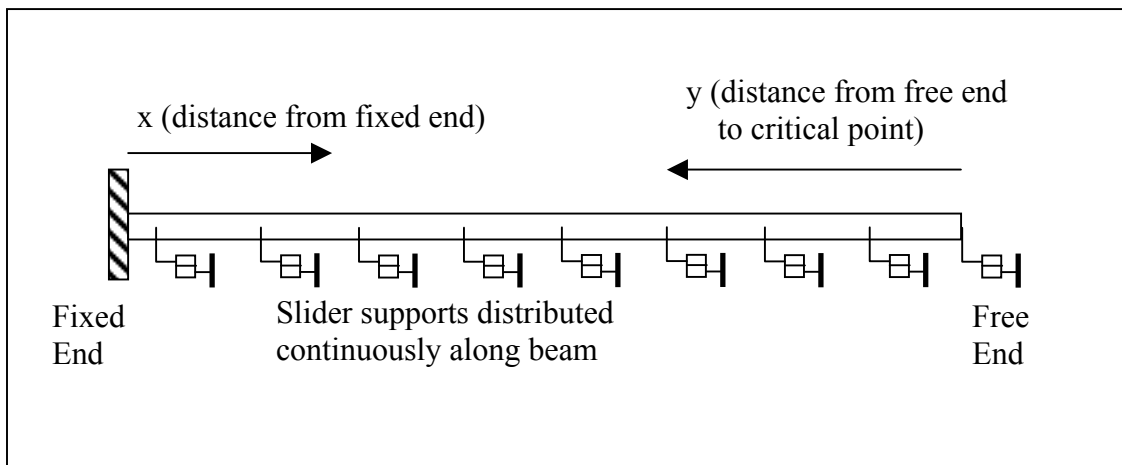
Figure 1.2.2 Frictional Restraint Model.

Mechanical Displacements

Recall that only locations between the critical point and free edge undergo deformation. Therefore, the frictional resistance is active only between the critical point and free edge. The mechanical displacements at the critical point, due only to the enacted frictional sliders, may be expressed as:

$$\delta_m = \frac{PX}{EA} \qquad\qquad (3)$$

where: δ_m = mechanical displacement (m)

P = net force acting at distance X (N)

X = distance from fixed end to critical point (m)

E = Young's modulus (N/m^2)

A = cross sectional area of beam (m^2)

Since P results from the accumulation of frictional forces from the free end, it may be expressed as:

$$P = f_s \cdot Y \tag{4}$$

where: f_s = frictional sliding force per length (N/m)

Y = distance from free end to critical point (m)

Substituting (*4*), equation (*3*) becomes

$$\delta_m = \frac{f_s Y \cdot X}{EA} \tag{5}$$

Superposition

The principle of superposition states that the total displacements must equal the sum of the thermal and mechanical displacements, or:

$$\delta_{total} = \delta_{th} + \delta_m = X\alpha\Delta T + \frac{f_s Y \cdot X}{EA} = X\left(\alpha\Delta T + \frac{f_s Y}{EA}\right) \tag{6}$$

Constraints

At the critical point, the total displacement must be zero, therefore:

$$X\left(\alpha\Delta T + \frac{f_s Y}{EA}\right) = 0 \tag{7}$$

Since x is always greater than or equal to zero and assuming ΔT is always less than zero:

$$\frac{f_s Y}{EA} = a\Delta T \tag{8}$$

solving for Y yields:

$$Y = \frac{EA\alpha\Delta T}{f_s} \tag{9}$$

where: Y = distance from free end to critical point (m)

Stress Considerations

According to the formulation presented above, the beam may be divided into two portions. The first portion is a fixed-fixed beam while the second portion deforms, having longitudinal dimension, Y. Figure 1.2.3 illustrates the two-part beam.
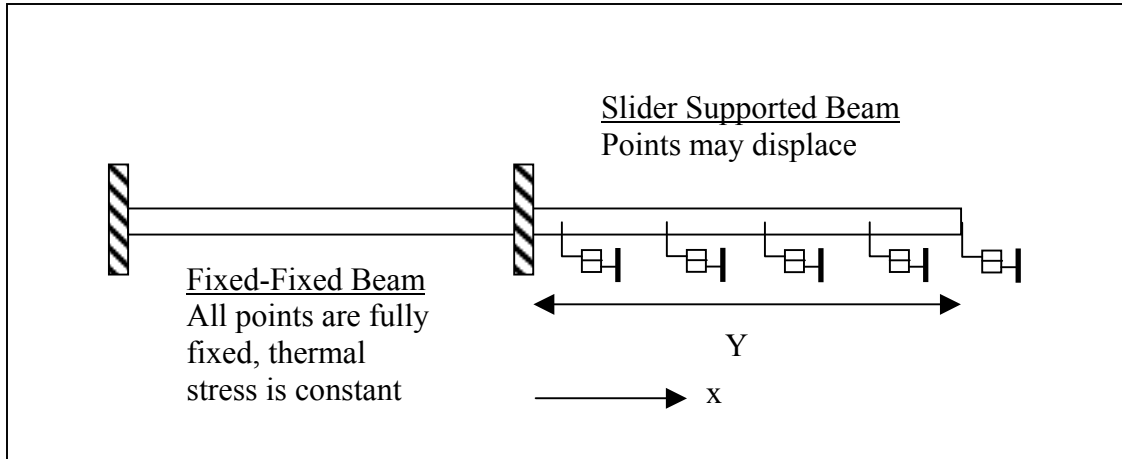
Figure 1.2.3 Two-Part Beam.

Part 1: Fixed-Fixed

As shown previously, for a fixed-fixed elastic beam, the stress due to cooling is constant along the length of the beam:

$$\sigma_x = E\alpha\Delta T \tag{10}$$

where: σ_x = stress along x-axis (Pa)

Part 2: Slider Support

The slider support condition may be analyzed by considering a free-body-diagram of an element as shown in Figure 1.2.4 and determining the conditions of static equilibrium:

$$\sum \vec{F_x} = 0 = -\sigma_x dz + \left(\sigma_x + \frac{\partial \sigma_x}{dx}\right)dz + f_s dx \tag{11}$$

After canceling terms, assuming dz = 1 and rearranging, the integral may be taken to determine σ_x:

$$\int \frac{\partial \sigma_x}{dx} dx = -\int f_s dx \qquad (12)$$

which yields:

$$\sigma_x = -f_s x + C_1 \qquad (13)$$

where: $C_1 = E\alpha\Delta T$ as in equation (*10*)

x = distance from critical point (m)
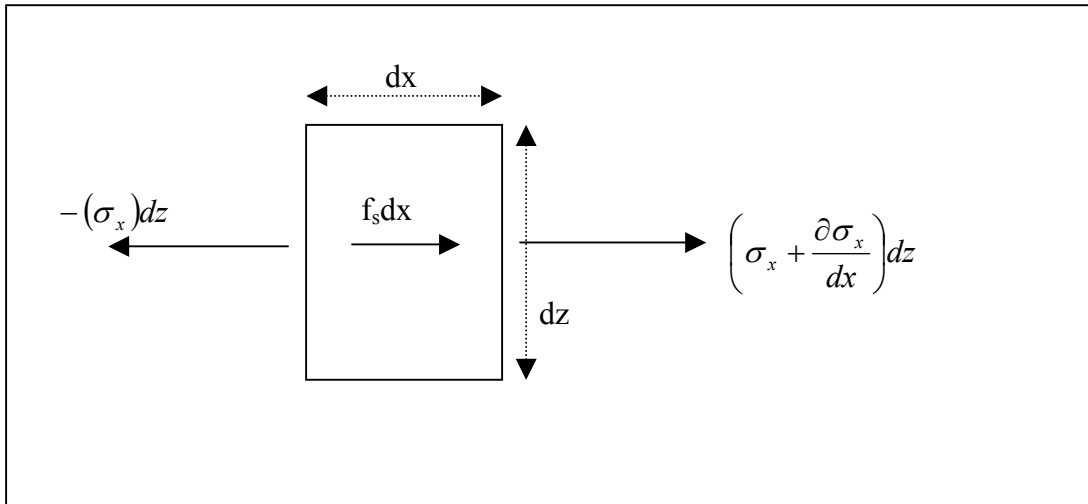
Figure 1.2.4 Free Body Diagram of a Portion of Slider Supported Beam.

Entire Beam:

Putting the two parts together yields a stress curve as depicted in Figure 1.2.5. Note that this is quite different from the fixed-fixed condition depicted in Figure 1.2.1.
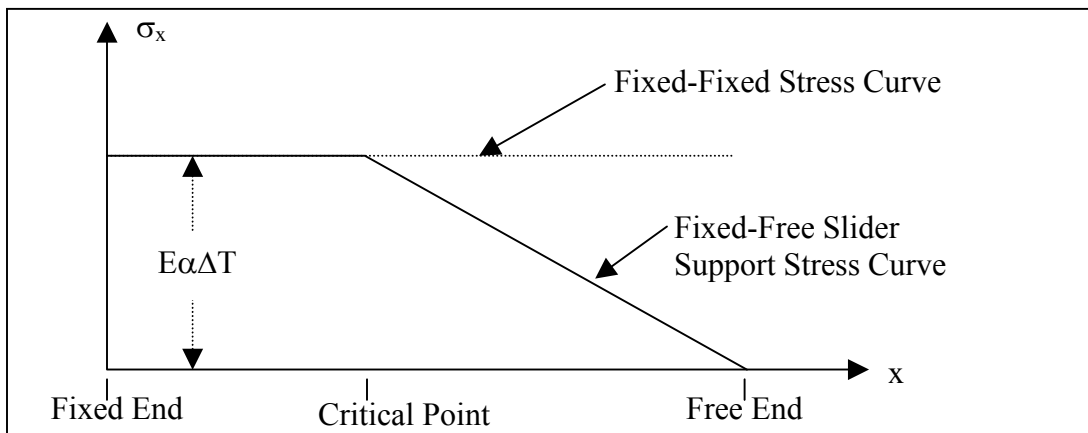
Figure 1.2.5 Stress Curve for Slider Supported Beam vs. a Fixed-Fixed Beam.

EXTENSION OF ONE-DIMENSIONAL MODEL TO TWO-DIMENSIONS

In a two-dimensional framework that considers the entire surface and supporting layers, the stress analysis becomes more complex but can be accomplished by numerical simulation. The commercially available computer program FLAC was used to solve the two-dimensional thermal stress relief problem. FLAC (Fast Lagrangian Analysis of Continua), developed by the ITASCA Consulting Group, is an explicit finite difference program that has been used to solve a large number of continuum mechanics problems and has been verified and validated against other solution schemes (39).

Two main factors were considered in selecting FLAC. First, FLAC has a number of built-in models well suited for the thermal cracking problem. Elastic and Mohr-Coulomb models may be used, in conjunction with a thermal model, to simulate the thermo-mechanical effects in the asphalt concrete and underlying layers, respectively. The second factor is that FLAC is relatively easy to use and provides a variety of graphical and numerical output. It was decided that proceeding with modeling rather than developing customized computer code to fully analyze the problem would be the most efficient approach.

Figure 1.2.6 illustrates a two-dimensional pavement simulated using FLAC. The hot-mix asphalt concrete (HMAC) was modeled as a linear elastic isotropic material while the base layer was modeled as a Mohr-Coulomb material. As shown in Figure 1.2.6, the pavement surface layer was modeled with a free edge while the remaining edges were fixed in either the x, z or both directions. The constitutive relationships, as described below, are applied to the plane strain case illustrated in Figure 1.2.7.
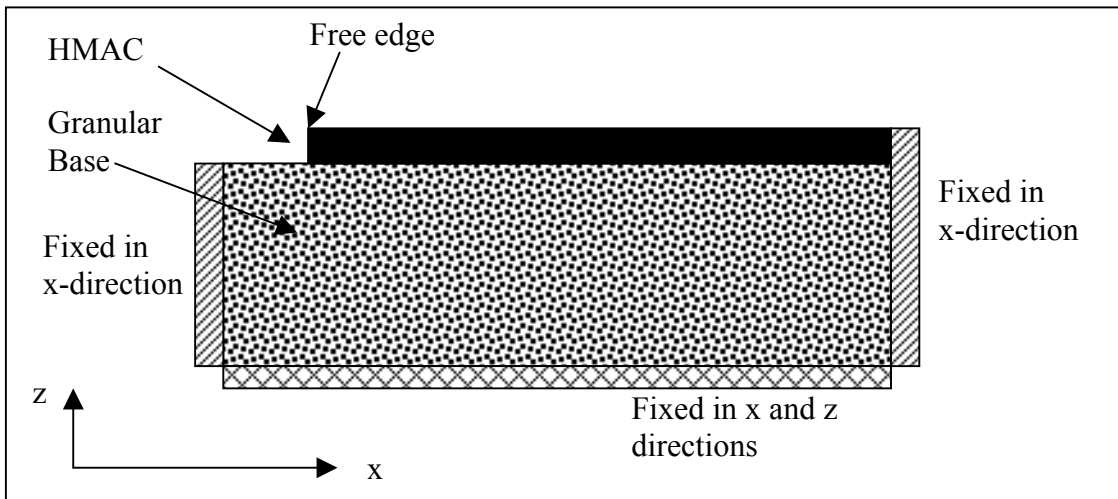
Figure 1.2.6 Two Dimensional Pavement Model.
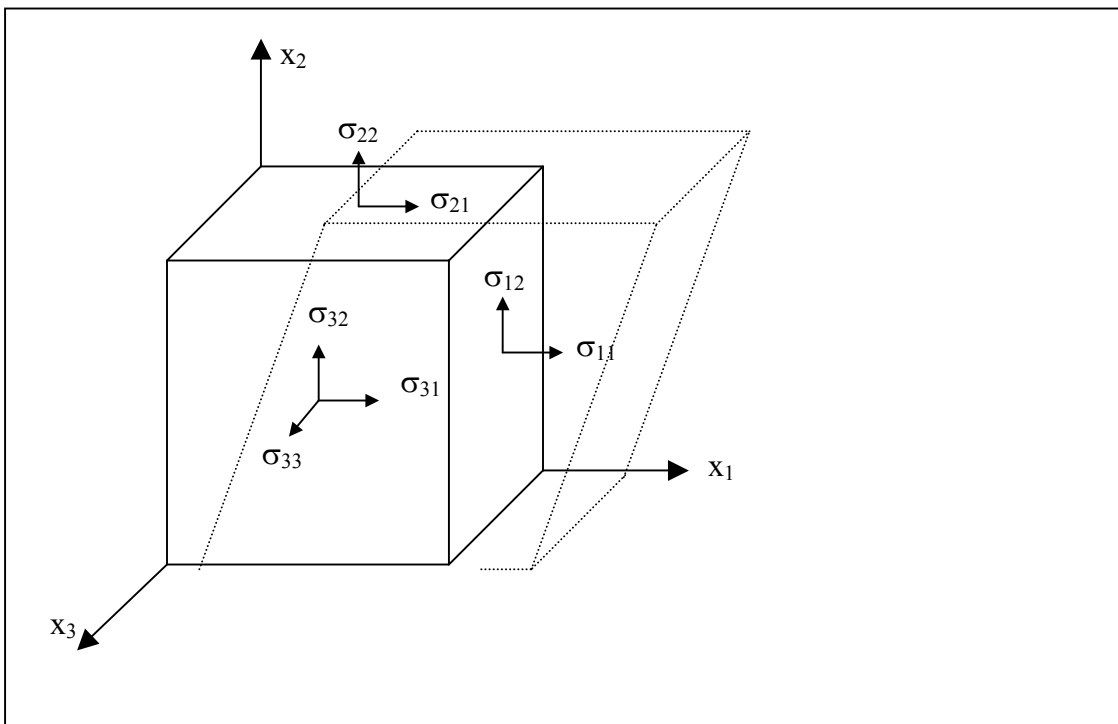
Figure 1.2.7 State of Stress and Strain for Plane Strain Case.

Governing Equations

Equation of Equilibrium

To solve solid-body mechanics problems, equations of equilibrium and constitutive equations must be invoked, like the one-dimensional solution previously described. Newton's second law of motion serves as the equation of equilibrium:

$$\rho \frac{\partial \dot{u}_i}{\partial t} = \frac{\partial \sigma_{ij}}{\partial x_j} + \rho g_i \qquad (14)$$

where: ρ = mass density

t = time

x_i = components of coordinate vector

g_i = components of gravitational acceleration (body forces)

σ_{ij} = components of stress tensor (pictured in Figure 1.2.7)

$\dot{u}_i$ = velocity component

i,j = component directions in Cartesian system shown in Figure 1.2.7

Constitutive Equations

Rate of Strain and Velocity Relationship

Constitutive equations comprise the second set of formulas required to solve a solid-body mechanics problem. The first constitutive equation is general to any deformable body and relates the rate of strain to the velocity gradient obtained from the equation of equilibrium (*14*):

$$\dot{\varepsilon}_{ij} = \frac{1}{2}\left[\frac{\partial \dot{u}_i}{\partial x_j} + \frac{\partial \dot{u}_j}{\partial x_i}\right] \qquad (15)$$

where: $\dot{\varepsilon}_{ij}$ = strain rate components

A more common form of (*15*) expresses the strain rather than the strain rate and is known as the Cauchy infinitesimal strain tensor:

$$\varepsilon_{ij} = \frac{1}{2}\left[\frac{\partial u_i}{\partial x_j} + \frac{\partial u_j}{\partial x_i}\right] \qquad (16)$$

39

However, the differential form shown in (*15*) is used in FLAC since it fits naturally into the explicit time-stepping scheme during simulation.

Isotropic Linear-Elastic Constitutive Equations

Equation 16 determines the state of strain, however additional equations are necessary to determine the state of stress, and are dependent upon the type of material being modeled. As mentioned above, the surface layer was modeled as a linear elastic isotropic material. Hooke's law expresses the behavior of this type of material according to the constitutive equation:

$$\sigma_{ij} = \frac{Ev}{(1+v)(1-2v)} \varepsilon_{kk} \delta_{ij} + \frac{E}{1+v} \varepsilon_{ij} \qquad (17)$$

where: E = Young's modulus

v = Poisson's ratio

ε_{kk} = volumetric strain

δ_{ij} = Kronecker delta = 1 when i=j, otherwise = 0

Mohr-Coulomb Constitutive Equations

The granular base was modeled as a Mohr-Coulomb material having shear and tensile failure limits illustrated schematically in Figure 1.2.8. Any state of stress inside the failure envelope corresponds to an linear elastic response of the material as described in equation (*17*). If the state of stress falls outside the envelope, the material behaves perfectly plastic (i.e., permanent deformation). The shear envelope and tensile stress cutoff equations are:

$$\tau_f = c + \sigma \tan \phi \qquad (18)$$

$$\sigma_t = 0 \qquad (19)$$

where: τ_f = shear stress limit on failure plane

c = cohesion of material (material property)

σ = normal stress on failure plane

ϕ = internal angle of friction (material property)

σ_t = tensile strength of material (material property), typically assumed to be zero
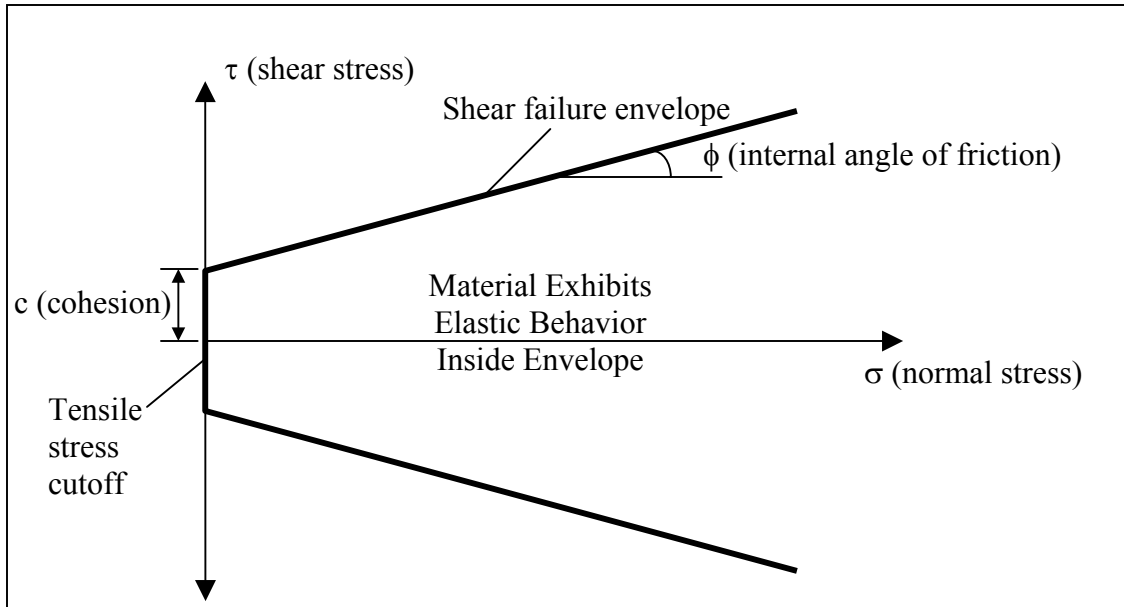
Figure 1.2.8 Mohr-Coulomb Failure Criteria.

Heat Transfer and Thermal Stress Equations

While FLAC contains a heat transfer model based on Fourier's Second Law, it was decided not to make use of this feature. As will be described later, the initial simulations assumed a uniform temperature change in the surface layer and therefore did not require a heat transfer solution. The temperature was simply changed by ΔT. Further, the field-validation pavement sections were instrumented with numerous thermocouples that measured in situ temperatures at various depths at fifteen minute increments. Measured thermal gradients were input into FLAC rather than simulating the temperature profile which greatly reduced the complexity of the simulations.

The final constitutive equation relates changes in temperature to a change in the stress state. Assuming elastic deformation and the plane strain case, the constitutive equation is (40):

$$\Delta \sigma_{ij} = -\delta_{ij} 3K\alpha\Delta T \qquad\qquad (20)$$

where: $\delta = 1$ if i=j and $\delta = 0$ if i≠j

$K = \text{bulk modulus} = \dfrac{E}{3(1-2\nu)}$

$\alpha = \text{linear coefficient of thermal contraction}$

41

ΔT = change in temperature

Equation (*20*) is essentially the same as that proposed by Hills and Brien (1966), but is for the plane strain case rather than plane stress represented by an infinite slab.

Boundary Conditions

The proposed model has several boundary conditions that deserve further explanation. First, the nature of asphalt pavement construction, where the warm asphalt mixture is compacted on top of the granular medium, requires that the model have fully bonded layers. Consequently, in the model, there is no slip allowed at the interface between layers and stresses are fully transferred from one layer to the other across the interface.

Secondly, the presence of a free edge or existing crack is essential to the stress relief behavior shown in Figure 1.2.5. As previously mentioned, there must always be a free edge somewhere in the pavement and therefore it is reasonable to model the stress relief next to the free edge. Clearly, the stress along the free edge must be zero. Also, the top of the pavement structure is a free edge, and the stress along this edge is also zero.

Third, the vertical and horizontal displacements are fixed along certain boundaries as shown in Figure 1.2.6, and the fixed-end of the model could be viewed as the line of symmetry for the simulation. Alternatively, the fixed-end condition in Figure 1.2.6 could be viewed as the pavement extending "infinitely" to the right. The left fixed-end condition on the base material certainly represents the base extending infinitely in the horizontal condition. Fixing the base material in both the horizontal and vertical directions along the bottom simulates the infinite half-space of the field condition.

The Finite Difference Grid

As with any numerical solution (e.g., finite element, finite difference) the problem geometry must be subdivided into a grid (or mesh) so that the governing equations may be solved. The mesh for the two-dimensional problem shown in Figure 1.2.6, was graded vertically to help reduce the computational requirements of FLAC. Smaller control volumes were used in the asphalt concrete layer, slightly larger in the upper portion of the supporting granular layer and larger still in the lower portions of the granular layer. Generally speaking,

a finer mesh was used in regions of greater interest (i.e., asphalt concrete layer and layer interface).

Figure 1.2.9 illustrates a portion of the graded mesh. Note that the aspect ratio in each layer of the mesh is 5:1 (length:width). Initially a 1:1 ratio was used, however, after running a number of simulations, it was found that a 5:1 ratio produced identical results and dramatically reduced the computation time during simulation.

The vertical dimension of the mesh in the asphalt concrete layer was selected based on the concept of the representative elementary volume (REV), which is the smallest control volume over which average material properties may be assumed. The REV (illustrated in Figure 1.2.10) is particularly important when modeling materials such as asphalt concrete that are comprised of asphalt cement, aggregate and air since too fine a grid would attempt to model the interaction between these components and a different set of constitutive equations would be needed. Since typical aggregate used in asphalt concrete has a maximum particle diameter of 19 mm it was decided to use about 2.5 times that diameter or 50 mm. The upper portion of the base layer had a minimum dimension of 63 mm, again about 2.5 times the maximum particle diameter used in granular base materials. The mesh in the lower portion of the base layer was significantly larger since this portion of the cross section was away from the higher shear stresses imposed by the temperature change and was not as an important region to model as the upper regions.

FLAC Numerical Solution

Once the problem geometry was established and the constitutive models selected, FLAC was executed to solve the problem. The general solution scheme employed by FLAC is illustrated in Figure 1.2.11 where each complete loop constitutes a single time-step. A key component of this or any explicit solution scheme is that all calculations are based entirely on known values from the previous time-step. Consequently, relatively small time-steps are required to provide a stable solution. The time-step taken in FLAC is automatically calculated by the program to ensure an accurate solution. A full explanation of the time-step selection may be found in the FLAC User's Guide (40). The equilibrium and constitutive equations in Figure 1.2.11 are solved in FLAC by discretizing equations (*14*) and (*15*). A

43

full explanation of the solution scheme employed in FLAC is beyond the scope of this thesis, but may be found in the FLAC User's Guide (40).
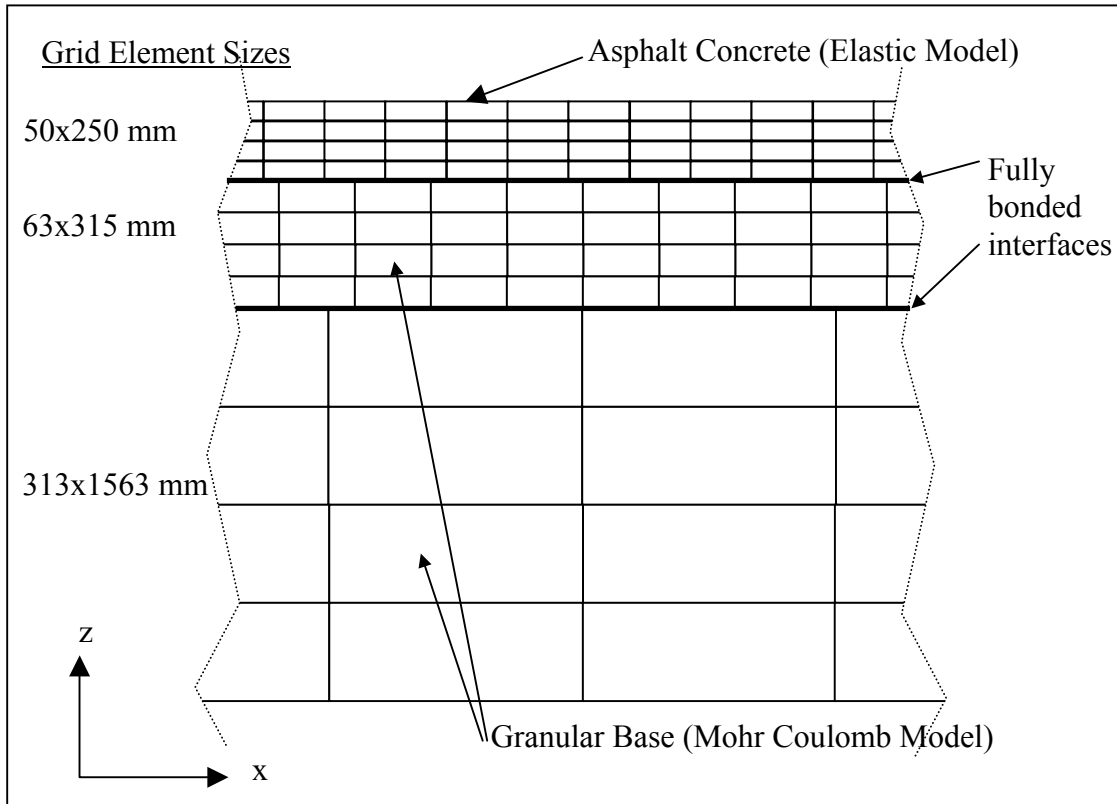
Figure 1.2.9 Vertically Graded Mesh (Not to Scale).
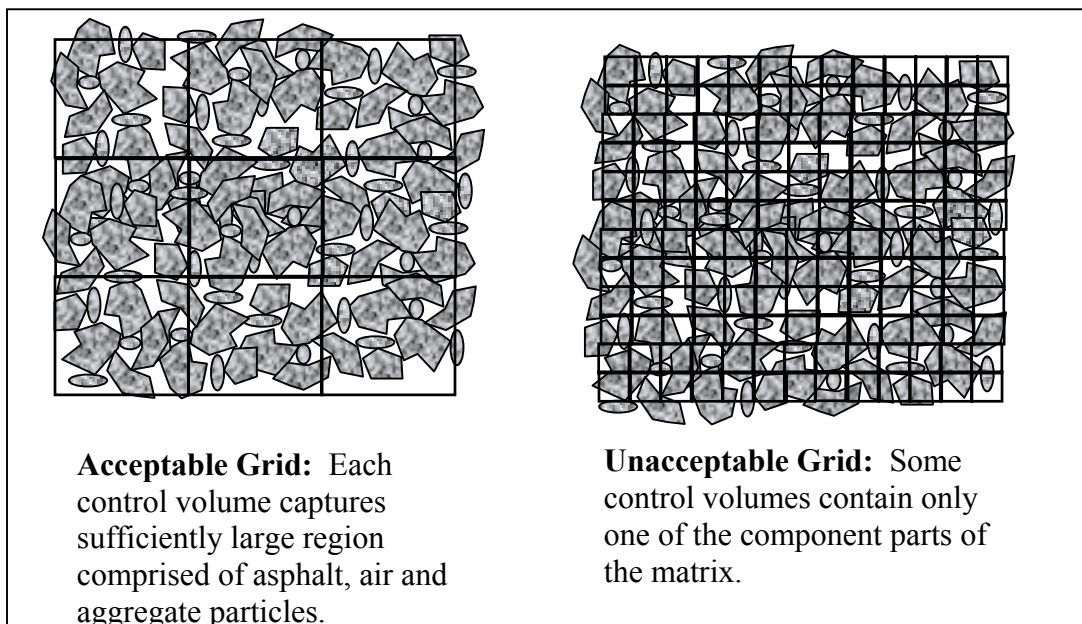
Figure 1.2.10 Representative Elementary Volume.
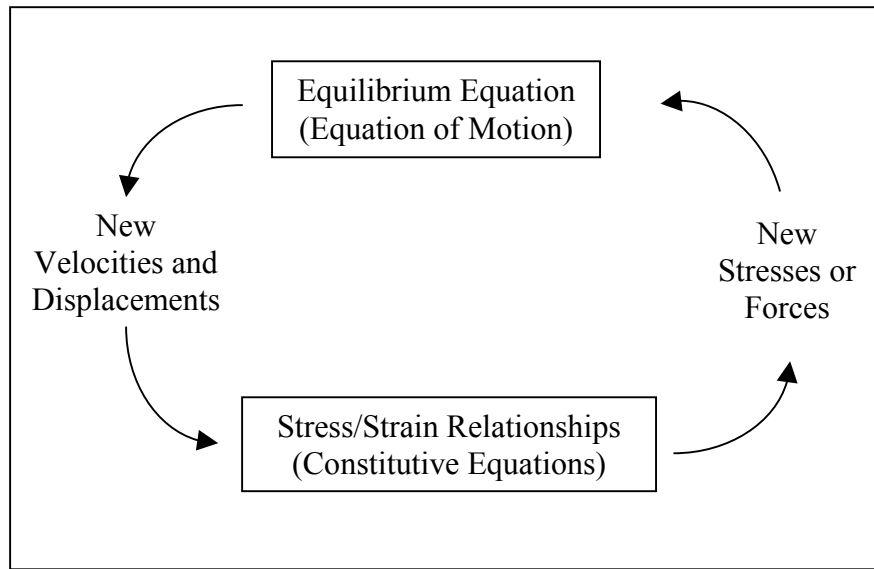
Figure 1.2.11 FLAC Explicit Calculation Cycle (after FLAC, 1995).

SIMULATION AND RESULTS OF THE TWO-DIMENSIONAL MODEL

Three scenarios are investigated below. The first simulates the stress field a pavement surface develops when a uniform temperature change is applied. While a uniform temperature field may be unrealistic, the scenario serves to check the model against the one-dimensional model proposed above. The second scenario simulates the thermal stress developed when a thermal gradient is applied to the surface layer. Third, a wheel load was applied to the surface of the pavement, in addition to a thermal gradient with depth, to simulate the stress field under thermal-mechanical loads.

Uniform Temperature Field

Model Inputs

Using the framework described above, the pavement illustrated in Figure 1.2.6 was simulated with FLAC. Table 1.2.1 contains the constant input parameters used in simulation. The main purpose of this part of the modeling was to understand how the frictional properties of the base could affect the stress field near a pavement edge for a given temperature change.

Therefore, only two friction angles were simulated, a uniform temperature change was applied and the rest of the inputs were held constant.

Analysis of Results

FLAC calculates the state of stress shown in Figure 1.2.7 for every control volume within the finite difference mesh. In the case of thermal cracking, the stresses of main interest are the maximum tensile stresses along the length of the asphalt concrete surface. Therefore, by definition, the stresses of interest are the major principle stresses along the length of the pavement. According to the theory of Mohr's circle, these are:

$$\sigma_1 = \frac{\sigma_{22} + \sigma_{11}}{2} + \sqrt{\left[\frac{\sigma_{22} - \sigma_{11}}{2}\right]^2 + \sigma_{12}^2} \qquad (21)$$

$$\sigma_3 = \frac{\sigma_{22} + \sigma_{11}}{2} - \sqrt{\left[\frac{\sigma_{22} - \sigma_{11}}{2}\right]^2 + \sigma_{12}^2} \qquad (22)$$

In FLAC, tensile stresses are positive, so equation (*21*) was used to calculate the maximum tensile stresses from the components of the stress tensor. The resulting tensile stress distribution, in the surface layer is depicted in Figure 1.2.12, for the temperature change and two friction angles. Since a uniform temperature change was applied to the pavement, the stresses were uniform with depth and only the tensile stresses at the midpoint of the top row of elements are shown in Figure 1.2.12.

Table 1.2.1 Two Dimensional Model Inputs.

Input Symbol	Meaning	Value
H_1	HMAC[*] thickness	0.3 m
H_2	Top of GB[**] thickness	0.2 m
H_3	Bottom of GB thickness	1.8 m
L_1	Length of HMAC	72 m
L_2	Length of GB	82 m
E_1	Young's modulus of HMAC	6895 MPa
E_2	Young's modulus of GB	275 MPa
v_1	Poisson's ratio of HMAC	0.35
v_2	Poisson's ratio of GB layer	0.40

C	Cohesion of GB	0 Pa
GB_t	Tensile strength of GB	0 Pa
ρ_1	Density of HMAC	2200 kg/m^3
ρ_2	Density of GB	2000 kg/m^3
α_1	Coefficient of thermal contraction of HMAC	$1*10^{-5}/°C$
α_2	Coefficient of thermal contraction of GB	$0/°C$
G	Gravity	9.81 m/s^2
ΔT	Change in temperature	5 °C
ϕ	GB internal angle of friction	40°, 70°

[*]Hot Mix Asphalt Concrete Layer   [**]Granular Base Layer

Several key points may be made with respect to the curves in Figure 1.2.10. First, the curves are similar in shape to that postulated by the one-dimensional model (Figure 1.2.5). Therefore, the mechanistic explanation derived for Figure 1.2.5 may be used to understand the more complicated two-dimensional case. There is a linear region of stress increase that reaches the maximum tensile stress region predicted by the fixed-fixed end condition. There is an intermediate region, due to the two-dimensional nature of the problem, that transitions along a parabolic curve from the stress-increase to stress-constant regions.

Secondly, the frictional properties of the base material have an effect on the slope of the stress curve up to the critical point as illustrated for the 5°C temperature change. Increasing the angle of internal friction decreases the region of stress relief and would lead to shorter crack spacing as observed in the field. Figures 1.2.13 and 1.2.14 further illustrate the role played by the supporting frictional layer for the $\phi = 40°$ and $\phi = 70°$ cases, respectively. The figures compare the sine of the angle of mobilized friction (ϕ_m) to the sine of the angle of internal friction (ϕ) along the length of the base material at the midpoint of the top-most row of elements. These two friction angles are shown schematically in Figure 1.2.13 and ϕ_m was determined from the normal stresses calculated by FLAC. When $\sin(\phi_m)$ approaches $\sin(\phi)$, there is an indication that plastic deformation has occurred or is about to occur which signifies that stress relief was provided to the surface layer. Notice that the sharp decline in $\sin(\phi_m)$ coincides with the end of the linear portion of stress increase shown in Figure 1.2.12.
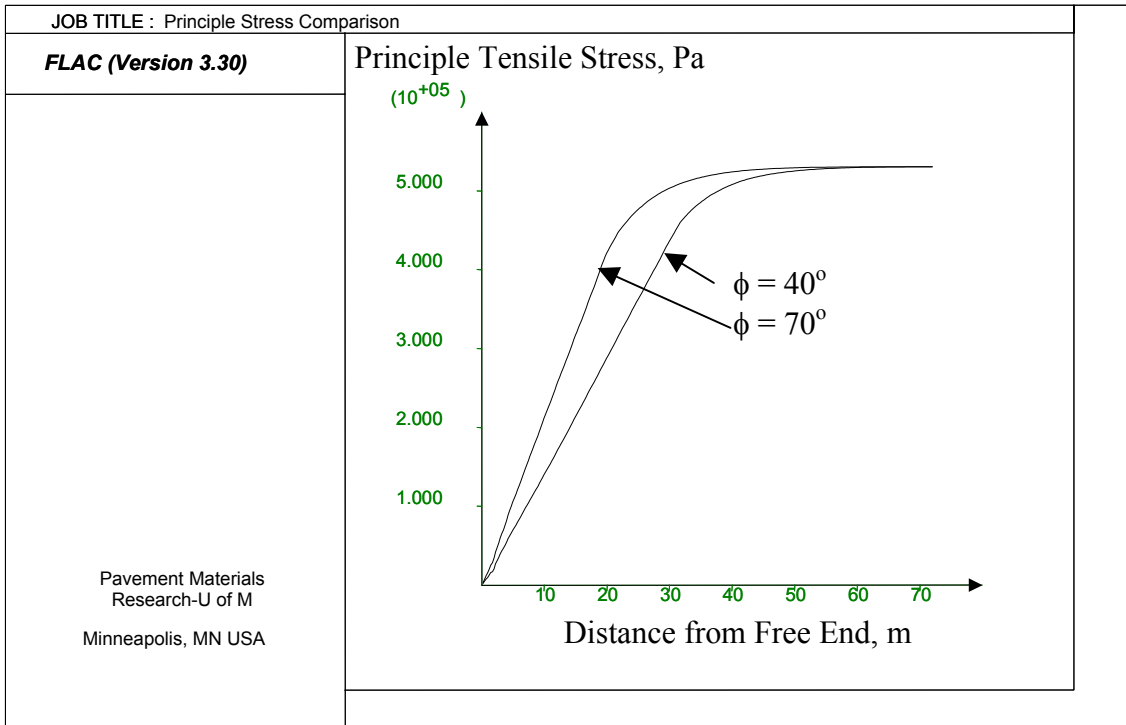
Figure 1.2.12 Tensile Principle Stress Comparison.

Finally, the point at which the maximum stress is reached in Figure 1.2.12 corresponds directly to the point at which no deformation is occurring in the asphalt concrete layer. Figure 1.2.15 illustrates this by plotting the magnitude of x-displacement of points along the length of the asphalt concrete surface layer.
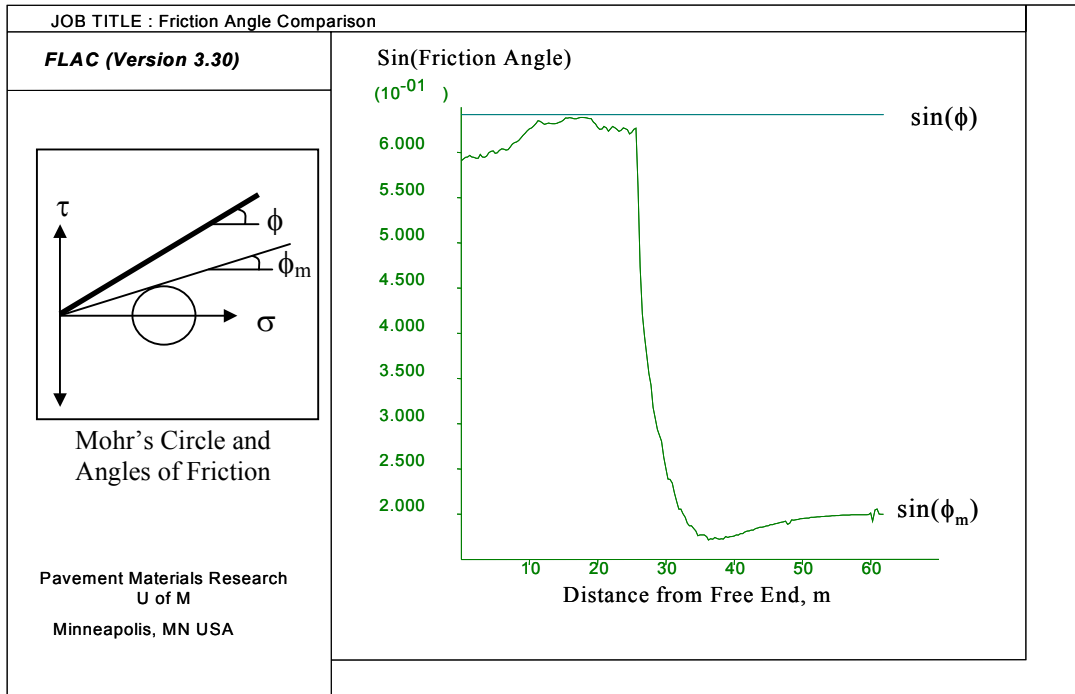
Figure 1.2.13 Comparison of Friction Angles ($\phi = 40^\circ$).

In summary, when a free edge is considered in the development of thermal stresses, the stress will increase linearly from the free edge to the maximum stress at some point in the longitudinal direction of the asphalt concrete. The maximum stress is dependent primarily upon the magnitude of the temperature change, while the rate of increase is dependent upon the frictional properties of the supporting material. More importantly, from a crack spacing perspective, the model introduces a length parameter (distance from free edge to critical point) that is essential to crack spacing regularity and will be at the end of this chapter.

JOB TITLE : Friction Angle Comparison

FLAC (Version 3.30)

Sin(Friction Angle)

sin(ϕ)

.900
.800
.700
.600
.500
.400
.300
.200

sin(ϕ_m)

10   20   30   40   50   60

Distance from Free End, m

Pavement Materials Research
U of M

Minneapolis, MN USA
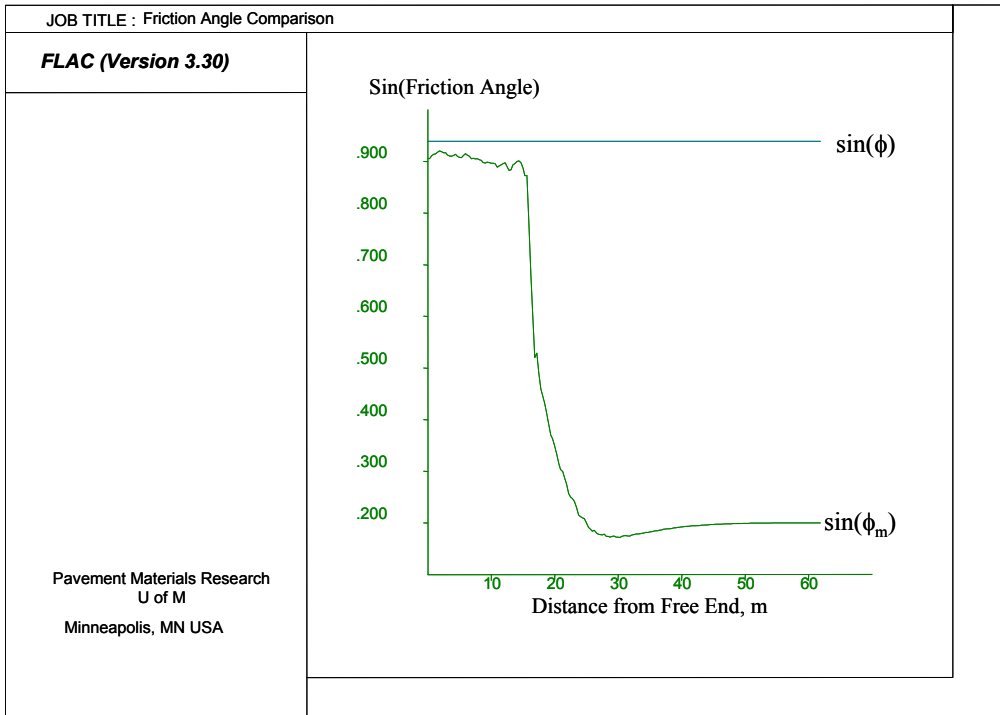
Figure 1.2.14 Comparison of Friction Angles (ϕ = 70º).

JOB TITLE : Frictional Comparison

FLAC (Version 3.30)

Displacement Along X-Axis, m

(10^{-03})

1.200
1.000
.800
.600
.400
.200

ϕ=40º

ϕ=70º

10   20   30   40   50   60   70

Distance from Free End, m

Pavement Materials
U of M

Minneapolis, MN USA
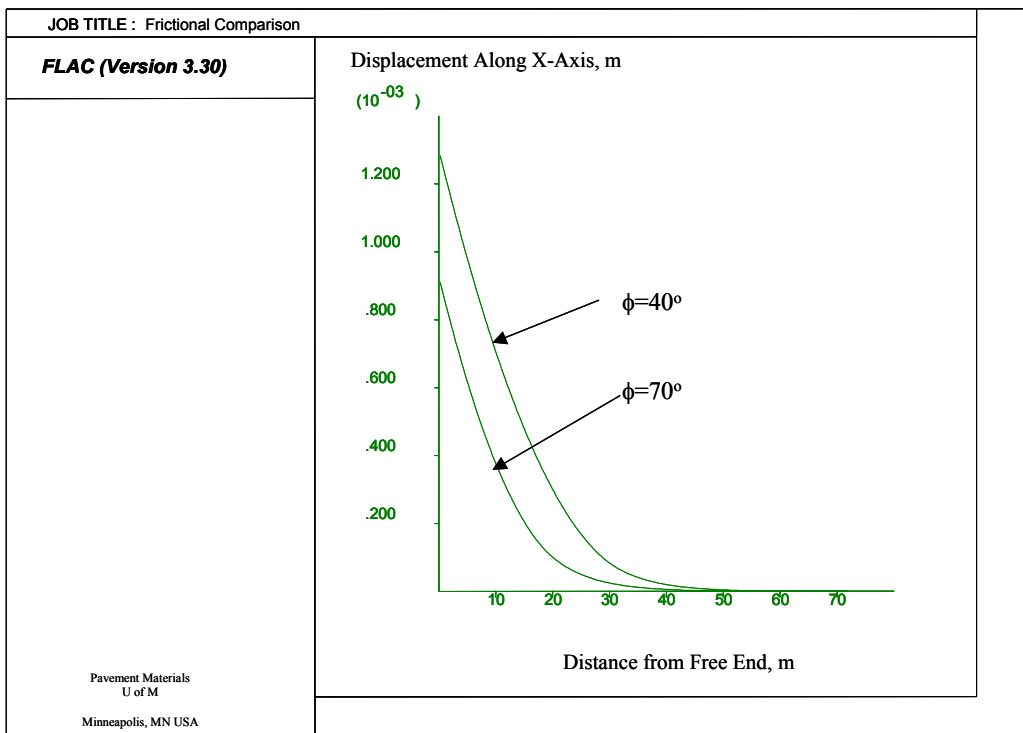
Figure 1.2.15 Magnitude of Thermally-Induced Displacements Along Surface Layer.

50

Thermal Gradient

A more realistic representation of the temperature change in asphalt pavements is to apply a thermal gradient with depth. A second set of simulations was conducted to assess the effects of thermal gradients on thermal stress development. The inputs were the same as in Table 1, however a five-degree linear temperature gradient was applied from top to bottom in the asphalt concrete layer. The results of the simulations, comparing the curves from Figure 1.2.12 to the thermal gradient curves, are shown in Figures 1.2.16 and 1.2.17 for the $\phi = 40°$ and $\phi = 70°$ cases, respectively.
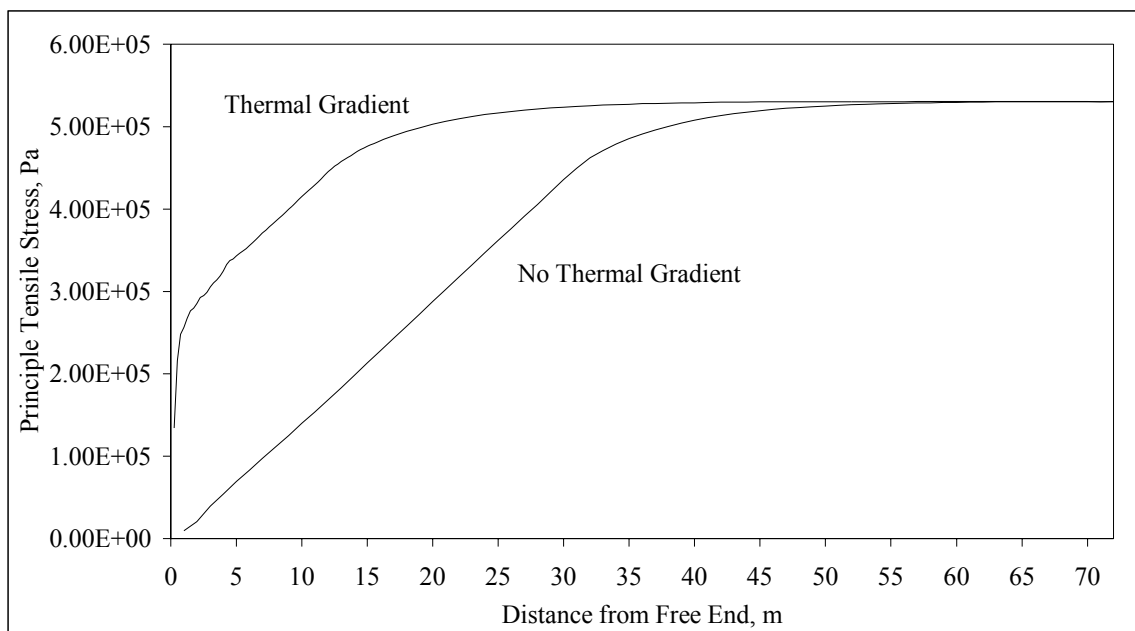
Figure 1.2.16 Comparison of Principle Stresses Along Top of Pavement between Thermal Gradient and Non-Thermal Gradient Cases (ϕ=40º).

Adding a thermal gradient to the problem significantly changed the principle stress curve along the top of the asphalt concrete layer. The curves from Figure 1.2.12 and shown again in Figures 1.2.16 and 1.2.17 had essentially three regions; a linear increase followed by a parabolic curve leading to the maximum stress. The principle stress curves obtained from applying a thermal gradient exhibit a fourth region near the free end. In this region there is a rapid increase in stress over the first meter to an inflection point. The stress level at the

inflection point may be predicted from one-dimensional beam mechanics. According to theory, the beam is subjected to a bending moment due to a thermal gradient:

$$M = \frac{\alpha EI(T_2 - T_1)}{h}$$ (23)

where: M = Bending moment (N-m)

α = Thermal coefficient of contraction (/^{o}C)

E = Young's modulus (N/m^2)

I = Moment of inertia (m^4)

T_2 = Temperature at bottom of beam (^{o}C)

T_1 = Temperature at top of beam (^{o}C)
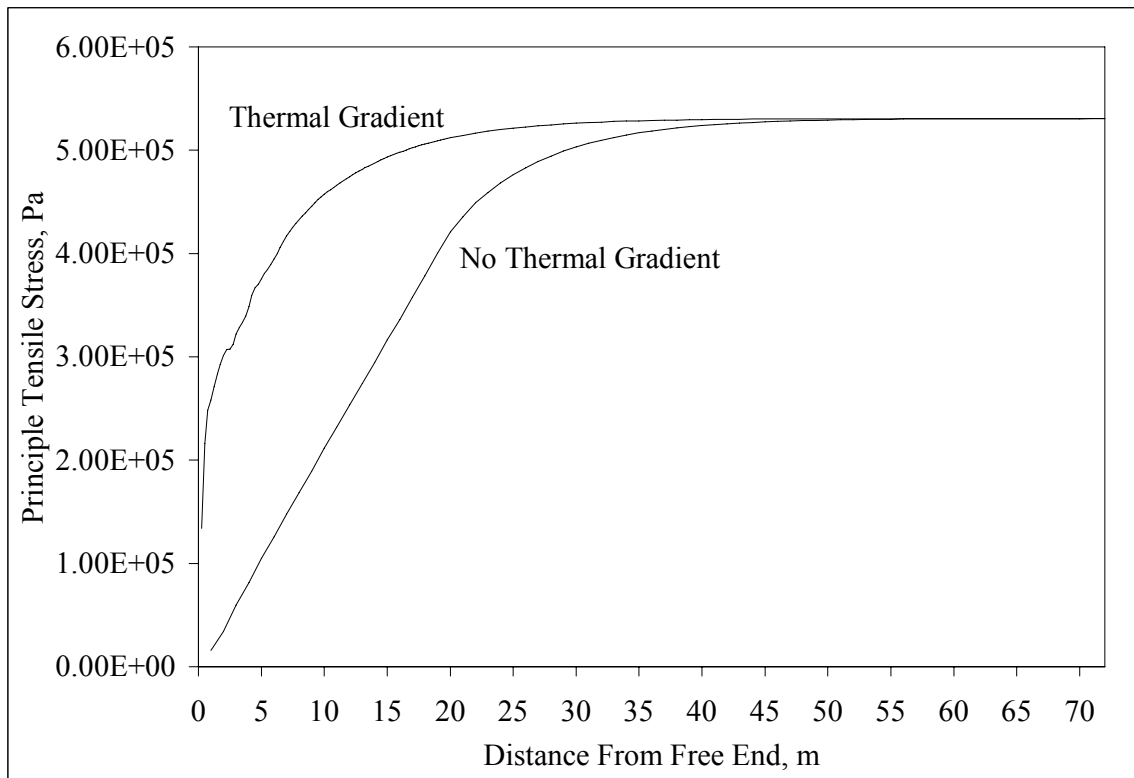
Figure 1.2.17 Comparison of Principle Stresses Along Top of Pavement between Thermal Gradient and Non-Thermal Gradient Cases (ϕ=70°).

The stress due to a bending moment in a beam may be calculated by:

$$\sigma_x = \frac{My}{I}$$ (24)

52

where: σ = stress

y = distance from neutral axis to point of interest

Near the crack edge, the asphalt concrete is in pure bending and the neutral axis lies along the centerline of the layer. Therefore, $y = \dfrac{h}{2}$ and equations 23 and 24 may be combined and terms canceled to yield:

$$\sigma_x = \frac{aE(T_2 - T_1)}{2} \tag{25}$$

which is exactly half the maximum stress predicted by equation 1 and is shown in Figures 1.2.16 and 1.2.17. Additionally, the beam is in tension in the upper portions of the layer since the layer tends to curl upward but is restrained by gravitational forces. In the absence of gravity, the stress in the top portion of the layer would be compressive.

Away from the crack edge, the layer behaves exactly as was observed in the non-thermal gradient cases. The linear stress increase, parabolic curve and maximum stress are not affected by the thermal gradient. However, the linear increase is shortened due to the thermal gradient effects.

In summary, the presence of a thermal gradient can significantly shorten the region of stress relief. Tensile bending stresses are evident near the crack edge followed by a linear increase in stress followed by a parabolic transition to the maximum thermal stress.

Traffic Loads

The second objective of the model development phase was to simulate traffic loads and assess their effect on thermal cracking. To achieve this end, a series of distinct static loads were applied, in separate simulations, to the pavement surface at increasing distance from the free end as shown schematically in Figure 1.2.18. The load magnitude and pressure were set at reasonable levels to simulate a single tire load (i.e., 20 kN and 690 kPa, respectively).

FLAC Simulation

The solution scheme was identical to that outlined previously, in addition to applying a static load after the pavement had reached mechanical equilibrium. Comparative

simulations were run to assess the effect of applying the load before or after the temperature change and nearly identical results were obtained. Loads were subsequently applied after the temperature change to minimize computation time by simply continuing FLAC simulations from the thermal gradient cases.
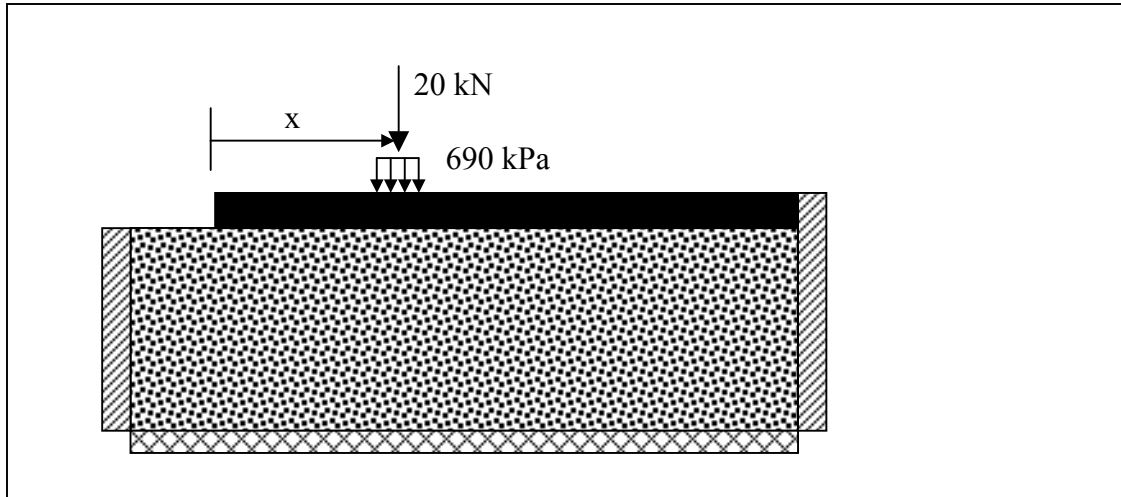
Figure 1.2.18 Application of Traffic Loads on Two-Dimensional Model.

In FLAC, external loads may be specified in a number of manners. The method utilized in this study was to apply a stress boundary condition at particular locations. The stress, as shown above, was set to 690 kPa, compressive in the vertical direction. The length of the pavement covered by the stress corresponded to a load of 20 kN. The loads were applied in 5 m increments for a total of 13 separate simulations per friction angle case.

Results

The maximum principle stresses at the midpoint of the top row of control volumes and the midpoint of the bottom row of control volumes in the asphalt concrete layer, for a load placed at 10 m, are shown in Figure 1.2.19. According to the curves, the applied load has a localized effect when compared to the complete horizontal span of the pavement structure. The thermal stress curves observed in previous graphs (Figures 1.2.16 and 1.2.17) are evident beyond a 5 m region on either side of the 10 m mark. Further demonstration of the localized effect is shown in Figure 1.2.20 where two stress curves are superimposed.

Again, away from the load, the stress curves are unaffected. In effect, the traffic load stresses have been superimposed on the thermal stresses for the total effect shown in Figures 1.2.19 and 1.2.20.
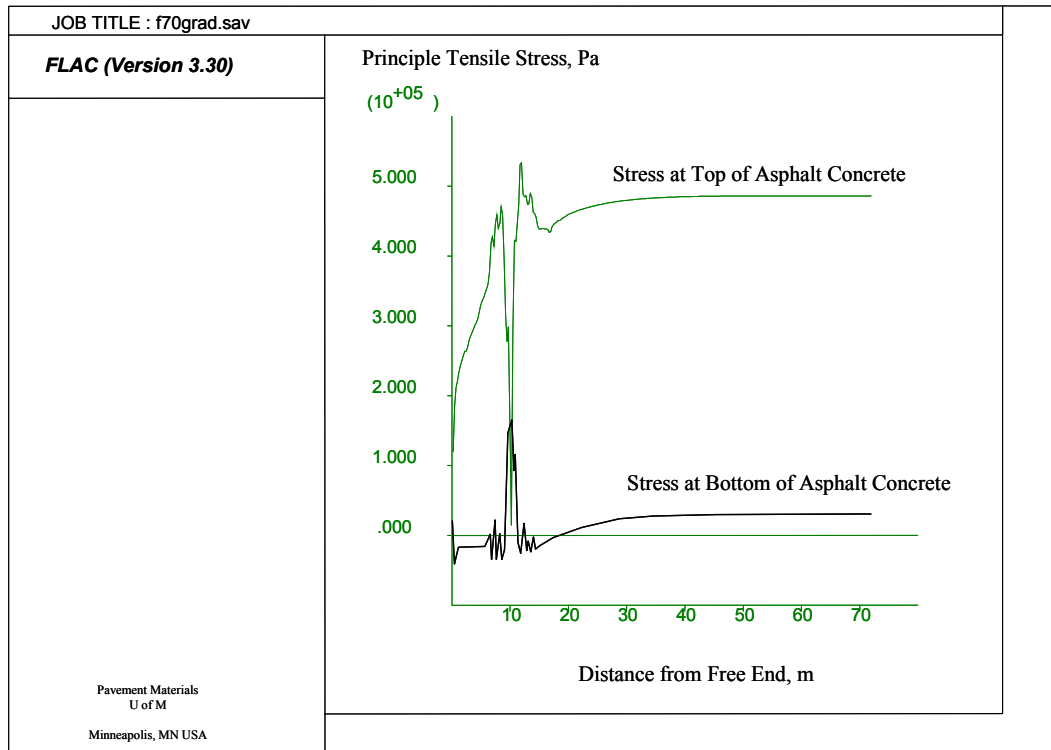
Figure 1.2.19 Traffic Load Effects at Top and Bottom of Asphalt Concrete ($\phi=70°$).

It is important to point out the net reduction in stress at the surface of the pavement, directly beneath the applied traffic load as shown in Figure 1.2.19. While the resulting principle stress is still tensile, in the absence of thermal stresses it would be compressive. This behavior is due to the compressive wheel load placed at the surface and is consistent with classical bending beam theory illustrated in Figure 1.2.21. At the bottom of the pavement, there is a net increase in the tensile principle stress. This behavior is consistent with bending beam theory that predicts tensile stress at the bottom of a bending beam as shown in Figure 1.2.21.

The stress curves in Figures 1.2.19 and 1.2.20 indicate that a short distance away from the load, the pavement experiences a net increase in tensile stress at the top of the pavement. Since cracking is most related to the level of tensile stress, these stresses could

contribute to thermal cracking. Also, since the maximum tensile stresses at the top of the surface layer far exceed those at the bottom, the stresses at the top of the pavement will receive focus for the duration of the discussion.

JOB TITLE : f70grad.sav

FLAC (Version 3.30)

Principle Tensile Stress, Pa
(10^{+05})

6.000
5.000
4.000
3.000
2.000
1.000
.000
-1.000

Load Placed at 10 m   Load Placed at 5 m

10   20   30   40   50   60   70

Distance from Free End, m

Pavement Materials
U of M

Minneapolis, MN USA
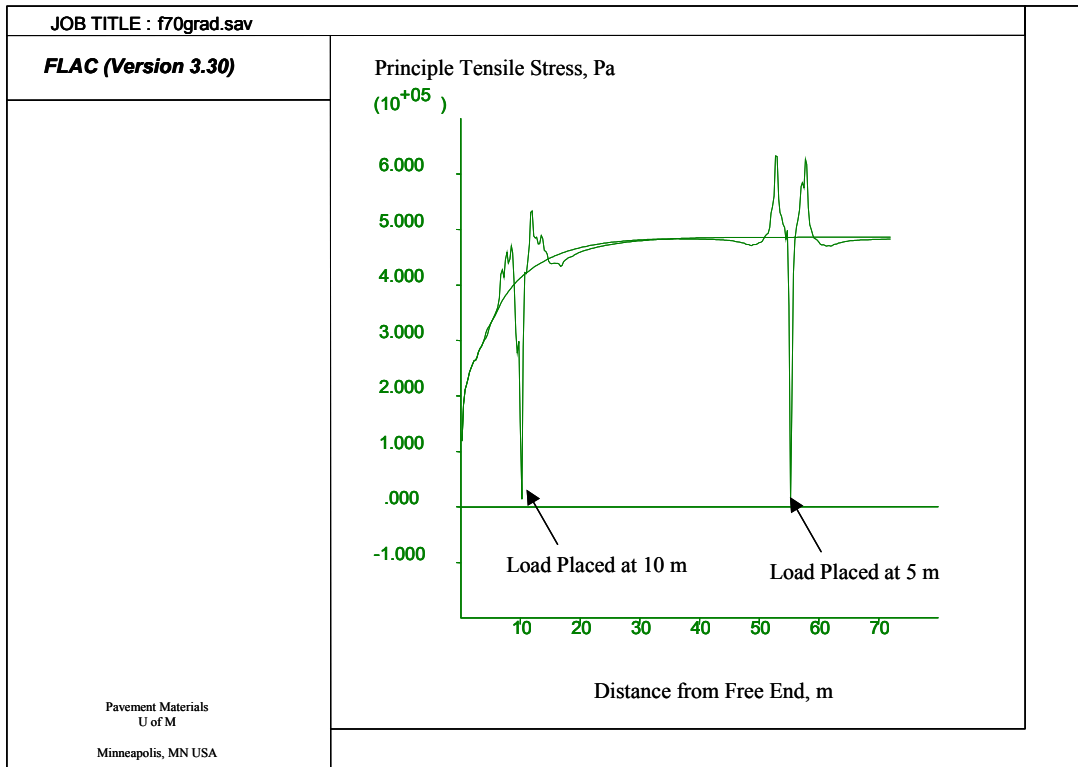
Figure 1.2.20 Localized Effect of Traffic Loads at Pavement Surface (ϕ=70º).

Vertical Load

Compressive Stresses

Neutral Axis

Tensile Stresses
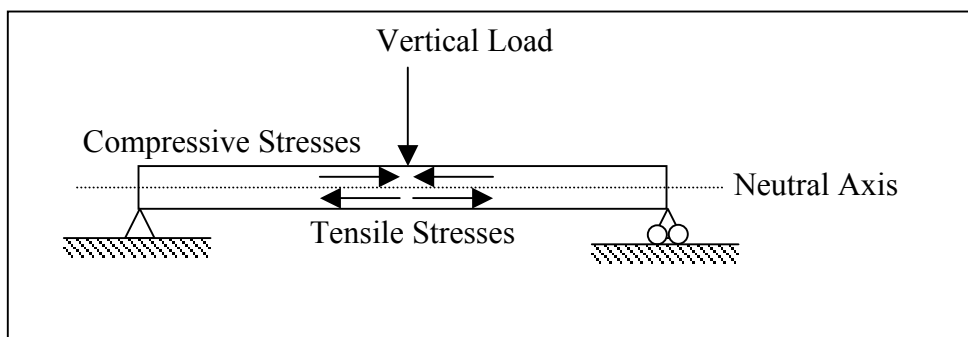
Figure 1.2.21 Schematic of Stresses in a Bending Beam.

The time scale difference between thermally-induced stresses and load-induced stresses deserves discussion. Typically, thermal stresses develop over a period of hours or

even days as the pavement cools due to environmental effects. Conversely, traffic loads at typical operating speeds exert impact-type loads (i.e., duration of load is very short). Therefore, it is possible to consider the total stress field as comprised of an existing thermal stress condition with traffic load stress effects superimposed, as was done in the simulations. Further, as a wheel loads move along the pavement, another stress curve could be drawn through the maximum stresses obtained for each location it occupies. The results of this analysis are shown in Figures 1.2.22 and 1.2.23 for $\phi = 70°$ and $\phi = 40°$, respectively.

Figures 1.2.22 and 1.2.23 demonstrate that the pavement surface experiences a higher level of tensile stress due to wheel loads, while maintaining the general shape of the previously determined thermal principle stress. There still remains a region of stress relief, followed by a maximum level of stress. The net effect of the traffic loads is to increase the principle stresses and ultimately shorten the thermal crack spacing as observed in the field.
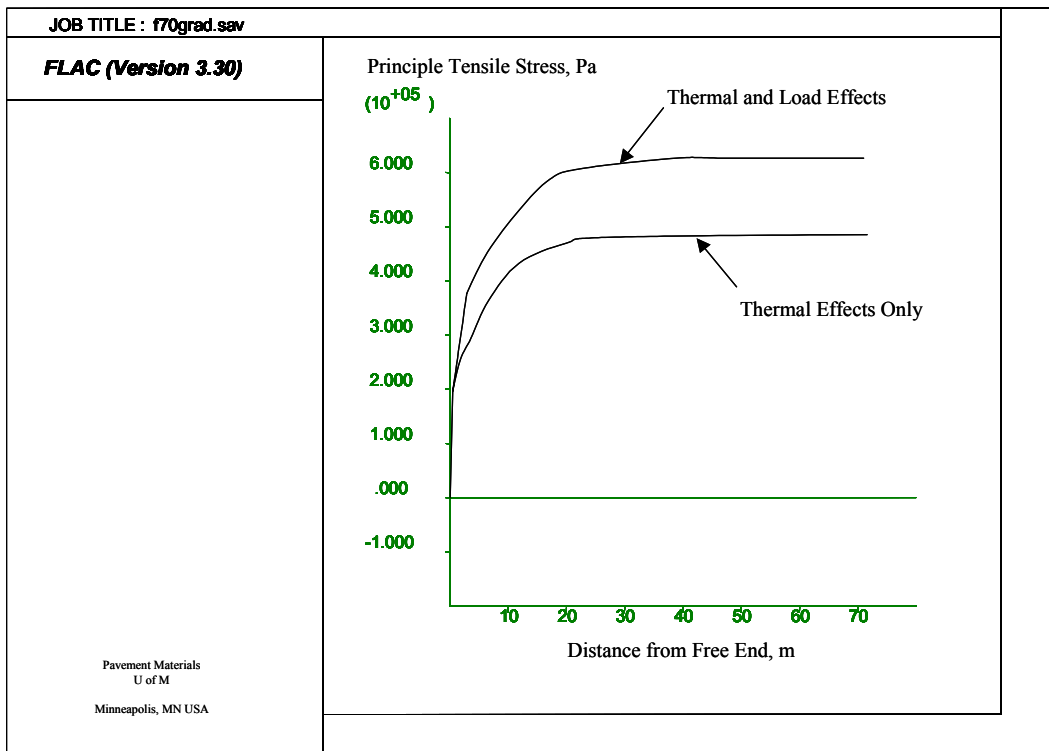
Figure 1.2.22 Stress Curve Comparison (ϕ=70º).

FLAC (Version 3.30)

Principle Tensile Stress, Pa

$(10^{+05}$)

Thermal and Load Effects

6.000

5.000

4.000

3.000

2.000

1.000

.000

-1.000

Thermal Effects Only

10   20   30   40   50   60   70

Distance from Free End, m

Pavement Materials
U of M

Minneapolis, MN USA
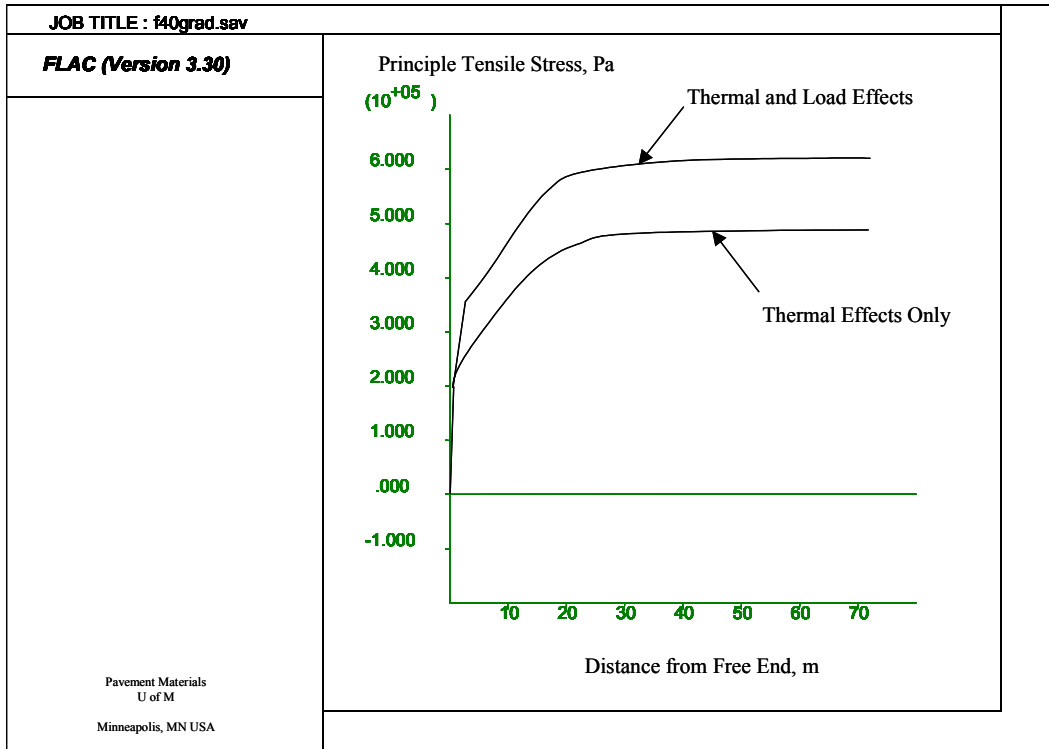
Figure 1.2.23 Stress Curve Comparison (ϕ =40°).

CRACK SPACING DERIVED FROM FRICTIONAL RESTRAINT MODEL

The previous section examined the tensile stress fields developed under a variety of thermal and loading conditions. While the development of a fracture parameter to predict thermal cracking is beyond the scope of this work, it is possible to postulate the thermal crack spacing from the stress fields as described below.

Assume that thermal cracks will develop when some tensile strength or fracture parameter (S_t) is exceeded due to thermal or combined thermo-mechanical stresses. This corresponds to the concept developed by Hills and Brien (17) and illustrated in Figure 1.2.2.3. Applying the concept to the tensile stress field is illustrated in Figure 1.2.24.

According to Figure 1.2.24, cracking will not occur between the free edge and x_c since the thermally induced stress is less than S_t. Beyond x_c a crack could form anywhere, however the minimum is x_c and therefore the minimum crack spacing is x_c. The maximum crack spacing, according to this model, would be $2*x_c$ since two consecutive free edges

would have x_c stress relief as shown in Figure 1.2.25. The average crack spacing, assuming cracks will form with equal probability between x_c and $2*x_c$ would be $1.5*x_c$.
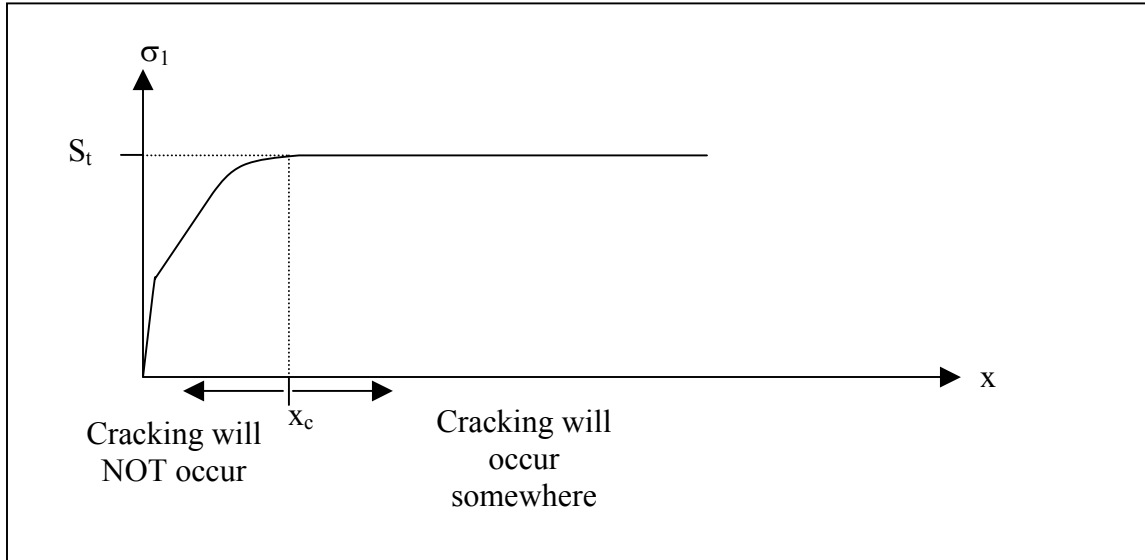
Figure 1.2.24 Stress, "Strength" and Regular Crack Spacing.
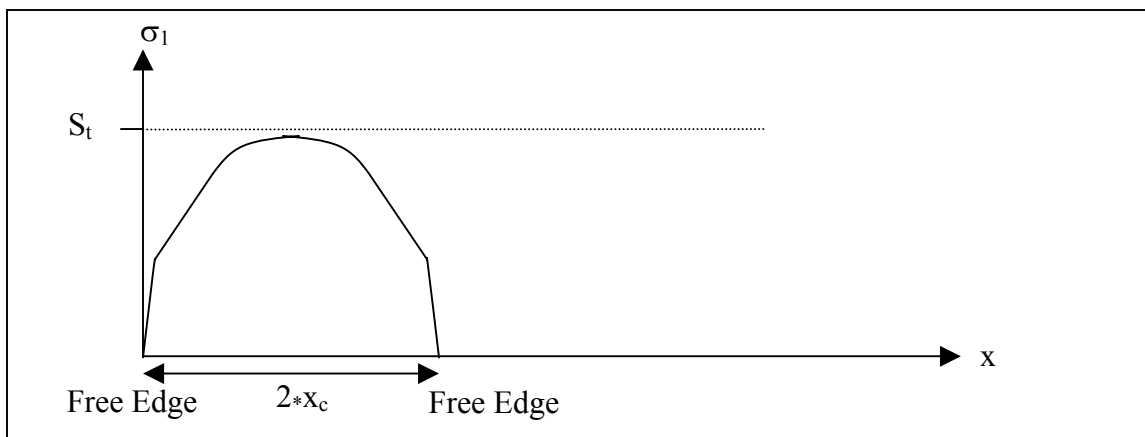
Figure 1.2.25 Maximum Crack Spacing.

SUMMARY

This chapter served to describe a mechanistic pavement model that predicts thermal crack spacing. The model was based upon a two-dimensional continuum, solved by the finite

difference method employed in FLAC, and considers the frictional properties of the supporting granular material in the analysis.

It was found that the frictional properties of the supporting layer have a significant effect on the stress relief near the free edge of a pavement surface layer. The stress relief region was used to explain the regularity of crack spacing in that cracks will not form in regions below a threshold stress level. Further, through simulation, it was found that the addition of thermal gradients and traffic loads to the model would effectively shorten the crack spacing and increase the amount of cracking. These observations are consistent with thermal cracking field performance.

PART 1. MODELING
Chapter 1.3. Field Comparison

INTRODUCTION

The chapter 1.2 described a mechanistic two-dimensional model to predict the thermal crack spacing of asphalt pavements. While the model was qualitatively consistent with field observations of thermal cracking, a more detailed study was required to ascertain whether thermal cracking predictions made by the model are reasonable. Therefore, the objective of the comparison study was to assess whether the two-dimensional model yielded reasonable predictions of thermal crack spacing when compared to measure thermal crack spacing.

Observed thermal cracking on test sections at the Minnesota Road Research Project (Mn/ROAD) were used for comparison. Mn/ROAD is a full-scale outdoor pavement testing facility, constructed in 1992 and 1993 by the Minnesota Department of Transportation and located approximately 65 km northwest of the Minneapolis/St. Paul metropolitan area. The facility is comprised of forty 150-m pavement test sections that are fully instrumented to monitor states of pressure, strain, temperature and moisture. The test sections, or cells, are divided between a low-volume loop trafficked by a single truck and a mainline that is subjected to live interstate traffic. Further, the cells were constructed with various layer thicknesses and differing types of pavement layers, including both rigid (portland cement concrete; PCC) and flexible (hot mix asphalt concrete; HMAC) pavement structures.

It should be noted that Mn/ROAD was not designed to study thermal cracking exclusively. However, thermal cracking has been observed at Mn/ROAD and the amount of data gathered for other research projects associated with Mn/ROAD, in addition to thermal cracking maps and in situ sensors, made it the best candidate for field comparison of the thermal cracking model in Minnesota.

One of the challenges posed by the field comparison study was that neither new nor additional laboratory testing was conducted as part of the study. It was therefore necessary to obtain the best-available model input values from the Mn/ROAD database and existing

literature. For some inputs, such as layer thickness, the data had been measured as part of the Mn/ROAD project and were readily available. For other inputs, such as Poisson's ratio, the literature was consulted and engineering judgment was used to establish the model input value. In total, the field comparison study examined whether the thermal cracking model would produce reasonable predictions of crack spacing given reasonable input values.

METHODOLOGY

The field comparison study was divided into a number of steps that will be fully described in the following sections. The steps, in order, were as follows:

1.   Select Mn/ROAD test sections for inclusion in the study.

2.   Analyze the thermal crack spacing for each test section.

3.   Analyze in situ thermal conditions for each test section.

4.   Gather material property data required for numerical simulation.

5.   Input environmental and material property data to the thermal cracking model and perform simulation to determine average predicted crack spacing.

6.   Compare predicted average crack spacing to measured average crack spacing.

7.   Evaluate whether thermal cracking model has made reasonable predictions.

SELECTION OF MN/ROAD TEST SECTIONS

There are 17 flexible pavement cells at Mn/ROAD, all of which have experienced varying degrees of thermal cracking distress. The cells are divided into those on the mainline which are loaded by Interstate-94 traffic and those on the low-volume loop that are subjected to repeated loading by a single truck. Further, the mainline cells are divided into the 5-year and 10-year sections. The 5-year sections are typically thinner in terms of total pavement thickness since they were designed to fail in approximately five years while the 10-year sections are relatively thicker to withstand more traffic. The low-volume cells are thinner since they were designed for low levels of traffic and an approximate design life of three years.

Although thermal cracking was observed on all the test cells at Mn/ROAD, it was decided to perform the study on a limited number of test cells. This was done since the

objective of the study was to assess the reasonableness of the thermal cracking model in predicting thermal crack spacing and not to calibrate the model. With that in mind, only the 5-year test cells were used in the study. These cells were chosen based on their common thickness design, identical asphalt binder type and common subgrade type. Additionally, as will be discussed below, the cells exhibited different cracking patterns and were constructed with different types of base materials. Therefore, these cells were the best candidates to verify the model and to assess the effects of the supporting material type on thermal crack spacing.

Description of Test Cells

Figure 1.3.1 illustrates the structural cross-sections of the four test cells used for the model comparison. Each cell was constructed on the same subgrade soil, which was a silty-clay material. Also common between the cells was the 120/150 penetration graded asphalt binder and the aggregate gradation in the HMAC. The thickness of the asphalt concrete layers was approximately the same between cells 1, 2 and 3 while cell 4 was constructed as a full-depth pavement with a thicker HMAC layer. The thicknesses in Figure 1.3.1 were used in simulating the four test cells.

The primary difference between the cells, as shown in Figure 1.3.1, was the supporting unbound layers. In general, a higher numerical classification corresponds to a higher quality base material. For example, a class 6 base material (used in cell 2) is crushed granite aggregate, while there is no crushing requirement for the other classes. Additionally, the class 5 and 6 materials are often used as base layers while the class 3 and 4 are usually used as subbase materials. Based on these specifications, it is possible to speculate that the internal angle of friction increases with increasing base class number as a result of increased crushing and quality requirements. Rapid shear testing on the Mn/DOT materials indicates that friction angle does increase for the class 6 material, over the other materials, as shown in Table 1.3.1 (41). Additionally, cohesion appeared to increase with increasing classification.

Table 1.3.1 Average Angle of Internal Friction and Cohesion of Mn/ROAD Materials (after Alvarez and Thompson, 1998).

Base Classification	Friction Angle (^{o})	Cohesion (kPa)
3	44	48
4	38	83
5	41	65
6	49	110
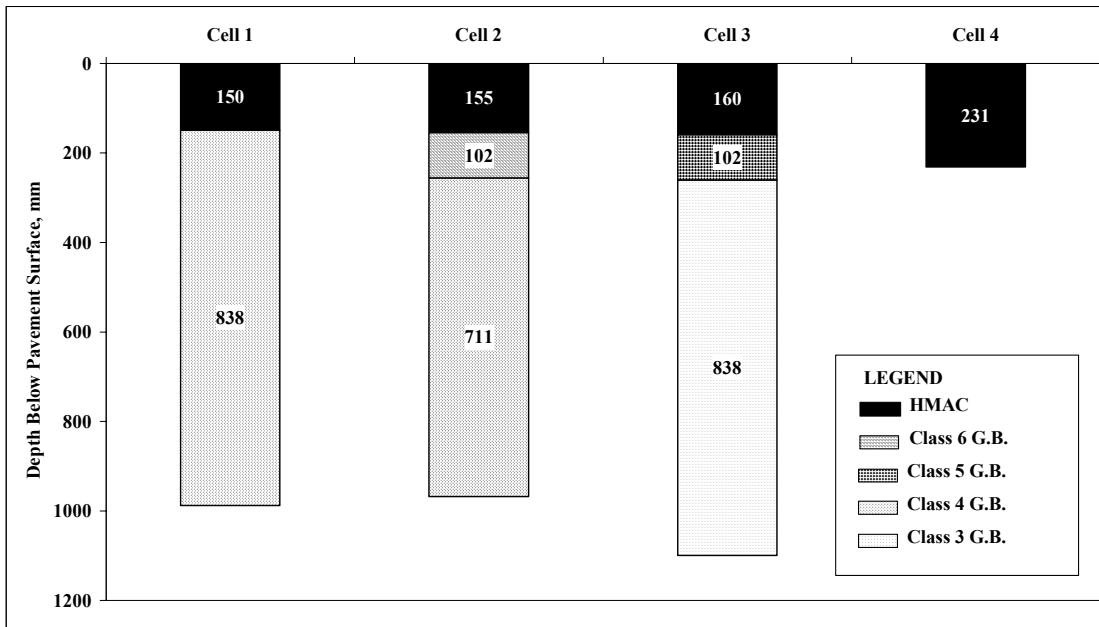
Figure 1.3.1 5-Year Mainline Mn/ROAD Cells.

CRACKING CHARACTERISTICS

Since the construction of the 5-year test cells in 1992, pavement surface surveys were conducted by Mn/ROAD staff under the direction of David Palmquist. The surveys, represented by maps spanning 15 m increments, depicted the locations of transverse cracks. For this study it was assumed that transverse cracks were in fact thermal cracks. These highly detailed maps were obtained, combined onto a larger scale covering the entire test

cell, and are illustrated in Figure 1.3.2 through 5 for cells 1 through 4, respectively. The horizontal scale represents the entire length of the test section in meters. The vertical scale indicates the location each of the lanes where 0 to 0.5 corresponds to the truck lane and 0.5 to 1.0 corresponds to the passing lane.
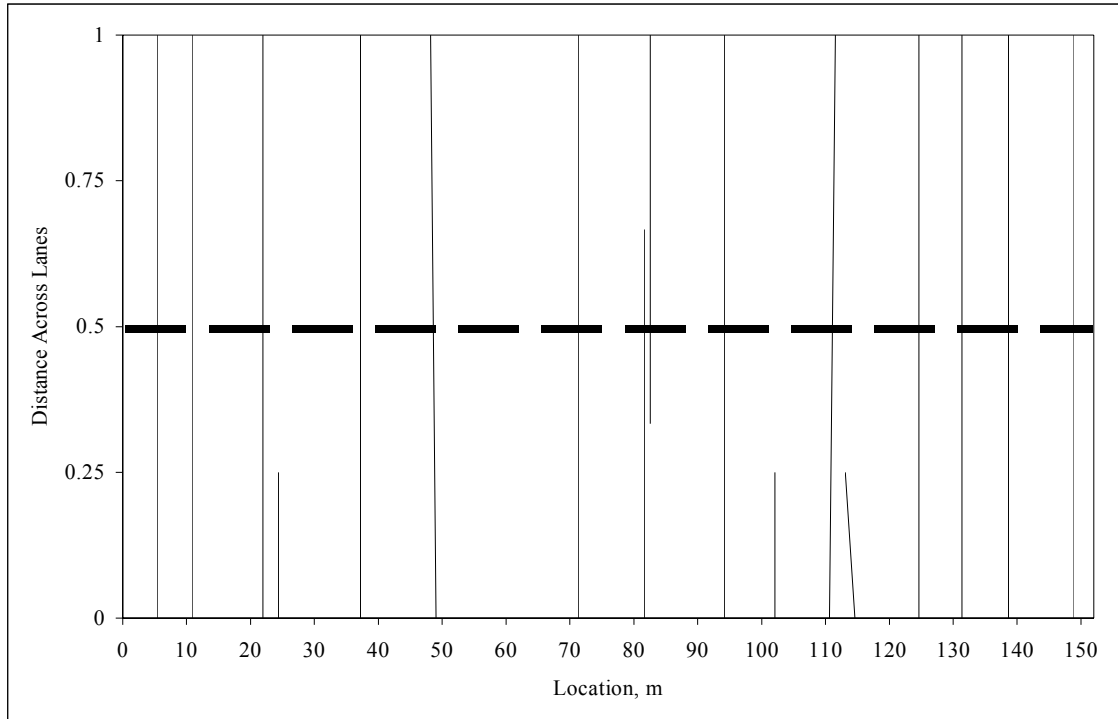
Figure 1.3.2 Cell 1 Cracking Map.
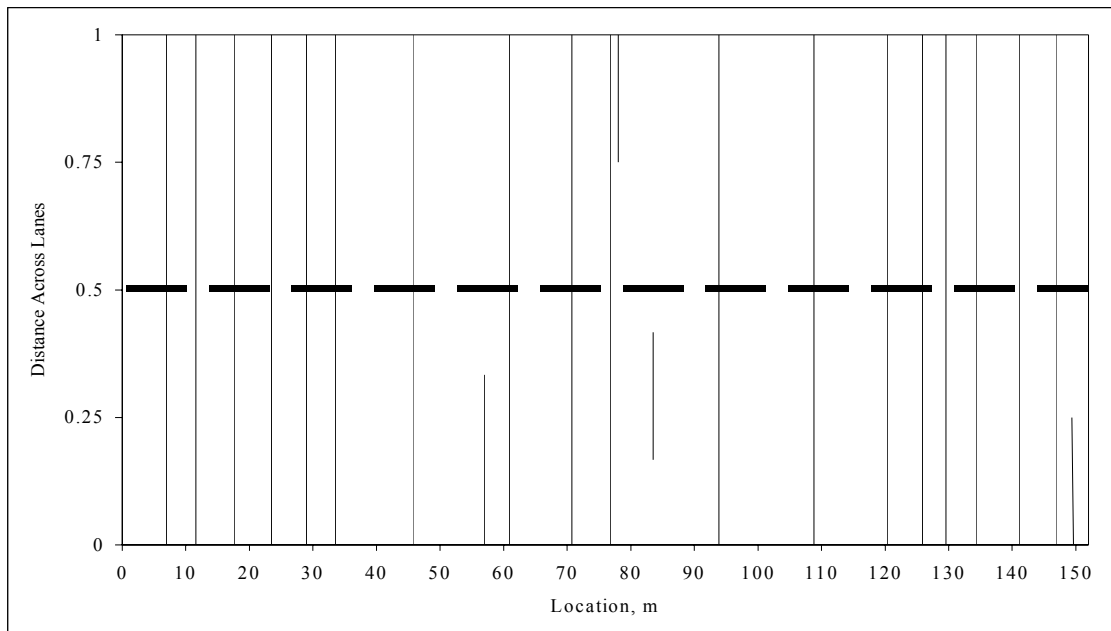
Figure 1.3.3 Cell 2 Cracking Map.
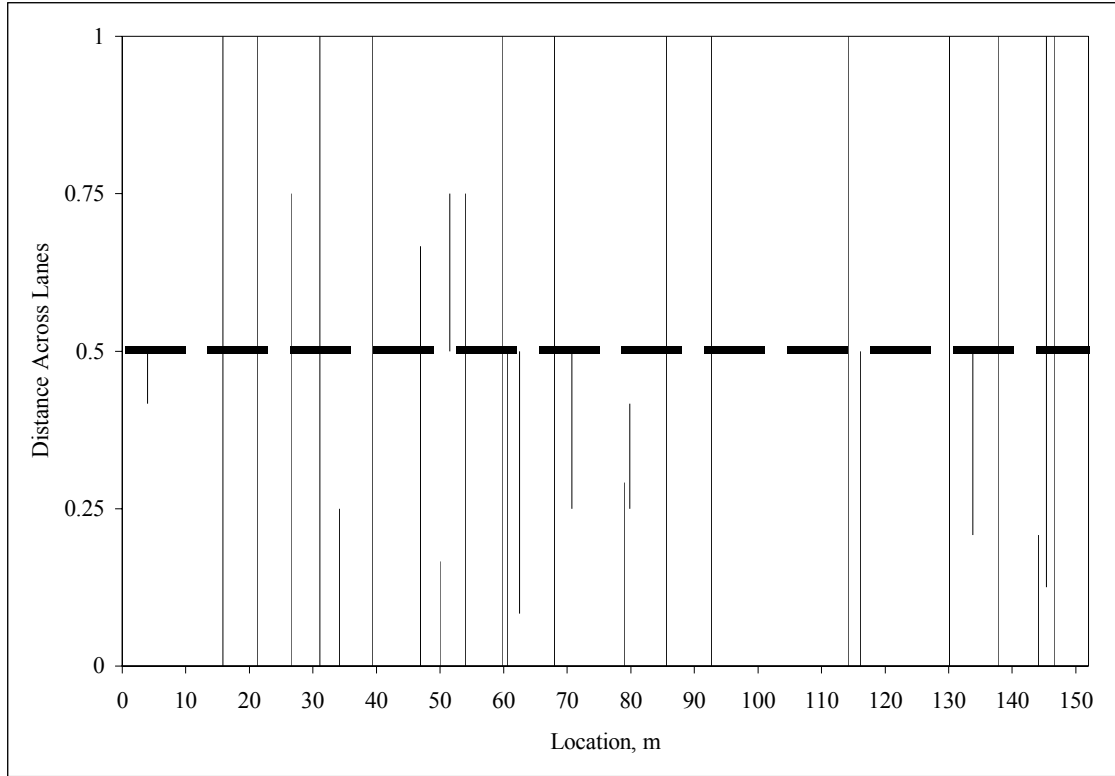
Figure 1.3.4 Cell 3 Cracking Map.
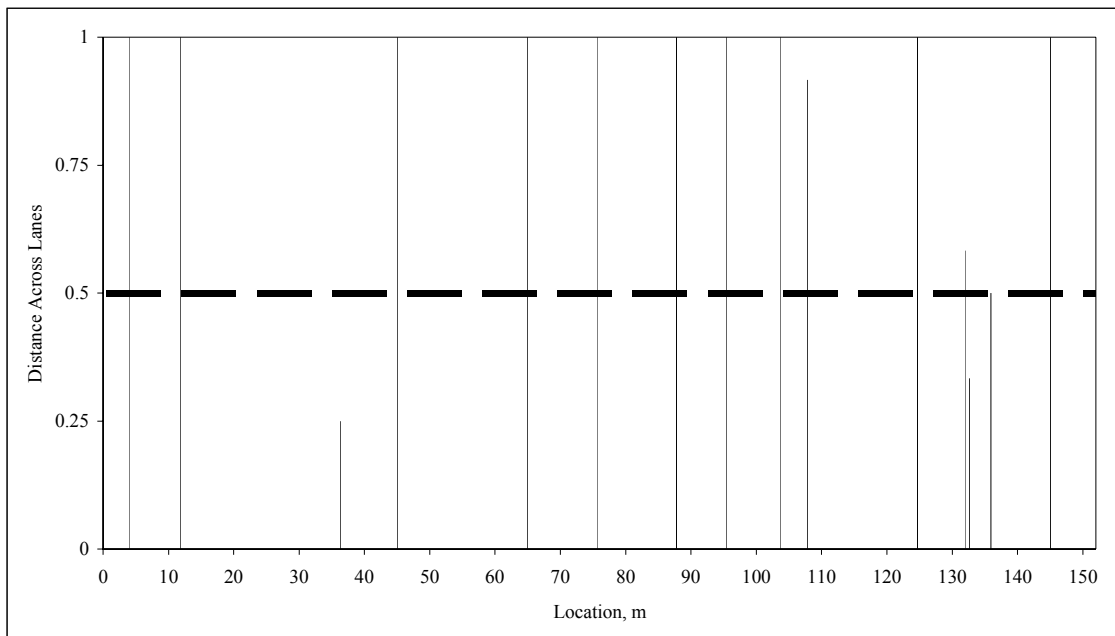
Figure 1.3.5 Cell 4 Cracking Map.

The majority of the cracking occurred during the winter of 1995-1996 when pavement surface temperatures dropped below -30°C. Figure 1.3.6 clearly shows that prior to the winter of 1995-1996 no cracking had occurred on cells 1-4. Further, little or no additional cracking developed since the 1996. Therefore, it was decided to focus on the thermal events of 1996 for the numerical simulation. Further discussion of pavement temperatures is provided below.
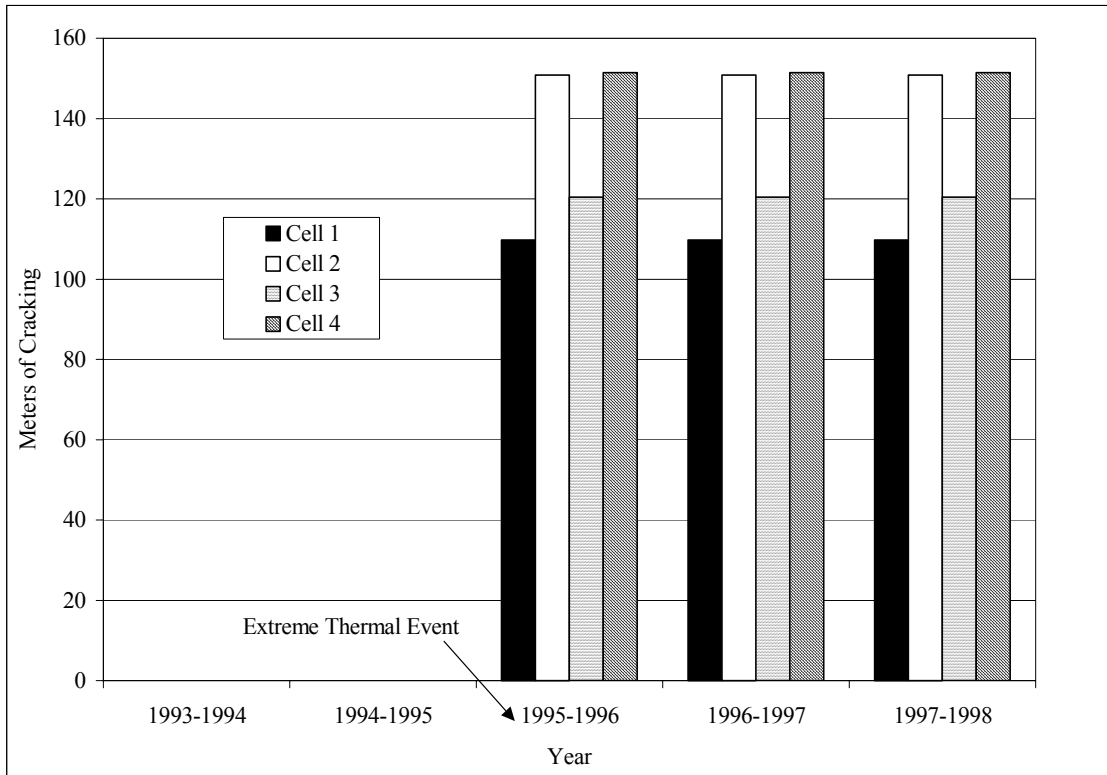
Figure 1.3.6 Thermal Cracking with Time at Mn/ROAD.

The cracking maps were used to determine the average and standard deviation of crack spacing for each of the four test cells. As seen in Figures 2 through 5, there were a number of partial and very closely spaced cracks. Only cracks spanning at least half the total pavement width were used to determine the spacing. In some cases, it was necessary to average the location of a group of cracks that were close together and could be considered, for the purposes of the comparison study, a single crack. The criterion was that consecutive cracks within 1.5 meter were counted as a single crack. Table 1.3.2 lists the average and standard deviation of crack spacing for each test cell.

Table 1.3.2 5-Year Mainline Cracking Statistics.

Cell	Average Spacing, m	Standard Deviation, m
1	12	4.88
2	8	4.27
3	13	8.23
4	9	5.49

Small sample student t-tests were conducted to assess whether any of the four cells were statistically different from the other cells in terms of average crack spacing. The t-test was used since the sample size for each cell was relatively small; typically less than 20 cracks per cell.

Each cell was compared to the other three cells, at a confidence level (α) of 0.05, with null and alternative hypotheses, respectively:

$$H_0: (\mu_i - \mu_j) = 0 \tag{1}$$

$$H_a: (\mu_i - \mu_j) \neq 0 \tag{2}$$

where: H_0 = null hypothesis

H_a = alternative hypothesis

u_i = population mean for cell i

u_j = population mean for cell j

Accepting the null hypothesis in equation (*1*) means the two cells are not statistically different, at a confidence level of 0.05, in terms of average crack spacing. Rejecting the null and accepting the alternative hypothesis (equation (*2*)) means the two cells are statistically different.

The data in Table 1.3.2 were used to conduct the t-tests between all the cells and Table 1.3.3 summarizes the findings. It was found that cell 2 was statistically different from both cells 1 and 3 while it was statistically the same as cell 4. Cell 4 was statistically indistinguishable from each of the other cells. It is important to note that cell 2 had a class 6 base material underlying the HMAC that could have contributed to the smallest measured crack spacing among the 5-year cells by having a high angle of internal friction.

Table 1.3.3 T-test Results for 5-Year Cells.

Cell	1	2	3	4
1		Reject	Accept	Accept
2	Reject		Reject	Accept
3	Accept	Reject		Accept
4	Accept	Accept	Accept	

To summarize the thermal cracking observed at Mn/ROAD on the 5-year cells, the following points may be made:

1. The majority of cracking occurred during the winter of 1995-1996.

2. Cell 2 exhibited significantly smaller thermal crack spacing than either cells 1 or 3.

3. Though cell 4 had an average crack spacing similar to cell 2, it was not statistically distinguishable from any of the cells.

Finally, it should be pointed out that these data were extracted from a relatively limited data set. While the data suggest, through statistical measures, some differences amongst the cells, a more rigorous investigation in the future should include pavements of much greater length than 150 m to increase the size of the data set.

THERMAL CONDITIONS

The coldest air and pavement temperatures were recorded at Mn/ROAD on February 2, 1996. While cracking likely occurred over a series of days or even weeks, it is possible to use the thermal cracking model developed in subtask 1-2 to assess the average crack spacing that would result from a thermal gradient occurring in the pavement. Thermal couples embedded in the pavement with depth recorded this extreme cold event and the temperature field for Cell 1 is illustrated in Figure 1.3.7. The data were downloaded from the Mn/ROAD database specifically for this study.

As shown in Figure 1.3.7, the uppermost sensors in the HMAC experienced the most extreme thermal cycling, while lower layers of the pavement were not subjected to such extreme thermal changes. In fact, the temperature in the lower two-thirds of the base and subgrade remained relatively constant during the daily temperature cycling observed in the upper regions.
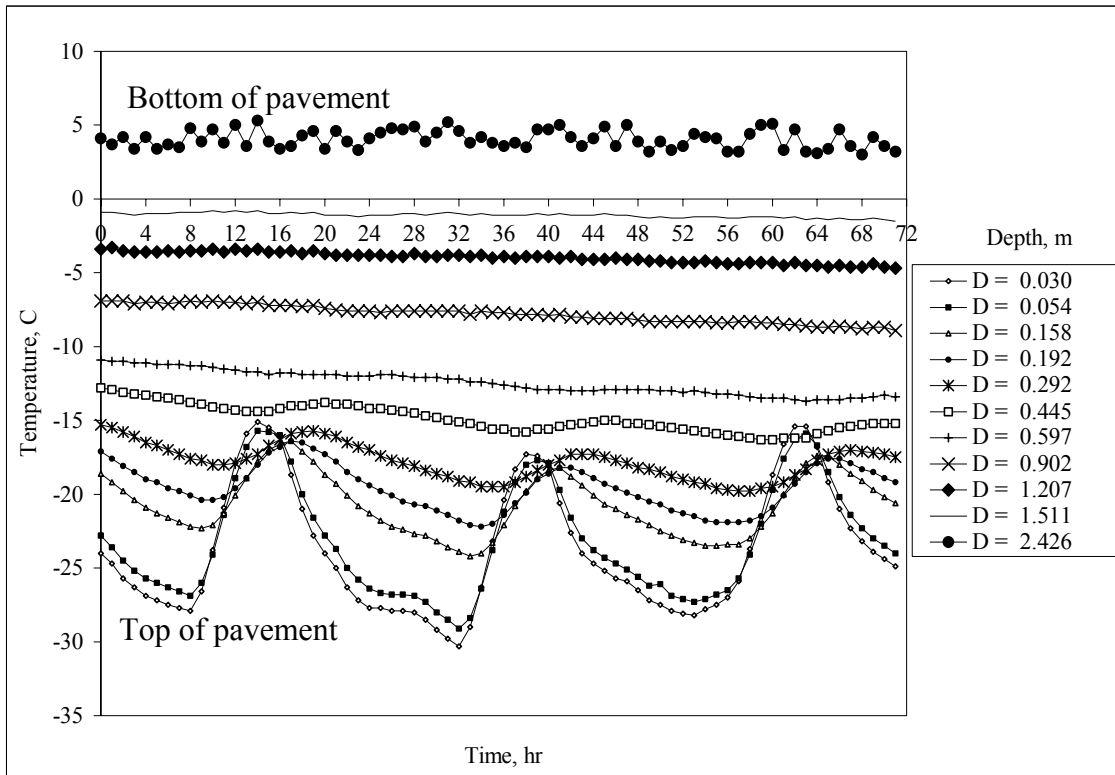
Figure 1.3.7 Cell 1 Daily Cycling - February 1 - 3, 1996.

For the purposes of verifying the model through simulation, it was decided to use the single day temperature decrease leading to the maximum cold pavement temperature on February 2, 1996. It is likely that cracks began to initiate during this time period since the HMAC would become very brittle at the extreme cold temperature. The temperature change experienced by the pavement between the maximum and minimum surface temperatures was calculated and input directly into the thermal cracking model. Figures 8 through 11 illustrate the single day temperature changes, with depth, for cells 1 through 4, respectively. The figures also show the delineation between the different pavement layers.
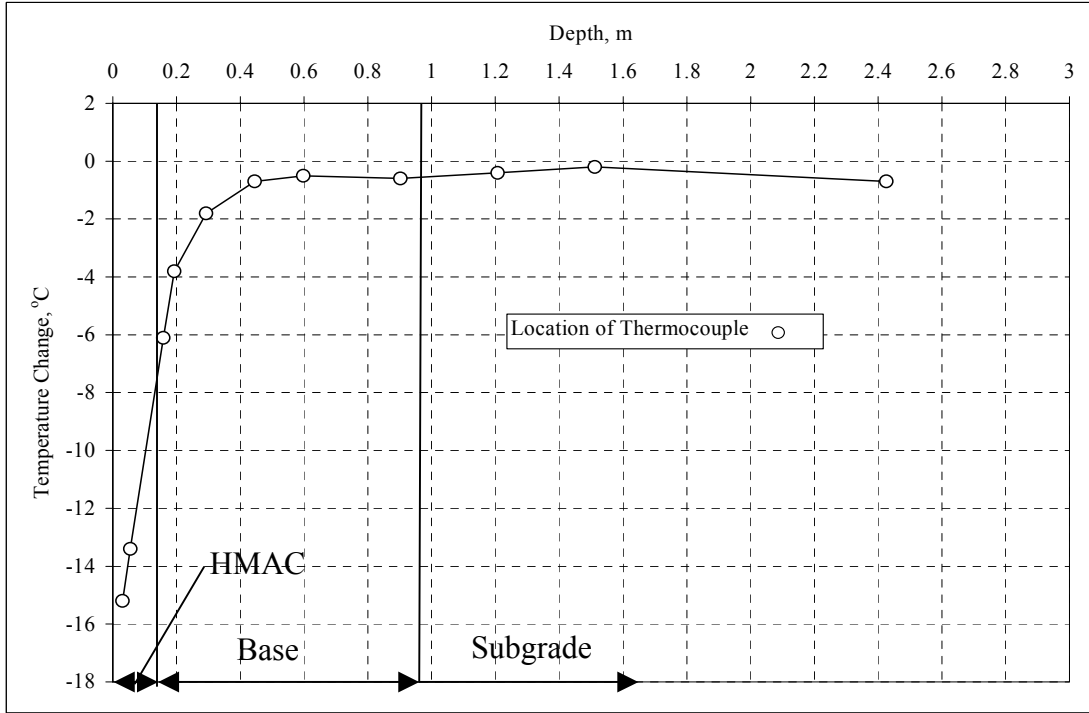
Figure 1.3.8 Cell 1 Temperature Change.
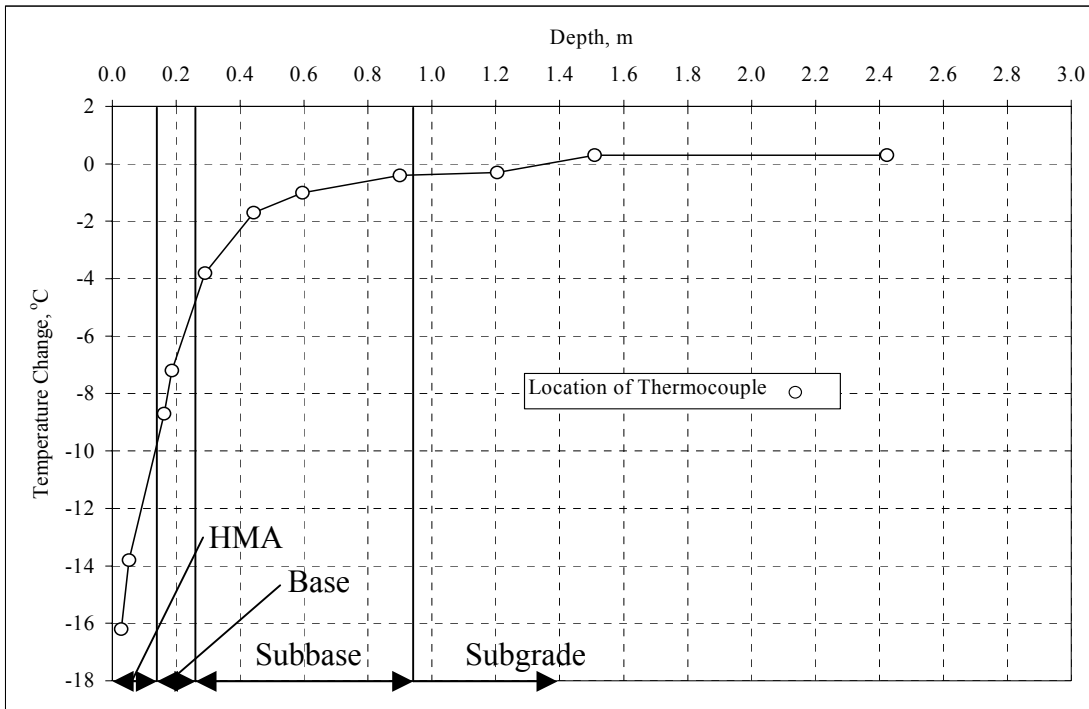
Figure 1.3.9 Cell 2 Temperature Change.

71
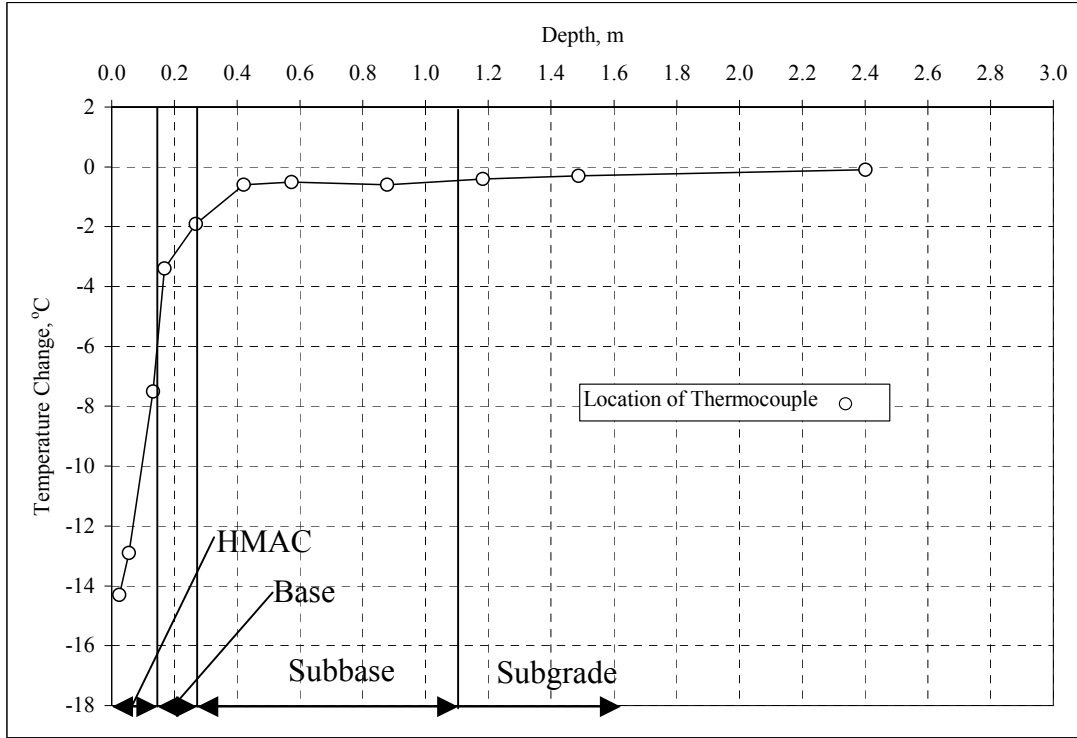
Figure 1.3.10 Cell 3 Temperature Change.
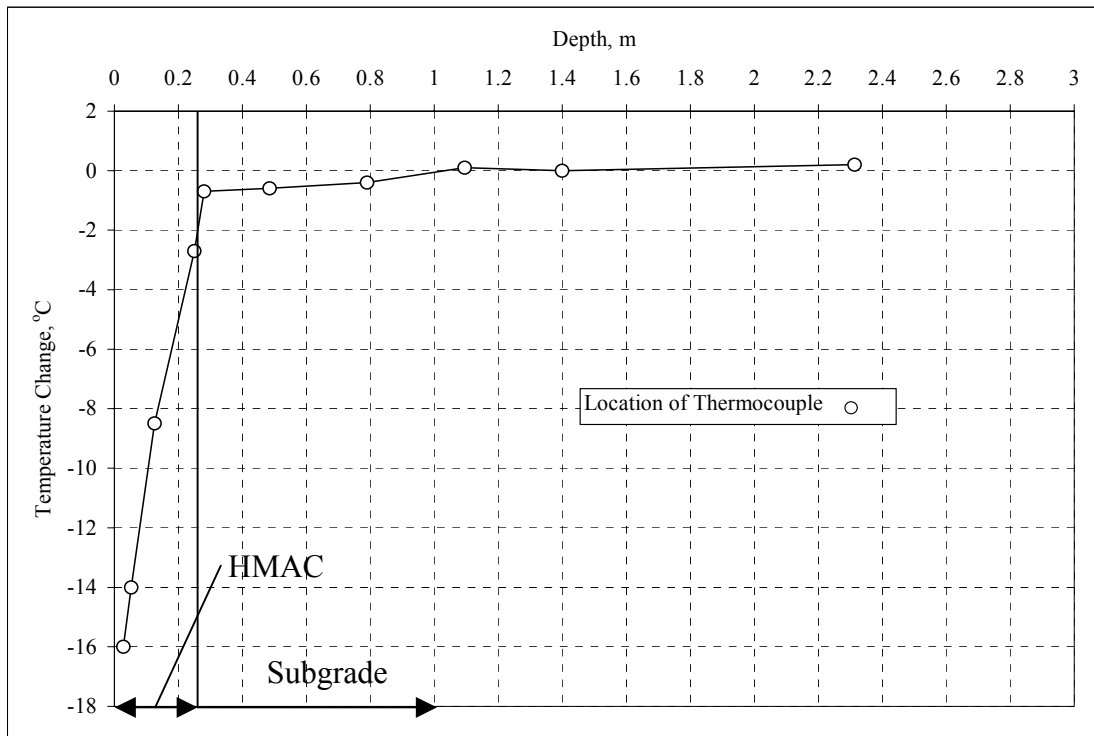
Figure 1.3.11 Cell 4 Temperature Change.

It is important to note that all the cells experienced approximately the same thermal gradient through the depth of the HMAC layer (i.e., on the order of 0.06°C/mm). However, the HMAC thickness of cell 4 was much greater than the other three cells, so the temperature change from the surface to the bottom of the HMAC was greater in cell 4. The temperature difference in Cell 4 was approximately 15°C from top to bottom in the HMAC layer. The temperature difference in the other three cells, from top to bottom in the HMAC layer, ranged from approximately 7°C to 9°C. Therefore, even though the gradients were approximately the same between all cells, cell 4 experienced a more severe thermal change from the top to bottom of the pavement which could have contributed to higher bending stresses near the free edge and ultimately to the more closely spaced cracks.

Figures 1.3.8 through 1.3.11 were used to determine the nodal temperatures for the thermal cracking model. As shown in the figures, a linear change between thermocouple locations was assumed. The temperatures in the figures were then transferred onto the thermal cracking model finite difference grid to perform the simulations. Recall, as explained in subtask 1-2, the importance of characterizing the thermal change so that the incremental thermally induced stress increase ($\Delta\sigma_{ij}$) can be calculated:

$$\Delta\sigma_{ij} = -\delta_{ij}3K\alpha\Delta T \qquad\qquad (3)$$

where: $\delta = 1$ if i=j and $\delta=0$ if i≠j

K = bulk modulus = $\dfrac{E}{3(1-2\nu)}$

α = linear coefficient of thermal contraction

ΔT = change in temperature

MATERIAL PROPERTIES

In addition to layer thickness and temperature data, the material properties needed to be determined. Since no new or additional testing was conducted as part of the comparison study, these inputs were determined from the existing literature and data pertaining to the Mn/ROAD project. The sources of these data are discussed below.

Layer Stiffness

The thermal cracking model requires Young's modulus, a measure of stiffness, since the HMAC layer is modeled as an elastic material and the unbound granular layers as elastic-perfectly plastic materials. One method of determining material stiffness is by backcalculation of falling weight deflectometer (FWD) data. While laboratory methods of determining modulus are available, it was advantageous to use backcalculated data since they represent in situ conditions. A full discussion of FWD backcalculation is provided by Van Deusen (42).

Ovik (15) analyzed backcalculated moduli from Mn/ROAD to determine seasonal average moduli for the test sections at Mn/ROAD. The results of Ovik's seasonal analysis were used to determine the Young's modulus for each pavement layer, by cell, in the frozen condition as shown in Table 1.3.4. It is important to point out that the backcalculation procedure was not able to distinguish between the base and subbase since the base layer was relatively thin in Cells 2 and 3. Therefore, for cells 2 and 3, the same stiffness was assigned to both the base and subbase layers in the model study.

Table 1.3.4 Mn/ROAD Layer Stiffnesses Used in Model Comparison (after Ovik, 1998).

	Backcalculated Modulus, MPa			
Cell	HMAC	Base	Sub-base	Subgrade
1	14,000	5,500	Not Applicable	1,700
2	14,000	5,500	5,500	1,700
3	14,000	5,500	5,500	1,700
4	14,000	Not Applicable	Not Applicable	1,700

Laboratory testing to determine resilient modulus (M_R) was conducted by the Cold Regions Research and Engineering Laboratory (CRREL) on the Mn/DOT materials. While resilient modulus is not truly the elastic modulus, it is often used in pavement engineering as a proxy for elastic modulus. Figure 1.3.12 summarizes the findings of the laboratory study on frozen base materials (43). It was found that the resilient modulus is a function of temperature, in the laboratory, and the modulus tended to increase with increasing base classification. Though the values in Figure 1.3.12 are somewhat higher than those

backcalculated by Ovik, they are on the same order of magnitude and it was therefore decided to use the field determined elastic moduli as listed in Table 1.3.4.
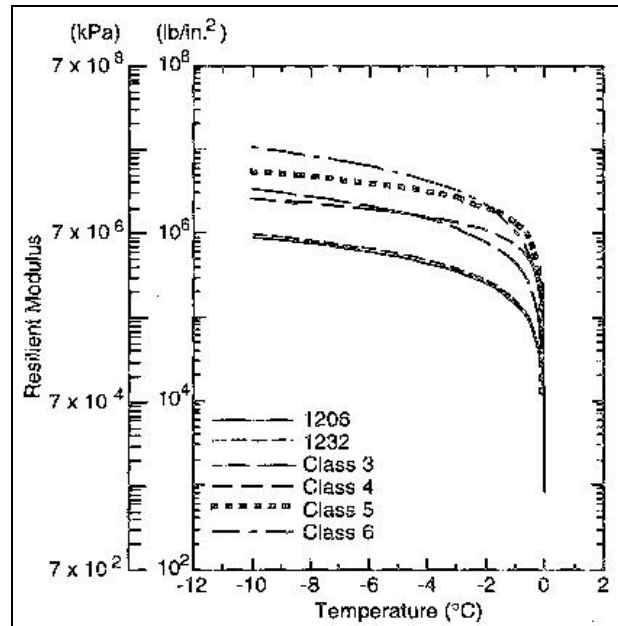
Figure 1.3.12 Resilient Modulus vs Temperature Relationship for Mn/DOT Base Materials (Bigl and Berg, 1996).

Poisson's Ratio

Poisson's ratio represents the volumetric strain response of a material to loading. While Poisson's ratio has not been measured for any of the Mn/ROAD materials, typical values reported by Yoder and Witczak are shown in Table 1.3.5. It is noted that Poisson's ratio of HMAC tends to decrease with temperature. Based on Table 1.3.5, and taking into account the temperature at which the simulation would be run, Poisson's ratios were assigned as shown in Table 1.3.6.

Density

The density of the pavement layers is required since gravitational effects were accounted for in the model simulation. Density measurements of asphalt concrete cores extracted from each of the test cells were reported by Stroup-Gardiner and Newcomb (44).

75

The values ranged from 2,200 kg/m^3 to 2,300 kg/m^3. For the modeling study, all density values were set at 2,200 kg/m^3 for the asphalt concrete as shown in Table 1.3.7.

The base materials were tested for density at Mn/ROAD and Ovik (15) reported dry densities of approximately 2,000 kg/m^3. This value was used for base and subbase density as shown in Table 1.3.7. Data obtained from the Mn/ROAD database indicated the subgrade density of Cells 1 through 4 to also be approximately 2,000 kg/m^3 as listed in Table 1.3.7.

Table 1.3.5 Poisson's Ratio of Paving Materials (after Yoder and Witczak, 1975).

Material	Range	Typical
HMAC	Temperature Dependent 0.25 at 4°C 0.50 at 60°C	0.35 at 25°C
Unbound Granular	0.2 – 0.45	0.5 (Cohesive) 0.3 (Non-Cohesive) 0.45 (Soft Clay)

Table 1.3.6 Mn/ROAD Poisson's Ratio Used in Model Comparison.

Cell	Poisson's Ratio			
	HMAC	Base	Sub-base	Subgrade
1	0.20	0.40	Not Applicable	0.45
2	0.20	0.40	0.40	0.45
3	0.20	0.40	0.40	0.45
4	0.20	Not Applicable	Not Applicable	0.45

Table 1.3.7 Mn/ROAD Layer Density Used in Model Comparison.

Cell	Assumed Layer Density, kg/m³			
	HMAC	Base	Sub-base	Subgrade
1	2,200	2,000	Not Applicable	2,000
2	2,200	2,000	2,000	2,000
3	2,200	2,000	2,000	2,000
4	2,200	Not Applicable	Not Applicable	2,000

Coefficient of Thermal Contraction / Expansion

The linear coefficient of thermal contraction / expansion (α) is critical since it describes the volumetric response of a material to a change in temperature. While α has not been measured for the Mn/ROAD materials, there was some guidance available from the literature.

Hiltunen and Roque (24) recommend using a modified volumetric relationship that was originally developed by Jones, et al (45). As shown in the equation, the $\frac{1}{3}$ term is necessary to convert from a volumetric to linear coefficient:

$$\alpha_{mix} = \frac{VMA \cdot \beta_{ac} + V_{agg} \cdot \beta_{agg}}{3 \cdot V_{total}} \qquad (4)$$

where:

α_{mix} = asphalt concrete linear thermal coefficient of contraction/expansion (/°C)

VMA = percent volume of voids in the mineral aggregate

β_{ac} = asphalt cement volumetric coefficient of thermal contraction/expansion (/°C)

V_{agg} = percent volume of aggregate in mixture

β_{agg} = aggregate volumetric coefficient of thermal contraction/expansion (/°C)

V_{total} = total volume of mixture = 100%

The VMA and V_{agg} were determined for the Mn/ROAD mixtures as part of routine mixture testing after construction, but testing was not conducted to determine β_{ac} nor β_{agg}. However, Hiltunen and Roque (24) found that β_{ac} does not vary greatly between asphalt

cements and recommend using an average value of $3.45*10^{-4}$ /°C. They also found that β_{agg} is typically two orders of magnitude less than β_{ac}. Therefore, for simulation purposes and lacking better information regarding the Mn/ROAD materials, β_{agg} was set at $3.5*10^{-6}$ /°C. These data were used with volumetric data from Mn/ROAD (44) and equation (*4*) to calculate asphalt concrete linear thermal coefficients for each test cell, which are shown in Table 1.3.8.

In determining the thermal coefficient for the unbound layers, β_{agg} was divided by 3 to convert from the volumetric to linear thermal coefficient. While this does not take into account the presence of air voids or moisture present in the unbound layers, it was deemed sufficient for comparison purposes since, as shown in Figures 1.3.8 through 1.3.11, the temperature change in the lower pavement layers was significantly less than the HMAC layer and therefore less critical in terms of calculating thermal stresses.

Table 1.3.8 Mn/ROAD Thermal Coefficients Used in Model Comparison.

| Cell | Linear Thermal Coefficient of Contraction/Expansion, /°C | | | |
	HMAC	Base	Sub-base	Subgrade
1	$1.800*10^{-5}$	$1.1*10^{-6}$	Not Applicable	$1.1*10^{-6}$
2	$1.969*10^{-5}$	$1.1*10^{-6}$	$1.1*10^{-6}$	$1.1*10^{-6}$
3	$1.862*10^{-5}$	$1.1*10^{-6}$	$1.1*10^{-6}$	$1.1*10^{-6}$
4	$1.800*10^{-5}$	Not Applicable	Not Applicable	$1.1*10^{-6}$

It is interesting to note that Cell 2, which had the lowest average crack spacing also had the highest thermal coefficient for the asphalt concrete layer. Since maximum thermal stresses are linearly related to the thermal coefficient this could have contributed to the more frequent cracking.

Angle of Internal Friction and Cohesion

Since the inputs described above were relatively well known, as compared to the frictional properties of the supporting granular media, it was decided to use the internal angle of friction (ϕ) and cohesion (c) as factors to tune the model to the observed performance.

While it is tempting to call these parameters "calibration factors," it must be reemphasized that this was a comparison study and to truly calibrate the model would require comprehensive laboratory testing to accurately measure all of the model input parameters.

Practical limits were established for the angle of friction and cohesion parameters. Das (46) listed typical internal angles of friction for gravels with some sands, which could be used to describe the Mn/ROAD base materials, in the range of 34º to 48º. Testing was conducted on the Mn/ROAD class 5 base material and found ϕ to range from 38º to 51º (47); increasing with a reduction in moisture content. Further, a typical range for silts (Mn/ROAD has a silty-clay subgrade) is 26º to 35º (46). Based on these values, and keeping in mind the values reported in Table 1.3.1, the practical limits for ϕ were set as follows:

Granular Base/Subbase Material: 30º - 50º

Subgrade Soil: 20º - 40º

With respect to cohesion, Das (46) states that over consolidated clays are cohesive while sands are typically noncohesive. However, these statements do not take into consideration that the material is in a frozen condition. Research by Sayles (48) on Ottawa sands in a frozen condition has shown cohesion on the order of 1 MPa. Additionally, work by Isackson et al (47) established the level of cohesion at approximately 30 kPa for the Mn/ROAD class 5 materials in an unfrozen condition. Additionally, Table 1.3.1 indicated that cohesion for the Mn/ROAD materials could range between 40 to 110 kPa. Taken as a whole, these numbers suggest that the base and subgrade materials at Mn/ROAD are cohesive materials and a range of cohesion was set between 0 and 240 kPa.

Tensile Strength Criteria

As described in subtask 1-2 and by Hills and Brien (17), the tensile strength of the HMAC can be used as a limiting quantity to describe the stress at which cracking will develop. Stroup-Gardiner and Newcomb (44) conducted indirect tensile strength tests on asphalt concrete cores extracted from Mn/ROAD after construction. Although the cores were tested at a variety of temperatures and loading rates, the slowest loading rate (0.025 mm/min) and coldest test temperature (-18ºC) were thought to be the best approximation of field conditions of those tested. Table 1.3.9 lists the tensile strengths used as cracking criteria for each of the 5-year test cells at Mn/ROAD.

MODEL COMPARISON PROCEDURE

Comparison of the thermal cracking model developed in chapter 1.2 to field data was done as an iterative process to develop a better understanding of how the frictional properties (c, ϕ) of the supporting layers could contribute to crack spacing.

The inputs described above were used in the model and the minimum crack spacing, X_c, was determined at the end of the cooling cycle. In the context of the model comparison study, X_c was the distance from the free end to the point at which the tensile strength of the material was exceeded by the thermally induced tensile stress (σ_1). The average crack spacing was then determined by multiplying $1.5 * X_c$, as described in subtask 1-2. The average predicted crack spacing was compared to the measured average crack spacing for each test cell. It was decided that a prediction within $\pm 20\%$ of the measured average value would suffice for comparison purposes. If the model prediction fell outside this range, then the frictional parameters (c and ϕ) of the pavement layers were adjusted accordingly and another simulation was conducted. Figure 1.3.13 illustrates the iterative validation procedure.
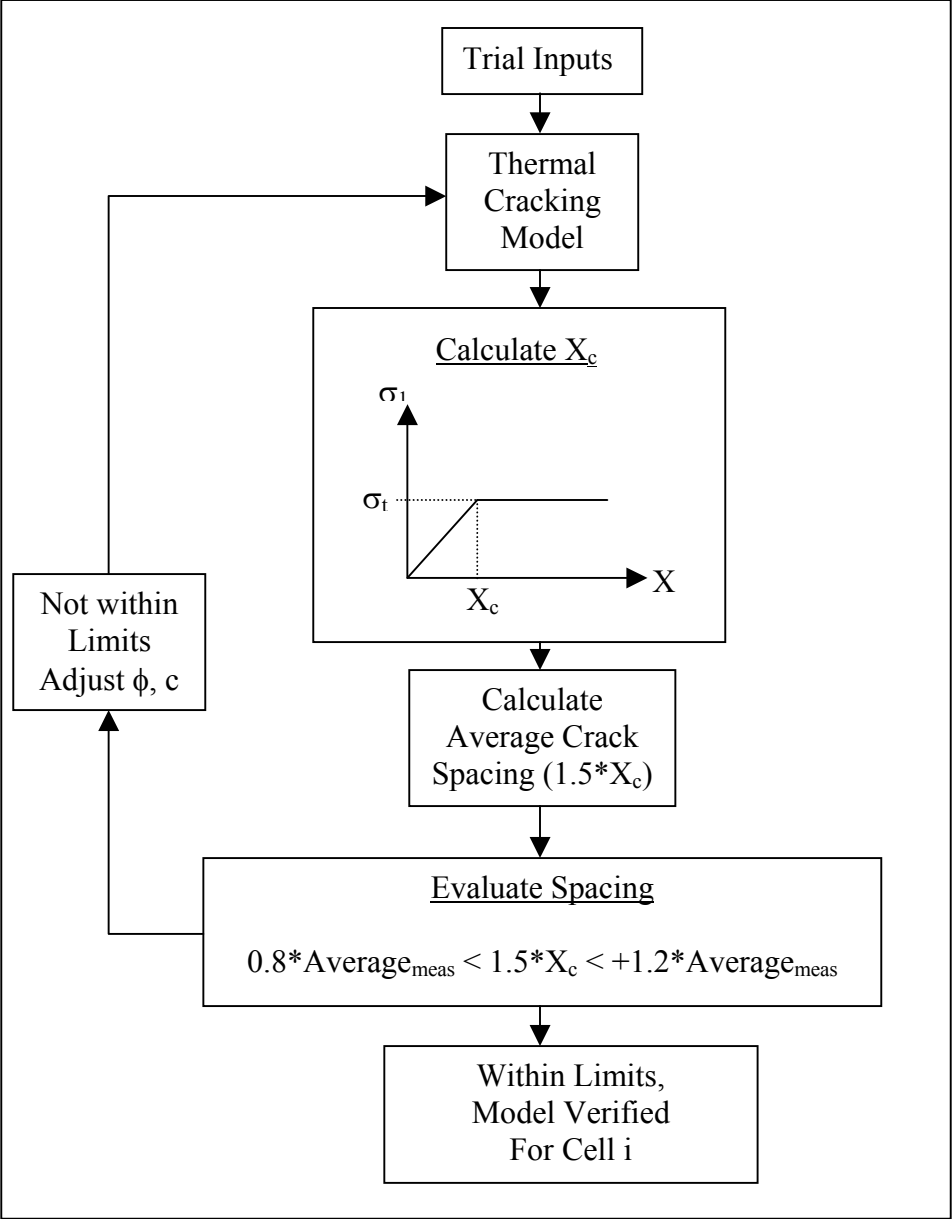
Figure 1.3.13 Model Comparison Procedure.

Table 1.3.9 Tensile Strength of Mn/ROAD Mixtures (after Stroup-Gardiner and Newcomb, 1997).

Test Cell	Tensile Strength, kPa
1	1,862
2	1,901
3	1,636
4	1,772

RESULTS AND DISCUSSION

The first observation made in the study was that the maximum tensile stresses developed by the end of the cooling cycle far exceeded the tensile strength of the HMAC in each of the four test cells. Figure 1.3.14, for example, illustrates the thermal stress curves, in 1^oC increments, for cell 1 with the approximate tensile strength superimposed. Therefore the model does predict that cracks would have formed under these conditions.

The figure 1.3.indicates that the stress was exceeded after the sixth temperature change (the simulations were conducted in 1^oC increments to maintain an accurate numerical solution). At this point in the simulation X_c would have been approximately 18 m, resulting in an average predicted spacing of 27 m. However, the pavement did continue to cool and the predicted stresses continued to increase beyond the tensile strength of the material. The question naturally arises regarding whether the stress field predicted for a long pavement section could be used to predict the stresses in a shorter section. In other words, if the pavement were to crack, forming a shorter section, could the stress field from the long, intact section, be used to determine the stress in the short section?

To investigate this question, additional simulations were conducted with shorter pavement sections and comparisons were made between the long and short simulations. Figure 1.3.15 compares the stress field developed over the first 10 meters between the 72 m section shown in Figure 1.3.14 and a shorter 10 m section at two temperature changes, representing two thermal gradients. Figure 1.3.15 shows that the shorter section has nearly the same thermal stresses as the long section. The -5^oC temperature change curves are almost indistinguishable. The greater temperature change does introduce some differences,

however the plots are fairly close. Based on these data, it can be surmised that the length of the section simulated does not greatly affect the resulting stress plot. As the pavement cools and potentially cracks, the stress field does not change, it is simply limited by the length of the resulting section. Consequently, it is possible to calculate the critical length (X_c) at the end of the cooling cycle by determining the intersection of material strength and thermal stress curve.
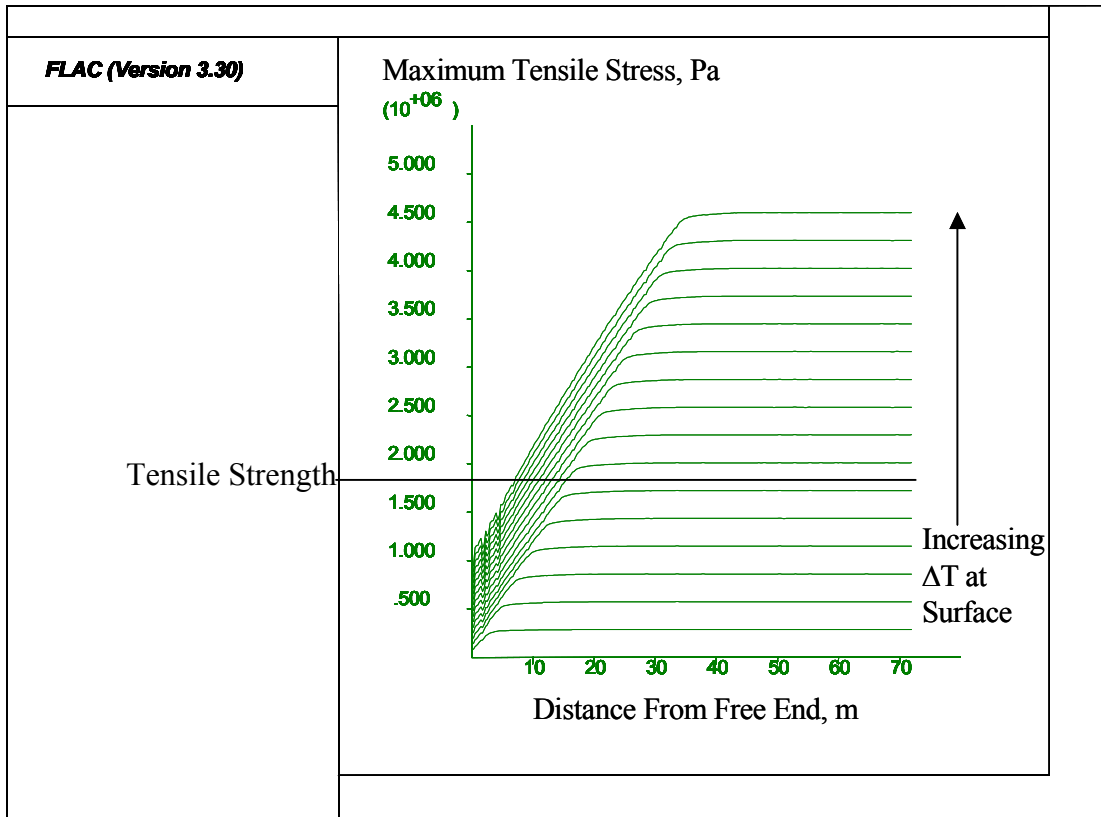
Figure 1.3.14 Thermal Stress Curve – Mn/ROAD Cell 1.

The second step of the verification procedure was to adjust the frictional parameters of the supporting granular media and run additional simulations until the model was within 20% of the observed thermal cracking at Mn/ROAD. It was found during the iteration process that the level of cohesion, within the practical limits, had a much greater affect on the thermal stress curve than adjusting the internal angle of friction. This effect is further investigated and discussed in subtask 1-4. It was also found that the computation time to complete one simulation was significantly increased when considering the more complicated

pavement structure (i.e., surface, base, subbase, subgrade) and thermal conditions (i.e., thermal gradients spanning 15°C to 20°C over the depth of the pavement). The computation time increased from the order of hours to that of days. Although for research purposes this may not be an issue, in practice the long computation time may need to be addressed.
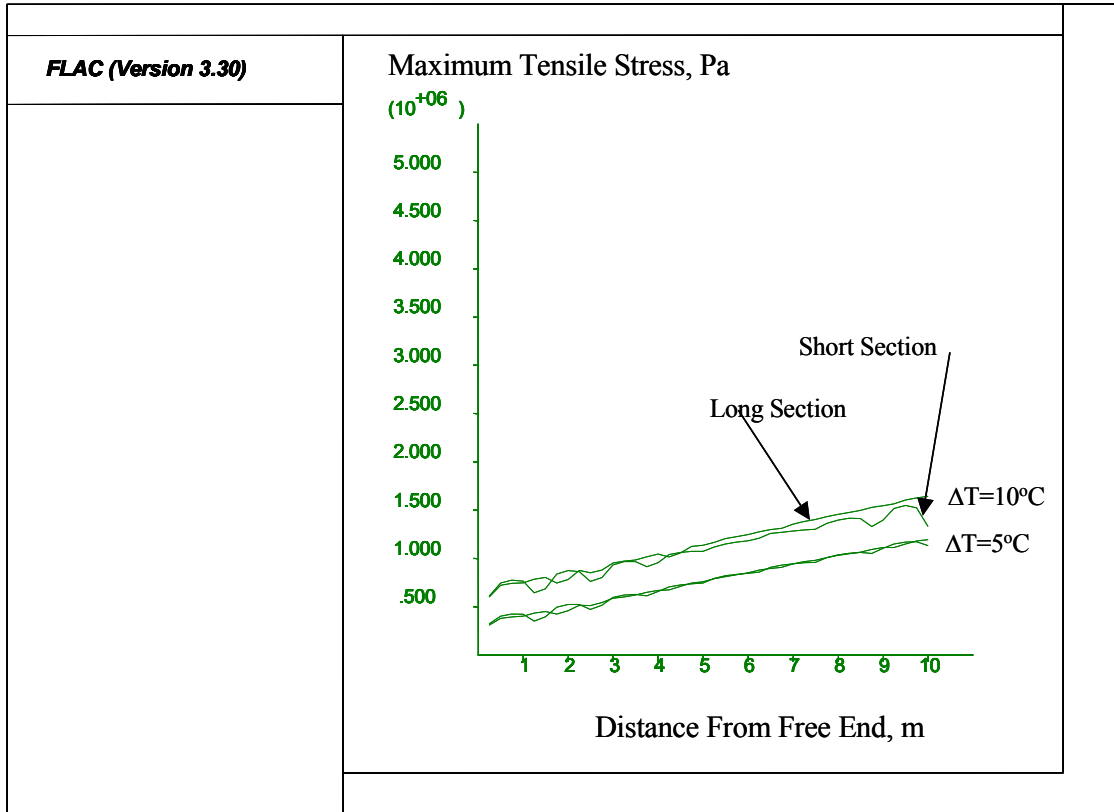
Figure 1.3.15 Comparison of Short vs. Long Pavement Sections - Mn/ROAD Cell 1.

Table 1.3.10 lists the resulting frictional parameters obtained from the validation procedure in addition to the predicted average and measured spacing. Figure 1.3.16 illustrates the predicted spacing compared to the average measured spacing.

Since Table 1.3.10 shows that the maximum difference between a prediction and measured average spacing was 15%, the model has compared favorably with each of the four cells. It was found that cell 2, which had the closest crack spacing, required the highest internal angles of friction and cohesion of the four cells investigated. It is difficult to compare cell 4 directly to the other cells since it experienced greater temperature change

from top to bottom of the HMAC, as discussed previously, which could have been a dominating factor in the resulting thermal crack spacing observed in the field.

Table 1.3.10 Frictional Parameters Obtained From Comparison Procedure.

Cell	Base ϕ, °	Base c, kPa	Subbase ϕ, °	Subbase c, kPa	Subgrade ϕ, °	Subgrade c, kPa	Predicted	Measured	% Off by
1	30	10	--	--	25	240	10.7	12	11%
2	50	15	35	25	25	240	7.6	8	5%
3	35	10	25	10	25	240	14.9	13	-15%
4	--	--	--	--	25	10	7.9	9	12%
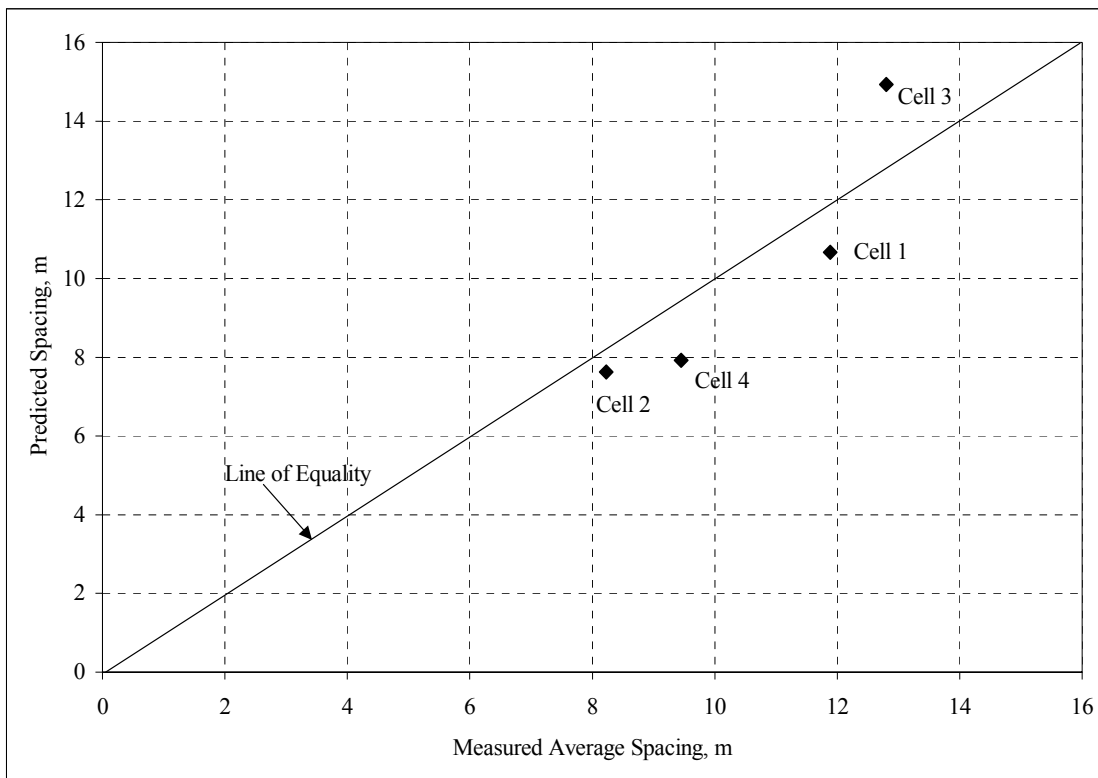
Figure 1.3.16 Comparison of Predicted and Measured Average Crack Spacing.

SUMMARY

The goal of the model comparison study was to assess whether the thermal cracking model would predict crack spacing consistent with field observations. Data pertaining to four full-scale pavement test sections at Mn/ROAD were gathered and entered into the thermal cracking model. Based on the results of the comparison procedure it may be stated that the thermal cracking model does pass the test of reasonableness. The next subtask will reexamine the model by performing a parametric study to develop a better understanding of how the model behaves and identify the key input variables.

PART 1. MODELING
Chapter 1.4. Parametric Study

INTRODUCTION

The fundamental mechanisms of the thermal cracking model were described in chapter 1.2. Chapter 1.3 compared the model to field data by using observed thermal cracking at the Minnesota Road Research Project (Mn/ROAD). The final part of the modeling task was to perform a parametric study with the model. With any numerical modeling study, an understanding of the relative influence of the input parameters on the output is useful for the following reasons:

1. Identifying the key input parameters (i.e., those having the greatest influence) can help guide laboratory work in that more resources can be devoted to measuring those inputs.
2. Understanding the relative influence of the input parameters gives a more complete understanding of how the model behaves under a variety of conditions.
3. From a design standpoint it is useful to know how the selection of materials, and consequently material properties, will potentially affect the solution.

The study focused on evaluating several aspects of the thermal stress curve as pictured in Figure 1.4.1. Namely, the rate of stress increase from the free end, the maximum stress achieved away from the free end and the amount of bending stress, if any, near the free end.

The critical distance (X_c) was not calculated as part of the parametric investigation. Recall that X_c was the longitudinal distance from the free end to the point at which the strength of the material was exceeded. X_c was not calculated since the investigation examined the development of stresses. However, for each of the thermal stress curves presented in this chapter, a strength parameter (S_t) could be used to determine X_c and predict the average crack spacing. In general, a faster rate of stress increase, higher bending stresses or higher maximum stress would correspond to more thermal cracking (i.e., more closely spaced thermal cracks).
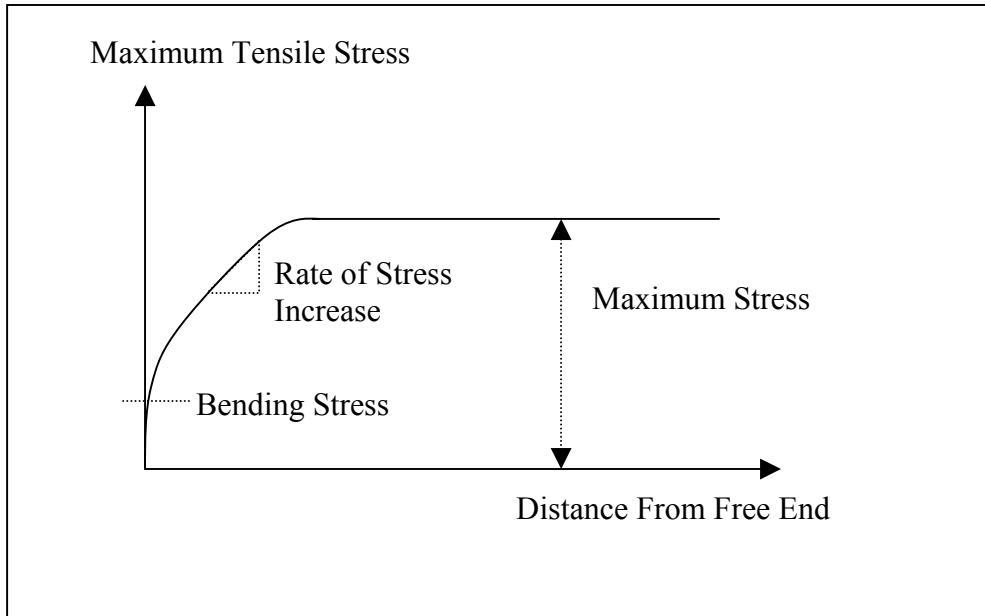
Figure 1.4.1 Thermal Stress Curve - Parameters Investigated.

METHODOLOGY

While a parametric investigation could consider an infinite number of pavement cross-sections, materials, and thermal conditions it was necessary to limit the scope in a number of areas to make the investigation feasible. First, the parametric investigation focused solely on a two-layer pavement structure as illustrated in Figure 1.4.2 to reduce the total number of input parameters that would be investigated. The two-layer structure captures the essence of the model by characterizing the interaction between the surface and base layers and was deemed sufficient for the parametric study.

Second, the study considered a uniform temperature change with depth in the asphalt concrete surface layer. This was done for a number of reasons. As shown in chapter 1.2, the presence of a thermal gradient only affected the thermal stress curve near the free edge in terms of bending stresses. Away from the free edge, the stress plot followed the same curve and reached the identical maximum stress as a non-thermal gradient case having the same ΔT at the surface. Also, computationally, the simulations run much more quickly when a constant ΔT is used. Therefore, the study was most efficiently conducted using a constant ΔT with depth.

Third, only a single temperature change ($\Delta T=5°C$) was used throughout all the simulations. This was done to examine how the material parameters affected the stress development and a single temperature change was sufficient to accomplish this task.

Given the above statements, there were ten input parameters required for the parametric investigation and they are listed in Table 1.4.1 and shown in Figure 1.4.2. For each of the input parameters, a range was established based on information from the available literature and data from Mn/ROAD. The data were then used to determine low, medium and high values for each of the inputs. Once these values were determined a series of simulations were conducted varying the input parameters between the three possible input levels. A total of 21 simulations were initially performed. First, a baseline simulation using all the medium, or average, values was run. Then additional simulations (totaling 20) were completed, changing only one parameter at a time to either the low or high value, keeping the rest at the medium level.

Table 1.4.1 Model Input Parameters.

Input Parameter	Symbol	Units
HMAC* Young's Modulus	E_1	Pa
HMAC Poisson's Ratio	ν_1	unit less
HMAC Density	ρ_1	kg/m^3
HMAC Thickness	H_1	cm
HMAC Thermal Coefficient	α_1	/°C
GB** Young's Modulus	E_2	Pa
GB Poisson's Ratio	ν_2	unit less
GB Density	ρ_2	kg/m^3
GB Cohesion	c_2	Pa
GB Angle of Internal Friction	ϕ_2	°

*Hot Mix Asphalt Concrete

**Granular Base
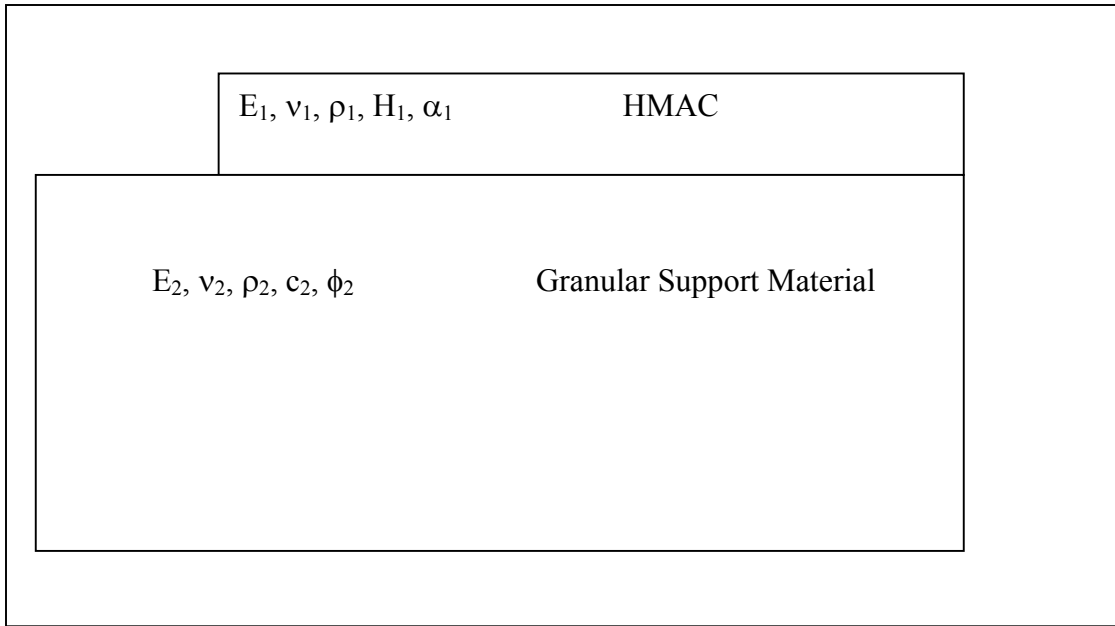
Figure 1.4.2 Parametric Investigation – Input Parameters (Not to Scale).

Once all the simulations were complete, graphs of the maximum tensile stress at the surface were created and comparisons were made between the simulations. Particular attention was paid to the rate of stress increase from the free end and the maximum stress achieved away from the free edge in addition to the bending stresses, if any, near the free end.

PARAMETRIC INVESTIGATION INPUTS

For each of the inputs listed in Table 1.4.1 and shown in Figure 1.4.2 a range was established. The input values are summarized in Table 1.4.2 and each is described in more detail below.

HMAC Modulus (E_1)

The baseline modulus was taken from Ovik's (15) work on backcalculating deflection data at Mn/ROAD as described in chapter 1.3. The low and high values were roughly one-third and double of the baseline value, respectively.

HMAC Poisson's Ratio (ν_1)

The medium level Poisson's ratio was the same as used in chapter 1.3, which was based on data from Yoder and Witczak (12). The high and low values were ±25% of the medium level, respectively.

<p align="center">Table 1.4.2 Parametric Investigation Input Parameters.</p>

Layer	Parameter	Units	Low	Medium (Baseline)	High
1	E_1	Pa	$5*10^9$	$1.4*10^{10}$	$3*10^{10}$
	ν_1	unitless	0.15	0.20	0.25
	ρ_1	kg/m^3	2,200	2,300	2,400
	H_1	cm	7.6	15	30
	α_1	/°C	$1.33*10^{-5}$	$2.15*10^{-5}$	$2.97*10^{-5}$
2	E_2	Pa	$5.5*10^7$	$5.5*10^8$	$5.5*10^9$
	ν_2	unitless	0.35	0.4	0.45
	ρ_2	kg/m^3	1,800	2,000	2,200
	c_2	Pa	0	70,000	140,000
	ϕ_2	°	20	40	60

HMAC Density (ρ_1)

As discussed in chapter 1.3, the densities at Mn/ROAD varied primarily between 2,200 kg/m^3 and 2,400 kg/m^3. These values were used for the low and high and the midpoint (2,300 kg/m^3) for the baseline value.

HMAC Thickness (H_1)

Most agencies have a minimum thickness design for asphalt concrete surface layers. In Minnesota, the minimum thickness is 7.6 cm (50). This value was then doubled to yield the baseline value and the baseline doubled to reach the high value.

HMAC Thermal Coefficient (α_1)

Thermal coefficients measured by Stoeffels and Kwanda (50) showed a practical range of $1.33*10^{-5}/°C$ to $2.97*10^{-5}/°C$ with an average of $2.15*10\text{-}5/°C$ for a variety of asphalt concrete materials. These represented the low, high and medium levels in the parametric investigation, respectively.

Granular Material Modulus (E_2)

As discussed in chapter 1.3, there was some uncertainty regarding the correct order of magnitude for the granular base modulus in a frozen condition. Recall that backcalculated data by Ovik (15) put the frozen modulus at 5,500 MPa and CRREL measured it almost an order of magnitude higher. Therefore, as part of this study, it was decided to include a broad range of moduli to assess the effects on model output. Consequently, the baseline modulus was set at $5.5*10^8$ Pa, low modulus at $5.5*10^7$ and high modulus at $5.5*10^9$.

Granular Material Poisson's Ratio (ν_2)

The Poisson's ratio used in chapter 1.3, based on Yoder and Witczak's (12) table 1.4.was used as the baseline value for the parametric study. The low and high values represented a range of materials from non-cohesive to cohesive materials.

Granular Material Density (ρ_2)

The density of the Mn/ROAD materials was measured to be approximately 2,000 kg/m^3 and was fairly consistent between the different types of materials. The measured density at Mn/ROAD ranged from 2,042 kg/m^3 to 2,192 kg/m^3. The low and high values represented ±10% around the baseline value, respectively, to capture Mn/ROAD range.

Granular Material Cohesion (c_2)

Recall in chapter 1.3 that there was some uncertainty from the literature as to what the level of cohesion should be for the frozen base materials. Therefore, the cohesion was varied over a large range to account for the uncertainty and better understand how cohesion affects the model. The three levels were: 0 kPa, 70 kPa and 140 kPa.

Granular Material Angle of Internal Friction (ϕ_2)

The angles of internal friction determined in the model validation study were in the 30° to 50° range. The midpoint of this range (40°) was used as the baseline value. The low and high values were extended slightly to 20° and 60°, respectively, to incorporate a wider range.

RESULTS AND DISCUSSION

Graphs of maximum principle tensile stress along the midpoint of the top row of control volumes in the finite difference grid were created. The graphs compare the results between the low, baseline and high simulations for each input parameter. The following sections present these graphs and discuss the results.

HMAC Modulus (E_1)

Figure 1.4.3 compares the baseline case to the low and high HMAC modulus cases. As predicted in the Hills and Brien (17) solution for an elastic slab described in chapter 1.1:

$$\sigma_x = \frac{E\alpha\Delta T}{1-\nu} \qquad\qquad (1)$$

the maximum stress has a linear relationship to the modulus. In other words, doubling the stiffness of the asphalt concrete will double the maximum stress level due to a temperature change. The figure 1.4.also shows a slight increase in slope with increasing E_1. However, the primary effect of E_1 is in the magnitude of the maximum tensile stress achieved away from the free edge.

It is important to recognize that the stress curves in Figure 1.4.3 have an inflection point near the free edge, which is the bending stress, since it appeared in each of the simulations discussed below. However, in most cases, the range of values did not affect a change in the magnitude of the inflection point.

To explain the bending stress, recall from chapter 1.2 that when constant ΔT was applied with depth, the bending stress was not identified. The primary difference between these simulations was that the cohesion was set to zero in chapter 1.2 while cohesion was 70 kPa in Figure 1.4.3. By increasing cohesion there is an increase in the frictional resistance provided by the base layer. Consequently, there is more restraint at the bottom of the HMAC

layer than at the top and the HMAC and bending results. At zero or low cohesion the frictional restraint was low enough that the bending effect was limited and the stress approached zero at the free end without an inflection point. Figure 1.4.4 illustrates this concept.
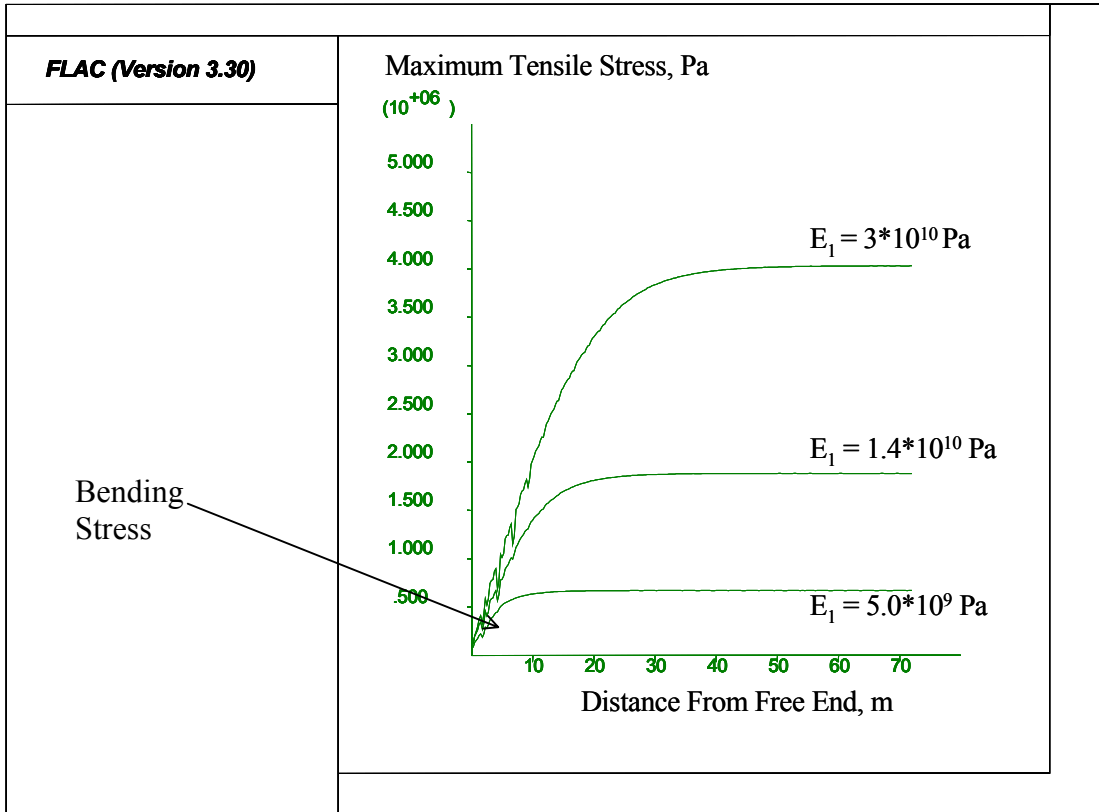
Figure 1.4.3 Effect of E_1 on Thermally Induced Stresses.

HMAC Poisson's Ratio (ν_1)

The Poisson's ratio of the HMAC had only a minor effect on the maximum stress achieved away from the crack edge as illustrated in Figure 1.4.5. Again, this was expected from the Hills and Brien (17) solution for an elastic slab shown in equation (*1*). Also, as predicted, the stress increased with increasing Poisson's ratio according to $\frac{1}{1-\nu}$. Although the parametric study only investigated the stresses from 0.15 to 0.25, Figure 1.4.6 illustrates the rate of stress increase over the complete range of possible Poisson's ratio. The figure

1.4.shows that increasing from 0 to 0.5 would double the maximum stress. In addition to the observation regarding maximum stress, Figure 1.4.5 also shows that the HMAC Poisson's ratio had virtually no effect on the rate of stress increase over the expected range of values.
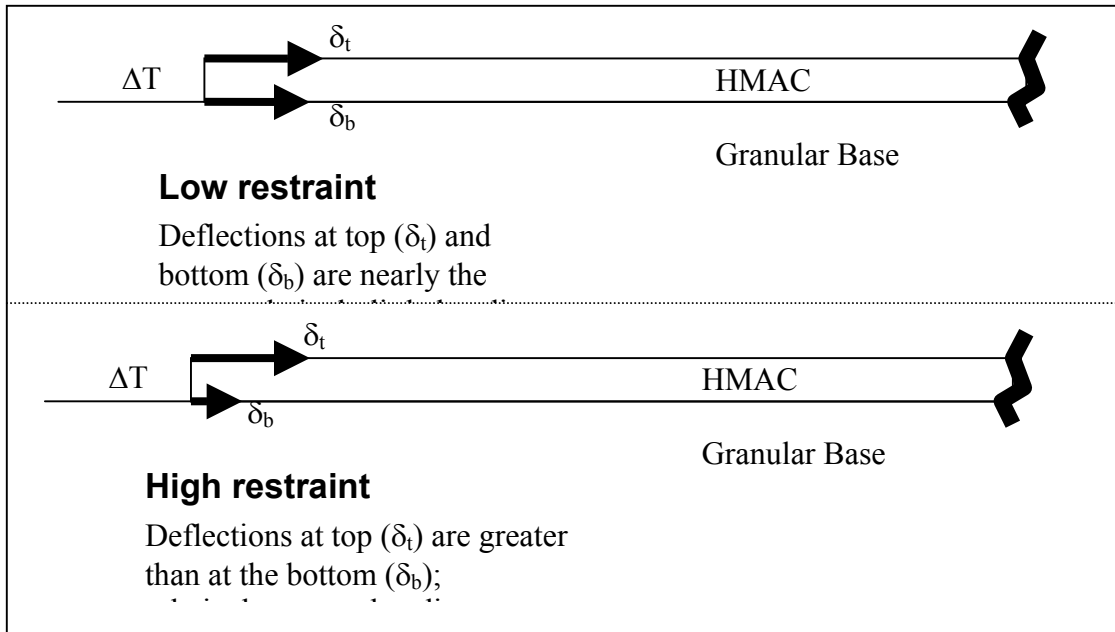
Figure 1.4.4 Presence of Bending with Constant ΔT; Different Restraint.

HMAC Density (ρ_1)

The density of the surface layer had no effect on the maximum stress as shown in Figure 1.4.6. This was expected since density does not appear in equation (*1*). Figure 1.4.6 also showed that density did not affect the rate of stress increase. One could expect that increasing the density would increase the normal force, due to gravity, that the asphalt concrete layer exerts on the supporting granular material. This would conceivably increase the frictional drag experienced by the asphalt concrete and could increase the slope of the stress increase region from the free end. However, this was not evident in the three cases considered in Figure 1.4.6 and could be a result of the change in density being too small between the cases to affect any change in the stress graph.
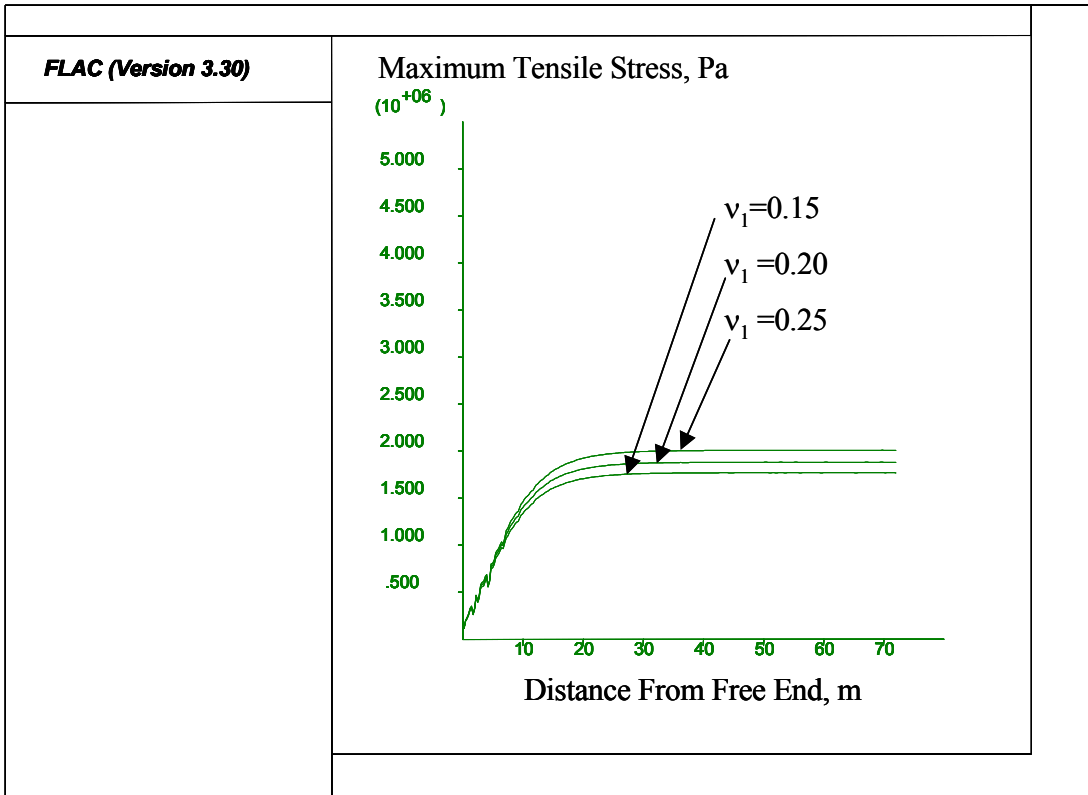
Figure 1.4.5 Effect of ν_1 on Thermally Induced Stresses.
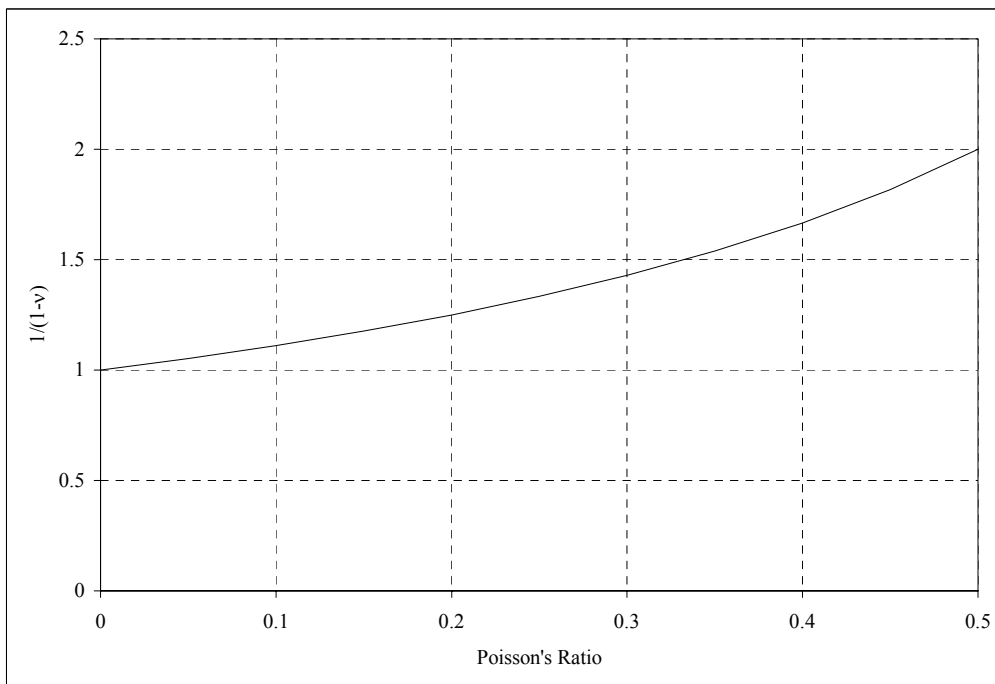
Figure 1.4.6 Effect of Poisson's Ratio; $\dfrac{1}{1-\nu}$ Function.

FLAC (Version 3.30)

Maximum Tensile Stress, Pa
(10^{+06})

5.000

4.500

4.000

3.500

3.000 $\rho_1 = 2,200 \text{ kg/m}^3$

2.500 $\rho_1 = 2,300 \text{ kg/m}^3$

          $\rho_1 = 2,400 \text{ kg/m}^3$

2.000

1.500

1.000

.500

10   20   30   40   50   60   70

Distance From Free End, m
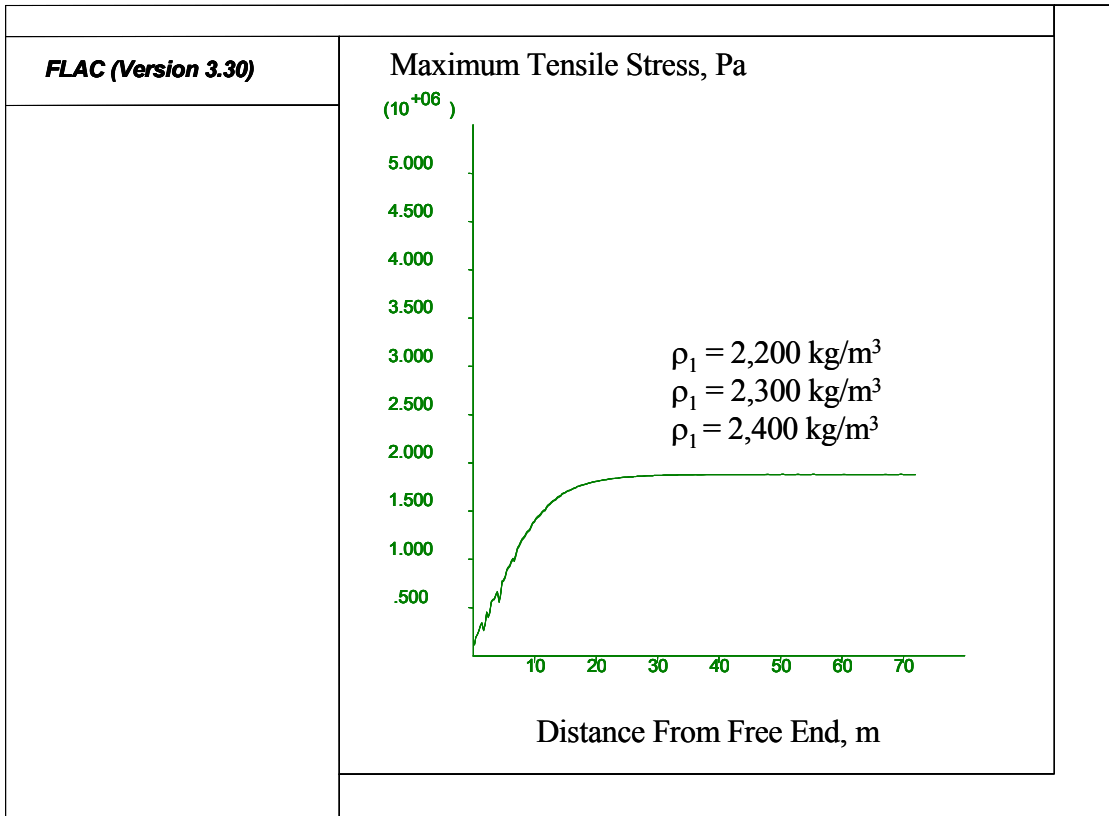
Figure 1.4.7 Effect of ρ_1 on Thermally Induced Stresses.

HMAC Thickness (H_1)

Figure 1.4.8 shows that increasing the pavement thickness, for constant ΔT between simulations, had no effect on the maximum stress achieved away from the free end. This was expected since H_1 does not appear in equation (*1*).

Figure 1.4.8 also shows that increasing the pavement thickness decreases the stress near the free edge known as the inflection point, or bending stress. The presence of the bending stress was discussed above in the E_1 subsection and was attributed primarily to the level of cohesion. However, increasing the thickness effectively increases the mass of the HMAC and it is therefore less likely to curl upward due to an increased self-weight acting in the opposite direction.
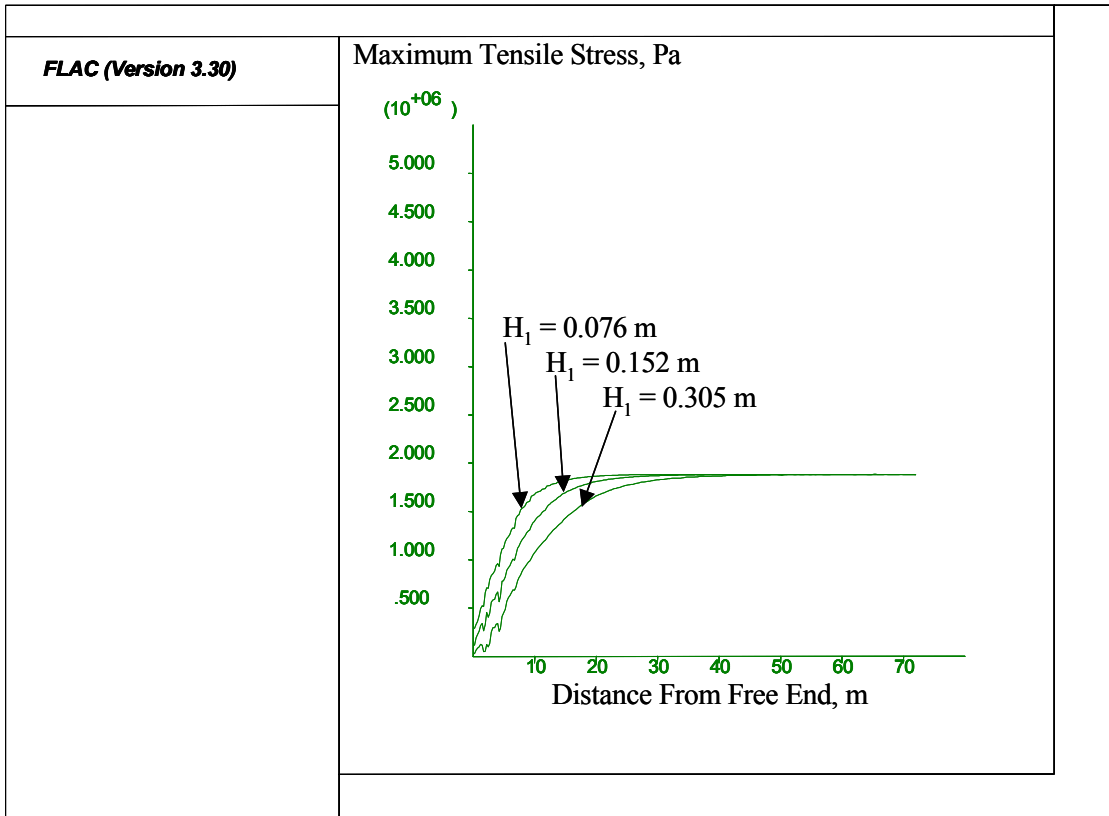
Figure 1.4.8 Effect of H_1 on Thermally Induced Stresses.

HMAC Thermal Coefficient (α_1)

Referring again to equation (*1*) shows that the maximum stress is linearly related to the thermal coefficient and this is also shown in Figure 1.4.9. As with the HMAC modulus, there does appear to be a slight effect of α_1 on the rate of stress increase from the free end.

Granular Material Modulus (E_2)

As shown in Figure 1.4.10, the modulus of the granular base layer has a significant impact on how stresses develop from the free end. Notice that the stress plot for the low modulus case follows a gradual curve that corresponds to primarily elastic deformation of the base material. Increasing the stiffness, as shown in the figure, drastically reduces the curved portion and introduces the linear increase from the free edge. In both the baseline and high modulus cases there was combined plastic and elastic deformation of the base layer. Figure 1.4.10 highlights the importance of accurately determining the base modulus in a frozen

condition since very different stress curves are possible even though they all approach the same maximum value away from the free edge.

Granular Material Poisson's Ratio (ν_2)

    Figure 1.4.11 showed that Poisson's ratio did not affect the thermal stress curve over the range of values used in this study.

Granular Material Density (ρ_2)

    As with the Poisson's ratio of the base layer, the density of the base layer also did not impact the stress curve over the range of values investigated as shown in Figure 1.4.12. Since the density primarily plays a role in determining geostatic stresses only in the base layer, this was an expected result.

FLAC (Version 3.30)

Maximum Tensile Stress, Pa (10^{+06})

5.000
4.500
4.000
3.500
3.000
2.500
2.000
1.500
1.000
.500

10 20 30 40 50 60 70

Distance From Free End, m

$\alpha_1 = 2.97*10^{-5}$

$\alpha_1 = 2.15*10^{-5}$

$\alpha_1 = 1.33*10^{-5}$

Figure 1.4.9 Effect of α_1 on Thermally Induced Stresses.

Maximum Tensile Stress, Pa

(10^{+06})

5.000

4.500

4.000

$E_2 = 5.5 \times 10^9$ Pa

3.500

$E_2 = 5.5 \times 10^8$ Pa

3.000

2.500

2.000

1.500

$E_2 = 5.5 \times 10^7$ Pa

1.000

.500

10   20   30   40   50   60   70

Distance From Free End, m
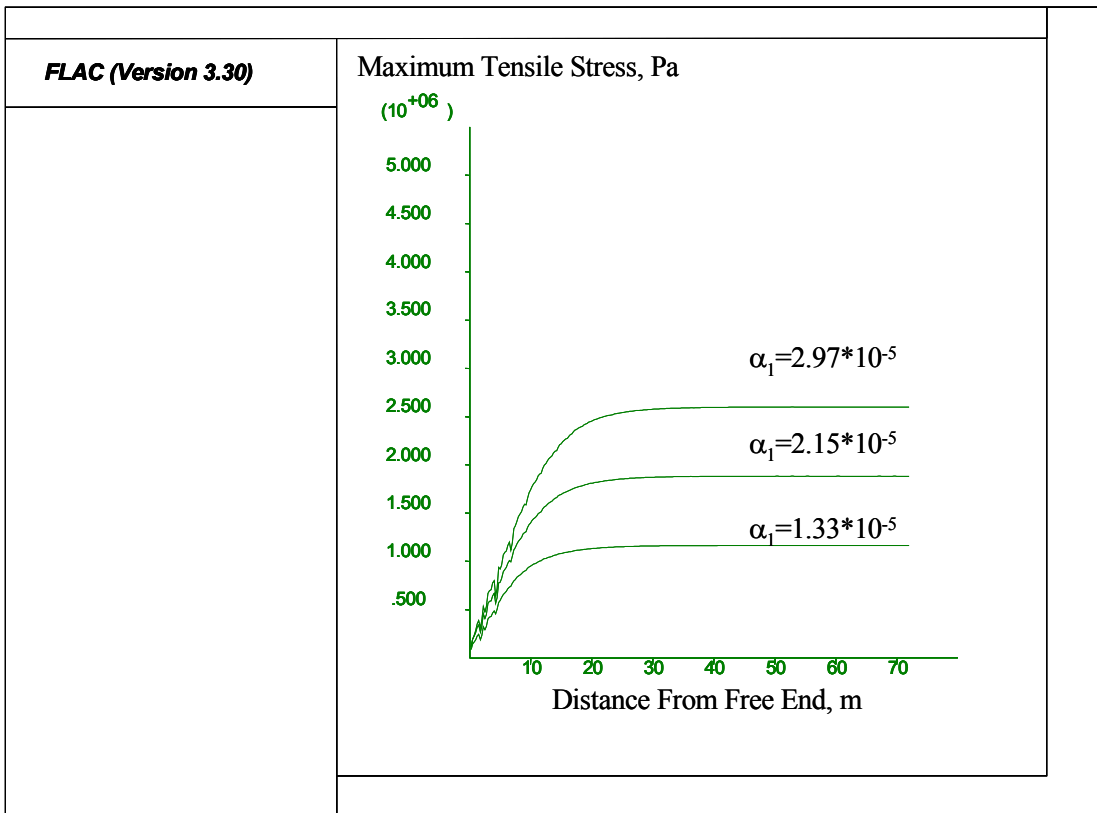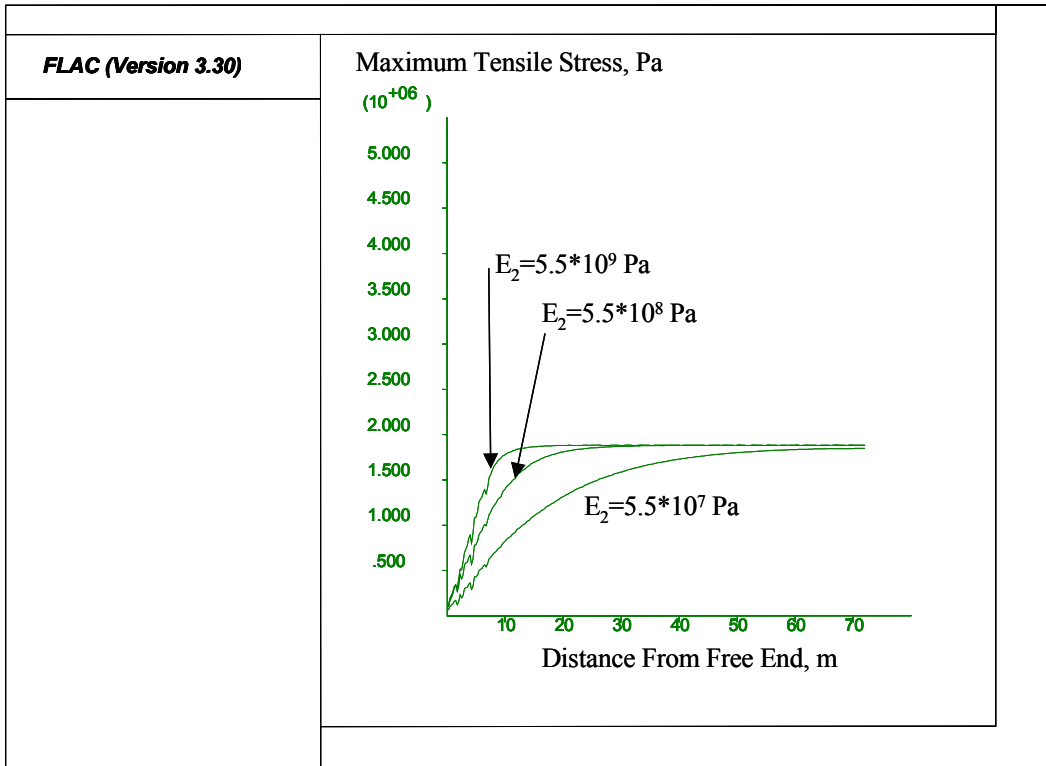
Figure 1.4.10 Effect of E_2 on Thermally Induced Stresses.

Maximum Tensile Stress, Pa

(10^{+06})

5.000

4.500

4.000

3.500

$\nu_2 = 0.35$

3.000

$\nu_2 = 0.40$

2.500

$\nu_2 = 0.45$

2.000

1.500

1.000

.500

10   20   30   40   50   60   70

Distance From Free End, m
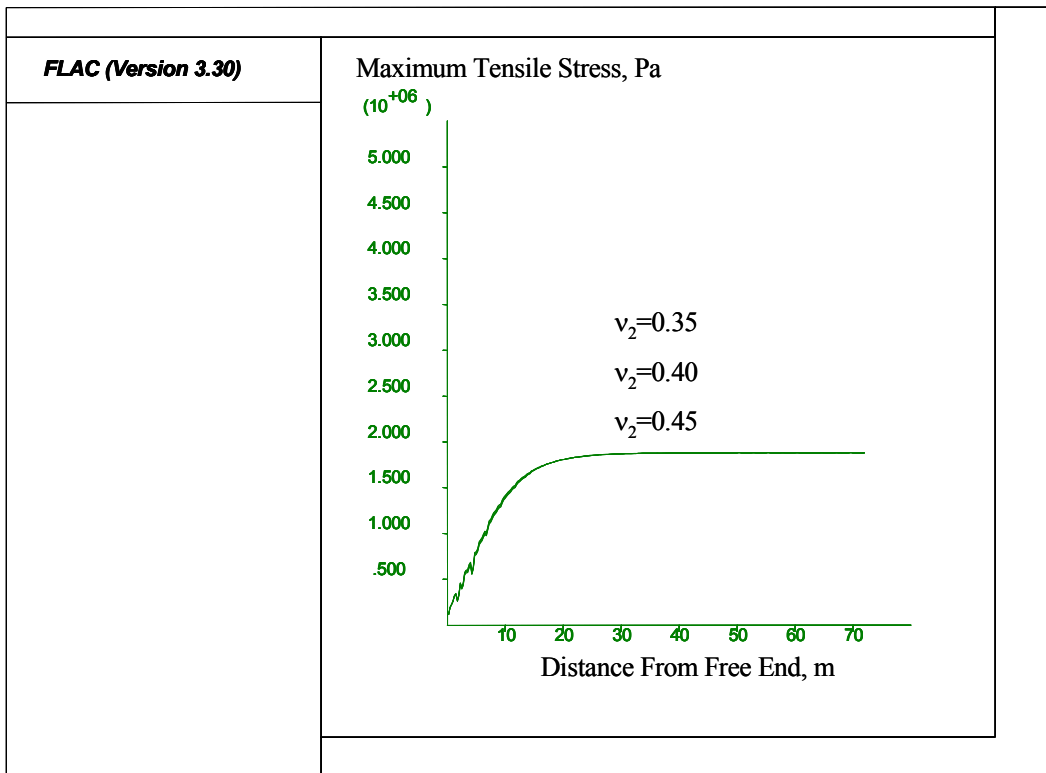
Figure 1.4.11 Effect of ν_2 on Thermally Induced Stresses.

100
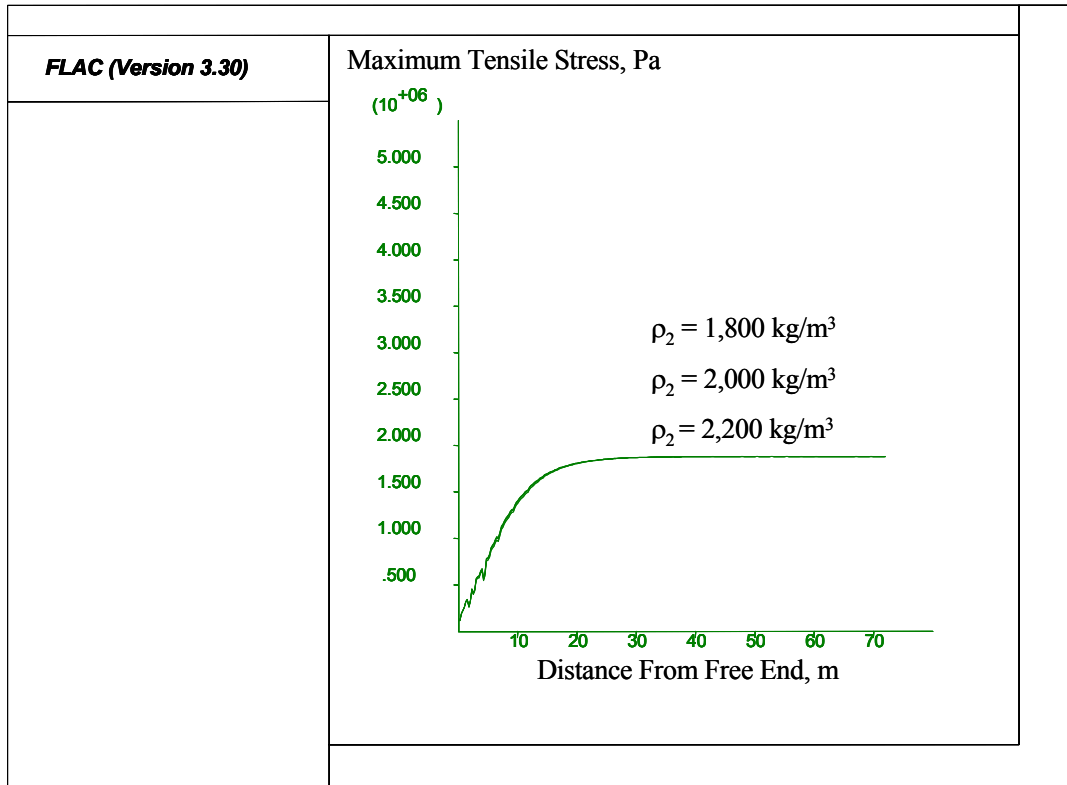
Figure 1.4.12 Effect of ρ_2 on Thermally Induced Stresses.

Granular Material Cohesion (c_2)

The sensitivity of the model to the cohesion of the supporting material is illustrated in Figure 1.4.13. It appears that cohesion has a dramatic effect on the rate of stress increase. In the case of zero cohesion, the stress never reached the theoretical maximum since the length of the pavement was too short for the maximum stress to be achieved. The baseline and high levels of cohesion drastically increased the slope of stress increase from the free end when compared to the zero cohesion case.

Figure 1.4.13 also demonstrates that above a certain level of cohesion, as shown when comparing the baseline (70 kPa) and high (140 kPa) levels of cohesion, the model produced the same stress curve. To explain this observation, it is important to keep in mind that cohesion (c) and internal angle of friction (ϕ) define the Mohr-Coulomb failure envelope according to:

$$\tau = c + \sigma \tan \phi \qquad\qquad (2)$$

$$\sigma_t = 0$$

where: τ = shear stress on failure plane

σ = normal stress on failure plane

σ_t = tensile strength (assumed to be zero)

The failure envelope represents the limit state between elastic and plastic behavior as described in chapter 1.2. When the state of stress at any point in the continuum is within the failure envelope, the material exhibits elastic response. By definition, the material cannot sustain a state of stress outside the envelope. Therefore, the state of stress is limited by equation (*2*) and plastic deformation occurs when the Mohr-Coulomb state is achieved.

Figure 1.4.14 compares the state of stress, represented by Mohr's circle, for the two higher levels of cohesion at a point in the granular base layer. Notice that the state of stress is similar between both cases even though the cohesion increases from 70 kPa to 140 kPa. It is important to realize, as shown in Figure 1.4.14, that the stress is not limited by the shear criteria, but by the tensile strength of the failure envelope. In other words the material is deforming plastically due to tensile failure rather than shear failure. However, as shown in the figure, the state of stress is nearly the same and therefore no change in the principal stress curve observed at the surface is evident.

Figure 1.4.15 further illustrates the point made above by plotting Mohr's circle for the same location in the base material but for the case where cohesion was zero. As shown in the figure, the stress is limited by the cohesion and angle of internal friction. The comparison between Figures 14 and 15 indicates that there exists a level of cohesion such that, for a given set of input parameters, the thermally induced stresses cause tensile failure rather than shear failure. Consequently, above the threshold level of cohesion, the resulting principal stress curve at the surface of the HMAC layer will not change.

To further investigate the effect of cohesion, and attempt to identify the threshold level of cohesion, four additional simulations were performed at levels of cohesion between 0 kPa and 70 kPa. The cohesion levels in the additional runs were 10 Pa, 100 Pa, 1,000 Pa and 10,000 Pa. The results are illustrated in Figure 1.4.16.

The largest change in the model's response occurred between the 1 kPa and 10 kPa simulations. Taken as a whole, the results from these simulations indicate that cohesion is very important in determining thermal stresses and ultimately the crack spacing. Also, for

the given set of input parameters, the threshold level of cohesion appears to be between 10 kPa and 70 kPa

| FLAC (Version 3.30) | Maximum Tensile Stress, Pa |

Maximum Tensile Stress, Pa
(10^{+06})

$c_2=70$ kPa
$c_2=140$ kPa

$c_2=0$ kPa

Distance From Free End, m
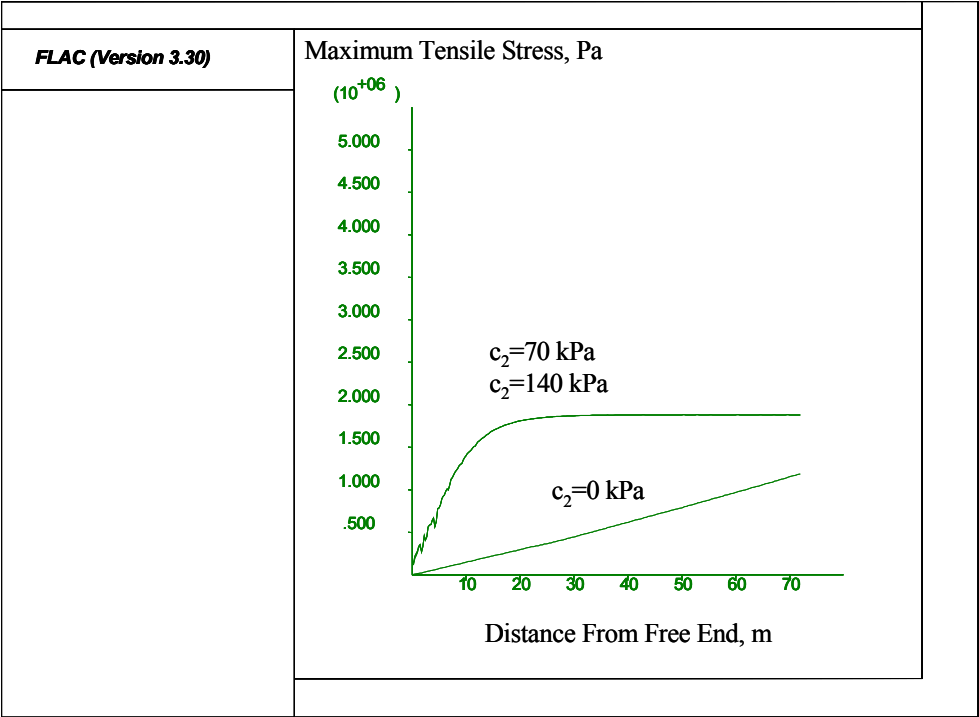
Figure 1.4.13 Effect of c_2 on Thermally Induced Stresses.
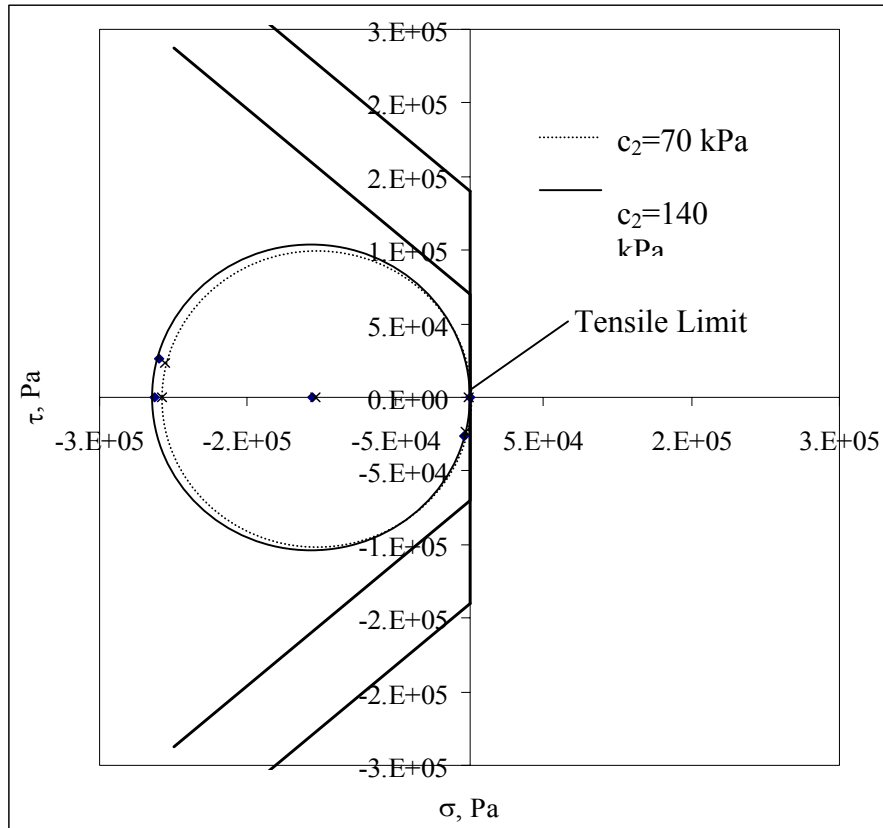
Figure 1.4.14 Mohr's Circle and Failure Envelope for c_2 = 70 and c_2 = 140 kPa.
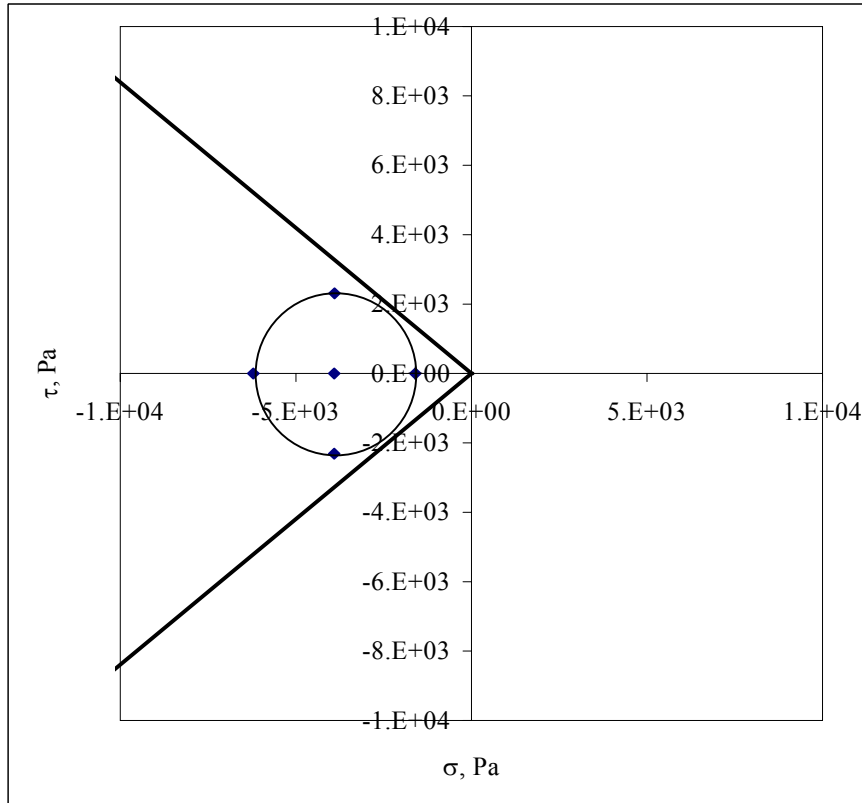
Figure 1.4.15 Mohr's Circle and Failure Envelope for $c_2 = 0$ kPa.
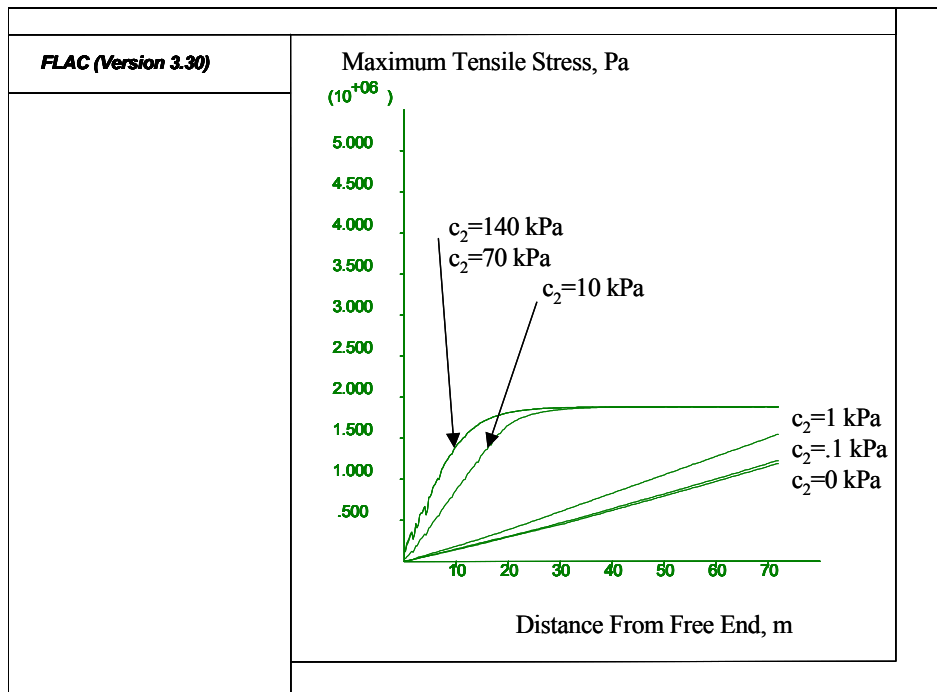
Figure 1.4.16 Effect of c_2 on Thermally Induced Stresses - Additional Simulations.

Granular Material Angle of Internal Friction (ϕ_2)

The sensitivity of the model to the angle of internal friction is illustrated in Figure 1.4.17. At first glance, it would appear that the friction angle has no effect. However, this is a result of the cohesion being at a relatively high level ($c_2 = 70$ kPa) as explained above. However, it was shown in Chapter 3 that friction angle does play a role in the rate of stress increase from the free edge. Therefore, to further investigate the effects of the friction angle, additional simulations were conducted with three friction angles and two levels of cohesion. The input data for these two parameters are listed in Table 1.4.3. The results are shown in Figures 18 and 19, respectively.

FLAC (Version 3.30)

Maximum Tensile Stress, Pa
(10^{+06})

5.000
4.500
4.000
3.500
3.000
2.500
2.000
1.500
1.000
.500

$\phi_2 = 20°$

$\phi_2 = 40°$

$\phi_2 = 60°$

10 20 30 40 50 60 70

Distance From Free End, m
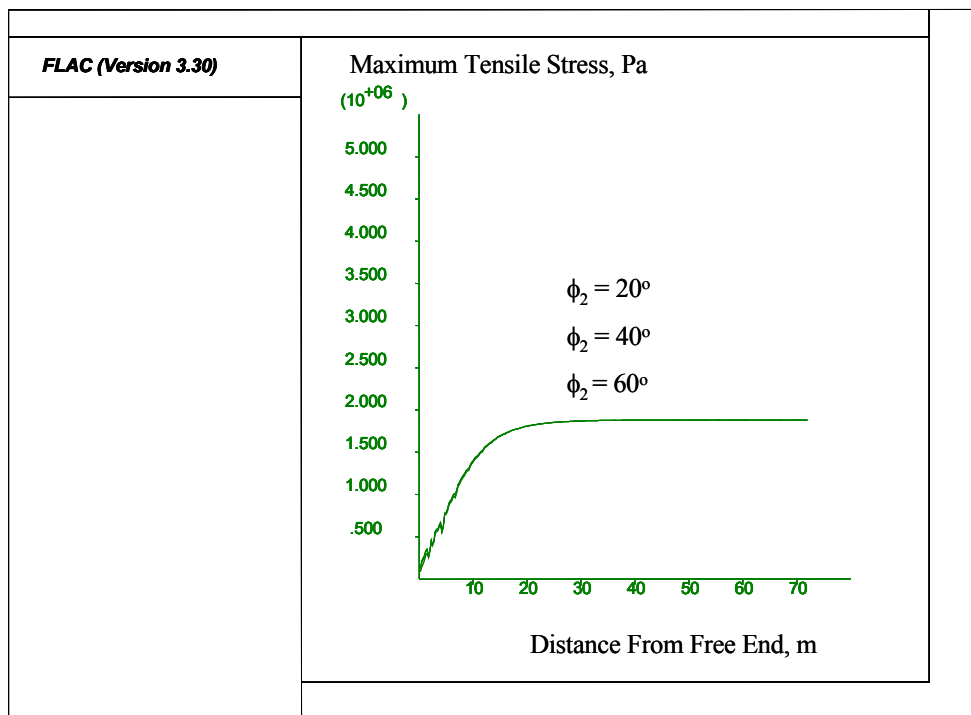
Figure 1.4.17 Effect of ϕ_2 on Thermally Induced Stresses.

As expected, lower values of cohesion resulted in a greater influence of ϕ_2 on the model output. Figure 1.4.18 shows a relatively greater influence of ϕ_2, when increasing from 20º to 60º, than in Figure 1.4.19. Also, as expected, as the friction angle increases the slope of stress increase from the free end also increases. In other words, more restraint corresponds to a shorter region of reduced stress before reaching the maximum.

The graphs in this subsection indicate that the angle of internal friction becomes a primary factor at low levels of cohesion. However, as cohesion increases, the angle of internal friction has a lesser effect on the resulting stress curve.

Table 1.4.3 Additional Simulations with ϕ_2.

Cohesion, kPa	Angle of Internal Friction, $^\circ$
	20
5	40
	60
	20
10	40
	60
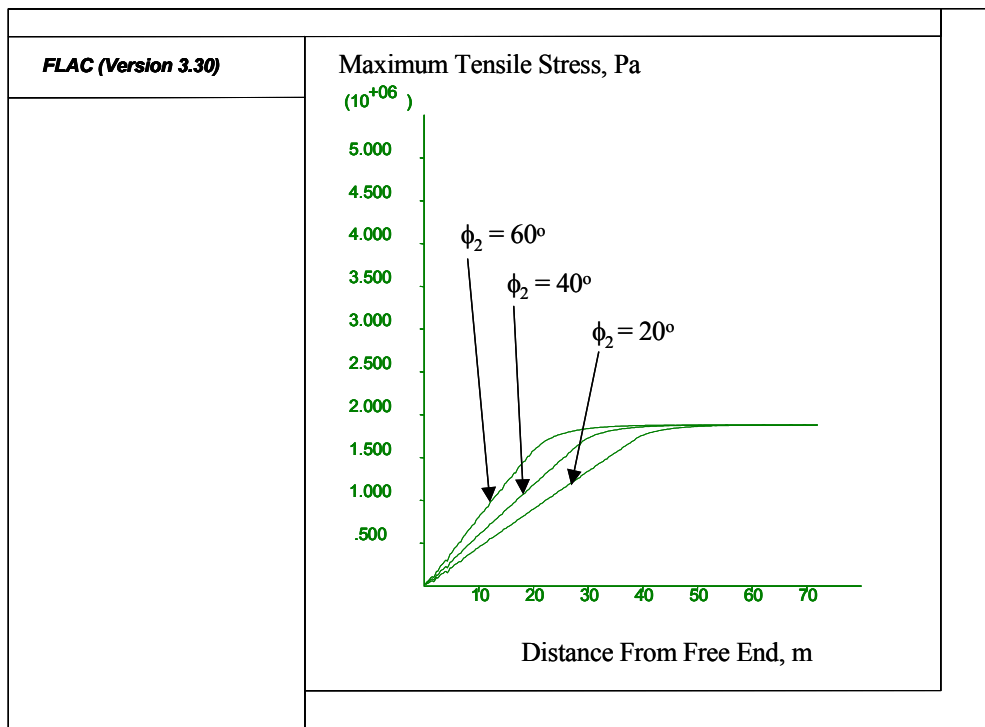
Figure 1.4.18 Effect of ϕ_2 on Thermally Induced Stresses - Additional Simulations (c_2 = 5 kPa).

FLAC (Version 3.30)

Maximum Tensile Stress, Pa
(10^{+06})

5.000
4.500
4.000
3.500
3.000
2.500
2.000
1.500
1.000
.500

$\phi_2 = 60°$
$\phi_2 = 40°$
$\phi_2 = 20°$

10   20   30   40   50   60   70

Distance From Free End, m
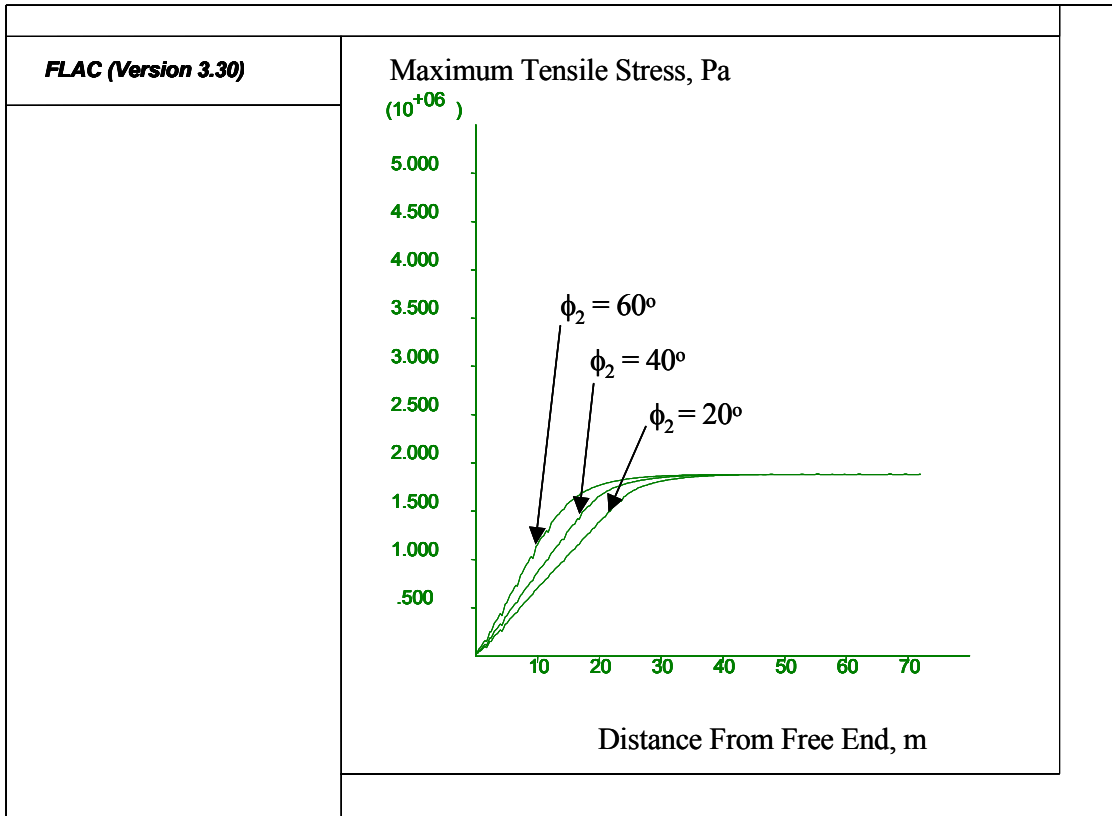
Figure 1.4.19 Effect of ϕ_2 on Thermally Induced Stresses - Additional Simulations (c_2 = 10 kPa).

SUMMARY

The results of the parametric study can be categorized into how each parameter affects the maximum stress, the rate of stress increase from the free end and the magnitude of bending stress near the free end. A relative ranking was given to each parameter describing its influence on each of the three specified criteria. Table 1.4.4 lists the ranking system and Table 1.4.5 summarizes the findings according to the ranking system.

Table 1.4.1 indicates that the HMAC properties govern the maximum stress developed in the surface layer. The rate of stress increase is primarily controlled by the stiffness and frictional properties of the base layer. The amount of bending stress is a function of the thickness of the surface layer and the cohesion of the base material. In summary, the key input parameters over the ranges investigated are E_1, α_1, E_2, c_2, and ϕ_2.

Table 1.4.4 Relative Ranking System.

Relative Ranking	Meaning
3	Primary Factor
2	Secondary Factor
1	Minor Factor
--	No Influence

Table 1.4.5 Relative Influence of Model Input Parameters.

	Relative Influence on Each Criteria		
Input Parameter	Maximum Stress	Rate of Stress Increase	Bending Stress
E_1	3	1	--
ν_1	2	--	--
ρ_1	--	--	--
H_1	--	--	3
α_1	3	1	--
E_2	--	3	--
ν_2	--	--	--
ρ_2	--	--	--
c_2	--	3	3
ϕ_2	--	2	--

   This chapter did not attempt to characterize the crack spacing that would result from the thermal stress curves. However, it can be said that for a given strength parameter (S_t), more closely spaced cracks would occur when there is a rapid increase in stress from the free end. Also, cracks are more likely to form when maximum thermal stresses and bending stresses are higher. Therefore, Table 1.4.1 can also be used to gauge how each parameter affects thermal cracking. For example, an HMAC with high stiffness or thermal coefficient would be more likely to crack for a given change in temperature. Further, crack spacing would decrease with an increase in the base layer stiffness, cohesion or internal angle of friction.

PART 2. LABORATORY TESTING
Chapter 2.1. Review of Fracture Mechanics Based Tests

BACKGROUND

Good fracture properties are an essential requirement for asphalt pavements built in the northern part of the US and in Canada for which the prevailing failure mode is cracking due to low-temperature shrinkage stresses. Cracking can occur as a result of a single severe temperature drop (single event) or of multiple cycles of less severe temperature change (thermal fatigue).   Low-temperature cracking is manifested as a set of surface-initiated transverse cracks of various lengths and widths.

SUPERPAVE SPECIFICATION

The current Superpave specifications address this distress mechanism through the use of strength and creep tests performed on un-notched samples. For asphalt binders two laboratory instruments were developed during the SHRP research effort to investigate the low temperature behavior of these materials (51): the Bending Beam Rheometer (BBR) and the Direct Tension Tester (DTT). They make the object of two AASHTO specifications (52, 53) and are used to obtain the performance grade (PG) of asphalt binders in the US and Canada (54).

The BBR is used to perform low-temperature creep tests on beams of asphalt binders conditioned at the desired temperature for 1 hour. Based on the elastic solution for a simple supported beam and the correspondence principle that relates the governing field equations of elasticity and the Laplace transforms with respect to time of the basic viscoelastic field equations, the creep compliance is obtained. The final results are reported in the form of a plot of the inverse of the creep compliance, used as surrogate stiffness, versus time. The stiffness (S) and the m-value, which represents the slope of the log stiffness as a function of log time, are used to determine a critical temperature value based on limiting values imposed on S and m obtained at 60s loading time.

The DTT is used to perform low-temperature uniaxial tension tests at a constant strain rate of 3% per minute on dog-bone shaped samples.   From the stress-strain curves obtained

on a number of six replicates an average stress and strain at failure are obtained. The fracture strain is used to determine an additional critical temperature value by imposing a limiting value of 1% to the fracture strain.

In an effort to improve the current low-temperature specifications a new standard has been recently proposed (55). Following an approach similar to the one used in asphalt mixture specifications, a critical low-temperature is calculated at the intersection of the thermal shrinkage stress curve obtained from the BBR creep compliance data with the strength master curve obtained form the DDT data.

For asphalt mixtures one laboratory testing device was developed during the SHRP program (56): the Indirect Tension Tester (IDT). In this test, a cylindrical specimen is loaded in compression along the diameter. This is similar to the splitting tension test, also known as the Brazilian test, which is the standard test for determining the indirect tensile strength of rocks (57). Both a creep test and a strength test are performed on the specimen as part of the specification requirements.

An increasing number of researchers realized the limitations associated with predicting true fracture properties based on tests performed on un-notched samples. These limitations are primarily related to the initiation and propagation mechanisms of the cracks. As a consequence, a number of studies started to investigate the application of the more complex fracture mechanics concepts to the behavior of bituminous materials. One of the first attempts to test notched beams of asphalt mixtures at low temperatures predates SHRP (58). However, the use of fracture mechanics approach in bituminous material research did not become significant until after the end of SHRP.

FRACTURE MECHANICS

In the traditional approach a material meets the design requirements if its strength is greater than the largest expected stress. A safety factor, sometimes combined with limiting the tensile strain, is imposed. Fracture mechanics approach analyzes the critical combinations of three variables instead of two: the additional variable is the flaw size and the strength is replaced by fracture toughness (59). There are two approaches to the fracture analysis; one is the energy approach and the other one is the stress intensity approach. Both were initially used for the simple case of linear time-independent materials; this is called

linear elastic fracture mechanics (LEFM). Later on, the analysis was extended to the more complex nonlinear time-independent materials; this is called elastic-plastic fracture mechanics (EPFM). In addition LEFM and EPFM were extended to time-dependent materials. A number of laboratory tests were developed to investigate the fracture properties of different materials. A summary of some of the more important test methods with potential application to asphalt materials is given below.

Fracture Tests On Metals

Most of the pioneering work in fracture mechanics was done in metals. One of the most investigated and well-documented fracture tests is the standard single edge notched bending (SENB) beam test on metals (60). This method was first published in 1970 and its latest version was published in 1997.

Due to the fact that plane strain, transitional plain strain to plane stress, and full plain stress exist in service simultaneously, there are strict requirements for specimen sizes in this test method. The use of the recommended standard specimen, shown in figure 2.1.1, results in fracture toughness values, K_{IC}, that are reproducible to within 15% by different laboratories.

The equation of K_{IC} for this specimen is:

$$K_{Ic} = \frac{LOAD*S}{BW^{\frac{3}{2}}} * f(\frac{a}{W}) \tag{1}$$

where

$$f(\frac{a}{W}) = \frac{3(\frac{a}{W})^{\frac{1}{2}}[1.99 - \frac{a}{W}(1 - \frac{a}{W})(2.15 - 3.93(\frac{a}{W}) + 2.7(\frac{a}{W})^2)]}{2(1 + 2\frac{a}{W})(1 - \frac{a}{W})^{\frac{3}{2}}} \tag{2}$$

B = width of specimen;

W = thickness of specimen;

S = span of specimen;

a = crack length.
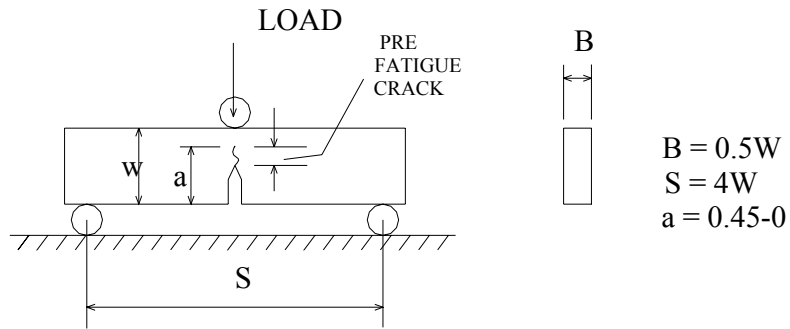
Figure 2.1.1. Single Edge Notched Bending Beam Test.

K_{IC} is calculated using LEFM approach. However, most materials crack with a plastic zone ahead of the crack tip, and therefore do not meet the LEFM assumptions. If the plastic zone is small enough, its effect on K_{IC} can be ignored. In order to reduce the effect of the plastic zone and ensure a predominant plane strain condition, three geometric requirements need to be met:

$$\left. \begin{array}{l} a \geq 2.5(\dfrac{K_{Ic}}{\sigma_{ys}})^2 \\[2mm] B \geq 2.5(\dfrac{K_{Ic}}{\sigma_{ys}})^2 \\[2mm] W \geq 5.0(\dfrac{K_{Ic}}{\sigma_{ys}})^2 \end{array} \right\} \tag{3}$$

where

σ_{ys} = yield strength and the other parameters are the same as described above.

The steps involved in setting up and conducting SENB beam test are:

1. Determine the critical dimensions of the specimen and manufacture specimens.

2. Obtain the test fixture and the clip gauge for the crack opening displacement measurement.

3. Analyze load-displacement records and calculate the conditional K_{IC} (K_Q) - First determine the load P_Q that corresponds to K_Q. On the plot of the load against displacement, draw a tangent line from the origin and draw a secant line from the origin with a slope 5% less than the tangent line. P_Q is the maximum value of the load between these two lines. Then apply the value to the equation for K_{IC} and get the conditional K_Q. In order to make sure this value is a valid K_{IC} equation (3) must be satisfied.

4. Finally check K_{IC} validity - Check whether the crack front symmetry requirements are met. This step checks the length of the crack at position a_1, a_2, a_3 (figure 2.1.2) and at the side surface, at the end of this test. Let a_1, a_2, a_3 and a_s stand for the crack length at these four places respectively and "a" stand for the mean value of a_1, a_2 and a_3. If a_1, a_2 and a_3 are within 5% of a, and if a_s is within 10% of a, then K_Q that met all other requirements is considered a valid K_{IC}.
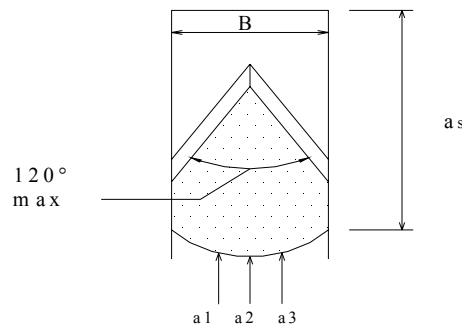
Figure 2.1.2. Checking crack symmetry.

Fracture Tests On Rocks

Five types of fracture test have been extensively documented in the area of rock mechanics. Two of them are International Society of Rock Mechanics (ISRM) standard tests: the short rod (SR) test and chevron bend (CB) test (61). The other three tests are the cracked chevron notched Brazilian disc (CCNBD) test (62), the semi-circular bend (SCB) test (63) and the modified ring test (64).

The samples for SR test, CB test and CCNBD test are shown in figures 2.1.3 and 2.1.4 respectively.

Short Rod (SR) Test   Chevron Bend (CB) Test
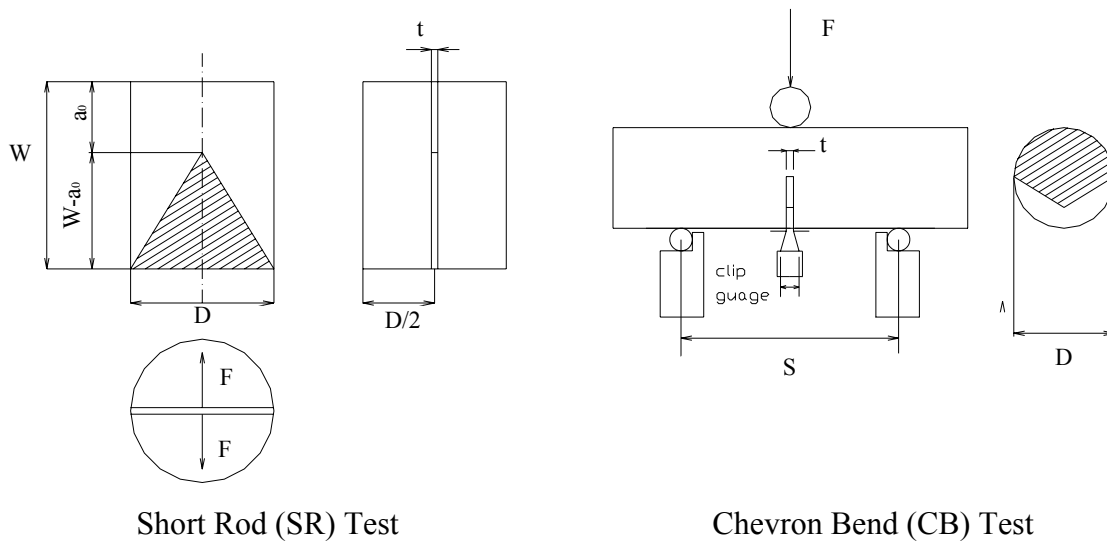
Figure 2.1.3. The International Society of Rock Mechanics standard tests.

The first three tests do not seem suitable for studying fracture properties of asphalt materials. The sample preparation is relatively complex and it becomes even more difficult for composite materials such as asphalt mixtures. The test configuration is not simple either and some of the restrictions imposed on the sample geometry increase the complexity involved in performing these tests. For example, in the CCNBD test method three parameters and six geometry requirements are employed to ensure LEFM conditions. As a consequence further investigation of using these test configurations for asphalt mixture fracture testing was abandoned.
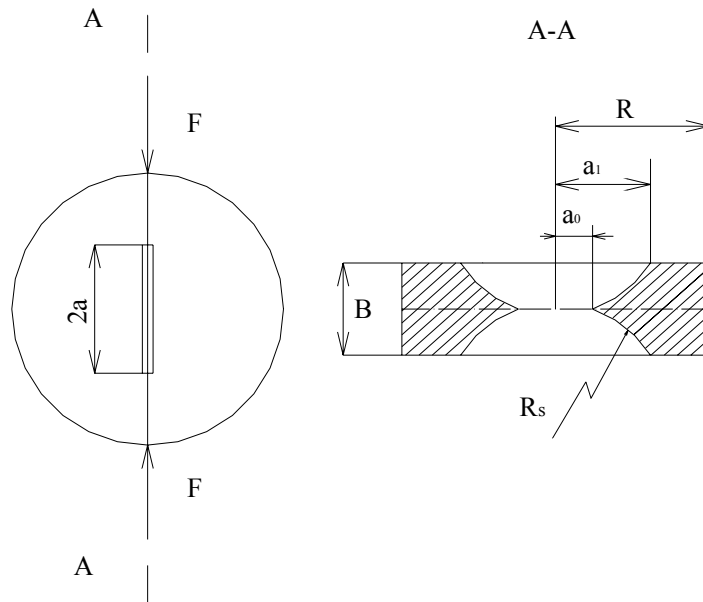
Figure 2.1.4. Crack Chevron Notched Brazilian Disc (CCNBD) Test.

Semi-Circular Bend (SCB) Test

The semi-circular bend (SCB) test was first proposed by Chong and Kurrupu (63). Lim et al. (65,66) used it to test soft rock and published a detailed study on the advantages and limitations of this type of configuration as a fracture test. The specimen of SCB is a half cylinder with a notch of length of a and makes an angle α with the center axle of the cylinder. The test is schematically shown in figure 2.1.5.

This test can be used to determine the mode Ⅰ stress intensity factor, or the mixed mode Ⅰ and Ⅱ stress intensity factor, depending on the angle of the notch with the base line of the specimen (65). However in our research only mode Ⅰ fracture will be studied and the equation for the mode Ⅰ stress intensity factor is:

$$K_{\mathrm{I}} = \sigma_0 \sqrt{\pi a} Y_{\mathrm{I}} \qquad (4)$$
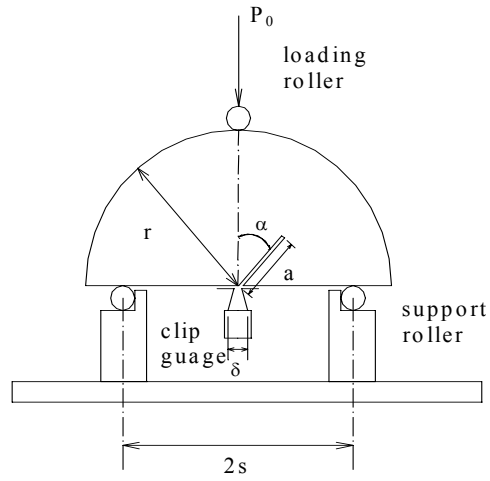
Figure 2.1.5. Semi-Circular Bend Test

where

$$\sigma_0 = \frac{P_0}{2rL}$$

r = the specimen radius

L = the specimen thickness

P_0 = the pertinent force

Y_I = the normalized stress intensity factor, from finite element calculations and

$$Y_I = Y_{I\{S_0/r\}} + \frac{\Delta S_0}{r}B, \quad 0.5 \leq \frac{S_a}{r} \leq 0.8$$

S_a : *Actual half span*

S_0 : *Analysed half span*

ΔS_0 : $S_a - S_0$

$$Y_{I\{S_0/r\}} = C_1 + C_2(\frac{a}{r}) + C_3\, \mathbf{exp}(C_4(\frac{a}{r}))$$

and $B = 6.55676 + 16.64035(\frac{a}{r})^{2.5} + 27.97042(\frac{a}{r})^{6.5} + 215.0839(\frac{a}{r})^{16}, \, 0.03 \leq (\frac{a}{r}) \leq 0.8$

117

Lim et al. (66) also investigated the influence of specimen size, deformation rate, and type of test materials. Their results showed that:

1. The fracture toughness is independent of the specimen thickness (10mm to 50mm) over the range of conditions tested in this study.
2. Neither the specimen size nor the notch length appears to have an appreciable effect on the apparent fracture toughness.
3. Notch lengths between 3 mm and 0.8 times the SCB specimen radius seem to provide valid K_{IC} values.

Modified Ring Test

This test was described in detail by Thiercelin and Roegiers (64). The test specimen consists of a thick hollow cylinder with two diametrically opposed flat loading surfaces. For non-sub-sized samples (for which the size of the process zone ahead of the crack is negligible compared to the crack length) prepared from fine-grained Vosges sandstone and Indiana limestone they obtained toughness values in the range of values obtained with more traditional geometries. Their results also indicated that the fracture toughness, obtained by this test geometry, is independent of the crack length in the sample.

Fracture Tests On Asphalt Materials

One of the first research studies on the application of fracture mechanics concepts to the behavior of bituminous materials comes from the Chemistry Department of Queens University in Canada. Hesp and his collaborators documented the use of a simple test to measure the plane strain fracture toughness and energy of asphalt binders in three-point bending (67, 68). The proposed test follows closely the ASTM E399 standard for testing metals that assumes the materials to be linear elastic (60). A mode I critical stress intensity factor K_{IC} is calculated using the formula given in the standard and the fracture energy is then calculated assuming a Poisson's ratio of 0.5. Later on they showed that the three-point bend test could also be used for the fracture testing of mastics at low temperatures (69), and explained the beneficial effects of some types of fillers by the crack pinning theory as developed by Evans for brittle fracture in filled composite systems (70). This concept was recently used to design dense-graded asphalt mixtures with improved fracture properties (71).

118

Other researchers used the method described by Hesp in their fracture studies. Researchers at Elf proposed a methodology for studying the relationship between the low-temperature fracture behavior and the morphology of polymer- modified asphalt binders based on linear elastic fracture mechanics (LEFM) and confocal laser scanning, environmental scanning, and cryo-scanning electron microscopy (72). A joint research effort between Penn State University and Elf clearly showed that the current asphalt binder specifications did not discriminate between polymer-modified asphalt binders characterized by significantly different fracture toughness values (73).

One of the drawbacks of the fracture toughness measurements based on the ASTM E399 test method is the limitation to linear elastic behavior. Another one is the difficulty in accurately measuring the crack length used in K_{IC} calculation. Recent work by Hesp and Roy (74) and Hesp and Marasteanu (75) address these issues through the use of elasto-plastic fracture mechanics concepts. In their approach, they proposed the use of the Crack Tip Opening Displacement (CTOD) method that describes the fracture properties of materials that exhibit time-independent, non-linear behavior. The CTOD concept was developed by Wells and was first used for predicting failure in welded metal structures (76,77). Due to the less restrictive requirements and the ability to predict failure conditions even when crack tip plasticity occurs, the CTOD concept has been extensively used for both metal and plastic materials (77, 78, 79).

If for asphalt binder fracture testing the three-point bend test on a single edge notched beam (SENB) seems to be the geometry of choice, for asphalt mixtures a number of different sample geometries have been investigated. Although fracture on SENB samples has been extensively used in metals and rocks, its application to asphalt mixtures is restricted due to the sample preparation requirements. The compaction method of choice for asphalt mixtures in the US and Canada is the gyratory compactor (80). Most of the traditional research on asphalt mixtures employs tests performed on cylindrical specimens. The shape of the cores extracted form already built pavements is also cylindrical. Therefore, preparing beams of asphalt mixtures would require additional expensive equipment, such as a slab compactor and would make further comparison of material properties obtained from different testing

119

configurations impossible. As a consequence, most of the asphalt mixtures fracture investigations are based on cylindrical specimens.

One of the first post SHRP studies on the application of fracture mechanics concepts to asphalt mixture characterization was published by Labuz and Dai (81). Closed-loop, computer-controlled fracture tests were conducted using an unload-reload procedure so that multiple measurements of fracture toughness K_{IC} could be obtained from a single beam specimen in three-point bending. As with any bend test, an accurate measurement of the load-point displacement is complicated by nonlinear deformation and crushing at the roller to specimen contacts. These factors were eliminated by measuring a differential displacement: the deflection of the notch relative to points directly above the supports provides a displacement that avoids the contact problem. This method provides an estimate of Young's modulus E through a compliance calibration.

The behavior (E and K_{Ic}) of the asphalt concrete tested at an air voids content of about 10% was dependent upon temperature. Assuming linear fracture mechanics is valid, the fracture toughness was found to be 0.5 MPa-m$^{0.5}$ at -18°C and at -34°C. However, the loading records indicate that nonlinear behavior is more pronounced at -18°, which means that more energy would be needed to initiate the fracture. In terms of pavement performance, this asphalt concrete would be more resistant to cracking at -18° than at -34°C. The air void content influences the asphalt's fracture toughness. For tests conducted at -18°C, specimens prepared at a lower air voids (7%) exhibited K_{Ic} of 0.7 MPa-m$^{0.5}$, while at higher air voids K_{Ic} was 0.2 MPa-m$^{0.5}$ tested the fracture toughness of a standard MnDOT asphalt mixture using the SENB configuration. They observed the non-linear behavior of asphalt mixture at –18°C and –34°C. With the compliance method, they plotted the R-curve of the asphalt mixture.

In a number of recent papers Roque and his collaborators have investigated the use of the Indirect Tension Test to determine fracture properties of asphalt mixtures (82, 83). In their research they tested IDT cylindrical specimens with an 8-mm diameter hole drilled in the center of the specimen (figure 2.1.6). Their research focused on obtaining suitable crack growth rate parameters to describe the fatigue cracking of asphalt mixtures under traffic loading at intermediate temperatures. This type of testing geometry has many advantages over other conventional geometrical configurations. One of the major advantages is the

presence of compressive stresses close to the loading contact area, which results in a smaller process zone and makes the application of LEFM possible (64).
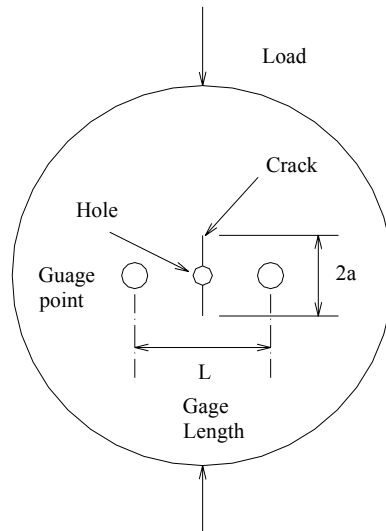
Figure 2.1.6. Modified IDT specimen.

In reference (82) tests were performed at a single temperature of 10°C. Specimens were placed in an environmental chamber and allowed to reach temperature equilibrium overnight. The specimens were also allowed to dry for at least 24h after sawing. The load applied consists of a 0.1-second haversine load followed by a 0.9-second rest period. A summary of the steps followed in the analysis is given below.

1. Plot resilient horizontal deformations as a function of loading cycles and determine the initial resilient horizontal deformation (δ_0) that corresponds to the response of the specimen in the undamaged state.

2. From the data above, calculate the crack length by both the close form equation and the finite element method. The close form equation is as follows:

$$\frac{\delta}{\delta_0} = 2\sqrt{1 + \frac{c^2}{L^2}} - \frac{(1+\upsilon)}{\sqrt{1 + \frac{c^2}{L^2}}} + \upsilon \qquad (6)$$

where

δ = resilient horizontal deformation across the crack length

121

δ_0 = resilient horizontal deformation of the uncracked specimen (this corresponds to the deformation measured on the first cycle of loading and calculated in step 1)

L = guage length of which deformation is measured;

c = crack length;

υ = Poisson's ratio.

3. Plot the crack length against the load cycles and determine the crack growth rate (da/dN) at each point.

4. Calculate the stress intensity factor K by checking the graph of the relation of normalized K and crack length, which is produced with either the close form equation or the finite element method.

   The equation for the stress intensity factor with this type of geometry is:

$$K = \sigma\sqrt{\pi a} \tag{7}$$

5. Plot the crack growth rate as a function of the stress intensity factor using a log-log scale, which reflect the power law nature of Paris' law. With regression analysis determine the parameters A and n in Paris' law.

This test takes advantage of existing test equipment, reduces the cost for the new test method and avoids the strict size requirement in the SENB beam test. Especially noteworthy is the fact that this test avoids direct measuring of K and of the crack length C. K is calculated with the graph of the relationship between the normalized stress intensity factor and the normalized crack length. C is calculated by the horizontal deformation. However, in a later study (83), Roque and Zhang showed that the plastic deformation at the crack tip is significant for this geometry at the test temperature used (10ºC) and as a consequence the application of Paris law to describe the crack propagation under LEFM conditions is not valid.

Another type of geometry that has received attention in the past years is the semi-circular bending test. Most of the fracture research on asphalt mixtures performed in Netherlands used this type of test. Molenaar et al. (84) tested seven standard asphalt mixtures using three different specimen sizes, four test temperatures and three loading rates. The research team concluded that:

1. K_I is almost independent of the specimen diameter for a deformation rate of 0.05 mm/s if the diameter is greater than 220 mm. For a deformation rate of 0.005 mm/s the diameter must be greater than 150 mm.

2. The dependence of the apparent fracture toughness on the specimen thickness is weaker than its dependence on the specimen diameter.

3. The apparent fracture toughness and indirect tensile strength are positive related, and apparent fracture toughness can be interpreted as tensile strength for a notched specimen. For temperatures below 15℃, the variation coefficient of the fracture toughness is about half that of the indirect tensile strength.

4. The discriminative ability of the SCB test as a fracture toughness test is fair, whereas the discriminative ability of the indirect tensile test, to determine the indirect tensile strength, is poor.

Conclusion

Based on the results of the literature search two configurations emerged as potential candidates for the low-temperature fracture testing of asphalt mixtures: the modified IDT test and the semi-circular bend test.   However, the SCB test presents a number of advantages over the modified IDT test. The use of SCB test is better documented for both rocks and asphalt materials and a repeatable numerical solution is available for the fracture toughness obtained with this configuration. The SCB experience with fatigue testing of asphalt mixtures is very positive in relating fracture properties to field performance. In addition, sample preparation is easier: the notch can be easily cut and more samples can be obtained from the gyratory compacted cylindrical specimen. As a result, for this project the SCB configuration was selected. The test protocol proposed by Labuz and Dai (81) was selected for controlling the loading of the SCB specimens.

PART 2. LABORATORY TESTING
Chapter 2.2. Asphalt Mixture Laboratory Testing

MATERIALS

Three Superpave asphalt mixtures were studied in this project. These mixtures were used in cells 33, 34 and 35, respectively, at the Mn/ROAD test facility and have the same aggregate structure but different asphalt binders: PG 58-28 (cell 33), PG 58-34 (cell 34) and PG 58-40 (cell 35). The mixtures specimens tested in the lab were prepared from loose mix sampled out of the paver hopper during the construction of the test cells. They have a l maximum aggregate size of 19mm, an asphalt content of 5.8 percent, and air void content of 4 percent. The gradation of aggregate is listed in Table 2.2.1.

Table 2.2.1 HMA Aggregate Gradations

Sieve	Requirements		PG 58-28 Average	PG 58-34 Average	PG 58-40 Average
	Min	Max			
¾"	100	100	100	100	100
½"	90	100	92.2	93.6	93
3/8"	79	90	84.8	85.8	85.2
# 4	59	73	67.4	67.8	66.6
# 8	48	58	55.4	55.6	54.6
# 200	2.7	6.7	5.2	5.2	5.1
# of Samples			5	5	5
Sample Type			Averages for Ignition Oven and Core Extraction from Contractor and Mn/DOT samples		

SAMPLE PREPARATION

The loose mix was heated to the compaction temperature according to the job mix formula provided by Mn/DOT material laboratory. The five-gallon buckets of loose mixture

were initially heated up two hours and then were divided into 2000g for G_{mm} measurement and 6370g for specimen preparation. The pans were put back into the oven set to the compaction temperature and heated for another 1.5 hours. No additional aging was performed on the specimens since the mixtures had already been aged in the mixing plant.

The SCB specimens were obtained from Superpave gyratory compactor (SGC) cylindrical samples compacted to an air void level of 4%. The cylinder was sliced into six plates that are 25-mm thick. The center two plates were marked with "C", the middle two with "M". The difference between "C" specimen and "M" specimens from the same SGC cylindrical sample shows the effect of density gradients within the sample. The top and bottom plates were discarded. Each plate was cut in half and a vertical notch was made along the symmetrical axis of the semi circle specimen. Therefore, eight SCB specimens were cut from one SGC cylindrical specimen, four C and four M as shown in figure 2.2.1. Four SGC cylindrical replicates were tested for each of the three mixtures.
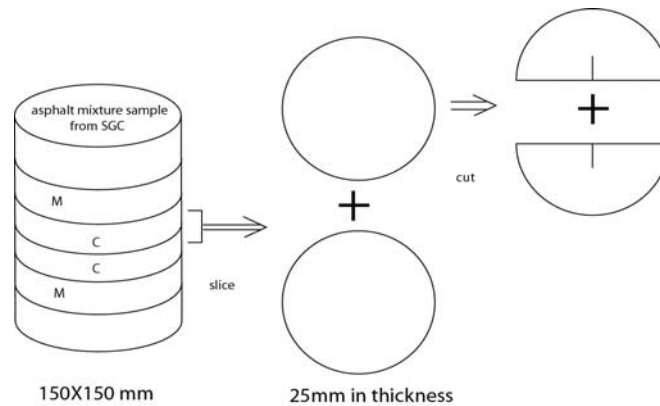
Figure 2.2.1. Sample Preparation

TEST SETUP

The semicircular bend test is identical with the classical single edge notched beam (SENB) test except for the specimen geometry: semicircular instead of a rectangular beam. The SCB specimen is supported symmetrically at the bottom, and loaded at the top. In order to reduce the friction in the contact area at the bottom of specimen, the SCB specimen is supported by two rollers, and the rollers are connected with two L-shape metal blocks, which are fixed on the support. The Indirect Tension test (IDT) loading plate is used to load the SCB specimens. The rollers and the supporting blocks were machined such that they fit in

the IDT loading plate and leave enough space for the extensometer mounted at the bottom of the SCB specimen. This experiment fixture is schematically shown in figure 2.2.2. The span of the support is 120 mm; as mentioned previously the diameter of the SCB specimen is 150 mm.

During the test, the load and load line displacement (LLD) are measured as shown in figure 2.2.3. Considering that the asphalt mixture at low temperatures is very brittle, a crack month opening displacement (CMOD) signal is used as the controlling signal to maintain the test stability in the post-peak region of the test. The CMOD is measured with an extensometer attached to the bottom of SCB specimen by means of two metal buttons glued on the specimen. The LLD is measured with an extensometer mounted vertically on the specimen; the upper part is attached to a button glued on the specimen and the lower part is in contact with a small frame attached to the support rollers. The range of the two extensometers is from -1 mm to 1 mm.
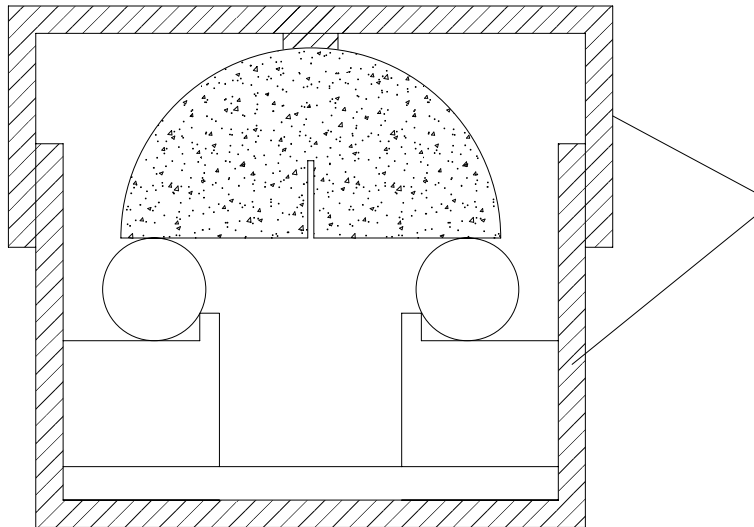
Figure 2.2.2. Schematic of the experimental setup.

TESTING PROCEDURE

The asphalt mixtures were tested at three temperatures, -20°C, -30°C, and -40°C using a MTS 810 testing system equipped with a Testar IIs system. Liquid nitrogen was used to obtain the desired test temperature in the environmental chamber. The built-in

126

thermocouple and an independent digital thermometer with the probe attached to the specimen were used to monitor and control the specimen temperature within 1ºC of the test temperature. The SCB specimen was stored at room temperature overnight before being placed into the test chamber. The specimen was kept in the chamber for three hours at the desired temperature before starting the test in order to avoid significant thermal gradients in the specimen.

Table 2.2.2. Loading Rates

Step	Control Type	Rate (mm/s)
Contact	Stroke	0.05
Seating	Stroke	0.005
Test	CMOD	0.0005
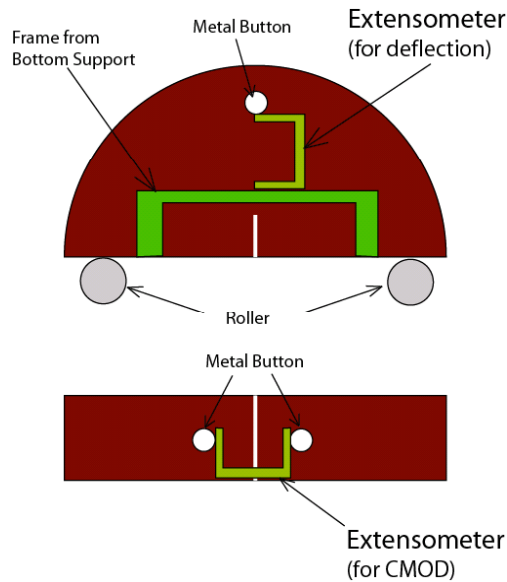
Figure 2.2.3. Extensometers locations.

A template was written using MTS TestStar IIs software to control the MTS machine and execute the experiment automatically. In this program three steps had to be completed. In the first step, called contact, the loading plate makes contact with the SCB specimen. In the second step, called seating, a small seating load is applied to the specimen. In the third step,

called test, the test is executed. The load, the CMOD and the LLD are measured and recorded. A number of criteria to terminate the test were pre-assigned in the template to prevent damage of the extensometers during the test. The same loading rate was used for all three temperatures as shown in table 2.2.2

PART 2. LABORATORY TESTING

Chapter 2.3. Interface Friction

INTRODUCTION

In the crack spacing model developed in part 1, an AC layer is supported on a base layer. The AC layer can slip when the temperature is reduced due to the existence of a "free edge". The base layer provides the friction to AC layer through the interface between the AC layer and the base layer. The equilibrium between temperature shrinkage and the friction on the interface controls the crack spacing, as shown below:

$$X_c = \frac{E\alpha\Delta T}{\dfrac{C}{h} + \rho g \tan\Phi}$$

(1)

where

X_c: longitudinal distance from free edge to point at which maximum tensile stress is achieved in the asphalt layer

E: asphalt mixture Young's modulus

α: asphalt mixture linear coefficient of thermal contraction

ΔT: temperature change

C: cohesion

h: thickness of pavement

ρ: density of asphalt mixture

g: gravity

Φ: friction angle

From a theoretical point of view the interface between asphalt layer and base represents a separate layer. Ideally, the interface properties should be measured in a field experiment; however this type of experimental data was not available. Anecdotal evidence seems to indicate that slipping occurs more often in the base layer rather than the interface layer. Thus, it is reasonable to assume that the C and Φ used in above model can be obtained from triaxial tests performed on the aggregate base material.

MOHR-COULOMB EQUATION

The aggregate in base layer is usually modeled using the Mohr-Column relation between the shear stress and the tensile stress:

$$\tau = C + \sigma \tan \Phi \tag{2}$$

where τ is the shear stress, σ is the normal stress and C and Φ are defined above.

In order to calculate the cohesion and friction angle two sets of values of (σ, τ) are needed to solve the two unknowns. In triaxial test results the confining pressure and deviator stress are reported. Knowing the deviator stress $(\Delta\sigma_d)$ and the confining stress (σ_3), the first principal stress (σ_1) is simply

$$\sigma_1 = \sigma_3 + \Delta\sigma_d \tag{3}$$

First principal stress σ_1 can also be written as:

$$\sigma_1 = \sigma_3 \tan^2(45 + \frac{\phi}{2}) + 2c \tan(45 + \frac{\phi}{2}) \tag{4}$$

From triaxial tests performed at two different confining pressures, two sets of (σ_1, σ_3) can be obtained, which can be further used to solve the system of two equations (3 and 4) to obtain the cohesion and friction angle.
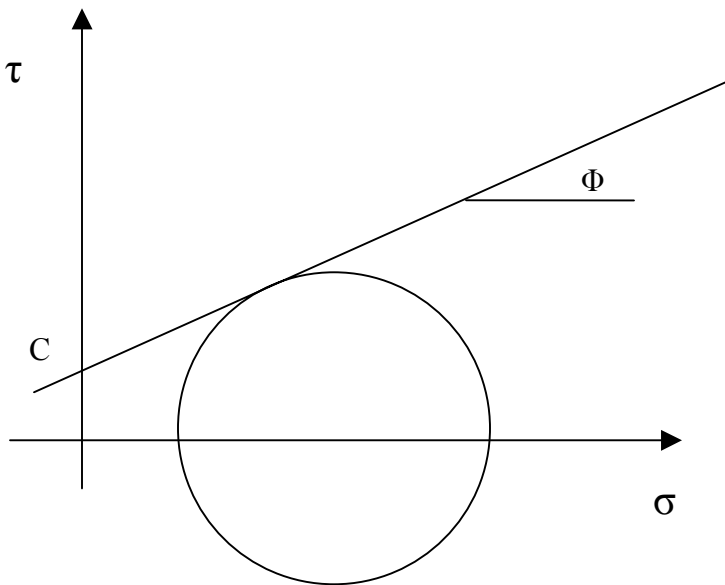
Figure. 2.3.1 Mohr's Circle

EXPERIMENTAL DATA

Experimental data on class 5 and class 6 aggregate base materials was obtained from MnDOT Office of Materials. Class 5 requires a minimum 10% crushed stone and maximum 10% shale. Class 6 requires minimum 15% crushed stone and maximum 7% shale. The detailed description of these two types of material can be found in Minnesota specification 3138.

Triaxial test were performed on these materials at two confining pressures, 4 and 8 psi, respectively and the results are listed in table 2.3.1. Typically, the properties measured at the optimum moisture content are used in pavement design. For class 6 material the two triaxial tests were performed at an optimum moisture content of 6.5%. For class 5 the available data did not indicate if the material moisture content was at the optimum level.

Based on these two sets of confining pressure and deviator stress the cohesion and friction angle were calculated for the two types of aggregates. The results are shown in table 2.3.2.

Table 2.3.1 Triaxial Test Data

Material	Test ID	Moisture (%)	Confining Pressure (psi)	Deviator Stress (psi)
Class 5	C5TC04R3	5.06	4	59.1086
	C5TC08R1	5.10	8	72.1613
Class 6	C6OM05D4	6.42	4	83.5614
	C6OM05A8	6.64	8	114.0562

Table 2.3.2 Cohesion and Friction Angle

Soil Type	Friction Angle (Φ)	tan(Φ)	Cohesion (psi)/(kPa)
Class 5	38.2°	0.787	11.2(77.2)
Class 6	52.4°	1.299	9.0(62.1)

Discussion

The cohesion (C) and friction angle (Φ) of base layer obtained from triaxial tests are used to compute the interface friction and then crack spacing in the crack spacing model developed in subtask 1. However, the thermal stress in AC layer reaches the tensile strength of asphalt mixture and initiates crack at very low temperatures at which most likely the base layer is in frozen state. A frozen aggregate base has different cohesion and friction angle values compared to the values obtained at room temperature and optimum moisture conditions. As indicated in task 1, research by Sayles (48) on Ottawa sands in a frozen condition have shown cohesion on the order of 1 MPa, which is much larger than what is reported in table 2.3.2. This difference significantly affects the prediction of crack spacing based on equation 1. This effect will be further discussed in subtask 3.3 on model testing.

PART 3. DATA ANALYSIS

Chapter 3.1. Laboratory Test Results and Analysis

In the SCB test, the load is applied on the top of the specimen that is symmetrically supported by two rollers at the bottom with a span of 120mm. The test is controlled by the crack month opening displacement (CMOD) with a fixed rate of 0.0005-mm/s. The load, deflection and CMOD were recorded and the load and load-line displacement (P-u) curves were plotted. Since the weight of the specimen was less than 2 percent of the peak load, no weight compensation was used. The test data obtained from the 150 SCB specimens tested was stored in data base format for future use.

This report is divided into two parts. The first part is the computation of the fracture parameters from the experimental data. The second part is the analysis of fracture parameters calculated with the methods described in the first part and the analysis of influential factors including the types of mixture components and the test temperature.

CALCULATION OF FRACTURE PARAMETERS

Three parameters were calculated from the experimental data obtained at –30°C and –40°C: the stiffness, the fracture toughness and the fracture energy.

Stiffness

The stiffness was calculated as the slope of the linear part of the initial P-u curve. Preliminary tests showed that at -30°C the curve before the load reaches 2kN was reasonably linear, and therefore the slope was simply calculated by fitting a line to the data obtained between 1 and 2kN loading as shown in Figure 3.1.1.
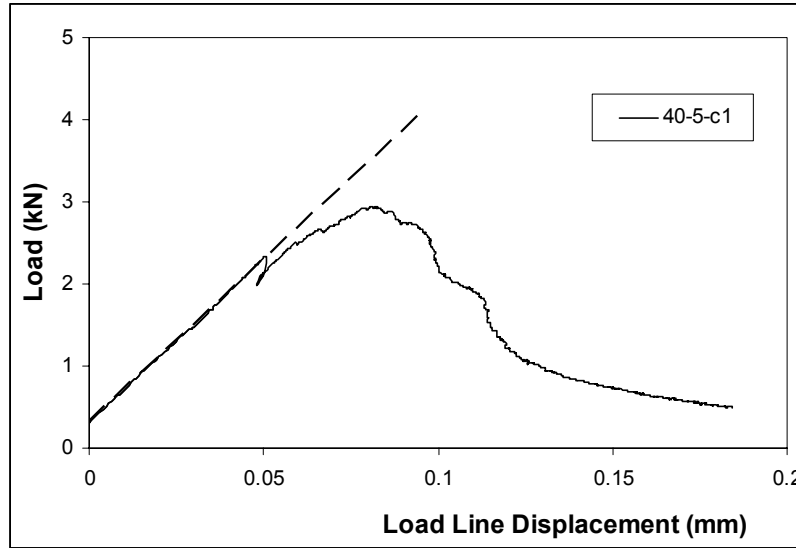
Figure 3.1.1. Stiffness Calculation

Fracture Toughness (K_{IC})

The stress intensity factor (SIF), which characterizes the stress state around the crack tip, is a function of the load and the geometry:

$$K = f(P, a, W) \tag{1}$$

where P is the load, a is the crack length, and W is the vector of the characteristic length of the geometry. For any particular specimen, before the crack begins to propagate, the geometry is constant and the SIF changes with the change of the load at different stages. At peak load the crack begins to grow and this critical SIF is a measure of the fracture toughness of the specimen.

The Mode I critical stress intensity factor K_{IC}, also referred to as fracture toughness, has received considerable attention to describe the fracture resistance of asphalt materials. Typically, K_{IC} calculations are based on LEFM concepts and plane stress conditions that assume that the material behaves linearly elastic and is homogeneous at the specimen scale.

In this study two different methods were used to calculate K_I. The first method used a freeware finite element program, FRANC2D, developed at Cornell University (85); the second method used the equation derived by Lim et al. (65). Both methods are based on LEFM analysis.

FRANC2D uses three algorithms to calculate K_I. One is the displacement correlation technique (86), marked as DSP in Figure 3.1.2; the second is the J-integral technique (87), marked as JINTEGRAL in Figure 3.1.2; the third is the modified crack closure integral technique (88). The mesh used in FRANC2D is shown in Figure 3.1.18 at the end of this chapter. The results from J-integral method and modified crack closure integral method were very close and therefore only the results from J-integral method were plotted in Figure 3.1.2.

Lim et al. numerically computed K_I for different SCB geometries and developed the following equation:

$$\frac{K_I}{\sigma_0 \sqrt{\pi a}} = Y_{I(s_0/r)} + \frac{\Delta s_0}{r} B \qquad (2)$$

where

$\qquad K_I \qquad$ = Mode I stress intensity factor;

$\qquad \sigma_0 \qquad$ = $P/2rt$

$\qquad$ P = applied load;

$\qquad$ r = specimen radius;

$\qquad$ t = specimen thickness.

$\qquad Y_I$ = the normalized stress intensity factor

$$\qquad Y_{I(s_0/r)} = C_1 + C_2(a/r) + C_3 \exp(C_4(a/r)) \qquad (3)$$

$\qquad C_i$ = constants;

$\qquad$ a = notch length;

$\qquad \Delta s_0/r = s_a/r - s_0/r$

$\qquad s_a/r$ = actual span ratio;

$\qquad s_0/r$ = nearest span ratio analyzed in the derivation of this equation (0.80, 0.67, 0.61, 0.50)

$$\qquad B = 6.55676 + 16.64035(\frac{a}{r})^{2.5} + 27.97042(\frac{a}{r})^{6.5} + 215.0839(\frac{a}{r})^{16}$$

The K_I values for the SCB mixture specimens with dimensions 75mm in radius and 25mm in thickness, and a notch length ranging from 3.75mm to 60mm were calculated using the two methods described above. The normalized K_I values from both methods were plotted

in Figure 3.1.6 that shows that the various calculation algorithms agree with each other very well. For convenience Lim's equation was used in the subsequent calculations.
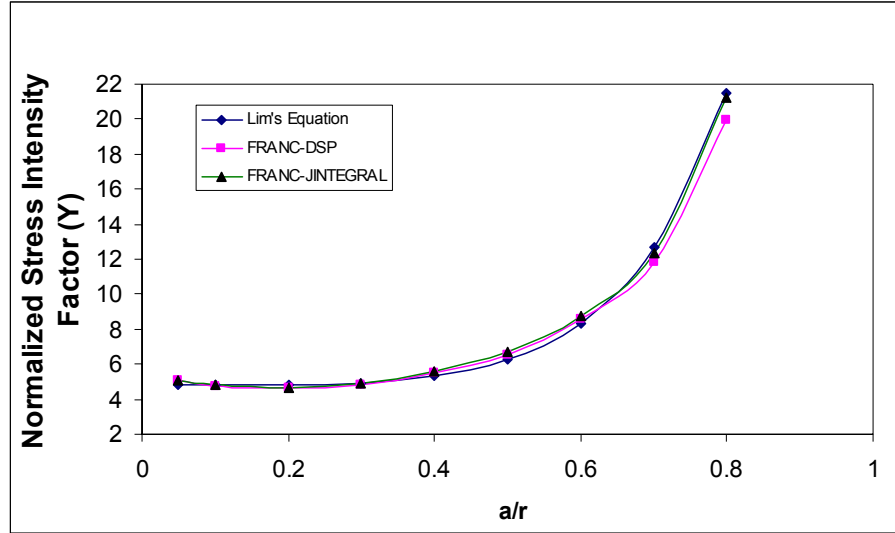
Figure 3.1.2. Normalized SIF with Different Methods

Fracture Energy (G_f)

Another fundamental fracture parameter that is less dependent on the assumptions of linear elasticity and homogeneity is the fracture energy (G_f). The fracture energy was calculated according to RILEM TC 50-FMC specification (89) that has been extensively used in the study of concrete. The work of fracture was computed as the area under the P-u curve and the fracture energy (G_f) was obtained by dividing the work of fracture with the ligament area (the product of the ligament length and the thickness of the specimen), as shown in equation (4):

$$G_f = \frac{W_f}{A_{lig}} \qquad\qquad (4)$$

where W_f is the work of fracture and

$$W_f = \int P du$$

A_{lig} is the area of the ligament.

With respect to the calculation of the area under the P-u curve two issues had to be addressed. The test was started at a seating load of 0.3kN as indicated in Figure 3.1.3. This triangular area (O'OA in Figure 3.1.3) is very small and it was not included in the energy calculation. Due to the limitation of the extensometers measuring range all tests were stopped when the load dropped to 0.5kN. Given that the peak load of the specimens was between 3-4kN, the tests were stopped at 12-17 percent of the peak load.

To better estimate the tail area of the curve W_{tail} the fictitious crack model (FCM) (33) and the rigid body kinematics method (90) were employed.
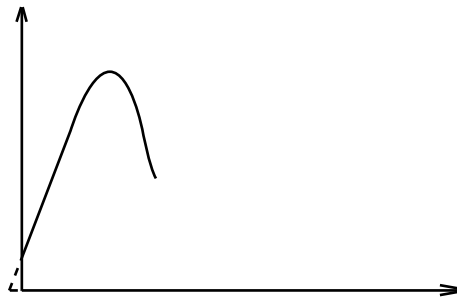
Figure 3.1.3. Load v.s. Load-Line Displacement

In the last phase of the SCB test, as sketched in Figure 3.1.4, it could be reasonably assumed that the two halves of the SCB specimen were connected only in the cohesive zone. FCM could be used to determine the distribution of the transferring stress between the two surfaces of the crack in the cohesive zone. It was also assumed that the crack path was a straight line and the compressive zone was reduced to zero.
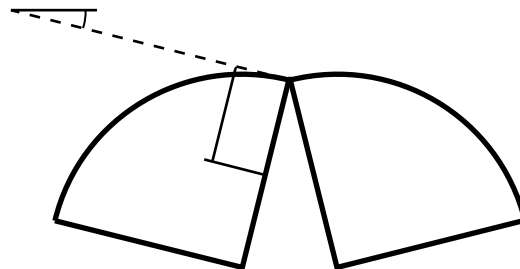
Figure 3.1.4. SCB Specimen at the Last Phase

137

When θ is very small, the crack opening w at a distance x from the joint point A can be calculated as

$$w = x\sin(\theta) \approx \theta x \qquad (5)$$

The moment provided by the transferring stress in the cohesive zone is

$$M = \int_0^{x_c} \sigma(w)Bxdx = B \int_0^{x_c} \sigma(\theta x)xdx = \frac{B}{\theta^2} \int_0^{w_c} \sigma(w)wdw \qquad (6)$$

where σ_w is a softening function that has a shape as shown in Figure 3.1.5. As described in FCM, the softening function is composed of two parameters: the tensile strength, f_t, and the maximum opening of the crack surface, w_c. The integral in equation (6) is the first order moment of σ_w and can be expressed as the product of the area enclosed between the positive axes and the softening curve, G_f, and the abscissa of the centroid of that area.
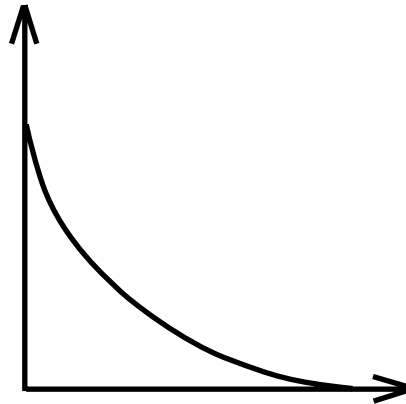
Figure 3.1.5. Softening Function

Thus

$$M = \frac{\alpha BG_f^2}{f_t\theta^2} = \frac{C}{\theta^2} \qquad (7)$$

The coefficient α depends on the shape of the softening function and for a rectangular softening function α is ½, for a linear function α is 2/3, and for an exponential function α is 1. Usually in the study of concrete, a bilinear function or an exponential function is used.

Considering the similarity between the asphalt mixture at low temperature and concrete, an exponential softening function was selected.

From the moment equilibrium condition,

$$M = \frac{P}{2} \cdot \frac{s}{2} = \frac{Ps}{4} = \frac{C}{\theta^2}$$
$$\Rightarrow P = \frac{4C}{s} \cdot \frac{1}{\theta^2}$$

(8)

since $\theta \approx \tan(\theta) = \frac{4u}{s}$

(9)

then $P = \frac{4C}{s} \cdot \frac{s^2}{16u^2} = \frac{C}{4} \cdot \frac{s}{u^2} = \frac{A}{u^2}$

(10)

which indicates that the tail of the P-u curve is a curve of power -2. Therefore

$$W_{tail} = \int_{u_c}^{\infty} Pd(u) = \frac{A}{u_c}$$

(11)

where u_c is the load line displacement value at which the test is stopped . The total work of fracture is calculated as the sum of the area under the experimentally obtained P-u curve plus the area under the predicted tail

$$W_T = W + W_{tail}$$

(12)

In addition, a regression method was used to compute the tail area. The data from 60 percent of peak load in the post-peak part of the curve to the end of the test was fitted with a power curve and the tail curve was obtained by extrapolating this fitted power curve from regression. The powers of tail curves from the regression on the data at -30°C are shown in Table 3.1.1.

The mean for all the specimens was -2.19 and the standard deviation was 0.37, which seems to indicate that considering the tail curve as a power function of order –2 is reasonable. Based on these results the following procedure is recommended to calculate the tail area of the P-u curve:

1. Fit the data to obtain the power of the curve.
2. Check the power of the curve. If the power is within one standard deviation from -2, use the power from regression. If the power is outside this range use one of the two values -2±0.37 that is closer to the regressed power value.

3. Calculate the tail area with the power of curve determined from above two steps.

Table 3.1.1. Power of the Tail Curve with Regression

Specimen	Mean	Standard Deviation
40-5-c	-2.00	0.36
40-6-c	-2.57	0.64
40-5-m	-1.69	0.08
40-6-m	-1.54	0.22
34-5-c	-2.18	0.21
34-5-m	-2.25	1.04
34-6-c	-2.49	0.58
34-6-m	-1.93	0.29
28-4-c	-2.76	0.84
28-4-m	-2.22	0.82
28-5-c	-2.56	0.54
28-5-m	-2.11	1.04

RESULTS AND ANALYSIS

SCB specimens with a nominal notch length of 15-mm were tested at three temperatures: -20°C, -30°C, and -40°C. A total of 150 SCB specimens were fabricated and tested: 48 specimens at -40°C, 76 specimens at -30°C, and 36 specimens at -20°C. The stiffness, fracture toughness and fracture energy were calculated using the methods previously described. The results are summarized separately for each temperature. The specimens from the same SGC cylindrical replicate were grouped together and the averages of the individual groups were connected with solid lines.

To statistically analyze the experimental data, a split-plot test was performed with statistics software, MacANOVA, at each temperature with the binder type (three levels) as whole plot factor and the specimen location (two levels) as split plot factor. Then the

analysis of data at all three temperatures with split-plot test concludes the part of result and analysis of subtask 3.1.

Analysis Of Data At -30°C

The experimental data at –30°C is shown in the Figures 9, 10, and 11 at the end of the document, and the p-values obtained in the analysis are shown in Table 3.1.2. The p-value for G_f was obtained after logarithmic transformation. The p-values indicate that for stiffness neither the binder nor the location had a significant effect. However, for fracture toughness and in particular for fracture energy the binder effect was significant. The location and the binder-location interaction did not have a significant effect on the two parameters, which indicates that the density gradient in the SGC sample does not affect the results.

The mean and standard deviation calculated with respect to the type of binder are summarized in Table 3.1.3. This shows that based on the means, the three mixtures are ranked differently by the two fracture parameters investigated:

Mix(58-40)>Mix(58-34)>Mix(58-28)   (by G_f)

Mix(58-34)>Mix(58-40)>Mix(58-28)   (by K_{IC})

Table 3.1.2. P-values for the Results Obtained at -30°C

	Stiffness	Fracture Toughness (K_{IC})	Fracture Energy (G)
Binder (B)	0.1785	0.0163	2.73e-07
Location (L)	0.4378	0.7674	0.5960
B.L	0.2070	0.3649	0.2876

The means were then compared to each other with the honest significant difference (HSD) method to show if they were statistically different. The results showed that with respect to G_f all three mixtures are different from each other. However, with respect to K_{IC} the 58-40 mixture was not different from the 58-34 mixture, while both of them were different from the 58-28 mixture.

Table 3.1.3. Mean and Standard Deviation Values at –30°C

	PG 58-28		PG 58-34		PG58-40	
	Mean	Standard Deviation	Mean	Standard Deviation	Mean	Standard Deviation
K_{IC} $(MPa.m^{0.5})$	0.88	0.10	0.99	0.12	0.97	0.11
G_f (N/m)	237	40	296	70	333	56

Analysis Of Data At -40°C

The experimental data at –40°C is shown in the Figures 12, 13, and 14, and the corresponding p-values obtained from the split-plot analysis are shown in Table 3.1.4. Similar to data at –30°C, the p-values indicated that for stiffness neither the binder nor the location had a significant effect. However, for both fracture toughness and fracture energy the binder effect was significant. The location and the binder-location interaction did not have a significant effect on these two parameters, which indicates that the density gradient in the SGC sample did not affect the fracture properties of asphalt mixture at –40°C either.

Table 3.1.4. P-values with Data at -40°C.

	Stiffness	Fracture Toughness (K_{IC})	Fracture Energy (G)
Binder (B)	0.4772	0.0016	0.0087
Location (L)	0.9551	0.2512	0.1007
B.L	0.6621	0.9795	0.3744

The mean and standard deviation calculated with respect to the type of binder are summarized in Table 3.1.5. Based on the means, the three mixtures are ranked in the same order of their binder grade:

Mix(58-40)>Mix(58-34)>Mix(58-28)   (by G_f and K_{IC})

Table 3.1.5. Mean and Standard Deviation Values at –40°C

	PG 58-28		PG 58-34		PG58-40	
	Mean	Standard Deviation	Mean	Standard Deviation	Mean	Standard Deviation
K_{IC} (MPa.m$^{0.5}$)	0.84	0.07	0.95	0.10	1.05	0.09
G_f (N/m)	217	34	263	69	309	79

Analysis Of Data At -20°C

The experimental data at –20°C is shown in the Figure 3.1.15, 16, and 17, and the corresponding p-values obtained from the split-plot analysis are shown in Table 3.1.6. Similar to data at the other two temperatures, the p-values indicated that for stiffness neither the binder nor the location had a significant effect. However, for fracture energy the binder effect was significant, while for fracture toughness it was insignificant, which is different from the analysis at the other two temperatures. The location, corresponding to the effect due to density gradient, and the binder-location interaction were statistically insignificant for these two fracture parameters, which indicates that the density gradient in the SGC sample does not affect the fracture properties of asphalt mixtures at -20°C.

Table 3.1.6. P-values with Data at -20°C

	Stiffness	Fracture Toughness (K_{IC})	Fracture Energy (G)
Binder (B)	0.1453	0.1369	0.0454
Location (L)	0.1084	0.6851	0.5328
B.L	0.8739	0.7575	0.4066

The mean and standard deviation calculated with respect to the type of binder are summarized in Table 3.1.7. Based on the means, the three mixtures are ranked in the different orders of their binder grade:

Mix(58-34)>Mix(58-40)>Mix(58-28)   (by G_f)

Mix(58-34)>Mix(58-28)>Mix(58-40)   (by K_{IC})

Table 3.1.7. Mean and Standard Deviation Values at –20°C

	PG 58-28		PG 58-34		PG58-40	
	Mean	Standard Deviation	Mean	Standard Deviation	Mean	Standard Deviation
K_{IC} (MPa.m$^{0.5}$)	0.90	0.07	0.97	0.11	0.85	0.07
G_f (N/m)	326	111	561	170	506	161

Based on the results obtained at the three test temperatures the following observations can be made:

- The type of binder is always significant with respect to fracture energy.

- The type of binder is significant at -40°C and -30°C and not significant at -20°C with respect to fracture toughness.

- The type of binder is not significant with respect to stiffness at any of the three temperatures.

- The density gradient is not significant for any of the three fracture parameters at any of the three temperatures.

It is also worth noting that based on fracture energy, the ranking of three mixtures agreed with the PG ranking at –40°C and –30°C. At –20°C, 58-40 mixture and 58-34 mixture switched the order, and both of them were better than the 58-28 mixture. For the fracture toughness at –40°C and –30°C the ranking was similar to the energy ranking. Although at –30°C the 58-34 mixtures showed narrow higher average fracture toughness (0.99MPa.m$^{0.5}$) than the 58-40 mixture (0.97MPa.m$^{0.5}$), considering the standard deviation (0.1 for 58-34 mixture and 0.12 for 58-40 mixture), these two mixtures should be considered as the statistically same. However, at –20°C the rankings based on toughness and energy were quite

144

different. Based on fracture energy, the 58-40 mixture was better than the 58-28 mixture, while based on fracture toughness, the order was reversed.

The change of ranking patterns at different temperatures suggests that the different fracture properties of asphalt mixtures change differently with temperature changes. This analysis is presented next.

Analysis Of Data At All Three Temperatures

The same split-plot design was applied to study the temperature effect. The temperature was used as a whole plot factor. Thus the split-plot design used in this part is with two whole plot factors, binder and temperature, and one split plot factor, location. However, in order to balance the data structure, only part of the data at –30°C was used in this analysis. The data was obtained on the cylindrical specimens 58-28-4, 58-28-5, 58-34-5, 58-34-6, 58-40-5 and 58-40-6. Thus the total number of the SCB specimens analyzed in this part is 132 with 48 at –40°C, 48 at –30°C and 36 at –20°C.

The p-values of the main effects and interactions are listed in Table 3.1.8. The mean values of the three parameters are plotted against the binder and the test temperature, as shown in Figure 3.1.6, 7 and 8.

For stiffness the p-values indicate that none of the factors tested in this project, the binder type, test temperature and density gradient are significant including. This is in agreement with the previous conclusions.

For the fracture toughness, the p-values show that the main effects of the binder and temperature are insignificant; however, the interaction between the binder and temperature is significant. This appears to contradict the previous conclusions obtained at the individual test temperatures. However, this can be explained by the fact that the strong interaction between the binder effect and the temperature effect hides the main effect for each of them.

With respect to the fracture energy, both the binder effect and the temperature effect are significant, while the interaction between them is not. This is evidenced by the interaction plot shown in Figure 3.1.8. The three lines, representing the change of the fracture energy of three mixtures, are almost parallel except the segment of 58-34 mixture between -30°C and -20°C. This indicates the interaction is not as significant as the main effects in this temperature range.
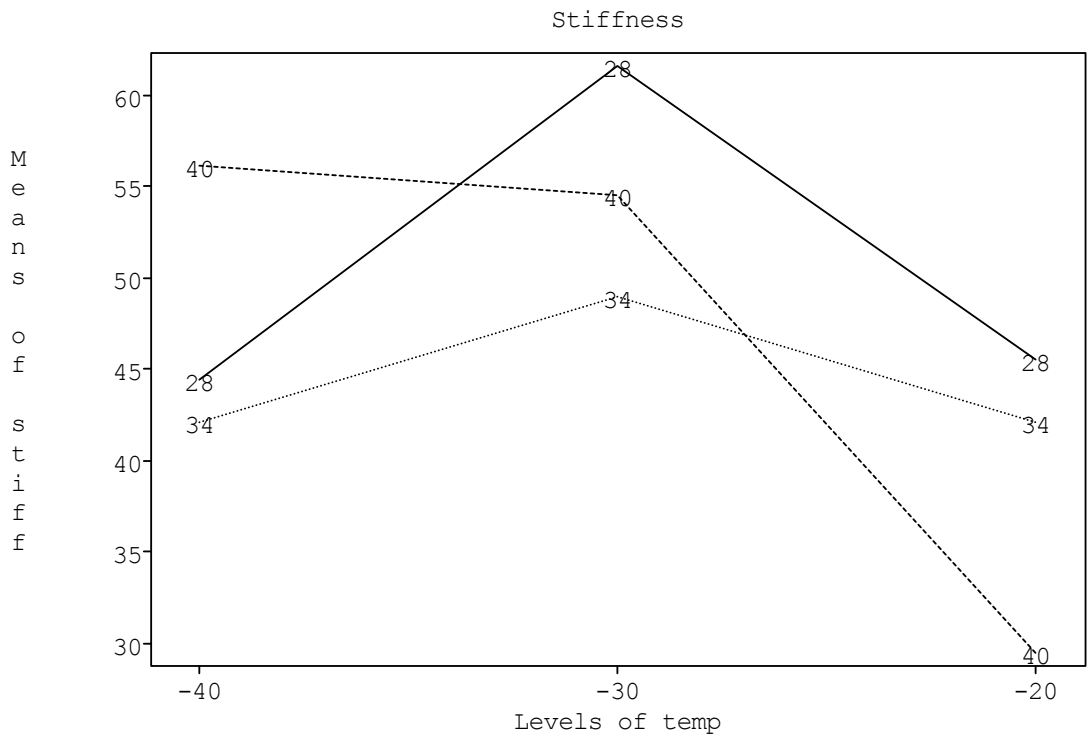
Figure 3.1.6. Interaction Plot of Stiffness from MacANOVA Output
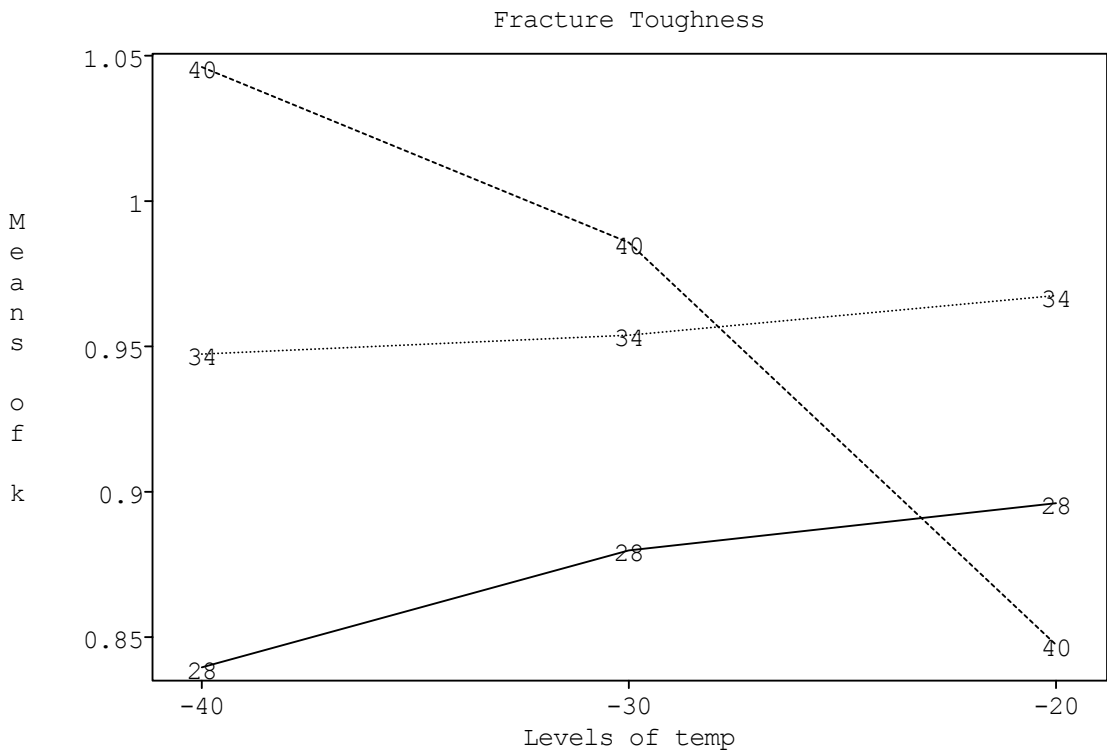
Figure 3.1.7. Interaction Plot of Fracture Toughness from MacANOVA Output

146
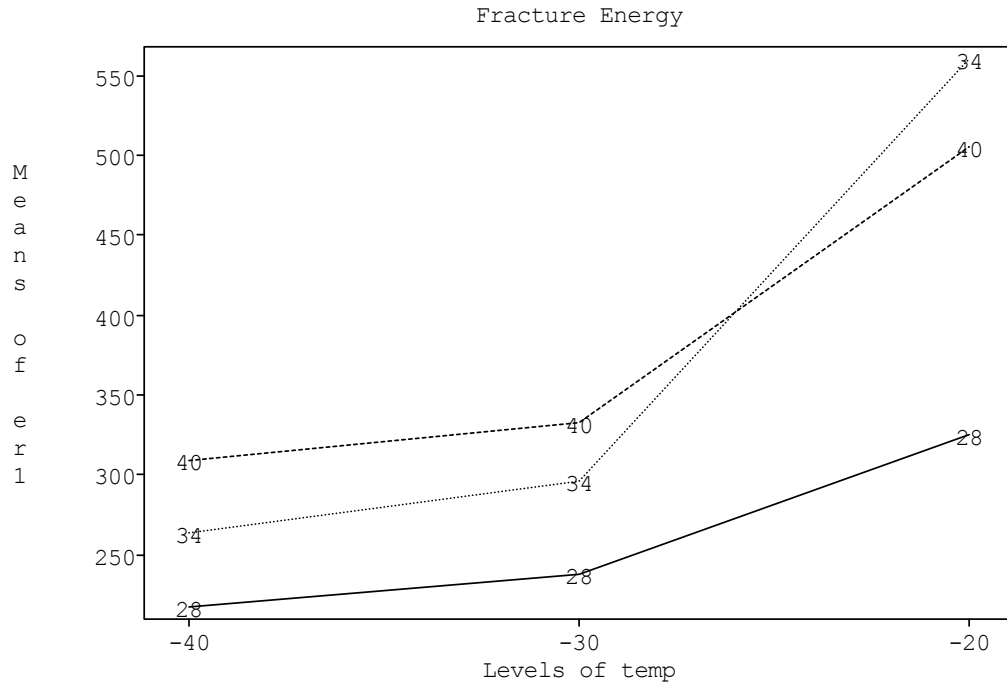
Figure 3.1.8. Interaction Plot of Fracture Energy from MacANOVA Output

Table 3.1.8. P-values with Data at All Three Temperatures

	Stiffness	Fracture Toughness (K_{IC})	Fracture Energy (G)
Binder (B)	0.8963	0.4201	0.0220
Temperature (T)	0.8430	0.7714	9.6E-05
B.T	0.3159	0.0723	0.1719
Location (L)	0.1038	0.2513	0.7201
B.L	0.8169	0.5665	0.4355
T.L	0.2653	0.8992	0.2967
B.L.T	0.8838	0.9666	0.2586

For the fracture energy, in this temperature range the general trend is that the lower the temperature, the lower the fracture energy. However, it is hard to tell how this trend would change at higher temperature. The fracture energy of 58-34 mixture increased at a faster rate when temperature increased from -30°C to -20°C such that it surpassed the 58-40

mixture at -20°C. There was not evidence this trend would continue at higher temperatures. It was also noticed that mixtures showed larger change with temperature changed between -20°C to -30°C than between -30°C to -40°C. This seems to indicate that as the temperature decreases, especially below the PG limit, the mixture becomes brittle and less dependent on temperature, which could partly explain the reduced binder-temperature interaction at lower temperatures. This agrees with the asymptotic behavior observed in the rheological characterization of asphalt binders.

Compared with the fracture energy, the fracture toughness showed quite different trend with temperature change. In the tested temperature range the 58-34 mixture showed almost no change with temperature while the 58-40 mixture showed the largest change. Furthermore, the fracture toughness of the 58-40 mixture decreased as temperature increased while that of the 58-28 mixture increased. Kim and Hussein (91) also reported on the change in fracture toughness with temperature change. They tested asphalt mixtures with binder of penetration grade of 85/100 from -5°C to -30°C at the interval of 5°C. They observed that the fracture toughness increased from -5°C to -15°C and decreased thereafter. They pointed out that fracture toughness evolution with temperature was based on the balance of two actions: the strengthening grip of the asphalt matrix and the micro damage that results from the differential shrinkages of asphalt matrix and the aggregate. However, they didn't explain how the relative contribution of these two actions changed with respect to temperature. The results in this project indicate that the strengthening action was dominant at temperatures higher than the PG lower limit when fracture toughness increased, while at temperatures lower than the PG limit the micro damage effect becomes significant and fracture toughness decreases.

SUMMARY

In this project three mixtures with three binders of PG 58-28, PG 58-34, and PG 58-40, were tested with the semi-circular test at three temperatures: -20°C, -30°C, and -40°C. Three parameters were computed for each specimen: stiffness, fracture toughness, and fracture energy and then analyzed statistically.

The split-plot test was used to determine the significance of the effects of the type of binder, the density, and the environmental temperature. In the analysis, the binder effect and

temperature effect were the whole plot factor, and the density effect was the split plot factor. The results showed that (1) the fracture toughness and fracture energy were better parameters to differentiate materials in terms of the fracture resistance than the stiffness; (2) the type of binder and the temperature had significant contribution to the fracture resistance of asphalt mixtures while the effect of density wasn't statistically significant.

Both the fracture toughness and the fracture energy changed as the test temperature changed. This fact indicated that the fracture property of asphalt mixture, like the other mechanical properties of asphalt mixture, was temperature-dependent and asphalt mixtures should only be compared at the same specified temperature.

However, for different fracture parameters different patterns of changing were observed. For the fracture energy the trend was consistent: the lower the temperature, the less the fracture energy. In addition, the 58-40 and 58-34 mixtures always had larger fracture energy than the 58-28 mixture as expected. For the fracture toughness the pattern of changing was more complex. When the temperature increased from -40°C to -20°C, the fracture toughness of 58-40 mixture decreased, while that of 58-28 mixture increased and that of 58-34 almost kept constant. Although it had been pointed out elsewhere that two actions, the strengthening grip of the asphalt matrix and the micro cracks due to the different thermal contraction of aggregate and asphalt matrix, contributed to the fracture toughness of asphalt mixture, it is not clear how the fracture toughness was affected by these two actions. Based on the limited data in this project, it appears that the lower limit of the PG grade is approximately equal to the critical temperature where the peak of fracture toughness is obtained. At temperatures was higher than the PG limit, the strengthening action appears to be dominant and the fracture toughness increases as temperature decreases; when the temperature is lower than the PG limit, the micro damage due to the micro crack controls the mixture system and the fracture toughness decreases as temperature decreases. Further research is needed to confirm this conclusion.
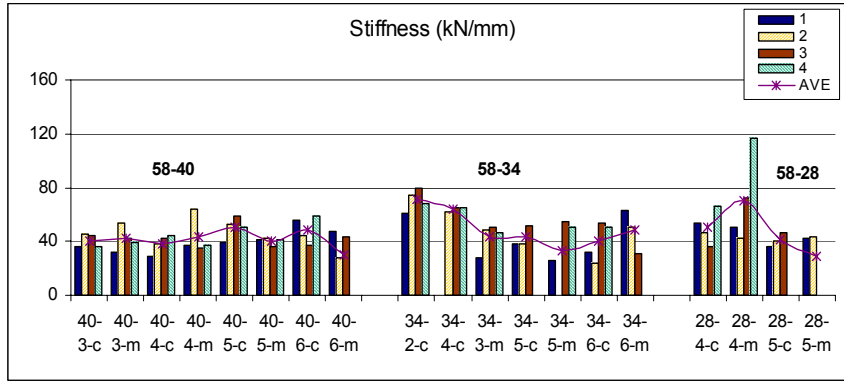
Figure 3.1.9. **Stiffness at -30°C**
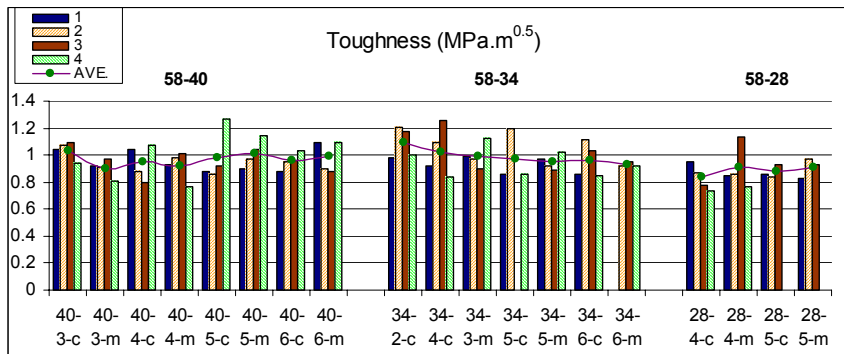
Figure 3.1.10. Fracture Toughness at -30°C
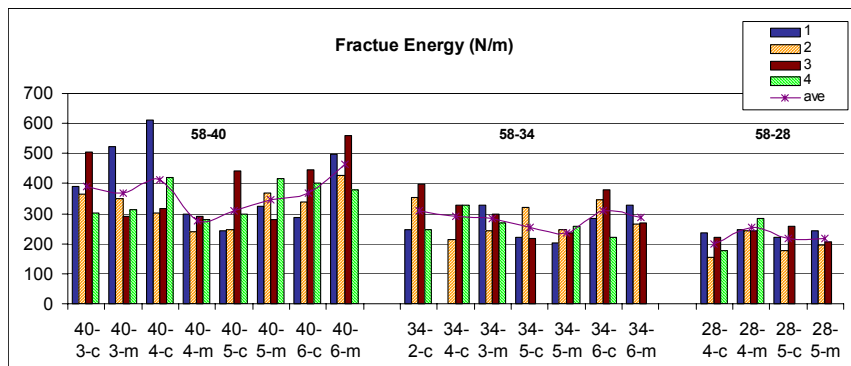
Figure 3.1.11. Fracture Energy at -30°C

150
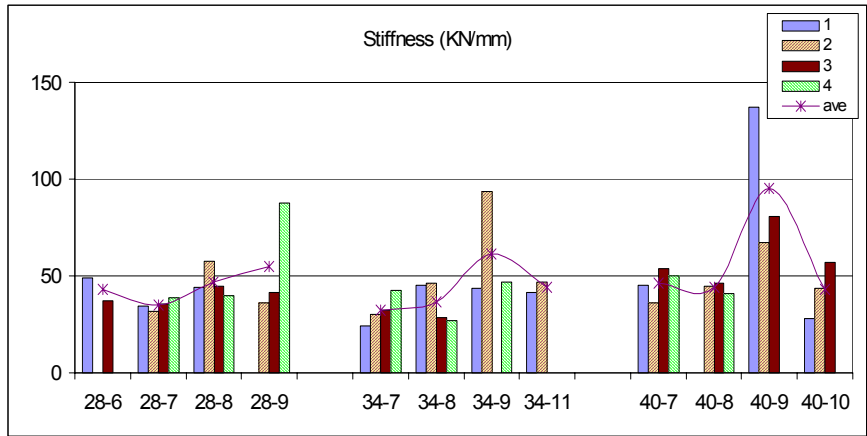
Figure 3.1.12. Stiffness at -40°C
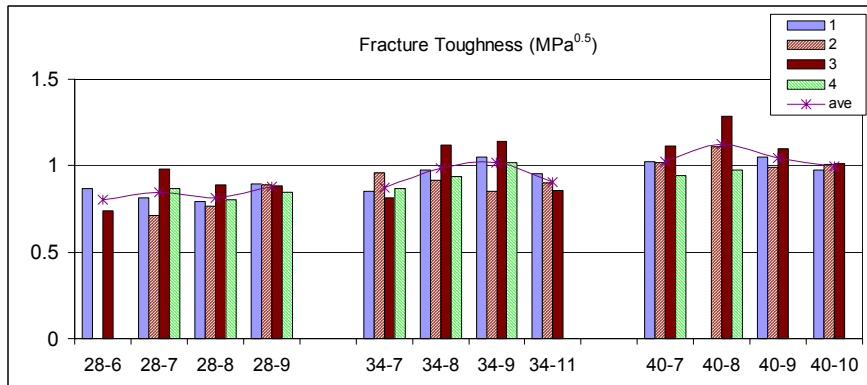
Figure 3.1.13. Fracture Toughness at -40°C
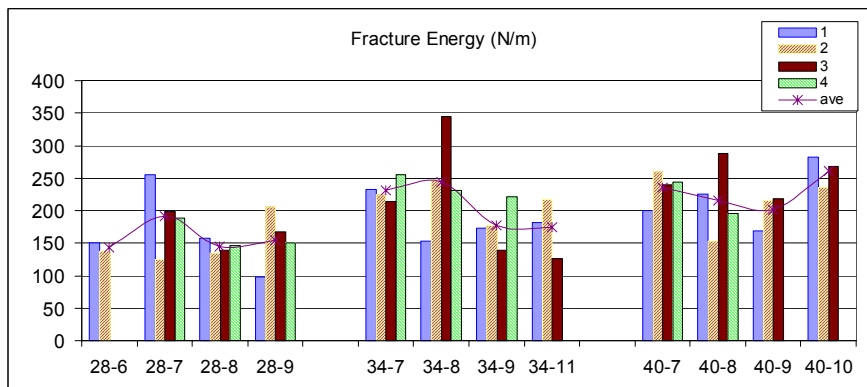
Figure 3.1.14. Fracture Energy at -40°C

151
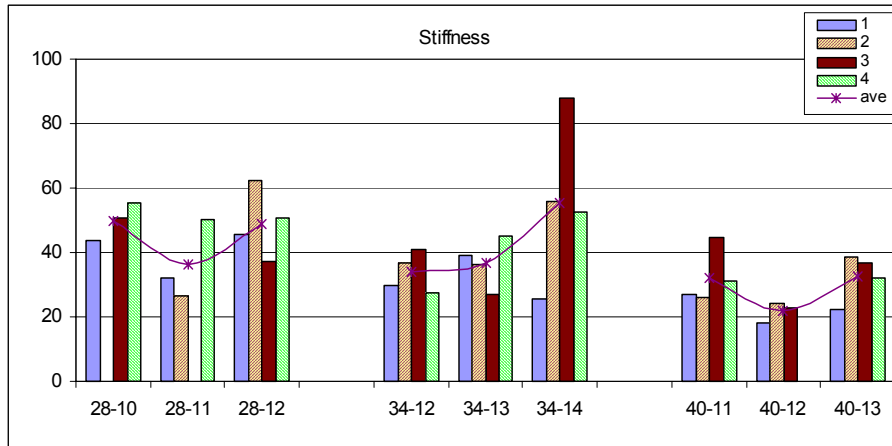
Figure 3.1.15. Stiffness at -20°C
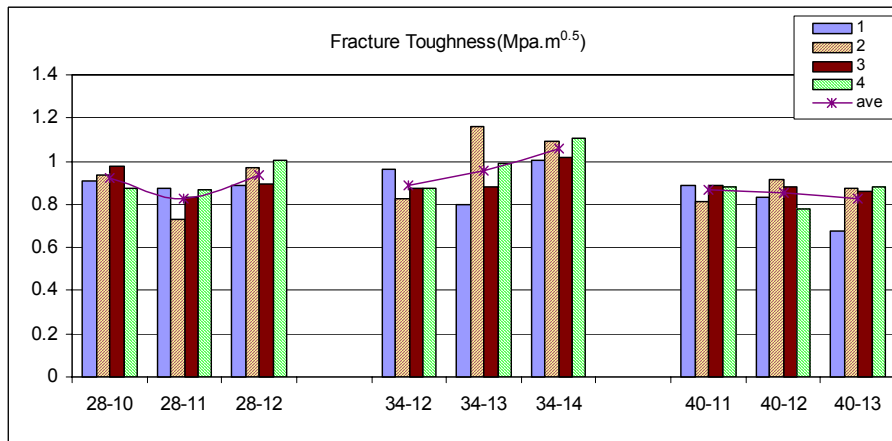
Figure 3.1.16. Fracture Toughness at -20°C
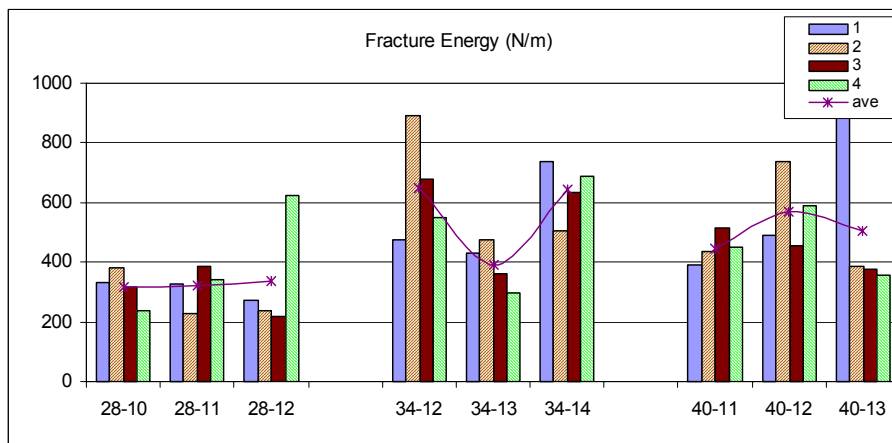
Figure 3.1.17. Fracture Energy at -20°C

152
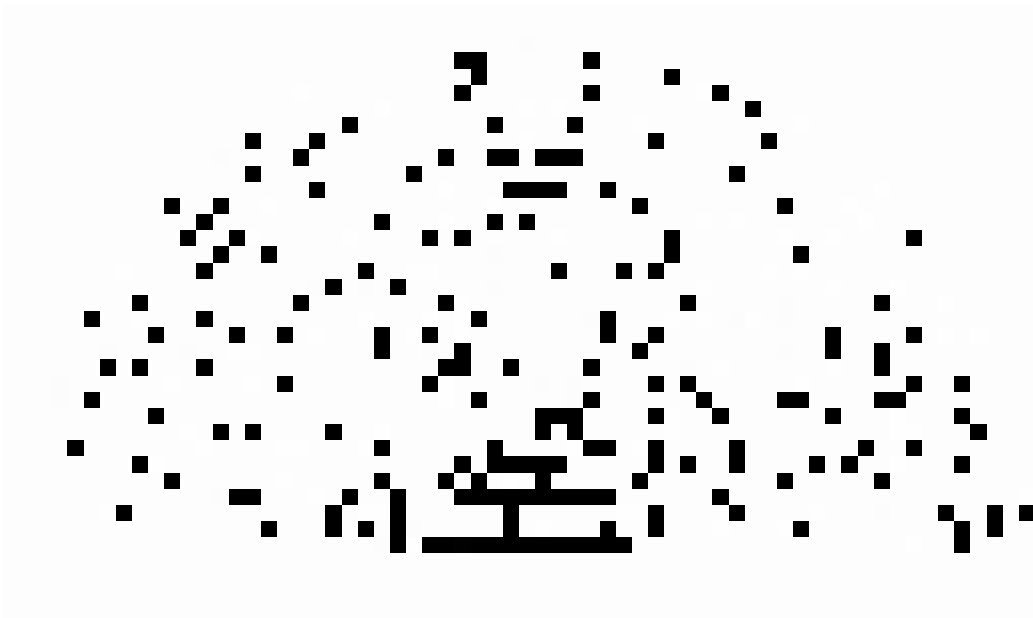
Figure 3.1.18 Finite Element Mesh in FRANC2D

PART 3. DATA ANALYSIS
Chapter 3.2. Reviewing of Crack Propagation Models

There are generally two types of crack propagation: fatigue based crack propagation and crack propagation under monotonic loading. These two types of crack propagation are quite different in terms of the fundamental theories and the experiments employed to analyze them. In order to differentiate between the two types, in this review the former is called "crack propagation", the latter is called "crack growth."

In the asphalt materials characterization area there are several empirical crack propagation models, which were reviewed in chapter 1.1. In this subtask only fracture mechanics-based models are reviewed.

CRACK PROPAGATION

Crack propagation is usually described by Paris law (26):

$$\frac{da}{dN} = A(\Delta k)^n \tag{13}$$

where

      a : the crack length

      N : the number of cycles

      k : the stress intensity factor

      A, n : regression parameters

In this expression the rate of crack growth is determined from the amplitude of stress intensity factor at each cycle. Paris law has been applied to the study of crack propagation in rocks and concrete although it is based on fatigue test data obtained for metals.

The Thermal Cracking (TC) model, incorporated in the recently released AASHTO Design Guide was originally developed as part of the SHRP A-005 contract by Hiltunen and Roque (24). It was later modified and refined in NCHRP 9-19 as part of the development of the Design Guide research effort. The TC model is composed of three parts:

1. Calculation of thermal stress
2. Calculation of crack propagation
3. Calculation of crack amount

Calculation Of Thermal Stress

Thermal Loading

The stress is calculated by first computing the thermal load through the linear coefficient of thermal contraction. The study by Jones et al. (45) showed that

$$B_{mix} = \frac{VMA * B_{AC} + V_{agg} * B_{agg}}{3V_{total}} \tag{14}$$

where

B_{mix} : linear coefficient of thermal contraction of the asphalt mixture (m/m/°C)

B_{AC} : volumetric coefficient of thermal contraction of the asphalt cement in the solid state (m/m/°C)

B_{agg} : volumetric coefficient of thermal contraction of the aggregate (m/m/°C)

VMA : percent volume of voids in the mineral aggregate

V_{agg} : percent volume of aggregate in the mixture

V_{total} : 100 percent

The measurement of the coefficient of thermal contraction of asphalt cement and aggregates are not part of routine mixture design. A constant value of 3.45×10^{-4} m/m/°C was assumed for all asphalt cement. For the coefficient of thermal contraction of the aggregates, the values published elsewhere were used. B_{mix} can then be determined from the VMA and V_{agg} determined as part of the mixture design. The thermal strain is simply calculated as

$$\varepsilon = B_{mix} \cdot \Delta T \tag{15}$$

where

ε : thermal strain

ΔT : temperature change

Creep Compliance

The relaxation modulus is computed indirectly by converting the creep compliance measured from the Indirect Tension test (IDT).

The 1000-second creep test is performed according to the IDT procedure at different temperatures in lab. Assuming the mixture is a thermorheologyically simple material, master curves of the creep compliance can be obtained by shifting the individual temperature curves to extend the reference temperature curve to higher and lower loading times. The reduced times are simply calculated as

$$\xi = \frac{t}{a_T} \tag{16}$$

where

ξ : reduced time

t : real time

a_T : shift factor

Two functions are fitted to the master curve. The first one is a 4-parameter Prony series described by the following expression:

$$D(\xi) = D(\infty) - \sum_{i=1}^{N} D_i e^{-\varsigma/\tau_i} + \frac{\xi}{\eta_\upsilon} \tag{17}$$

or

$$D(\xi) = D(0) - \sum_{i=1}^{N} D_i (1 - e^{-\varsigma/\tau_i}) + \frac{\xi}{\eta_\upsilon} \tag{18}$$

where

$$D(\infty) = D(0) + \sum_{i=1}^{N} D_i$$

$D(\xi)$: creep compliance at reduced time ξ

ξ : reduced time

$D(\infty), D(0), D_i, \tau_i, \eta_\upsilon$: Prony series parameters

The Prony series can be integrated in the convolution integral that relates the creep compliance and the relaxation modulus and the relaxation modulus can therefore be determined.

The second function to be fitted is a power function of the form

156

$$D(\xi) = D_0 + D_1 \xi^m \qquad (19)$$

where D_0, D_1, and m are coefficients for this power model, which are not related to the coefficients in the Prony series. The purpose of this step is to obtain the parameter m, which is an important parameter in the crack propagation model.

Relaxation Modulus

For a viscoelastic material, the creep compliance and the relaxation modulus are related by the convolution integral:

$$\int_0^\infty D(t-\tau) \frac{dE(\tau)}{d\tau} d\tau = 1 \qquad (20)$$

A computer program was developed to determine the relaxation modulus from the creep compliance expressed in the form of Prony series. Laplace transformation is used and the resulting relaxation modulus is calculated as

$$E(\xi) = \sum_{i=1}^{N+1} E_i e^{-\xi/\lambda_i} \qquad (21)$$

where

$\quad E(\xi)$: relaxation modulus at reduced time ξ

$\quad E_i, \lambda_i$: parameters for the master curve of relaxation modulus

Thermal Stress

The stress in a viscoelastic material can be computed with the one-dimensional hereditary integral that calculates the stress given a known strain history:

$$\sigma(\xi) = \int_0^\xi E(\xi-\xi') \frac{d\varepsilon}{d\xi'} d\xi' \qquad (22)$$

where

$\quad \sigma(\xi)$: stress at reduced time

$\quad E(\xi-\xi')$: relaxation modulus at reduced time

$\quad \varepsilon$: strain at reduced time

By changing the variables, this equation can be written in terms of real time, t, as

$$\sigma(t) = \int_0^t E(\xi(t) - \xi'(t)) \frac{d\varepsilon}{d't} d't \qquad (23)$$

The finite difference solution of this equation was developed by Soules et al. (92) with $E(\xi)$ represented by Prony series

$$\sigma(t) = \sum_{i=1}^{N+1} \sigma_i(t) \qquad (24)$$

where

$$\sigma_i(t) = e^{-\Delta\xi/\lambda_i} \sigma_i(t - \Delta t) + \Delta\varepsilon \cdot E_i \frac{\lambda_i}{\Delta\xi} (1 - e^{-\Delta\xi/\lambda_i})$$

$\Delta\varepsilon$ and $\Delta\xi$ are the changes in strain and reduced time over the time interval Δt.

The temperature gradient present in the asphalt layer was considered by dividing the total asphalt thickness into several sub-layers and assuming a constant temperature within each sub-layer.

Calculation Of Crack Propagation

Stress Intensity Factor

The stress intensity factor is calculated with a two-dimensional finite element program, CRACKTIP, developed by Chang et al. (27) at the Texas Transportation Institute. The thermal crack was modeled as a single vertical crack in the asphalt concrete layer in the program. However, the finite element computation is usually time-consuming and is not practical for pavement design purposes. As a consequence CRACKTIP was run for a broad range of conditions and the results were used to develop a simple regression equation that was easily incorporated in the design calculations:

$$K = \sigma(0.45 + 1.99 C_0^{0.56}) \qquad (25)$$

where

        K : stress intensity factor

        σ : far-field stress

        C_0 : current crack length

Crack Propagation Model

Paris law is used at this step to predict the crack length under thermal loading cycles:

$$\Delta C = A(\Delta k)^n \tag{26}$$

This equation is slightly different from its original form. In this model the change of temperature during one day is taken as one loading cycle, and the change of the crack length is computed and accumulated on a daily basis to determine the total crack length as a function of time. Thus the ΔN in the original form turns out to always be 1 and is ignored in equation (14).

In the propagation model the asphalt layer is divided into four sub-layers. The model is restricted so that no mater how large the thermal stress is the crack can only grow within one sub-layer in one thermal cycle. Even when there is an extreme low temperature in one day, the crack can only propagate to the bottom of one sub-layer, and cannot grow from one sub-layer to another. Therefore, four extreme cold days are needed to crack the asphalt layer all from top to bottom.

In Paris law A and n parameters are determined from fatigue tests that are very time-consuming. Schapery (93) showed that in nonlinear viscoelastic materials the fracture parameters A and n are theoretically related to other material properties:

- The slope of the linear portion of the log compliance-log time master curve determined from creep test (m)
- The undamaged strength of the material
- The fracture energy density of the material determined experimentally by monitoring the energy release through crack propagation

The m-value was obtained from the creep compliance. The average tensile strength at -10°C was selected to represent the undamaged tensile strength of the asphalt mixture at all temperatures. Based on the authors' experiments, the peak strength always occurred at temperatures lower than -10°C. Thus the strength at -10°C was selected as a conservative estimate of the undamaged tensile strength of the mixture.

The fracture energy density is hard to measure. However, work by Molenaar (30) showed that A can be empirically calculated as

$$\log A = 4.389 - 2.52 \cdot \log(E \cdot \sigma_m \cdot n) \tag{27}$$

where

E : modulus

σ_m : tensile strength

The experiments conducted by Lytton et al. (31) led to other relationships:

$$\log A = -\frac{n + 0.69}{0.511} \tag{28}$$

and

$$n = 0.8 \cdot (1 + \frac{1}{m}) \tag{29}$$

In TC model Lytton's equation to calculate n is employed. Parameter A is calculated with Molenaar's equation in which the material modulus E was replaced by a calibration coefficient k:

$$\log A = 4.389 - 2.52 \cdot \log(k \cdot \sigma_m \cdot n) \tag{30}$$

where

       k : coefficient from field calibration (10,000)

Thus, the two fracture parameters, A and n, can be computed from the master curve of IDT creep compliance and the IDT tensile strength determined at -10°C.

Calculation Of Crack Amount

An empirical equation based on field observations was developed to predict the amount of thermal cracking amount as follows

$$AC = \beta \cdot P(\log C > \log D) \tag{31}$$

where

       AC : observed amount of thermal cracking

       β : regression coefficient determined through field calibration

       $P(\ )$: probability that the condition in the parenthesis is true

       D : thickness of surface layer

The field calibration showed that β is equal to 353.5.

The authors of TC model pointed out that this model does not predict more than 50% of the total possible amount of cracking that can develop in the pavement. The minimum

crack spacing predicted by this model is 15ft per crack. Please note that the model assumes that a crack is counted only when it reaches the bottom of the asphalt layer.

Observations

The TC model is based on a slightly modified version of the Paris' law which is more suitable for the description of fatigue dominant cracking in asphalt pavement. However, in the case of thermal cracking, the role of single event thermal cracking or thermal cracking after several thermal cycles is very significant. It appears that the study of crack propagation under a quasi static monotonic load may be more representative of the thermal cracking mechanisms than a large number of loading cycles. The fictitious crack model (FCM) developed by Hillerborg in 1976 (33), also called cohesive crack model, is one of the major crack models used in the study of fracture in concrete. This model has the advantage of numerical implementation to simulate the crack propagation under quasi static load.

Crack Growth

The fictitious crack model (FCM) proposed by Hillerborg et al. assumes that a process zone exists ahead of the physical crack tip and that all damage, i.e. micro-cracking, is localized in this zone. The material in this zone is not physically completely open in the macroscopic sense, and the material ability to transfer stresses between the two sides of the zone is reduced. The stress within this process zone is not the uniformed yield strength of the material, as assumed in Dugdale (94) and Barenblatt (95) strip yield model, but depends on the distance from the crack tip. The longer the distance, the larger the stress is, up to the tensile strength of the material. This is shown in figure 3.2.1.

The FCM is based on the study of concrete behavior around the crack tip. Hillerborg et al. argued that the microcrack is the dominant state in the process zone in concrete, and that fracture in concrete is the process in which microcracks emerge to several visible macrocracks. The area near the physical crack tip contains more microcracks than the area further away, which therefore is less capable of transferring stresses between the two parts separated by the crack.

The concept of the FCM is clearly defined in a uniaxial tension test performed on a plain concrete beam (96). As shown in figure 3.2.2, the area under the σ-w curve is defined

as the fracture energy G_F consumed to create the unit crack surface; w is the additional deformation due to the formation of a process zone. Thus G_F is a pure material property. The σ-w curve, which describes the relationship between the stress in the process zone and the clearance between the two surfaces of the crack, represents the constitutive equation for the process zone. G_F can be measured under other loading configurations. In the RILEM method (89), G_F is calculated for a three-point bending beam configuration.
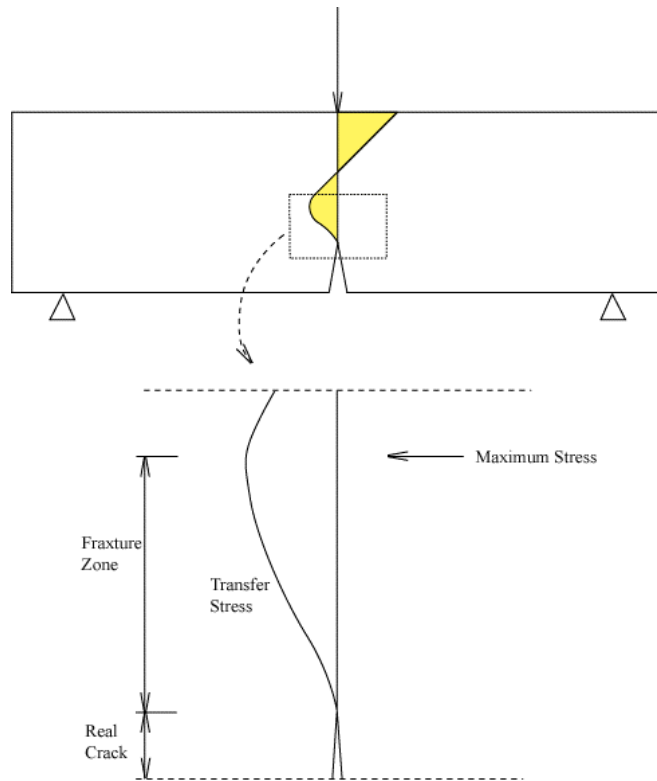
Figure 3.2.1. A Loaded Concrete Beam with a Crack and Process Zone

The FCM is very convenient to use in FEM analysis. In fracture problems the stress intensity factor is one of the most important parameters to be calculated. However, theoretically the stress approaches infinity at the crack tip. In order to catch the singularity at the crack tip, two methods are usually used. One is to use a very fine mesh around the crack tip. The other is to use a singular element at the crack tip. In the FCM the largest stress within the structure is the tensile strength and no singularity exists in the vicinity of a crack tip. This means the fracture problem can be computed with a rather coarse mesh.

The FCM has been applied to the study of rocks and concrete to simulate the crack growth and explain fracture phenomenon. This model was also introduced to asphalt materials. Shen and Kirkner (97) used the FCM to study the interaction between multiple cracks and predict the crack spacing. They assumed there is a set of fictitious cracks on the pavement. When temperature drops, some fictitious cracks become predominant to the others and turn out to be major cracks. A set of nonlinear equations were obtained by considering the pavement in 1D condition. The solutions of these equations provided the crack spacing in a pavement.

Jenq and Perng (35) applied the FCM to simulate the crack growth in a single notched bending beam. They obtained the load-displacement curve with FEM by assuming a bilinear constitutive equation in the process zone. Then, the load-displacement curve from the numerical simulation was calibrated with their experimental data. The parameters in the bilinear constitutive equation were also calibrated. They used the peak loads obtained with the calibrated bilinear constitutive equation to compute the critical stress intensity factors. They concluded that FCM could be employed to simulate the crack development in asphalt concrete and that FCM was a promising tool in the study of crack growth in asphalt pavement.

This type of application of the FCM has been widely used in concrete studies. Only two of the earlier references about the numerical application of the FCM are referred here: Hillerborg et al. (33) and Petersson (90). One of the advantages of the FCM is that by loading the structure step by step numerically, the initiation and development of the nonlinear part in the ascending part of the load-displacement curve, which represents the softening of material due to microcracking, can be studied.

Usually an assumption of the constitutive equation in the process zone is made before the simulation. Once the simulation is finished the load-displacement curve can be calibrated with the experimental data, and so is the constitutive equation. A FEM computer program is also needed. In the crack growing process, the stress at the crack tip nodes, σ, depends on the distance between these two nodes, w. On the other hand, w is constrained by σ through the constitutive equation. In this sense the system is nonlinear and iterations are needed.
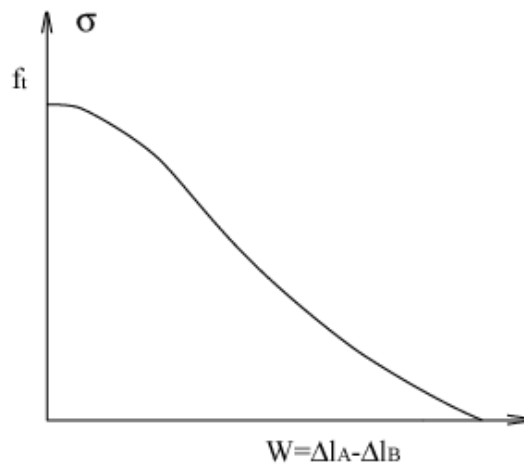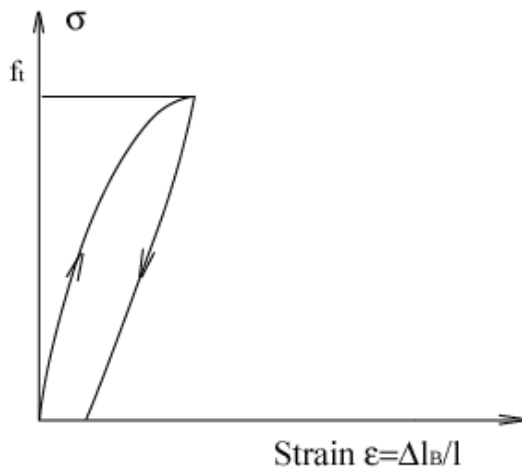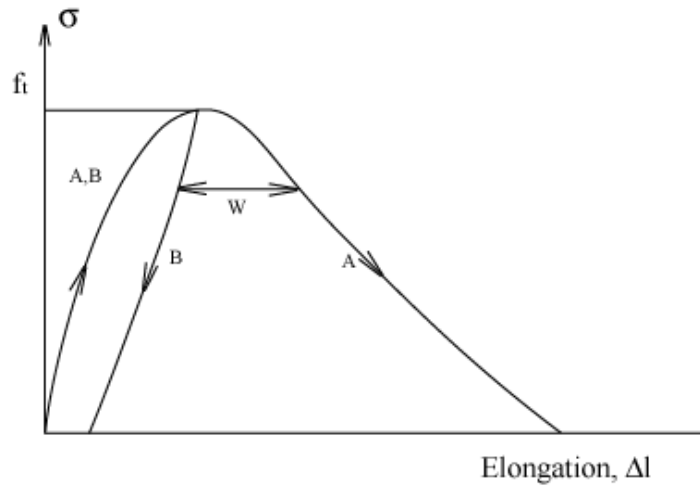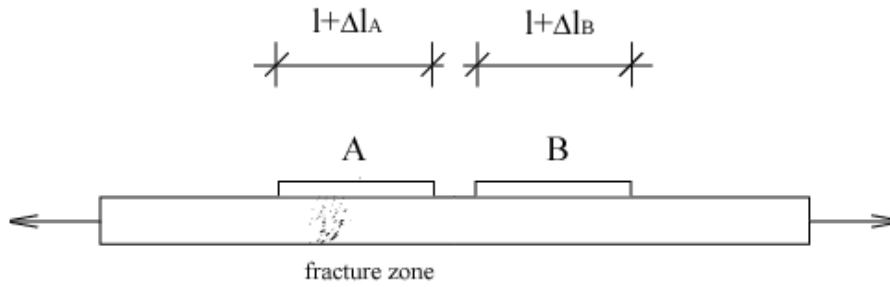
Figure 3.2.2. Fictitious Crack Model Developed by Hillerborg

PART 3. DATA ANALYSIS

Chapter 3.3. Model Testing

The recently released Design Guide incorporates a number of models that address the different distresses that occur in asphalt pavements. The model used for low temperature cracking is the TC model that was reviewed in chapter 3.2. The model is based on a modified Paris law approach that is more appropriate for thermal fatigue type of cracking. Based on an empirical statistical analysis the model uses the crack propagation evolution to predict the number of cracks and the crack spacing that can develop during the life of a given pavement.

In chapter 1.2 a simple model was developed based on the asphalt mixture tensile strength and the balance between temperature shrinkage and the friction at the interface between the asphalt layer and the aggregate base. The model requires both asphalt mixture properties and aggregate properties and, similar to the TC model, predicts the crack spacing for a given pavement configuration. However, unlike the TC model, it does not consider any crack evolution; cracks form instantaneously when the thermal stress that develops in the asphalt layer, which is influenced by the restraint provided by the aggregate base, exceeds the asphalt mixture strength.

In this chapter the TC model and the frictional restraint model were tested against field data from Mn/ROAD cells for which crack spacing information was available. Since the interface model uses the cohesion and friction angle of the aggregate base layer, which are not routinely determined in the pavement design process, the number of cells that could be used in this analysis was reduced to those cells for which the aggregate base properties were known. As indicated in chapter 2.3, only class 5 and class 6 aggregate base cohesion and friction angles were available. As a consequence, the only cells that were used to test the two models were cells 18 and 22, with class 6 aggregate base, and cell 21, with class 5 aggregate base.

Description of Cell 18, 21, and 22

       The pavement structures of the three cells are shown in figure 3.3.1. All three cells have a 7.9-in thick asphalt layer. Since these cells were built before Superpave mix design was adopted, traditional binder grades were used: AC 20 for cell 18 and cell 21 and pen 120/150 for cell 22. The mix design was the same for all three. Table 3.3.1 lists the asphalt mixture properties used in this chapter. Additional information is available in reference (44).

       The resilient modulus (E) was measured according to ASTM D4123 at a frequency of 1 Hz. and 0.1 second load duration at -18ºC. Two values of tensile strength, at two different loading rates, were determined for each mixture using specimens with dimensions of 100-mm (4 in.) in diameter and 60-mm (2.5 in.) in height.
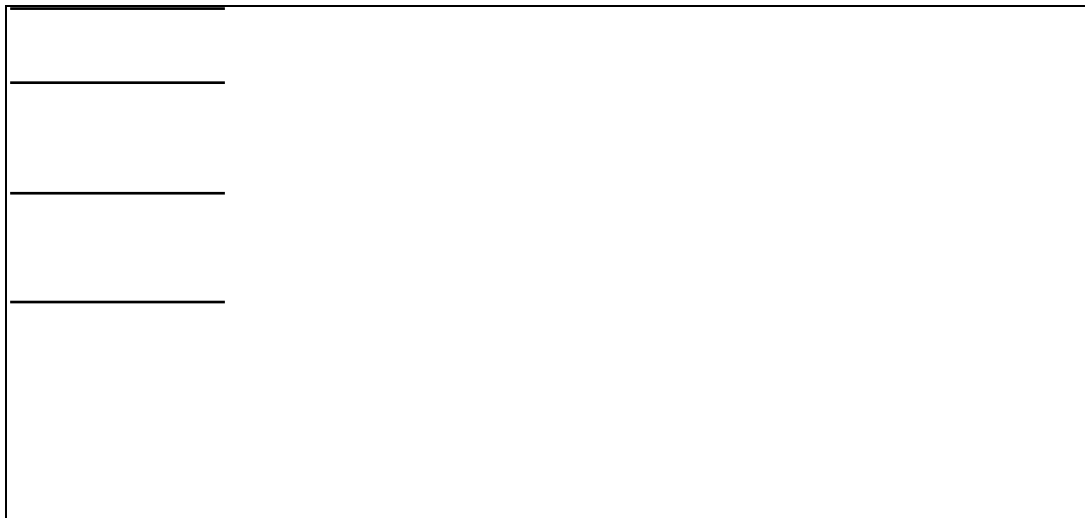
Figure 3.3.1. Pavement Structure of Cell 18, 21 and 22.

       The thermal coefficient of expansion/contraction of the asphalt mixture was calculated using the equation developed by Jones et al. (45) and given in chapter 3.2. With respect to the bulk specific gravity of the asphalt mixture, the asphalt layer was divided into four sublayers. The bulk specific gravity was measured for each sublayer and the average bulk specific gravity of the four sublayers is listed in table 3.3.1.

Crack Spacing Data

Transverse cracking is surveyed annually at Mn/ROAD and stored in a data base. The data collected for cells 18, 21, and 22 in 2003 is shown in table 3.3.2. The mean values shown at the bottom of the table 3.3.were used in the analysis.

Table 3.3.1. Asphalt Mixture Properties

Cell ID	18	21	22
Thickness (in.)	7.9	7.9	7.9
Binder	AC 20	120/150 Pen	120/150 Pen
Marshall Design	50	50	75
E @ -18°C (GPa)	16.76	16.24	17.59
σ_t @ -18°C and 0.25 in/min (kPa)	2,250	2,400	2,390
σ_t @ -18°C and 0.025 in/min (kPa)	2,270	2,230	1,810
Bulk Spec. Gravity	2.289	2.303	2.287
Thermal Coef. (α) (1.0E-5m/m/°C)	1.862	1.862	1.800

Crack Spacing - TC Model

The Design Guide software, which incorporates the TC model, was used to predict the crack spacing for the three Mn/ROAD cells. The software provides three levels of design that require different information. Level 1 requires the most detailed information about the asphalt mixture, base and subgrade materials used. Level 3 is mostly based on default values and requires much less information. Due to the limited information available for the materials used in the three cells the level 3 design was used in the analysis.

Table 3.3.2. Crack Spacing for Mn/ROAD Cells 18, 21 and 22 (February 2003).

Cell:	18		21		22	
Lane:	Driving	Passing	Driving	Passing	Driving	Passing
Crack Number						
1	0	0	0	0	0	0
2	20	20	22	40	36	36
3	19	19	22	58	29	12
4	23	22	54	26	46	17
5	10	25	18	24	20	15
6	6	22	8	17	21	31
7	8	21	23	25	27	41
8	16	35	24	16	20	27
9	8	21	5	10	24	20
10	20	17	12	12	7	24
11	30	34	14	126	38	17
12	5	22	26	100	30	28
13	18	22	10		3	28
14	19	28	9		11	18
15	18	14	8		15	36
16	16	15	13		19	48
17	16	15	24		2	54
18	6	21	8		25	23
19	22	9	5		25	
20	10	3	5		12	
21	18	17	44		37	
22	21	28	26		29	
23	8	23	17			
24	15	9	31			
25	21	13	21			
26	5		36			
27	4					
28	19					
29	29					
30	26					
31	19					
Mean	15.8	19.3	19.1	25.3*	22.2	27.0
STD.	7.35	7.89	12.51	15.22*	11.49	12.28

*The mean and standard deviation reported for cell 21 passing lane do not include the two outlier values shadowed in the table.

The results are summarized in table 3.3.3 and indicate that the TC model predicts no thermal cracking occurrence within the 10-year life of these three cells.

Table 3.3.3. Estimated Crack Spacing using the TC Model.

Cell ID	Crack Spacing
18	∞
21	∞
22	∞

Crack Spacing - Friction Model

The friction model developed in chapter 1.2 predicts a crack spacing equal to $1.5X_c$ with X_c computed as

$$X_c = \frac{E\alpha\Delta T}{\dfrac{C}{h} + \rho g \tan\Phi} \tag{1}$$

where

    X_c: longitudinal distance from free edge to point at which maximum tensile stress is achieved in the asphalt layer

    E: asphalt mixture Young's modulus

    α: asphalt mixture linear coefficient of thermal contraction

    ΔT: temperature change

    C: cohesion

    h: thickness of pavement

    ρ: density of asphalt mixture

    g: gravity

    Φ: friction angle

Because the model assumes instant crack formation when the thermal stress equals the mixture tensile strength, the numerator in the above equation can be replaced by the tensile strength σ_t

$$X_c = \frac{\sigma_t}{\dfrac{C}{h} + \rho g \tan \Phi}$$

(2)

Table 3.3.4 summarizes the input parameters values and the crack spacing values obtained from the X_c values calculated with equation 2.

Table 3.3.4. Estimated Crack Spacing using the Frictional Restraint Model.

Cell ID	18	21	22
Base Type	CL6	CL5	CL6
Cohesion, psi	9.0	11.2	9.0
tanΦ	1.299	0.787	1.299
Mixture Density, g/cm³	2.289	2.303	2.287
Thickness, in	7.9	7.9	7.9
Binder Grade	AC 20	Pen 120/150	Pen 120/150
σ_t at -18°C and 0.25-mm/min, kPa	2,270	2,400	2,390
X_c, ft	21.9	19.5	23.1
Estimated. Spacing =1.5 X_c, ft	32.9	29.3	34.7

Summary and Discussion

The estimated crack spacing and the average field measurements on crack spacing are summarized in table 3.3.5. It is obvious that the TC model that predicted no cracking did not match the field data. This can be explained by the fact that the TC model does not allow complete crack propagation even under the most severe temperature drop; a crack can propagate only through one sublayer at one time and therefore it takes at least 4 severe events to form one complete crack that is counted by the model. According to the records most of the thermal cracks in cells 18, 21 and 22 occurred during one extremely cold winter (1995-1996) after what appears to be a single extreme event during which the temperature dropped to -39°C. Unfortunately the records do not contain the exact time of the crack occurrence because the data was collected a few weeks after the -39°C night.

The crack spacing predicted using the frictional restraint model and the measured values are also plotted in figures 3.3.2 and 3.3.3. Figure 3.3.2 shows a similar trend in all three cells: the predicted value is higher than the measured value in the passing lane, which is larger than the measured value on the driving lane. The higher deterioration in the driving lane compared to the passing lane seems to indicate that traffic has a negative effect on the crack spacing. Figure 3.3.2 also indicates that the binder type has an effect: cell 18, which was built with AC20 binder has lower crack spacing than the two cells built with Pen 120/1450 binder.

Table 3.3.5. Summary of Crack Spacing [ft].

Cell ID		Measured	Frictional Restraint Model	TC Model
18	Driving lane	15.8	32.9	∞
	Passing lane	19.3		
21	Driving lane	19.1	29.3	∞
	Passing lane	25.3		
22	Driving lane	22.2	34.7	∞
	Passing lane	27.0		
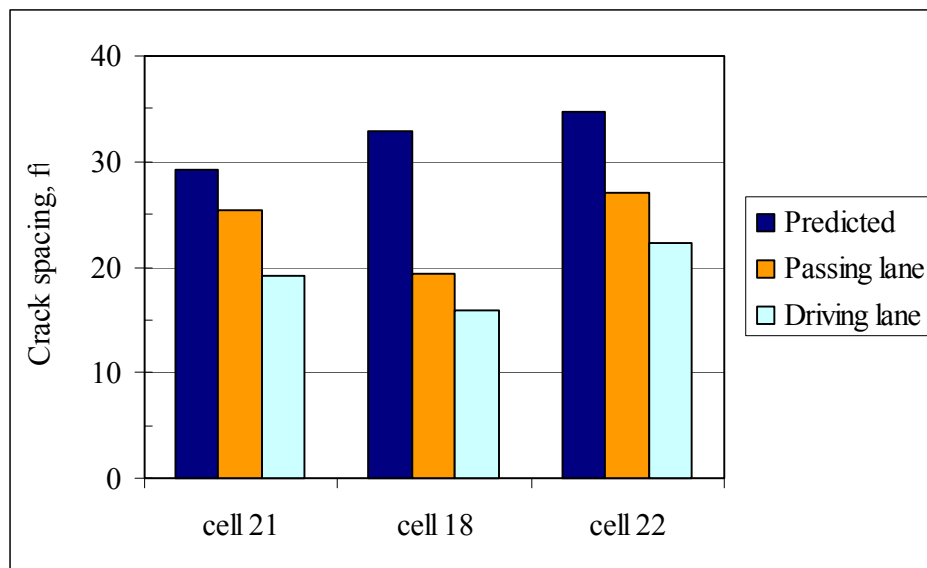
Figure 3.3.2. Predicted and measured crack spacing values for cells 18, 21 and 22.

Figure 3.3.3 indicates that there is no clear correlation between the predicted values and the measured values. However, this result is based on only three cases and indicates the need to expand this analysis with additional cells as more data becomes available in the future.
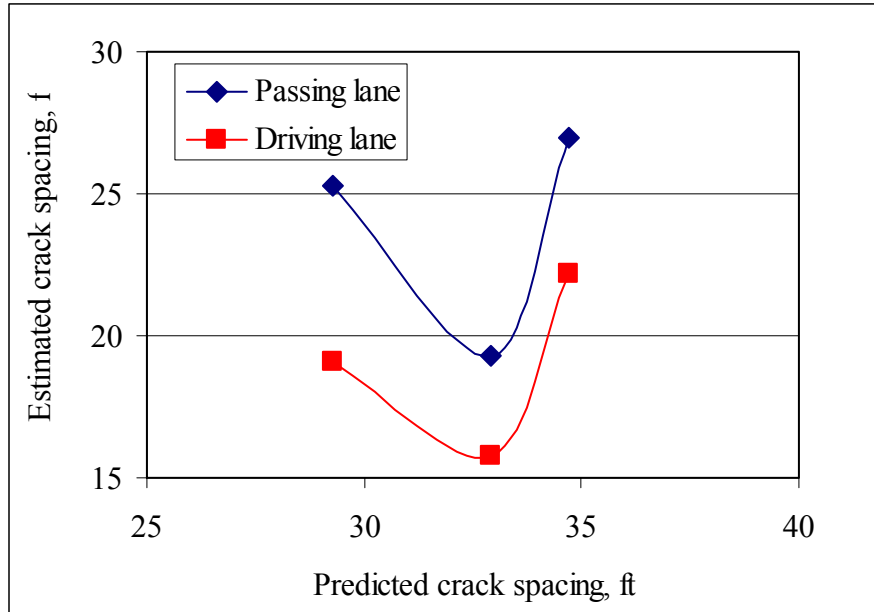
Figure 3.3.3. Predicted versus measured crack spacing for cells 18, 21, and 22.

Table 3.3.6. Comparison of measured and predicted crack spacing values.

			Cell 21	Cell 18	Cell 22
Prediction			29.3	32.9	34.7
Field Measurement	Passing Lane	Mean	25.3	19.3	27
	Driving Lane		19.1	15.8	22.2
	Passing Lane	Standard Deviation	15.22	7.89	12.28
	Driving Lane		12.51	7.35	11.49
	Passing Lane	# of Cracks	10	24	17
	Driving Lane		25	30	21
Hypothesis Test	Passing Lane	t Statistics	-0.83	-8.444	-2.59
	Driving Lane		-4.08	-12.74	-4.99
	Passing Lane	P-Value	0.214	9.19E-09	9.86E-03
	Driving Lane		2.15E-04	1.13E-13	3.56E-05

A simple statistical analysis was performed. The null hypothesis that the measured value is equal to the predicted value was tested against the alternative hypothesis that the measured value was less than the predicted value for both the passing and the driving lanes. The results are summarized in table 3.3.6 and indicate that in five of the six comparisons the measured values are less than the predicted values (small p-values). The only exception is cell 21 passing lane for which the predicted value is not statistically different than the measured value.

The difference between the predicted spacing and the measured crack spacing can be explained by the approximate material parameters values used in the model that can be very different than the material parameters in the field. In particular the values used for the aggregate materials were obtained at room temperature, while thermal cracking occurs at very low temperatures, when the aggregate base is in frozen condition. As discussed in Task 1 and chapter 2.3 a frozen aggregate base can have a very different cohesion and friction angle than at the room temperature. Cohesion values 1.5 to 2 times higher in the model would provide predicted values very close to the measured values, although it would not take care of the difference between the passing and the driving lanes.

A simple calculation was performed to determine if there is any merit in back-calculating the properties of the frozen aggregate by inversing the computation procedure for cohesion and friction angle described in chapter 2.3. Two pairs of cells were used to back-calculate the cohesion and friction angle of class 3 and class 6 aggregate base. The configurations of the two pairs are shown in figure 3.3.4 and the material properties used in the calculations are given in table 3.3.7.

Figure 3.3.4. Configuration of cells used in back-calculation.

The results of the back-calculation are shown at the bottom of table 3.3.7 and are not reasonable. This is not surprising taking into consideration the different crack spacing values measured in the field for configurations that are almost similar in terms of the parameters used in the frictional restrained model, see for example cells 17 and 19. This clearly indicates the importance of determining material parameters that are representative of the materials behavior at low temperatures in the field. Note that in chapter 1.3 a similar approach was taken to "tune" the model and obtain the cohesion and friction angle for each type of base. Table 3.3.7 reproduces the results reported in chapter 1.3 that indicate that the "fine-tuned" cohesion is less than the measured triaxial value. This is in contradiction to anecdotal evidence that the cohesion of frozen soils is much larger than the room temperature measured values.

Table 3.3.7. Back-Calculation of Soil Properties.

Base Type	Class 3		Class 6	
Cell ID	17	19	18	22
Mixture Density, g/cm^3	2.283	2.289	2.270	2.287
Thickness, in	7.9	7.9	7.8	7.9
Binder Grade	AC20	AC20	AC20	120/150 Pen
Tensile Strength, MPa	2.38	2.8	2.25	2.39
Field Crack Spacing, ft	23.9	15.8	10.9	22.2
Back-calculated C, MPa	9.96		-38.2	
Back-calculated tanΦ	-2203.5		8546.1	

Another alternative would be to use regression methods to correlate field observations to laboratory data. At this time the limited data available from the different Mn/ROAD cells in the crack spacing-model parameters space cluster together and do not cover a wider range of values required to obtain a meaningful regression expression. This indicates the need for additional field and laboratory information and for the further improvement of the frictional restraint model to include additional factors and to expand the analysis to 2D or 3D conditions.

Table 3.3.8. Results from chapter 1.3.

Base	Results from Task 1		Results from Triaxial Test	
	C (kPa)	Φ	C (kPa)	Φ
Class 5	10	25°	77.2	38.2°
Class 6	15	50°	62.1	52.4°

PART 3. DATA ANALYSIS

Chapter 3.4. Model Validation

Introduction

In chapter 3.2 the TC model and the frictional restraint model were discussed. The inherent fatigue character of the TC model makes this model less appropriate to simulate the low temperature cracking of asphalt pavements, which is mostly due to monotonic loading or few loading cycles of high amplitude with respect to the strength of the material. On the other hand, the frictional restraint crack spacing model is based on the classical continuum mechanics approach and can only address single event cracking in which the crack initiates and propagates instantaneously.

The fictitious crack model, or cohesive zone model, localizes the fracture process occurring in the whole body of material into a narrow area called cohesive crack, which is defined by two adjacent surfaces. This represents a reasonable simplification of the physical process in which many micro-cracks emerge into a macro-crack. Within this framework the accumulation of damage during loading and the behavior of the softening zone or process zone can be simulated numerically. Numerous references in the literature document the application of this model in the study of fracture in concrete, metals and rocks. The research published by Hillerborg et al. (33) and Petersson (90) are among the earliest applications of this model. In their work they proposed a pseudo boundary element method to implement this model numerically. Recently this method was implemented numerically using an interface element. In a finite element model the interface element is used to connect the normal solid elements. The stiffness matrix of interface element can be integrated into the tangent stiffness matrix of the normal solid elements which is very convenient in computation.

In the next paragraphs the interface element method is described in detail, which includes the constitutive behavior of the cohesive crack, the formulation of the interface element, and the performance testing of the numerical model. The model is then used to simulate the low temperature cracking in cells 33, 34, and 35 for which the fracture

properties of the asphalt mixtures were determined experimentally as described in chapter 3.3.

CONSTITUTIVE BEHAVIOR OF COHESIVE CRACK

The traction acting on the crack surfaces is derived through the energy potential ϕ in the form

$$T = \frac{\partial \phi}{\partial \delta} \tag{5}$$

where δ is the displacement jump, i.e. the separation across the crack surfaces. Since it is hard to measure the traction and separation experimentally, different mathematical formulations were developed for the energy potential. Two different formulations for the energy potential are presented in this chapter.

Polynomial Potential

The polynomial potential was proposed by Needleman in 1987 (98):

$$\phi = \frac{27}{4} T_0 \delta_0 [\frac{1}{2} (\frac{\delta^N}{\delta_0})^2 (1 - \frac{4}{3}(\frac{\delta^N}{\delta_0}) + \frac{1}{2}(\frac{\delta^N}{\delta_0})^2)$$
$$+ \frac{1}{2} \alpha (\frac{\delta^T}{\delta_0})^2 (1 - 2(\frac{\delta^T}{\delta_0}) + (\frac{\delta^T}{\delta_0})^2) \tag{6}$$
$$+ \frac{1}{2} \alpha (\frac{\delta^B}{\delta_0})^2 (1 - 2(\frac{\delta^B}{\delta_0}) + (\frac{\delta^B}{\delta_0})^2)]$$

where δ^N is normal separation, δ^T and δ^b are two shear separations in plane, δ_0 is a characteristic length, T_0 is the maximum traction transferred across the crack and α is the ratio of shear to normal stiffness of the interface. For $\delta^N \leq \delta_0$ the traction on the crack surface is derived as

$$T_N = -\frac{27}{4} T_0 \{ (\frac{\delta^N}{\delta_0})[1 - 2(\frac{\delta^N}{\delta_0}) + (\frac{\delta^N}{\delta_0})^2] + \alpha (\frac{\delta^T}{\delta_0})^2 [(\frac{\delta^N}{\delta_0}) - 1]$$
$$+ \alpha (\frac{\delta^B}{\delta_0})^2 [(\frac{\delta^B}{\delta_0}) - 1] \} \tag{7}$$

$$T^T = -\frac{27}{4} T_0 \{ \alpha (\frac{\delta^T}{\delta_0})^2 [1 - 2(\frac{\delta^N}{\delta_0}) + (\frac{\delta^N}{\delta_0})^2] \} \tag{8}$$

$$T^B = -\frac{27}{4}T_0\{\alpha(\frac{\delta^B}{\delta_0})^2[1-2(\frac{\delta^N}{\delta_0})+(\frac{\delta^N}{\delta_0})^2]\}$$ (9)

For $\delta^N > \delta_0$, $T^N \equiv T^T \equiv T^B \equiv 0$.

This model describes only normal separation and considers the existence of shear traction in two in-plane directions. In this chapter pure normal separation (Mode I fracture) is considered and the shear tractions are assumed nonexistent. Using the standard procedure to compute the J-integral leads to the following expression for the cohesive energy of the crack

$$\Gamma_0 = \int_0^\infty Td\delta$$ (10)

For the polynomial potential described above, the cohesive energy is

$$\Gamma_0 = \frac{9}{16}T_0\delta_0$$ (11)

Exponential Potential

There are several forms of exponential potential proposed (99, 100, 101). For computational convenience the following exponential form is employed:

$$\phi = exp(1)T_0\delta_c[1-(1+\frac{\delta}{\delta_c})exp(-\frac{\delta}{\delta_c})]$$ (12)

where $\delta = \sqrt{\beta^2(\delta^{T^2}+\delta^{B^2})+\delta^{N^2}}$, β is the weight assigned to the sliding and the opening displacement, and δ_c is the normal separation at $T^N = T_0$. All the other notations have the same meaning as in the polynomial potential. Since only pure mode I fracture is considered, the normal traction is given as

$$T^N = exp(1)T_0\frac{\delta^N}{\delta_c}exp(-\frac{\delta^N}{\delta_c})$$ (13)

and the corresponding cohesive energy is

$$\Gamma_0 = exp(1)T_0\delta_c$$ (14)

If the traction and the separation are normalized by the tensile strength and the characteristic separation, respectively, the exponential relationship can be plotted as shown in figure 3.4.1.
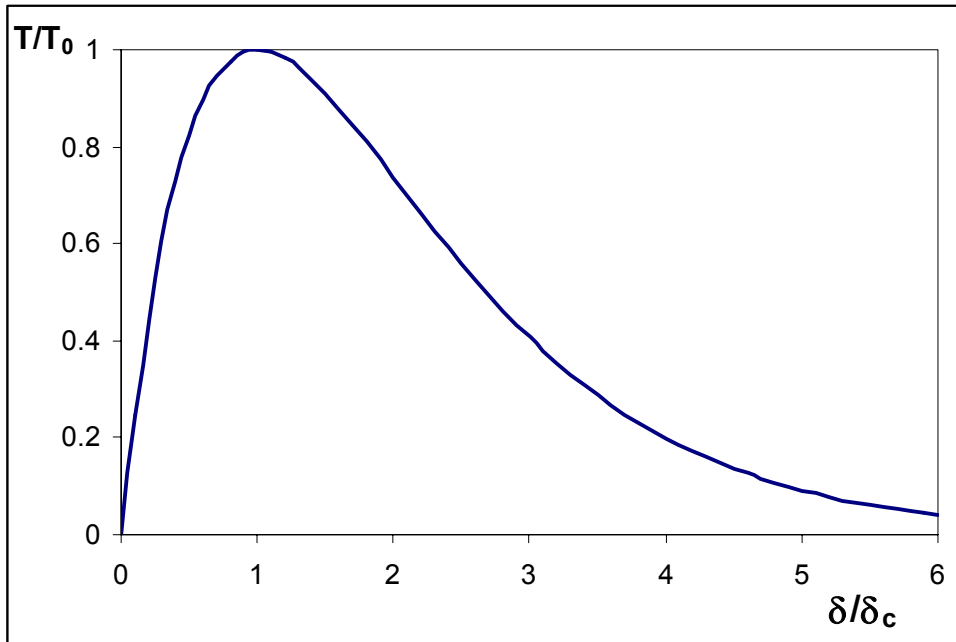
Figure 3.4.1. Exponential Traction Separation Relationship for the Cohesive Crack.

Other forms of potentials, which lead to a linear or bi-linear traction-separation relation, are also available in the literature. However, due to the inherent singularity of these types of potential, numerical difficulties may arise when the traction-separation relation is applied. In the analysis that follows the exponential potential is employed. The cohesive energy is assumed equal to the fracture energy measured in chapter 3.1 and T_0 is assumed equal to the IDT tensile strength of the mixture. The characteristic separation is calculated from equation (10) above.

Formulation of the Interface Element

The cohesive crack is usually implemented into finite element analysis through the interface element. There are two types of interface elements: lumped integrated interface element and continuous numerically integrated interface element. The difference between these two types of elements is that the former only uses relative displacements at the isolated nodes, while the latter uses interpolated relative displacement in integration points. In this research the continuous numerically integrated interface element is adopted. The formulation of this type of interface element is described below and is based on the work done by de Borst (102) and Paulino (103). Taking into consideration that for low temperature pavement

179

cracking plane strain is a reasonable approximation only the 2D situation is considered, which corresponds to a line interface element.

Consider the bulk material is connected by interface elements. If 4-node quadrilateral element is used to model the bulk material, the corresponding interface element is with two nodes at each side. If 8-node quadrilateral element is used, the corresponding interface element is with three nodes at each side. Only the formulation of the 4-node interface element, with two nodes at each side, is derived below. The formulation of 6-node interface element can be derived in a similar way.

Each node has two translation degrees of freedom and the corresponding nodal displacement vector for this 4-node interface element is defined as

$$V_{8\times1} = \{ v_n^1, v_n^2, v_n^3, v_n^4, v_t^1, v_t^2, v_t^3, v_t^4 \}^T \tag{15}$$

where n denotes the direction normal to the interface element and t denotes the direction tangential to the interface surface. The continuous displacement field vector is defined as

$$u = \{ u_n^-, u_n^+, u_t^-, u_t^+ \} \tag{16}$$

where the superscripts $+$ and $-$ denote the upper and lower side of the interface. This continuous displacement field can be constructed through the standard interpolation polynomials

$$u_{4\times1} = H_{4\times8} V_{8\times1} \tag{17}$$

Matrix H is composed of polynomial functions as

$$H = \begin{bmatrix} n & 0 & 0 & 0 \\ 0 & n & 0 & 0 \\ 0 & 0 & n & 0 \\ 0 & 0 & 0 & n \end{bmatrix} \tag{18}$$

where $n = \{ N_1, N_2 \}$ and

$$N_1 = \frac{1}{2}(1-\xi)$$
$$N_2 = \frac{1}{2}(1+\xi) \tag{19}$$

and ξ is the material coordinate. Figure 3.4.2 shows ξ reside in the tangent plane.
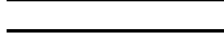
Figure 3.4.2. Interface Element

The relative displacement field Δ between the upper and lower surfaces can be obtained through operator matrix L

$$L = \begin{bmatrix} -1 & 1 & 0 & 0 \\ 0 & 0 & -1 & 1 \end{bmatrix} \tag{20}$$

and

$$\Delta = Lu \tag{21}$$

where $\Delta = \{\Delta_n, \Delta_t\}^T$. Combine equation (13) and (17), the relative displacement matrix in global coordinates can be written as

$$\Delta = Lu = LHV \tag{22}$$

Since the constitutive relation is based on the traction across the surface and the separation of surfaces, it is required to transform Δ from the global coordinates to a local coordinates defined for the interface element. Define matrix $R_{2\times2}$ to transform from the global system (X_1, X_2) to the local system (n, t), where n is the direction normal to the surface and t is in the surface.

Finally the relative displacement vector, $\bar{\Delta} = \{\bar{\Delta}_n, \bar{\Delta}_s\}^T$, is given as

$$\bar{\Delta} = RLHV = BV \tag{23}$$

where $B = RLH$ (24)

When a tangent modulus matrix, D, is used to describe the relation between the traction and separation

$$D = \begin{bmatrix} d_n & 0 \\ 0 & d_s \end{bmatrix} \tag{25}$$

the constitutive behavior can be written in the form of matrix

$$T = D \overline{\Delta} \tag{26}$$

The stiffness matrix K for the interface element can be obtained using the standard procedure of minimizing the total amount of potential energy. The amount of internal work done is

$$U = \frac{1}{2} \int_A \overline{\Delta}^T T dA \tag{27}$$

with equation (19) and (22)

$$U = \frac{1}{2} V^T \int_A B^T DB dA \, V \tag{28}$$

The external work is given as

$$W = -V^T f \tag{29}$$

where f is the external force. After variation with respect to the nodal displacement vector it is obtained

$$KV = f \tag{30}$$

where the stiffness matrix is

$$K = \int_A B^T DB dA \tag{31}$$

For the line interface element in 2D condition, the interpolation function N_i is only a function of ξ and equation (27) becomes

$$K = b \int_{\xi=-1}^{\xi=1} B^T DB \det J \cdot d\xi \tag{32}$$

where b is the width of the interface.

The calculation of the equivalent nodal forces, which is at the right hand side of the system of equations, results from the tractions on the surfaces of the interface element. The virtual work from traction is defined as

$$\delta \Pi_I = \int \delta \overline{\Delta}^T \cdot T dA \tag{33}$$

After invoking equation (19), it results in

$$\delta\Pi_I = \delta V^T \cdot \int B^T T dA \tag{34}$$

and the virtual work from the nodal force is

$$\delta\Pi_E = \delta V^T \cdot f \tag{35}$$

From the principle of virtual work

$$\delta\Pi_I = \delta\Pi_E \tag{36}$$

which leads to

$$f = \int B^T T dA \tag{37}$$

The corresponding form for numerical integration is

$$f = \int_{\xi=-1}^{\xi=1} B^T T \, det \, J \cdot d\xi \tag{38}$$

MODEL TESTING

The interface element is implemented through a user-defined subroutine, UINTER, in ABAQUS. The performance of this code is tested using the double cantilever beam (DCB) configuration. The configuration of DCB is shown in figure 3.4.3. The close form solutions for DCB provided by Mi and Crisfield (104) were used in this comparison. In a recent publication Paulino et al. (105) used the analytical solution for DCB described in reference (106). Two different relationships between the applied load P and the deflection Δ at the end of the DCB are considered.

Before crack initiates or damage starts to grow,

$$\Delta = \frac{2Pa_0^3}{3EI} \tag{39}$$

and during damage accumulates

$$\Delta = \frac{2}{3EIP^2}(BG_c EI)^{\frac{3}{2}} \tag{40}$$

where Δ : Separation of two arms of DCB

a_0 : Initial crack length

I : Inertial moment of each arm

B : Width of the beam

E :   Young's modulus
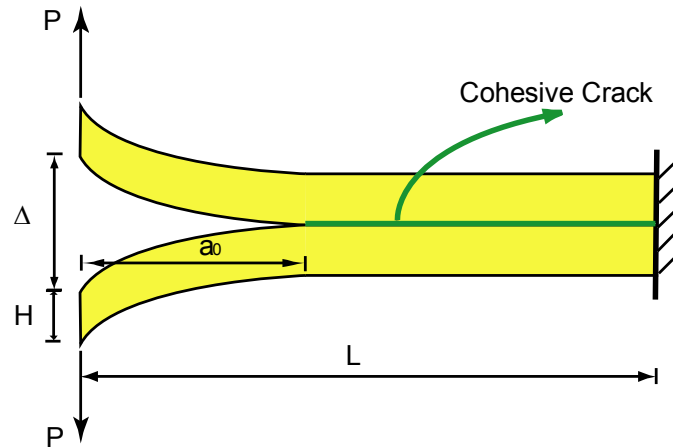
Figure 3.4.3. Double Cantilever Beam (DCB).

At the beginning of loading the separation Δ is small and the stress at crack tip is small and has very little effect on the crack. The prediction from equation (35) should be close to the real separation. When Δ becomes larger, it creates a large stress at the crack tip and its effect on the crack tip becomes significant. The crack starts to grow and damage begins to accumulate, and equation (36) provides a better prediction than equation (35). The transition from equation (35) to equation (36) should be smooth in experimental measurement unlike the intersection of the two curves predicted by equations (35) and (36), respectively. The experimental measurement must be close to the prediction from equation (35) at the beginning of the curve and then change gradually to the prediction from equation (36) when Δ increases.

A 2-D finite element mesh is build to model the DCB with the finite element software ABAQUS. The body of DCB is modeled with 4-node bilinear quadrilateral element, CPE4, with mesh density of 1mm/element. The crack is assumed to propagate in its own plane which means the location of cohesive crack is assumed to be the middle plane of the DCB with respect to its height. The behavior of this cohesive crack is defined by the user defined subroutine UINTER. The properties of this cohesive crack are listed in table 3.4.1 and the dimensions of the DCB are given in table 3.4.2.

A total of 200 4-node bilinear elements and one user defined interface were used in this finite element mesh, which is shown in figure 3.4.4. During the simulation an incremental-iterative approach was used for the nonlinear finite element analysis and

Newton's method available in ABAQUS was used to trace the load-separation curve of the DCB configuration with a displacement-control method.

Table 3.4.1. Material Properties

E	υ	T	G_f	Δ
150GPa	0.3	7.75MPa	0.54N/mm	2.56E-2 mm

Table 3.4.2. Dimensions of DCB.

a_0	L	H	B
50mm	100mm	2mm	1mm
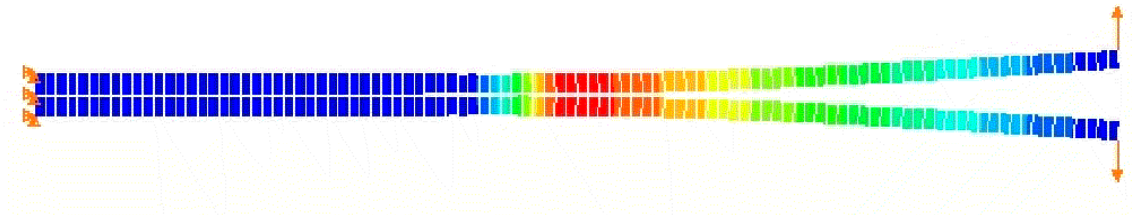
Figure 3.4.4. Finite Element Mesh for DCB Configuration

The comparison of the finite element solution and the close form solution from equations (35) and (36) is shown in figure 3.4.5. The response of DCB from the numerical simulation agrees well with the analytical solution, which validates the effectiveness of the user defined subroutine to simulate cracking using the cohesive crack approach.

Simulation of Low Temperature Cracking in Asphalt Pavements

The cohesive zone model model described in the previous paragraphs was used to simulate thermal cracking in an asphalt pavement exposed to a single temperature drop. In the simulation the material is assumed to be elastic and the material parameters used in the simulation do not change with temperature and time. This assumption represents the worst case scenario for the materials investigated, which in reality are viscoelastic materials.

185

Future research will incorporate the time-temperature dependent properties of the asphalt mixtures in the cohesive zone crack propagation model.
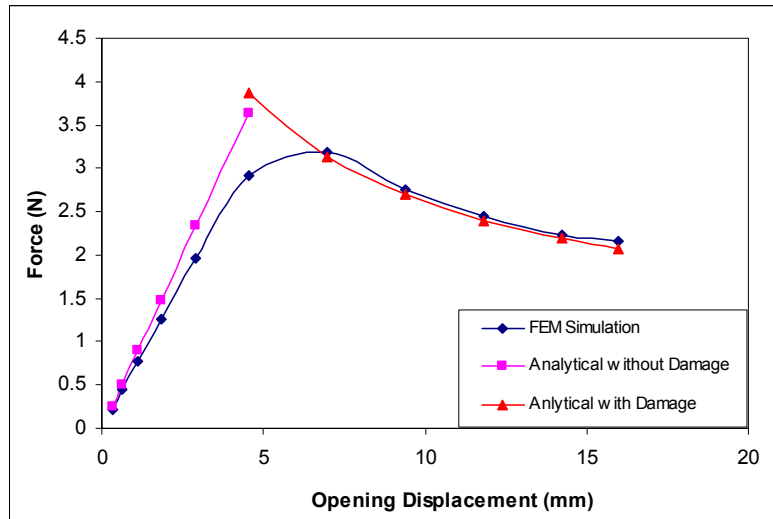
Figure 3.4.5. Analytical Solution and Finite Element Results for DCB Configuration.

Geometry Of Asphalt Layer

Initially, the asphalt layer is infinite in length. After it cracks, the pavement turns into consecutive segments with finite length defined as crack spacing. If we consider two consecutive segments, the middle planes of these segments in the longitudinal direction do not move due to symmetry. If a constant value of cracking spacing is considered then the asphalt layer can be simulated as a series of infinite similar segments with length equal to the constant crack spacing and thickness equal to the measured asphalt thickness, as shown in figure 3.4.6.
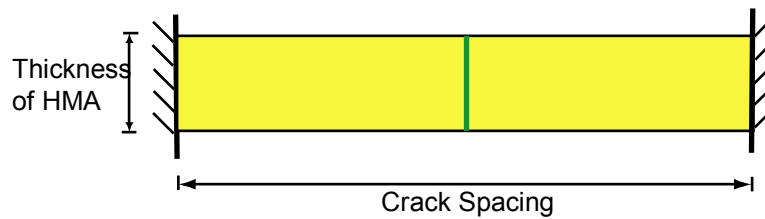
Figure 3.4.6. Geometry of Asphalt Layer in Numerical Simulation

186

At this time no frictional restraint is assumed at the bottom of the asphalt layer due to lack of reasonable information about the frozen base cohesion, friction angle, and thermal coefficient of contraction. However, the model allows adding this restraint once the data becomes available in the future.

Selection Of Parameters

The inputs parameters in this simulation include the field mean crack spacing, the elastic modulus, the tensile strength and the fracture energy of the asphalt mixtures, the thermal coefficient of contraction of asphalt mixture, and the temperature gradient within the thickness of the asphalt layer.

Mean Crack Spacing

The mean crack spacing used was calculated from the Mn/ROAD crack mapping data collected in February 2003. There are 14 flexible pavement cells in the mainline of Mn/ROAD with the thickness of asphalt layer varying from 5.9 in. (150 mm) in cell 1 to 11.1 in. (282 mm) in cell 15. Considering the effect of thickness on the crack spacing of asphalt pavement, the ratio of the mean crack spacing to the thickness is used to select the dimension of asphalt pavement segments (note that cells 33, 34, and 35 did not crack at the time this analysis was performed). This ratio varies between 15 and 35 in the 14 cells. A ratio of 20 was chosen to represent the average situation of transverse cracking in MnRoad and a length of 4000-mm and a thickness of 200-mm was used in the simulation.

Elastic Modulus, Tensile Strength and Fracture Energy

A constant value of 15GPa was assumed for the elastic modulus of the three mixtures. Previous work performed by Reinke (107) showed that the tensile strength for 58-28 and 58-34 mixture varied from 2.5MPa to 4.2MPa. A constant value of 3MPa was chosen for the three mixtures in the calculations. Two sets of values for the fracture energy were used in the simulation: the fracture energies determined at -40°C and at -30°C as described in chapter 3.1.

Thermal Coefficient of Contraction

Research performed by Stoffels and Kwanda (50) determined the thermal coefficient of contraction of different asphalt mixture varied from 1.33 to 2.95×10^{-5}m/m/ºC. A recent study by Nam and Bahia (108) showed that the same asphalt mixture had a different thermal coefficient of contraction above and below the glass transition temperature. Their data showed that above the glass transition temperature the thermal coefficient of contraction varied from 5.79 to 9.66×10^{-5}m/m/ºC, and below the glass transition temperature from 0.3 to 3.43×10^{-5}m/m/ºC. In this simulation a value of 2×10^{-5}m/m/ºC was used to represent the thermal coefficient of contraction at temperatures below the glass transition temperature.

Temperature Gradient

At the beginning of the simulation the asphalt layer has a uniform temperature field. To simulate the temperature gradient that exists in the field different temperature drop rates were used at the surface and at the bottom of asphalt layer such that at the end of the simulation the temperature gradient matched average values measured in the field at MnRoad facility. For this purpose the available temperature gradients measured at 8 am on February 2nd, 1996, when the pavement temperature dropped to -39ºC, were used tan average gradient. Based on the data included in table 3.4.3 a temperature gradient of 1:36 ºC/mm was used in the simulation. The temperature drop used in the simulation was 40ºC.

Results Of Simulation

The simulation shows the damage accumulation and crack propagation when temperature drops. The mesh used in the simulation is shown in figure 3.4.7. Since this is a symmetrical geometry, only half of the asphalt layer is shown.

Recall the exponential traction-separation constitutive behavior of the cohesive crack in figure 3.4.1 in which the traction is reduced to zero asymptotically as the separation increases after the peak traction. Physically, when the traction across the crack is reduced to a small value, it defines the complete separation of the two surfaces of the cohesive crack and therefore the crack front. In this research the location in the process zone where the traction is reduced to 5% of the tensile strength is taken as the crack front. From equation (10) the corresponding separations for the three mixtures were calculated to be 0.154-mm for 58-28 mixture, 0.187-mm for 58-34 mixture, and 0.22-mm for 58-40 mixture.

Table 3.4.3. Temperature Profile from MnRoad Cells 1, 14 and 15.

Cell ID	Depth (mm)	Temperature(C)	Gradient (C/mm)
Cell 1	30	-34.61	1:29
	55	-33.94	
	158	-31.06	
Cell 14	30	-34.44	1:36
	58	-33.83	
	134	-31.67	
	271	-27.83	
Cell 15	27	-35.17	1:36
	52	-34.5	
	131	-32.11	
	287	-27.06	
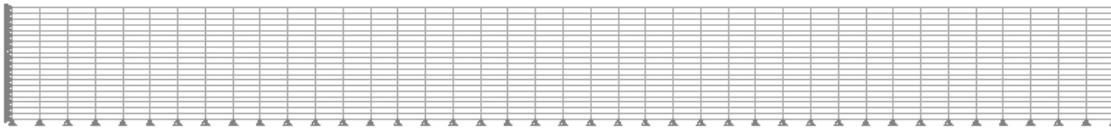
Figure 3.4.7. Mesh of Half of Asphalt Layer

The horizontal displacements of nodes at the left surface of cohesive crack, u_1, are extracted from the computation results and plotted in figure 3.4.8. Since this displacement u_1 is half of the separation, the plots of u_1 show the same trend of change as the separation of cohesive crack. All three mixtures show similar behavior with temperature drop. The u_1 curve is divided into three zones. The separation of cohesive crack starts to increase with a slow rate, called zone 1. At a step around 0.3, which corresponds to a temperature drop of -12°C at the surface, there is a sudden jump on the u_1 curve, called zone 2. Then the separation increases with a constant rate, which is higher than that in zone 1, until the end of the simulation, called zone 3.

a. u_1 **for 58-28 Mixture**

b. u_1 **for 58-34 Mixture**

190

c. *u₁* for 58-40 Mixture

Figure 3.4.8. *u₁* **for the Three Mixtures investigated.**

As discussed before, the cohesive crack model concentrates the global damage into a local area of the cohesive crack. In zone 1 is the localized damage accumulates and the soften zone in the material grows along the cohesive crack represented by the interface element in the numerical simulation. In zone 2 the crack starts to propagate and looses its stability quickly. In zone 3 the material shrinks freely due to the temperature drop.

There is no clear boundary between zone 1 and zone 2 because the damage in the material accumulates gradually. In order to show the accumulation of damage the stress contour is plotted at different increments. Since all three mixtures show the similar behavior, only the stress contour plots for 58-28 mixture are shown in figure 3.4.9. Different colors in the stress contour plot stand for different stress level and the corresponding stress level can be read from the legend at the top of figure 3.4.9. The number at the left of the stress contour

is the ID of the increment used in the simulation, which can be converted to the temperature drop at the surface of the asphalt layer. Within each increment an iterative process is performed based on the solution at the end of the previous increment to obtain a converged solution at the end of the current increment. This assures the reliability of the solutions at the end of the step.

At increment 16 the node at the surface of asphalt layer along the cohesive crack starts to soften, as the stress level reaches the tensile strength in the stress contour, and the damage stars to accumulate in the asphalt mixture. From increment 16 to 23 the nodes for which the stress reaches the tensile stress move down along the cohesive crack in the thickness direction and the stress at the node at the surface is reduced to less than the tensile strength, which means this node moved downwards on the post-peak part of the traction-separation curve. At the increment between 23 and 27 all the nodes on the cohesive crack reach and exceed the tensile strength and fall on the post-peak part of the traction-separation curve. At the increment 27 and 28 the separation of cohesive crack continues to increase and damage continues to accumulate with the temperature drop. During increment 29 at some of the nodes at upper part of the cohesive crack the traction dropped below the assumed criterion for the crack front and the crack tip emerged. At increment 30 tractions at all the nodes on the cohesive crack are lower than the pre-assumed criterion and the crack propagates down to the bottom of asphalt layer. After this increment the local stability is lost, the asphalt layer fractures into two parts and experiences the typical thermal shrinkage with one end fixed and the other end with small tractions and almost free of constraint.

Tables 4 and 5 show the temperature drop values for which the asphalt mixture starts softening (T_s) and the crack propagates to the bottom of asphalt layer (T_p). The crack separation (D_p) at the temperature where the crack propagates to the bottom of the asphalt layer and at the end of simulation when the temperature drop is -40°C (D_e) are also listed in tables 4 and 5. Note that in table 3.4.4 the fracture energies determined at -40°C were used while in table 3.4.5 the fracture energies determined at -30°C were used. The results indicate that for all three mixtures and for both sets of fracture energy values the crack start to propagate when the surface temperature dropped by approximately 11°C and that the crack propagates to the bottom of the asphalt layer after another half a degree drop in temperature which indicates an almost instant propagation after the softening point is reached.
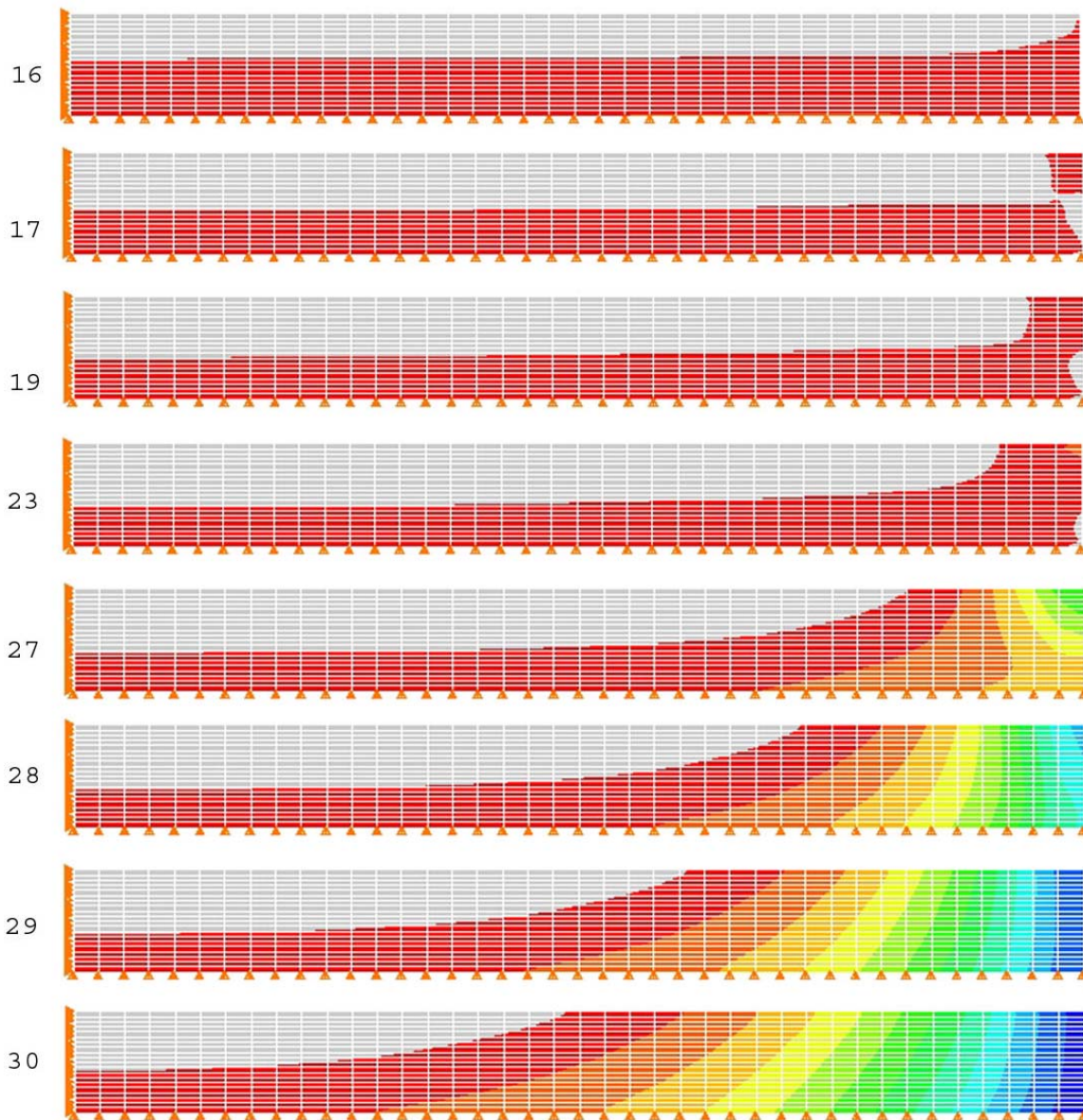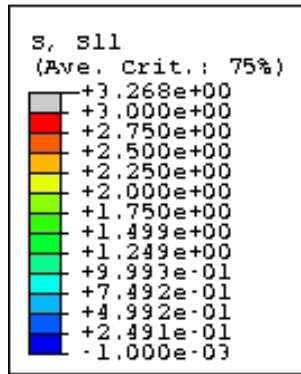
Figure 3.4.9. Material Softening.

193

Table 3.4.4. Characteristic Temperature Drops Using Fracture Energies Measured at -40°C.

Mixture	T_s (°C)	T_p (°C)	D_p (mm)	D_e (mm)
58-28	10.92	11.36	0.17	2.95
58-34	10.96	11.52	0.23	2.95
58-40	11.2	11.68	0.25	2.95

Table 3.4.3. Characteristic Temperature Drops Using Fracture Energies Measured at -30°C.

Mixture	T_s (°C)	T_p (°C)	D_p (mm)	D_e (mm)
58-28	11.1	11.44	0.22	2.95
58-34	11.2	11.68	0.26	2.95
58-40	11.3	11.72	0.27	2.95

Conclusions

In this chapter a cohesive crack model was developed to analyze the thermal cracking mechanism in asphalt pavements exposed to low temperatures. The numerical model was validated against the DCB configuration for which an analytical solution exists. Numerical simulations were performed for the three mixtures evaluated to simulate the thermal crack development in an asphalt pavement. Due to the high complexity of the calculations the model parameters were kept independent of time and temperature, which is not typical for asphalt pavement behavior at low temperatures. However, the cases analyzed are representative of worst case scenarios in which the pavement acts as an elastic material, with properties characteristic of extreme low temperatures, exposed to an increasing thermal stress. The results obtained indicate that based on the parameters values used the three mixtures do not behave very differently. The analysis also indicates that after the crack

initiates it takes very little additional temperature decrease, approximately 0.5°C, to propagate the crack completely. However, if the temperature drop is less than this value the crack does not propagate completely.

The results obtained in this analysis should be interpreted with caution. Asphalt materials are temperature and loading rate dependent and the analysis should include this variation in the future. A simple example is the accumulation of thermal stress which in viscoelastic materials is described by the hereditary integral due to the time and temperature dependence of the relaxation modulus. Some of the parameters used in the model were not available, such as strength, and average values determined in other research and at different temperatures were used. The frictional restraint from the aggregate base was not considered in the analysis due to the lack of consistent information on the properties of frozen base materials. Also the aging gradient that may play a significant role in the evolution of the crack was not considered.

In conclusion, the model developed in this chapter has a strong potential to effectively simulate the fracture mechanism in asphalt pavements at low temperatures. In future research the model will be modified to represent more realistic field conditions. However, as shown in this chapter, it is critical to obtain material properties that are representative of the material behavior for typical field temperature and loading conditions.

PART 4. DEVELOPMENT OF PERFORMANCE CRITERIA

Low temperature cracking is the major distresses in asphalt pavements in the northern U.S. and Canada. The current specifications address this issue based on creep and strength tests performed at low temperatures on both asphalt binders and asphalt mixtures. As part of the newly released Design Guide, a thermal cracking (TC) model was developed that predicts the performance of a given pavement in terms of crack spacing and service life. In the past years an increasing number of researchers have realized the limitations of the current system and started to investigate the use of fracture mechanics based tests and analyses to address the low temperature cracking issue. Anecdotal evidence also indicated the need to consider the effect of the entire pavement system, in particular of the granular base materials, in the analysis.

In this research the role of the aggregate base and the development of fracture mechanics based experimental procedures and analyses were investigated in order to refine the material selection process and to improve the prediction of field performance with respect to low temperature cracking. A summary of the findings is given below.

SUMMARY

In Part 1 a frictional restraint crack spacing model was developed and tested. First a literature search was performed on the existing thermal cracking models. It was found that none of the existing models accounted for traffic effects, and that only the Fictitious Crack Model took interface friction into consideration. As a consequence a mechanistic pavement model that can predict thermal crack spacing was developed. The model is based upon a two-dimensional continuum, solved by the finite difference method employed in commercial available software FLAC, and considers the frictional properties of the supporting granular material in the analysis. It was found that the frictional properties of the supporting layer have a significant effect on the stress relief near the free edge of a pavement surface layer. The stress relief region was used to explain the regularity of crack spacing in that cracks will not form in regions below a threshold stress level. Further, through simulation, it was found that the addition of thermal gradients and traffic loads to the model would effectively shorten

the crack spacing and increase the amount of cracking. These observations are consistent with thermal cracking field performance.

The model was then tested to assess whether the thermal cracking model would predict crack spacing consistent with field observations. Data pertaining to four full-scale pavement test sections at Mn/ROAD were gathered and entered into the thermal cracking model. The results of the comparison showed that the thermal cracking model passes the test of reasonableness.

In Part 2, a test procedure was developed to measure the fracture properties of asphalt mixtures at low temperatures. Based on the results of a comprehensive literature search, two configurations emerged as potential candidates for the low-temperature fracture testing of asphalt mixtures: the modified IDT test and the SCB test.   The SCB test was selected for further use in the experimental work and a test protocol based on CMOD control was selected to determine the fracture properties of three asphalt mixtures used at Mn/ROAD facility.

At the end of Part 2 the frictional restraint model developed in part 1 was revisited based on new information about the properties of the aggregate base materials that was not available at the time Part 1 was finalized. The cohesion (C) and friction angle (Φ) of the base layers obtained from triaxial tests were used to compute the crack spacing. Significant differences were found in some instances between the model prediction and the field crack spacing which indicated the need for obtain accurate material properties for base layers in frozen state.

In Part 3 the data analysis of the experimental work was performed and some of the material parameters obtained in the analysis were used to develop a crack propagation model based on the cohesive zone model approach. In the experimental work three parameters were calculated: stiffness, fracture toughness, and fracture energy. Statistical analysis was used to determine the significance of the effects of the type of binder, specimen location, and environmental temperature. Both the fracture toughness and the fracture energy changed as the test temperature changed, which clearly indicated that the fracture properties of asphalt mixtures, similar to other mechanical properties of asphalt mixture, are temperature-dependent. The binder effect was also found significant, which confirmes the significant role played by the asphalt binder in the low temperature fracture properties of asphalt mixtures

Also in Part 3 the Thermal Cracking (TC) model, incorporated in the recently released American Association of State Highway and Transportation Officials (AASHTO) Design Guide and the general cohesive zone model approach were reviewed and the advantages and disadvantages of the two models were discussed. The crack spacing prediction from the TC model and from the frictional restraint model developed in Part 1 were tested again field data collected from Mn/ROAD. It was found that the frictional restraint model predicted reasonable crack spacing values, which in one case were not significantly different than the field values, while the TC model did not predict any cracking.

The last chapter of Part 3 a cohesive crack model to analyze the thermal cracking mechanism in asphalt pavements exposed to low temperatures was developed. Numerical simulations were performed for the three mixtures to simulate the thermal crack development in an asphalt pavement. Due to the high complexity of the calculations, the model parameters were kept independent of time and temperature, which is an oversimplification of asphalt pavement behavior at low temperatures. The predicted crack evolutions indicated that, based on the material parameters used, the three mixtures do not behave very differently. The analysis also indicated that after the crack initiated it took very little additional temperature decrease, approximately 0.5°C, to propagate the crack completely. The analysis indicated that the model has the potential to effectively simulate the fracture mechanism in asphalt pavements at low temperatures. The effectiveness of the model is strongly dependent on material properties that are representative of the material behavior for typical field temperature and loading conditions, which were not available at the time this research was finalized.

RECOMMENDATIONS FOR DEVELOPMENT OF PERFORMANCE CRITERIA

The analyses performed in this research showed that the TC model included in the recently released Design Guide does is of limited value and does not correctly predict performance in climates dominated by severe temperature regimes in which single event cracking are the predominant failure mechanism at low temperatures. Based on the results obtained in the previous three parts the following recommendations are made for the development of future low temperature performance criteria:

1.   At this time the frictional restraint model developed in Part 1 can be used to obtain approximate crack spacing for comparison purposes only. In order to improve the model predictions to a confidence level that would allow the incorporation of the model into a design specification the following improvements are needed:

- First, the material parameters used in the model need to be determined at temperatures similar to the observed cracking temperatures in the field. This requires performing IDT strength tests at temperatures similar to the test temperatures used to determine the constituent asphalt binder PG lower limit. The loading rate should follow the current IDT specification until future research determines a loading rate that better simulates the field thermal stress development. It also requires determining the cohesion and friction angle of aggregate base in conditions that simulate closely field frozen base conditions. It is expected that using the material parameters recommended above the current 1D model could reasonably predict crack spacing for design scenarios that require a less complex level of analysis.

- Second, the model needs to incorporate the viscoelastic behavior of the asphalt mixtures and to be expanded to 2-D and 3-D conditions. The issue of a smooth versus rough interface between the asphalt layer and the aggregate base should be investigated as part of the expanded model.

These issues will be addressed in a comprehensive national pooled fund study which will continue the work performed in this research effort.

2.   In order to improve the selection process of asphalt mixture with increased fracture resistance at low temperatures it is recommended that SCB tests should be performed according to the procedure developed in Part 2. Tests should be performed at three temperatures similar to the test temperatures used to determine the constituent asphalt binder PG lower limit and both the fracture toughness and fracture energy should be calculated. Based on the limited results obtained in this study the following approach is recommended for the selection process:

- Plot the fracture toughness versus temperature and determine the temperature at which the toughness approximately reaches a peak value. This temperature represents the critical temperature for the mixture. For similar critical temperatures

higher toughness mixtures are expected to have better cracking resistance than the lower ones.

- Plot the fracture energy versus temperatures. For similar toughness behavior it is expected that mixtures with higher fracture energy at temperatures around the critical temperature will have better resistance to crack propagation than the lower fracture energy ones.

Future research may lead to the development of limiting values for fracture toughness and fracture energy similar to the current PG specification approach. At this time it is safe to say that at temperatures similar to the binders PG lower limits the asphalt mixtures that have higher fracture toughness and higher fracture energy values are better performers.

3. The analysis performed in Part 3 has demonstrated the potential of using the cohesive zone model approach to effectively simulate the fracture mechanism in asphalt pavements at low temperatures. The analysis incorporates the material parameters used in the material selection process described above. Based on the limited analysis performed in this study the following recommendations are made:

- The analysis based on the elastic approach and temperature independence of the material fracture parameters cannot reasonably predict the crack propagation in asphalt materials.
- Temperature specific values for the parameters used in the model need to be determined experimentally and the analysis needs to be changed to incorporate the viscoelastic thermal stress development in asphalt mixtures.

These issues will be addressed as part of a larger national research effort, which will also include the entire pavement system in the cohesive zone model and incorporate the frictional restraint model in the analysis. The model developed in part 3 represents only the first step in the developing of a comprehensive model that reasonably predicts low temperature behavior of asphalt pavements and should not be used for design purposes at this time.

REFERENCE

1. Anderson, K.O., et al, "Cracking of Asphalt Pavements Due to Thermal Effects," Proceedings, Association of Asphalt Paving Technologists, Vol. 35, 1966, pp. 247-262.

2. Fromm, H.J., Prepared Discussion, Proceedings, Association of Asphalt Paving Technologist, 1966, Vol. 35: 324

3. Culley, R.W., "Temperature Cracking of Flexible Pavements in Saskatchewan," Saskatchewan Department of Highways, Technical Report 3, June, 1966.

4. Deme, I., "Ste. Anne Test Road, Two Years Progress Report of Pavement Cracking," Manitoba Department of Transport, Internal Report 69-1, 1969.

5. McLeod, N.W., "Reduction in Transverse Pavement Cracking by Use of Softer Asphalt Cements," The Highway Research Board Western Meeting, Denver, August, 1968.

6. Kingham, R.I., Prepared Discussion, Proceedings, Association of Asphalt Paving Technologists, Vol. 35, 1966, p. 329.

7. Marker, V., "Introduction to Non-Traffic Load Associated Cracking of Asphalt Pavements," Proceedings, Association of Asphalt Paving Technologists, Vol. 35, 1966, p. 239-247.

8. Zube, E., "Cracking of Asphalt Pavements Associated with Absorptive Aggregates," Proceedings, Association of Asphalt Paving Technologists, Vol. 35, 1966, pp. 270-290.

9. Kelley, J.E., "Cracking of Asphalt Concrete Pavements Associated with Volume Changes in Underlying Materials and Base Courses," Proceedings, Association of Asphalt Paving Technologists, Vol. 35, 1966, pp. 290-292.

10. Campen, W.H., Prepared Discussion, Proceedings, Association of Asphalt Paving Technologists, Vol. 35, 1966, pp. 309-312

11. Serafin, P.J., Prepared Discussion, Proceedings, Association of Asphalt Paving Technologists, Vol. 35, 1966, pp. 314-318.

12. Yoder, E.J., and Witczak, M.W., Principles of Pavement Design, 2nd Edition, John Wiley and Sons, Inc., New York, 1975.

13. Kirkner, David J. and Shen, Weixin, "Numerical Simulation of Thermal Cracking of Asphalt Pavements," Transportation Research Board Preprint, Washington, D.C., 1999.

14. Fromm, H.J. and Phang, W.A., "A Study of Transverse Cracking of Bituminous Pavements," Proceedings, Association of Asphalt Paving Technologists, Vol. 41, 1972, pp. 383 - 423.

15. Ovik, Jill M., "Characterizing Seasonal Variations in Pavement Material Properties for Use in a Mechanistic-Empirical Design Procedure", Master's Thesis, University of Minnesota, 1998.

16. Haas, R., Meyer, F., Assaf, G. and Lee, H., "A Comprehensive Study of Cold Climate Airport Pavement Cracking," Proceedings, Association of Asphalt Paving Technologists, Vol. 56, 1987, pp. 198-245.

17. Hills, J.F. and Brien, D., "The Fracture of Bitumens and Asphalt Mixes by Temperature Induced Stresses," Prepared Discussion, Proceedings, Association of Asphalt Paving Technologists, Vol. 35, 1966, pp. 292 - 309.

18. Haas, R.C.G., "A Method of Design Asphalt Pavements to Minimize Low-Temperature Shrinkage Cracking," The Asphalt Institute, Research Report RR-73-1, College Park, Maryland, 1973.

19. Christison, J.T., Murray, D.W. and Anderson, K.O., "Stress Prediction and Low Temperature Fracture Susceptibility of Asphaltic Concrete Pavements," Proceedings, Association of Asphalt Paving Technologists, Vol. 41, 1972, pp. 494-523.

20. Shields, B.P., Anderson, K.O. and Dacyszyn, J.M., "An Investigation of Low Temperature Transverse Cracking of Flexible Pavements," *Proceedings of the Canadian Good Roads Association*, 1969.

21. Young, F.D., Deme, I., Burgess, R.A. and Kopvillem, O., "Ste. Anne Test Road--Construction Summary and Performance After Two Years of Service," *Proceedings of the Canadian Technical Asphalt Association*, 1969.

22. Finn, F., Saraf, C.L., Kulkarni, R., Nair, K., Smith, W., and Abdullah, A., "User's Manual for the Computer Program Cold," NCHRP Report 1-10B, Transportation Research Board, Washington, D.C., 1977.

23. Finn, F., Saraf, C.L., Kulkarni, R., Nair, K., Smith, W., and Abdullah, A., "Development of Pavement Subsystems," NCHRP Report 291, Transportation Research Board, Washington, D.C., 1986.

24. Hiltunen, D.R. and Roque, R., "A Mechanics-Based Prediction Model for Thermal Cracking of Asphaltic Concrete Pavements," Association of Asphalt Paving Technologists, Vol. 63, 1994, pp. 81-117.

25. Hiltunen, D.R. and Roque, R., "The Use of Time-Temperature Superposition to Fundamentally Characterize Asphaltic Concrete Mixtures at Low Temperatures," Engineering Properties of Asphalt Mixtures and the Relationship to their Performance, ASTM STP 1265, Gerald A. Huber and Dale S. Decker, Eds., American Society for Testing and Materials, Philadelphia, 1995.

26. Paris, P.C. and Erdogan, F., "A Critical Analysis of Crack Propagation Laws," Transactions of the ASME, Journal of Basic Engineering, Series D, 85, No. 3, 1963.

27. Chang, H.S., Lytton, L.R. and Carpenter, H.S., "Prediction of Thermal Reflection Cracks in West Texas," Report TTI-2-8-73-18-3, Texas Transportation Institute, Texas, 1976.

28. Schapery, R.A., "Correspondance Principles and a Generalized J Integral for Large Deformation and Fracture Analysis of Viscoelastic Materials," *International Journal of Fracture*, Vol. 25, 1984, pp. 195-223.

29. Schapery, R.A., "Time-Dependent Fracture: Continuation Aspects of Crack Growth," Encyclopedia of Materials Science and Engineering, M.B. Bever (Ed.), Permagon Press, Elmsford, NY, 1986, pp. 5043-5053.

30. Molenaar, A.A.A., "Structural Performance and Design of Flexible Road Constructions and Asphalt Concrete Overlays," Ph.D. Dissertation, Delft University of Technology, Netherlands, 1983.

31. Lytton, R.L., Shanmugham, U. and Garrett, B.D., "Design of Asphalt Pavements for Thermal Fatigue Cracking," Research Report 284-4, Texas Transportation Institute, 1983.

32. Wittmann, F.H., Fracture Mechanics of Concrete, Elsevier, New York, 1983.

33. Hillerborg, A., Modeer, M., Peterson, P.E. "Analysis of Crack Formation and Crack Growth in Concrete by Means of Fracture Mechanics and Finite Elements". Cement and Concrete Research, Vol. 6, 1976: 773-782

34. Ingraffea, A.R., "Nonlinear Fracture Models for Discrete Crack Propagation," Application of Fracture Mechanics to Cementitious Composites, Shah eds, 1984, pp. 247-285.

35. Jenq, Y.S. and J.D. Perng, "Analysis of Crack Propagation in Asphalt Concrete Using Cohesive Crack Models," *Transportation Research Record* No. 1317, Transportation Research Board, Washington, D.C., 1991, pp. 90-99.

36. Yao, B. and Murray, D., Prediction of Distributed Cracking in RC Analysis," *Journal of Structural Engineering*, Vol. 119, 1993, pp. 2813-2834.

37. Gerstle, W.H. and Xie, M., "FEM Modeling of Fictitious Crack Propagation in Concrete," *Journal of Engineering Mechanics*, Vol. 118, 1992, pp. 416-434.

38. Jung, D.H. and Vinson, T.S. "Low Temperature Cracking: Binder Validation", SHRP A-399, Strategic Highway Research Program, National Research Council, 1994.

39. Coetzee, M.J., Hart, R.D., Varona, P.M., Cundall, P.A., FLAC Basics, Revised Edition, Itasca Consulting Group, Inc., Minneapolis, MN, 1995.

40. FLAC User's Guide, Version 3.3, Itasca Consulting Group, Minneapolis, MN, 1995.

41. Alvarez, C. and Thompson, M., "Mechanistic-Empirical Evaluation of the Mn/ROAD Mainline Flexible Pavement Sections," Report No. FHWA-IL-UI-263, Project IHR-535, 1998.

42. Van Deusen, D., "Selection of Flexible Backcalculation Software for the Minnesota Road Research Project," Report No. MN/PR - 96/29, Minnesota Department of Transportation, 1996.

43. Bigl, S.R. and Berg, R.L., "Modeling of Mn/ROAD Test Sections with the CRREL Mechanistic Pavement Design Procedure," Report No. MN/RC-96/22, Minnesota Department of Transportation, St. Paul, MN, 1996.

44. Stroup-Gardiner, M. and Newcomb, D.E., "Investigation of Hot Mix Asphalt Mixtures at Mn/ROAD," Report No. MN/RC - 97/06, Minnesota Department of Transportation, 1997.

45. Jones, G.M., Darter, M.I. and Littlefield, G., "Thermal Expansion-Contraction of Asphaltic Concrete," Proceedings of the Association of Asphalt Paving Technologists, Vol. 37, 1968, pp. 56-97.

46. Das, B.M., Principles of Geotechnical Engineering, Third Edition, PWS Publishing Company, Boston, 1994.

47. Isackson, C., Boerner, D., and Dai, S., "Minnesota Road Research Project : Forensic Investigation," Report No. MN-RC-1999-33, Minnesota Department of Transportation, St. Paul, MN, 1999.

48. Sayles, F.H., "Triaxial and Creep Tests on Frozen Ottawa Sand," North Am. Contrib. 2d Int. Conf. Permafrost, Yakutsk, U.S.S.R., National Academy of Sciences, Washington, 1973.

49. "Minnesota Road Design Manual; Design Policy and Criteria," Minnesota Department of Transportation, 1982.

50. Stoffels, S.M. and Kwanda, F.D., "Determination of the Coefficient of Thermal Contraction of Asphalt Concrete Using the Resistance Strain Gage Technique," Journal of the Association of Asphalt Paving Technologists, Vol. 65, pp. 73-98, 1996.

51. Anderson, D. A., Christensen, D. W., Bahia, H. U., Dongre, R., Sharma, M. G., Antle, C. E., and Button, J., "Binder Characterization and Evaluation (SHRP A-369), Vol. 3, Physical Characterization", Strategic Highway Research Program, National Research Council, 1994.

52. "TP1-98, Method for Determining the Flexural Creep Stiffness of Asphalt Binder Using the Bending Beam Rheometer (BBR)," AASHTO Provisional Standards, Washington, D.C.: American Association of State Highway Transportation Officials, April 2000 edition.

53. "TP3-00, Method for Determining the Fracture Properties of Asphalt Binder Using the Direct Tension (DT)," AASHTO Provisional Standards, Washington, D.C.: American Association of State Highway Transportation Officials, April 2000 edition.

54. "MP1-98, Specification for Performance Graded Asphalt Binder," AASHTO Provisional Standards, Washington, D.C.: American Association of State Highway Transportation Officials, April 2000 edition.

55.   "MP1A-01, Specification for Performance Graded Asphalt Binder," AASHTO Provisional Standards, Washington, D.C.: American Association of State Highway Transportation Officials, to be printed.

56.   "TP9-96, Method for Determining the Creep Compliance and Strength of Hot Mix Asphalt (HMA) Using the Indirect Tensile Test Device," AASHTO Provisional Standards, Washington, D.C.: American Association of State Highway Transportation Officials, April 2000 edition.

57.   Bienawski, Z.T., and Hawkes, I., "Suggested methods for determining tensile strength of rock materials," International Journal of Rock Mechanics and Mining Sciences & Geomechanical Abstracts, 15: 99-103, 1978.

58.   Dongre, R., Sharma, M.G., Anderson, D.A., "Development of Fracture Criterion for Asphalt Mixtures at Low Temperatures," Transportation Research Record 1228, pp. 94-105, 1989.

59.   Anderson, T.L. "Fracture Mechanics: Fundamentals and Applications", 2nd edition, CRC Press, LLC, 1995

60.   Standard Test Method for Plane Strain Fracture Toughness for Metallic Materials (ASTM Method E399-90), Annual book of ASTM Standards, Part 10. American Society for Testing and Materials, Philadelphia, PA 506-515 (1992).

61.   Ouchterlony, Finn. "Fracture Toughness Testing of Rock with Core Based Specimens, The Development of an ISRM Standard", Engineering Fracture Mechanics 35: 351-366

62.   Fowell, R.J. (1995). "Suggested Method for Determining Mode I Fracture Toughness Using Cracked Cheveron Notched Brazilian Disc (CCNBD) Specimens", International Journal of Rock Mechanics and Mining Sciences & Geomechanics Abstracts, Vol. 32, No. 1: 57-64

63.   Chong, K.P. and Kuruppu, M.D. "New Specimen for Fracture Toughness Determination for Rock and Other Materials", International Journal of Fracture 26: R59-R62

64.   Thiercelin, M. and J. C. Roegiers (1986). "Toughness Determination with Modified Ring Test," 27th U.S. Symposium on Rock Mechanics, The University of Alabama, Tuscaloosa, Alabama: 615-619.

65. Lim, I. L., Johnston, I. W. and Choi, S.K. (1993). "Stress Intensity factors for Semi-Circular Specimens Under Three-Point Bending." Engineering Fracture Mechanics 44(3): 363-382.

66. Lim, I. L., I. W. Johnston, et al. (1994). "Fracture Testing of a Soft Rock with Semi-Circular Specimens Under Three point Bending. Part1-Mode I." International Journal of Rock Mechanics, Mining Science & Geomechanics Abstract 31: 199-212.

67. Lee, N. K. and S. A. M. Hesp (1994). "Low Temperature Fracture Toughness of Polyethylene-Modified Asphalt binders." Transportation Research Record 1436: 54-59.

68. Lee, N. K., G. R. Morrison, et al. (1995). "Low Temperature Fracture of Polyethylene-Modified Asphalt binders and Asphalt Concrete Mixes." Journal of the Association of Asphalt Paving Technologists 64: 534-574.

69. Garces Rodriguez, M., G. R. Morrison, et al. (1996). "Low Temperature failure in Particulate-Filled Asphalt Binders and Asphalt concrete Mixes." Journal of the Association of Asphalt Paving Technologists 65: 159-192.

70. Evans, A. G. (1972). "The Strength of Brittle Materials with Second Phase Dispersion." Philosophical Magazine 26: 1327-1344.

71. Hesp, S. A. M., B. J. Smith, et al. (2001). "The Effect of Filler Particle Size on Low and High Temperature Performance of Asphalt Mastics and Mixtures." Journal of the Association of Asphalt Paving Technologists, accepted for publication.

72. Champion, L., Gerard, J.F., Planche, J.P., Martin, D., Anderson, D.A. (2000). Low-Temperature Rheological and Fracture Properties of Polymer-Modified Bitumens. 2nd Eurasphalt and Eurobitume Congress, Barcelona.

73. Anderson, D. A., Champion – Lapalu, L., Marasteanu, M. O., Le Hir, Y., Martin, D., Planche, J. P., "Low-temperature Thermal Cracking of Bitumens as Ranked by Strength and Fracture Properties," Transportation Research Record 2001, in press.

74. Roy, S. D. and S. A. M. Hesp (2001). "Fracture Energy and Critical Crack Tip Opening Displacement: Fracture Mechanics Based Failure Criteria for Low-Temperature Grading of Asphalt Binders," Journal of the Canadian Association of Asphalt Paving Technologists, accepted for publication.

75.	Hesp, S.A., Marasteanu, M.O., Roy, S.D., Li, X., "Development of a Fracture Mechanics-Based Asphalt Binder Test Method for Low-Temperature Performance Prediction, " IDEA proposal submitted to NCHRP.

76.	Wells, A. A. (1962). "Unstable Crack Propagation in Metals," Proceeding of the Crack Propagation Symposium Cranfield, The College of Aeronautics, Cranfield, England.

77.	Ewalds, H. L. and R. J. H. Wanhill (1985). Fracture Mechanics. Delft, Holland.

78.	Gledhill, R. A., A. J. Kinloch, et al. (1978). "Relationship between Mechanical Properties of and Crack Propagation in Epoxy Resin Adhesive." Polymer 19: 574-582.

79.	Young, R. J. and P. W. R. Beaumont (1977). "Failure of Brittle Polymers by Slow Crack Growth." Journal of Materials Science 12: 684-692.

80.	"TP4-00, Method for Preparing and Determining the Density of Hot-Mix Asphalt (HMA) Specimens by Means of the Superpave Gyratory Compactor," AASHTO Provisional Standards, Washington, D.C.: American Association of State Highway Transportation Officials, April 2000 edition.

81.	Labuz, J.F. and Dai, S. (1994) "Cracking of Asphalt Concrete at Low Temperatures", final report, submitted to Center for Transportation Studies, University of Minnesota.

82.	Roque, R., z. Zhang, et al. (1999). "Determination of Crack Growth Rate Parameters of Asphalt Mixtures Using the Superpave IDT." Journal of the Association of Asphalt Paving Technologists 68: 404-433.

83.	Zhang, Z., R. Roque, et al. (2001). "Evaluation of laboratory Measured Crack Growth rate for asphalt Mixtures," Transportation Research Board, 80th Annual Meeting, Washington, D.C.

84.	Molenaar, J. M. M. and A. A. A. Molenaar (2000). Fracture Toughness of Asphalt in the Semi-Circular bend Test. 2000 Eurasphalt and Eurobitume Congress, Barcelona, Spain.

85.	Cornell Fracture Group http://www.cfg.cornell.edu/.

86.	Shih, de Lorenzi and German, "Crack Extension Modeling with Singular Quadratic Isoparametric Elements," International Journal of Fracture, 12, pp. 647-651, 1976

87. Dodds and Vargas, "Numerical Evaluation of Domain and Contour Integral for Nonlinear Fracture Mechanics: Formulation and Implementation Aspects," Report University of Illinois at Urbana-Champaign, Dept. of Civil Engineering, 1988.

88. Rybicki and Kanninen, "A Finite Element Calculation of Stress Intensity Factors by a Modified Crack Closure Iintegral," Engineering Fracture Mechanics, 9, pp 931-938, 1977.

89. RILEM Technical Committee 50-FMC. "Determination of the Fracture Energy of Mortar and Concrete by Means of Three-point Bend Tests on Notched Beams." Materials and Structures, No. 106, Jul-Aug, pp. 285-290, 1985

90. Petersson, P. E. "Crack Growth and Development of Fracture Zones in Plain Concrete and Similar Materials", Ph. D. Thesis, Lund Institute of Technology.

91. Kim, K. W., El Hussein, M. "Variation of Fracture Toughness of Asphalt Concrete under Low Temperature", Construction and building Materials, Vol. 11, No. 7-8, pp 403-411, 1997

92. Soules, T.F., Busbey, R.F., Rekhson, S.M., Markovsky, A. and Burke, M.A., "Finite Element Calculation of Stress in Glass Parts Undergoing Viscous Relaxation", Journal of the American Ceramic Society, Vol. 70, No. 2, 1987, pp 90-95

93. Schapery, R.A., " A Theory of Crack Initiation and Growth in Viscoelastic Media I: Theory Development", International Journal of Fracture, Vol.11, No.1, February 1975, pp. 141-159

94. Dugdale, D.S. "Yielding of Steel Sheets Containing Slits." Journal of the Mechanics and Physics of Solids, Vol. 8, 1960:100-108

95. Barenblatt, G.I. "The Mathematical Theory of Equilibrium Cracks in Brittle Fracture". Advances in Applied Mechanics (Dryden, H.L. and von Karman, Th., eds.), Vol. 7, Academic Press, Inc. new York, 1962: 55-129

96. Hillerborg, A. analysis of One Single Crack. Fracture Mechanics of Concrete (Wittmann, F.H., ed.), Elsevier Science Publishers, Amsterdam, The Netherlands, 1983: 223-249

97. Shen, W. and Kirkner, D.J. "Distributed Thermal Cracking of AC Pavement with Frictional Constraint", Journal of Engineering Mechanics, Vol. 125, No. 5, May, 1999: 554-560

98. Needleman, A. (1987). "A Continuum Model for Void Nucleation by Inclusion Debonding". Journal of Applied Mechanics, 54, 525–531

99. Needleman, A. (1990). "An Analysis of Decohesion along an Imperfect Interface". International Journal of Fracture, 42:21–40

100. Xu, X. and A. Needleman (1994). "Numerical Simulations of Fast Crack Growth in Brittle Solids". Journal of Mech. Phys. of Solids 42(9), 1397–1434

101. de Andres, A., Perez, J., and Ortiz, M. (1999). "Elastoplastic Finite Element Analysis of Three Dimensional Fatigue Crack Growth in Aluminum Shafts Subjected to Axial Loading". International Journal of Solid and Structure, 36:2231–2258

102. Schellekens, J. and R. de Borst (1993). "On the Numerical Integration of Interface Elements". International Journal for Numerical Methods in Engineering, 36, 43–66.

103. Z-H. Jin, G.H. Paulino and R. H. Dodds (2003). "Cohesive fracture modeling of elastic-plastic crack growth in functionally graded materials." Engineering Fracture Mechanics, Vol.70, No.14, pp.1885-1912.

104. Mi, Y., M. Crisfield, G. Davies, and H.-B. Hellweg (1998). "Progressive Delamination Using Interface Elements". Journal of Composite Materials, 32, 1246–1273.

105. Paulino, G.H., Song, S. H., Buttlar, W.G. (2004) "Cohesive Zone Modeling of Fracture in Asphalt Concrete". Preprint 5th International Conference RILEM "Cracking in Pavements" in Limoges, May 4-8, 2004

106. Rahulkumar, P., Jagota, A., Bennison, S.J., and Saigal, S. (2000) "Cohesive Element Modeling of Viscoelastic Fracture: Application to Peel Testing of Polymers". International Journal of Solids and Structures 37: 1873-1879

107. Reinke, G., Dai, S. (2001) "Performance Properties of Three Mixtures Constructed at the Mn/ROAD Test Site". Presented at 46th CTAA Meeting, November 19-21, Toronto, Ontario

108. Nam, K., Bahia, H. (2004) "Effect of Binder and Mixture Variables on Glass Transition Behavior of Asphalt Mixtures", presented at 2004 AAPT Annual Meeting, March 8-10, Baton Rouge, Louisiana.